AI-AEC-12721
GENERAL, MISCELLANEOUS,
AND PROGRESS REPORTS

NOTICE OF NONCLEARANCE PENDING PATENT REVIEW

ANNUAL TECHNICAL PROGRESS REPORT
AEC UNCLASSIFIED PROGRAMS
FISCAL YEAR 1968

The preceding Quarterly Progress Reports during GFY 1968 were:

NAA-SR-12570 - July-September 1967,
AI-AEC-12638 - October-December 1967, and
AI-AEC-12680 - January-March 1968.

ATOMICS INTERNATIONAL

A DIVISION OF NORTH AMERICAN ROCKWELL CORPORATION

CONTRACT: AT(04-3)-701
ISSUED:

DISCLAIMER

DISTRIBUTION

This report has been distributed according to the category "General, Miscellaneous, and Progress Reports," as given in the Standard Distribution for Unclassified Scientific and Technical Reports, TID-4500.

CONTENTS

AEC TASK	PROJECT	PAGE
5-A	Cross-Section Analysis	5
5-B	Fast-Spectrum Doppler Measurements	29
5-C	Basic-Theory Calculation – Region Dependent Flux Spectra	43
5-D	Integral Reactor-Physics Measurements	47
5-E	Basic-Theory Calculation – Monte Carlo Methods	61
6-A	Reactor Dynamics Simulator Development	69
6-C	Fission-Product Contamination and Control Studies	83
6-D & E	Sodium Fire Fission Product Release	111
6-G	Boiling-Studies for Sodium-Reactor Safety	131
8	Sodium-Reactor Experiment Operation	149
10-A	Coolant Management	155
10-B	Materials Management	161
10-C	Mechanical Properties in Sodium	165
10-D-1	Dynamic Loop Operation	185
10-D-2	Dynamic Loop Testing (Mechanical Properties)	187
10-D-3	Dynamic Loop Testing (Mass Transfer)	211
10-E-1	Modes-of-Failure and Helium Degradation	225
10-E-2	Modes-of-Failure (Engineering Properties)	243
11-A	Mixed Carbide Fuels (Basic Properties)	255
11-B	Mixed Carbide Fuels (Irradiation Studies)	261
11-C	Mixed Carbide Fuels (Casting Studies)	275
12	Sodium Chemistry	279
13	HNPF Retirement	309
15	High Temperature Chemistry	313
16	Radiation Chemistry	323
17	Electronic Structure of Metals and Alloys	329
18	Radiation Damage in Crystalline Solids	339
22	Radiation Chemistry of Chromosomes	357
25	Noise Analysis Instrumentation	363

UNCLASSIFIED TOPICAL REPORTS
PUBLISHED APRIL-JUNE 1968

AEC		Report No.	Title	Author(s)
Task	Distr			
10-C	UC-25	AI-AEC-12694	Biaxial Stress-Rupture Properties of Austenitic Stainless Steels in Static Sodium	W. T. Lee
10-D-2	UC-25	AI-AEC-12695	Thermal Gradient Effects on Stress-Rupture Behavior of Thin-Walled Tubing	J. H. Shively
10-D-3	UC-2	AI-AEC-12681	High Heat Flux Heater Development Status Report	R. L. McKisson, E. L. Babbe
10-E-1	UC-25	AI-AEC-12670	Helium Embrittlement of Type 316 Stainless Steel	D. Kramer
11-B	UC-25	NAA-SR-12629	Preparation of UC-W Specimens for an Irradiation Test of the Value of a Fine-Particle Dispersion in the Control of Fission Gas Swelling (EXP-NRX-9-101)	A. C. Hott
12	UC-4	AI-AEC-12671	Solubility of Copper in Sodium	R. L. Eichelberger, R. L. McKisson

Program: Reactor Development			
AEC Task: 5-A Reactor Physics, Cross Section Analysis			
Project Manager: H. A. Morewitz			
Reporting Period: Fiscal Year 1968			
General Order: 7701	Subaccount: 13130	AEC Category: 04-40-01-03.1	

Principal Scientists: H. Alter and C. L. Dunford

I. PROJECT OBJECTIVES

The objectives of this project include the evaluation, production, and maintenance of an up-to-date set of basic nuclear data; production and evaluation of multigroup constants; and the improvement of present day methods of neutronic calculations as related to microscopic and macroscopic nuclear data.

To accomplish these objectives, existing experimental and theoretical information on nuclear data will be surveyed, analyzed, and compiled. Automated methods will be developed for manipulating and evaluating large amounts of available nuclear data and for the periodic updating of compiled data. Nuclear model calculations will be developed, extended, and used to help fill gaps in the data. The optical model analyses have two prime goals: to develop and test improved nuclear optical models for energy regions of interest to the fast reactor program, and to develop sufficient confidence in the results of theoretical calculations so that they may be used confidently to predict neutron cross section data where no experimental data are available. An automated system will be developed and maintained for the ready production of multigroup constants, and spectra generating techniques for production of realistic multigroup constants will be developed and incorporated into the system.

II. TECHNICAL PROGRESS DURING FISCAL YEAR 1968

A. AUTOMATED (INTERACTIVE) NEUTRON CROSS SECTION EVALUATION SYSTEM, SCORE

Significant progress in the development of the interactive computer graphics program SCORE was made in a number of areas. These include data storage and retrieval, partitioned memory operation, data correction procedures, spline fitting methods, multilevel analysis of resonance cross sections, and the overlay of ENDF/B evaluated data with the experimental information from the SCISRS file.

A rapid data storage and retrieval system for SCISRS I experimental data was completed. Data for each element or isotope is stored in a separate data file in a convenient format for use by SCORE. A separate program SAP (SCISRS ADAPTION PROGRAM) was written to produce and maintain these data files. When a new isotope is requested by SCORE, the file handling procedures of OS/360 for the IBM 360 series computers are used to select the proper data file on the tape. The entire data file is then transferred to a direct access data set on a disk. In a direct access data set, any record may be accessed directly rather than sequentially. At present the direct access feature is only available in FORTRAN G. A search on reaction type and energy range is conducted in a set of tables contained in each file. If the search ends with a positive result, an index of a record in the direct access data set is returned. This index allows SCORE to begin retrieving data within 250 data points of the initial data point satisfying the evaluator's request. The improvement of this method over a sequential search of a 10,000 record data set is obvious.

SCORE has been successfully operated in a partition memory system. Briefly, a partitioned memory system contains two or more parts, each part containing a program to be executed. The partitions have a priority system, with highest priority having first call on the central processing unit. If the highest priority partition is in a "wait" state, the computer continues execution in the next highest priority partition. The display console is connected to the highest priority partition because a display console command to the central processing unit requires immediate response, but the time needed to satisfy the request is usually small. Normal operation of SCORE requires only 5 to 10 minutes of computer time for each hour of operation, thus allowing execution of batch jobs in the background partition with no noticeable loss of efficiency. The memory size required for operation of SCORE has been reduced to 200,000 bytes by efficient use of overlay features of the IBM-360 operating system.

A subprogram which incorporates a method for fitting spline curves[1] to experimental data has been added to the SCORE system. The curve fitting is accomplished by passing a spline curve through a series of nodes. The evaluator can enter a set of nodes which he believes will represent the experimental data. The method for entering nodes is through a tracking pattern which appears

on the face of the cathode ray tube.[2] This pattern may be moved to any position within the X-Y grid structure on the cathode ray tube by use of the light pen. When the center of the tracking pattern is properly located, the node is entered and appears as an asterisk on the face of the cathode ray tube. When all the required nodes have been entered, the evaluator may request a spline curve to be fit and displayed. The evaluator may proceed to improve the fit by adding, moving, or deleting nodes. Comparisons with linear fits to the nodes can be made through the linear fit option. Final adjustment of the nodes can be made with a least squares spline fitting procedure developed at Harwell.[3] A typical curve illustrating the results of spline fitting a set of experimental data is shown in Figure 1. The fitted spline is the curve that is passed through the asterisks; i.e., below about 13 Mev it is the lower of the two curves, while above that energy it is the curve extended over the full energy range.

An auxiliary computer program SCOFF, which reformats ENDF/B data tapes for the convenience of SCORE so that evaluated data from ENDF/B and experimental data from SCISRS may be displayed simultaneously was developed. The data currently retrieved includes ENDF/B Files 3, 4, and 5. Smooth cross

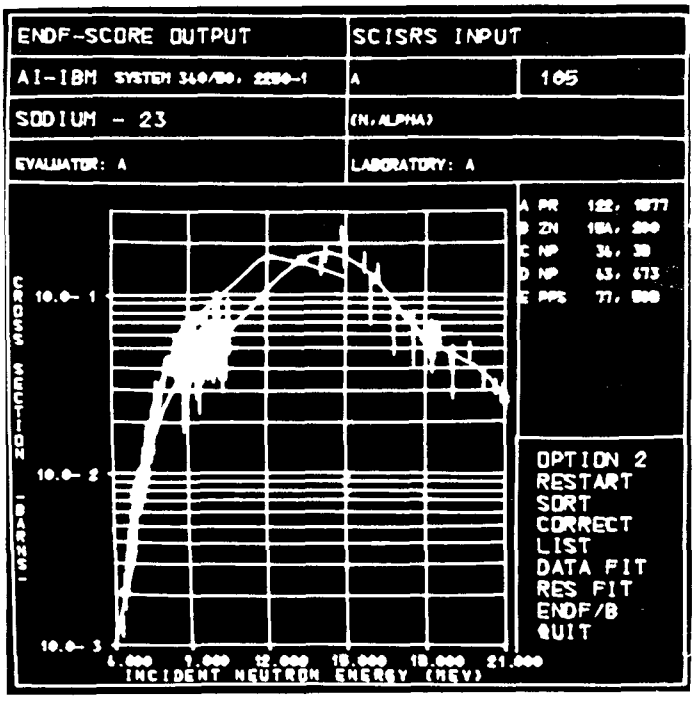

Figure 1. Spline Fit to Experimental Data

section data are retrieved from File 3. In File 4, the normalized angular distributions are formed and combined with the cross section value retrieved from File 3; in addition, the normalized discrete level inelastic data for a given energy range are formed and combined with the total inelastic cross sections retrieved from File 3. All of these capabilities have been successfully checked out and the necessary programming has been added to SCORE so that comparisons of the evaluated data from the ENDF/B files with the experimental data from the SCISRS files can be made rapidly. Such a comparison is presented in Figure 1. The SCISRS experimental data, represented by points with vertical error bars is compared with the ENDF/B evaluated data curve, the curve running from 6.0 to 15.0 Mev. This overlay is, in turn, compared with the fitted spline curve. In Figure 2, measured data representing a differential elastic scattering angular distribution is compared with an evaluated data set taken from the ENDF/B files.

A preliminary resonance parameter analysis of resonance cross sections with SCORE was completed. The current version of SCORE contains a resonance

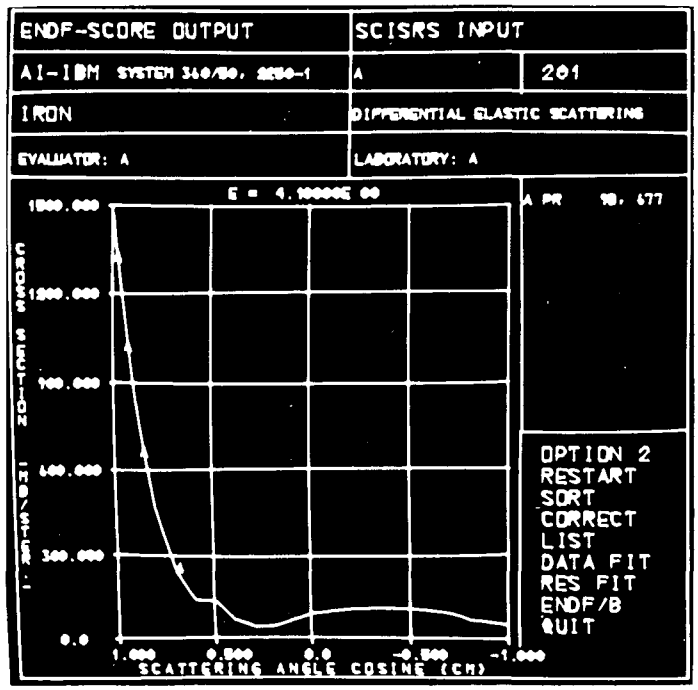

Figure 2. Comparison of Experimental and ENDF/B Evaluated Differential Elastic Scattering Data

region analysis module. A single-level or a two-channel Reich-Moore multilevel calculation has been incorporated, along with methods for resolution and Doppler broadening of the zero degree line shape. (That portion of the resonance region module which calculates the zero degree line shape and the resolution and Doppler broadened cross section was supplied by M. S. Moore and N. Marshall of the Idaho Nuclear Corporation.) The resonance region line shape is generated from a set of resonance parameters stored on a disk. The display generated, upon completion of the line shape calculation, compares the experimental cross section values and a curve representing the theoretical line shape.[4] An edit capability has been provided, in order to improve the fit to experimental data from a given set of resonance parameters. One can add or delete resonances, or modify the parameters for existing resonance data, and then recalculate the line shape for the new set of resonance parameters. In addition, it is possible to display a comparison of the revised line shape, the previously calculated line shape, and the experimental cross sections. A chi value is computed for each curve in order to provide a numerical comparison of the goodness of the fit of successive curves.

A comparison of single-level and multilevel fits to experimental data is illustrated in Figure 3. Superposed on the measured plutonium-241 fission cross section (dots), is the curve obtained from a multilevel fit, (curve through asterisks) and the curve due to a single-level analysis. Thus, an evaluator now has the capability for improving sets of resonance parameters, by interacting with his data through the computer and the console. Thus, a task which previously required several months to complete can now be performed in days, and perhaps even in hours.

B. ENDF/B COMPUTER CODES

In helping achieve the stated goals of ENDF/B development, a number of computer codes which manipulate, compare, and test data from the ENDF/B data files were written, checked out, documented, and distributed. Program PEND punches ENDF/B File 3 data for any specified reaction type; program CHEND processes AIENDF formated cross sections and adds a correction to any or all of the eleven cross section parameters; over a selected energy range, an option to calculate the total cross section by summing the partial cross sections

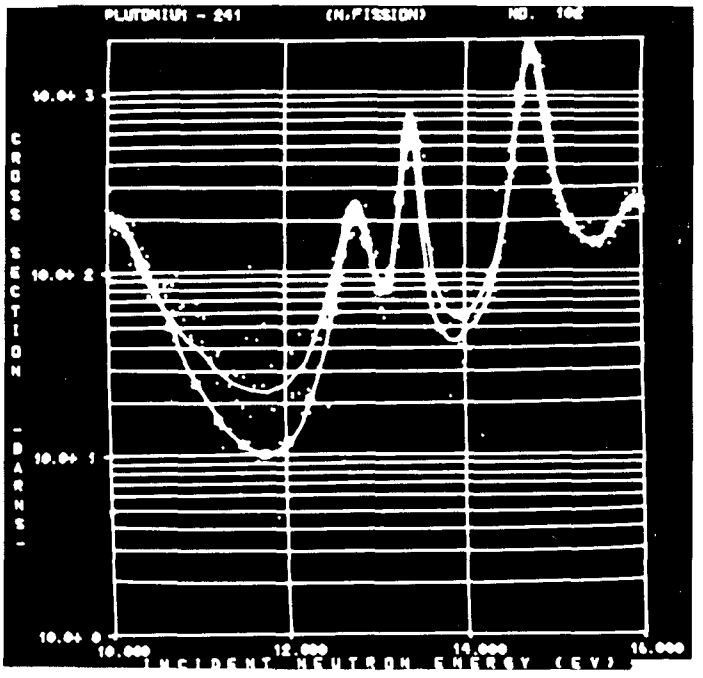

Figure 3. Comparison of Single Level and Multilevel Fits to Experimental Resonance Data

was introduced, and corrected cross section decks over the selected energy are punched. Program PLOTTER reads cross section data over a selected energy range for up to five sources of input and overplots the data on a single CRT frame for comparison. Program ENDFAI which punches cross section data from ENDF/B data tapes in the AIENDF format was modified in that the calculation or resonance elastic scattering now uses the single level Breit-Wigner formula without interference from neighboring resonances as required by the current ENDF/B specifications. The original version used the method taken from program UNICORN and will be retained for use when the ENDF/B specifications are changed.

A special prupose program MERGB3, was written to merge selected materials from up to 4 ENDF/B Mode 3 tapes. A considerable savings in machine time was realized in using this program instead of DAMMET for the merging of the data tapes.

Documentation on the computer program EDIT,[5] was released. This program is used to print and plot Files 1 through 4 for the new, Category I ENDF/B

Tapes 114, 115, and 116. All files on the ENDF/B preliminary distribution Tape 999 were plotted and examined.

Having written the ENDF/B subroutines for SCORE to retrieve required ENDF/B data needed to produce the discrete level inelastic scattering cross sections; these subroutines were incorporated into a special SCORE-ENDF/B program. The program which is operational on the IBM S/360-50 plots, prints, and/or punches discrete level inelastic cross section data obtained from a SCOFF tape. In addition, the program plots and/or prints any part of the File 3 data or any part of the combination of File 4 with File 3 data. This program was used to process ENDF/B sodium inelastic level data. Plots of the data for the first two levels appear in Figures 4 and 5.

Program OVERLAY was extended to include the plotting of Aldermaston cross section data. The program will now overlay plots of AIENDF, ENDF/B, and/or Aldermaston data for any desired energy range. The Aldermaston data input must be from cards using the MOMUS format; however, during the operation, this data is written on a tape which may be saved for future use. Figure 6 is an overlay plot of AIENDF, ENDF/B, and Aldermaston data for the fission cross section of Pu-239.

MC**2[6] was compiled and executed on the CDC-6600. The test problem for MC**2 was successfully run and requires less than 6 min on the CDC-6600. This compares to a running time of 27 min on the CDC-3600. The CDC-3600 is believed to be 2 to 4 times faster in execution than the IBM 360/50. The MC**2 test problem was kept simple and included only five nuclides.

A computer program to fit cubic spline curves to a set of differential elastic scattering data points was modified in order that one may optionally fit a cubic spline (a) directly to the input data or (b) to the log (base 10) of either one or both variables. A subroutine to generate a Legendre expansion of angular distribution data fitted by the spline curve was programmed and checked out. The fitting presently is being performed by linear interpolation on the spline curve with a mesh that may be varied from 201 to 1001 points. This program was to demonstrate the superiority of spline fitting angular data over the presently used linear fitting procedures. It was hoped that spline fitting of the angular data, being smoother in concept, would yield a smaller number of

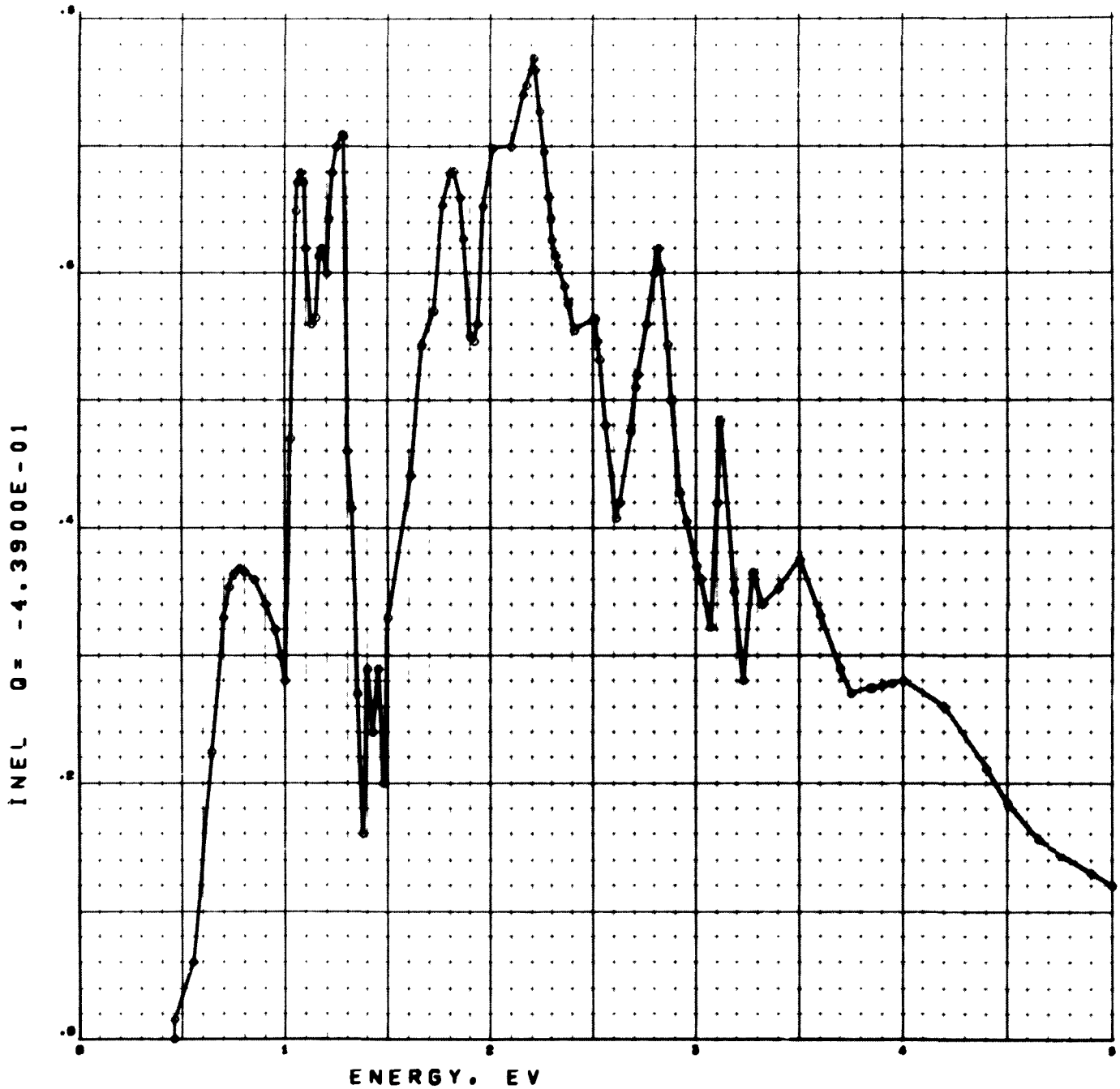

Figure 4. ENDF/B Inelastic Level Data (Sodium) Q = -0.439 Mev

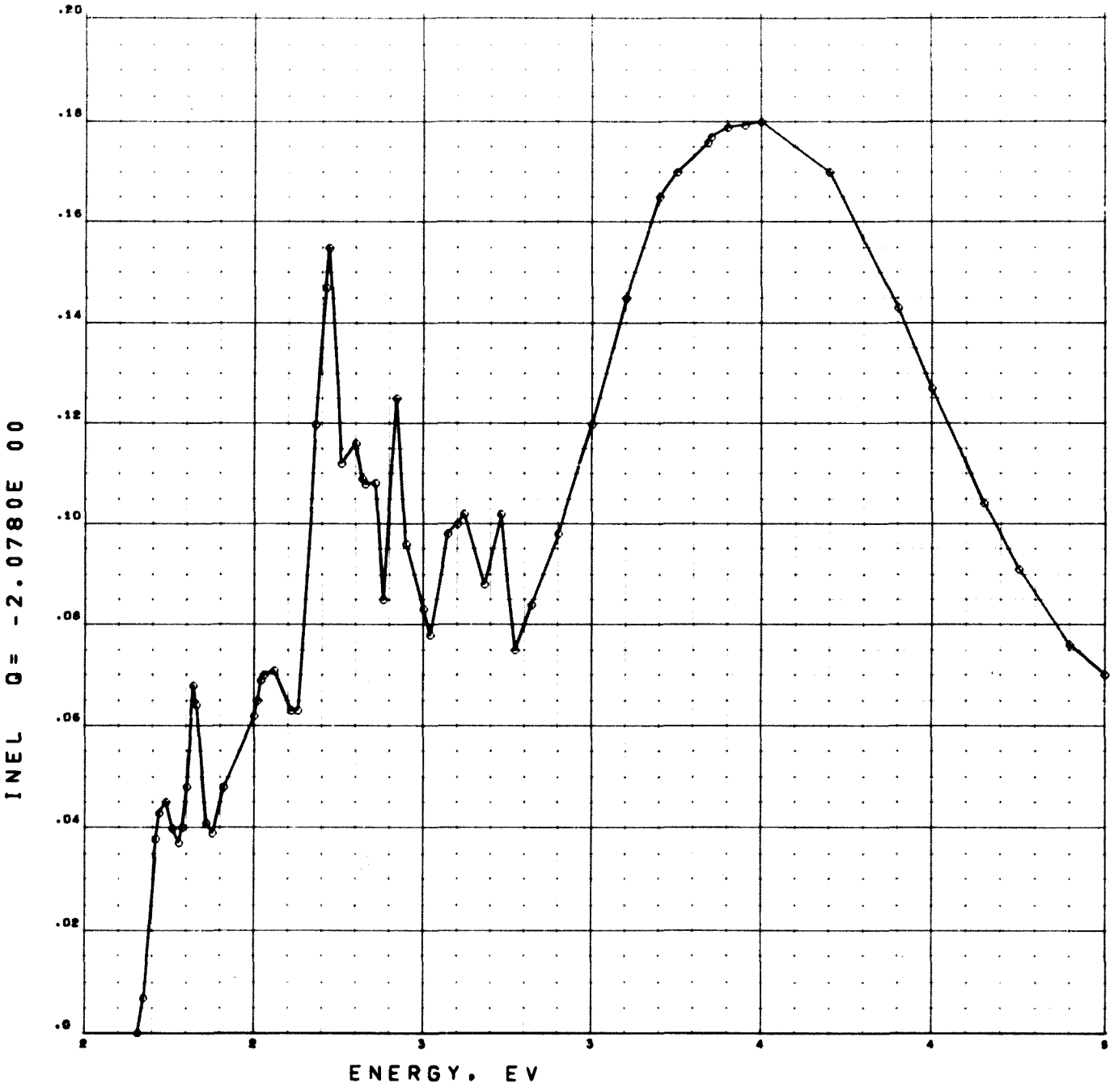

Figure 5. ENDF/B Inelastic Level Data (Sodium) Q = 2.078 Mev

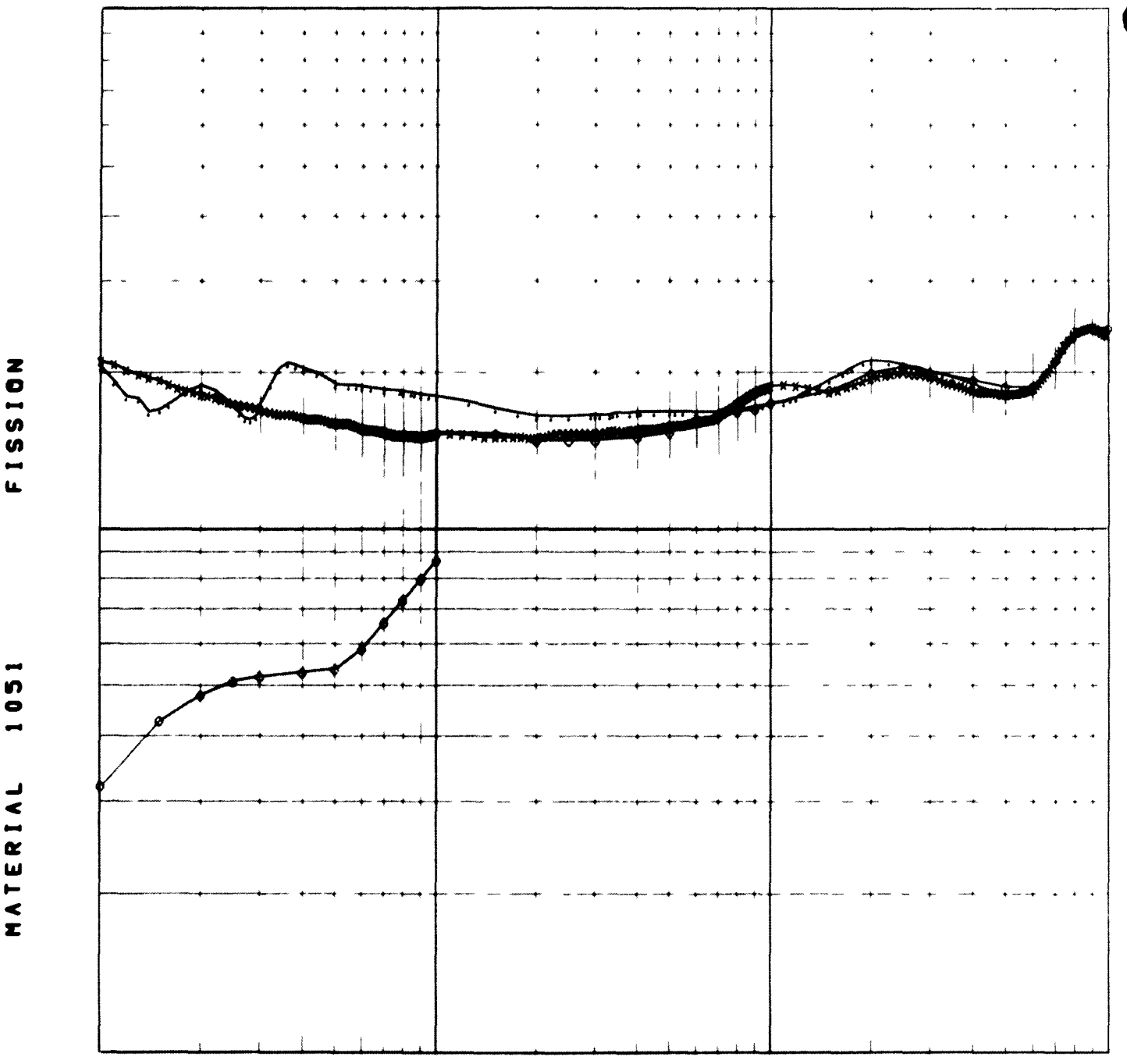

Figure 6. Comparison of Pu-239 Fission Data

0000 ENDF/B
xxxx AIENDF
●●●● Aldermaston

Legendre coefficients is obtained by fitting to the spline curve rather than using linear interpolation between data points. However, the curve fit to the angular information is superior to that obtained with linear interpolation.[7]

C. ENDF/B DATA

1. Evaluation of Copper Cross Sections

An evaluation of available measured cross sections, resonance parameters, and other pertinent data for the two naturally occurring isotopes of copper and for natural copper was completed. Some wide discrepancies between measured values for natural copper and values calculated by combining values for the isotopes weighted by their relative abundances were found. Parameters for negative energy resonances which provided matches to low energy absorption and scattering cross sections were computed. The evaluated parameters were checked by comparing calculations of absorption cross sections and resonance integrals from the TRIX-1[8] code with measurements. Adequate agreement was found. Calculated values favored the isotopic measurements over those for natural copper where discrepancies existed.

Unresolved $\ell = 1$ resonances were found to contribute importantly in the resolved resonance range (below 30 kev), although nearly all resolved resonances appear to have $\ell = 0$ line shapes. Pointwise cross sections were generated with the UNICORN[9] and TRIX-1 codes using resonance parameters and strength functions from the evaluations.

Results of these evaluations are given in Table 1. In addition, the resonance parameter E_o, Γ_n^o, g were taken from BNL 325, 2nd Ed., Supp. 2, Vol 2A.

Positive energy resonance contributions to 2200 m/s absorption cross sections were computed by the UNICORN code to be 0.49 and 0.09 barn for Cu-63 and Cu-65 respectively.

Negative energy resonance parameters for each isotope were selected which yielded the evaluated values of σ_{a2200} and σ_s ($E < 10$ ev). These values are given in Table 2.

TABLE 1

EVALUATED CROSS SECTIONS AND PARAMETERS FOR COPPER

X - Sec/Parameter	Cu-63	Cu-65	0.69 Cu-63 + 0.31 Cu-65	Nat Cu
σ_{a2200} (b)	4.5 ± 0.2	2.2 ± 0.3	3.8 ± 0.2	3.8 ± 0.1
σ_s (E < 10 ev) (b)	5.6 ± 0.4	15.4 ± 0.8	8.6 ± 0.4	7.7 ± 0.2
σ_{pot} (b)	(6.7)	(6.7)	-	6.7 ± 0.4
I_c (E_c = 0.5 ev) (b)	5.2 ± 0.2	2.3 ± 0.2	4.3 ± 0.2	4.0 ± 0.4
$<D>_{\ell = 0}$ (kev)	1.1 ± 0.2	1.4 ± 0.3	-	-
Γ_γ (ev)	0.55 ± 0.15	0.24 ± 0.05	-	-
$10^4 S_0$ (b/ev at 1 ev)	2.55 ± 0.5	1.7 ± 0.4	-	-
$10^4 S_1$ (b/ev at 1 ev)	1.0 ± 0.5	1.0 ± 0.5	-	-

TABLE 2

NEGATIVE ENERGY RESONANCE PARAMETERS FOR COPPER ISOTOPES

Isotope	Parameter			
	E_o	Γ_n	Γ_γ	g
Cu-63	-306.9	4.553	0.55	0.625
Cu-65	-947.6	92.07	0.24	0.625

Statistical estimations of the capture cross sections at 10 kev and 100 kev and the capture resonance integrals were made by using the TRIX-1 code as a check on the evaluated parameters. At 10 kev, the ℓ = 1 contributions to σ_a were comparable to the ℓ = 0 contributions. This was unexpected because the line shapes of nearly all the resolved resonances below 30 kev indicate that they should be alloted to the ℓ = 0 grouping. The resolution is sufficient to obviate missing any large resonance in that range of energy. A high level of relatively smooth ℓ = 1 capture is thus indicated. Calculations of σ_a at 10 and 100 kev

and of I_c for the combined isotopes are much closer to the combination of the measurements of the separated isotopes than to the measurement for natural copper. That agreement provides adquate substantiation of the evaluated parameters for the individual isotopes.

Above the resonance region, the main source of data was the UKAEA Nuclear Data Library files for copper as compiled by Offord and Parker.[10] These files combined the evaluations of Benzi and Haggblom along with several improvements. An analysis of this evaluation indicated that little improvement would be obtained by another complete evaluation at this time; thus, their results above 50 kev were used essentially as is. The one area of improvement was the use of more recent experimental angular distributions in the evaluation for elastic neutron scattering.

Where available cross sections for the separate isotopes were used (this included data for the (n, γ), (n, n'), (n, p), and (n, α) reactions) these were appropriately combined to obtain values for the naturally occurring element. Where cross sections were available for naturally occurring copper only, they were used to evaluate the separate isotopes.

Differential elastic scattering cross sections were obtained from the recent measurements of Smith,[11] and Holmquist and Wiedling[12] as well as from BNL-400.

The evaluated data were processed in appropriate ENDF/B format and sent to the National Neutron Cross Section Center at Brookhaven for distribution. A report describing the evaluation was written and reviewed preparatory to publication.

2. Legendre Coefficients (A > 20)

Angular data obtained from theoretical nuclear model calculations performed at Los Alamos, was analyzed in terms of Legendre expansions.

The theoretical calculations were performed by Agee and Rosen (LA-3538-MS, Vol I and II) and were based on combined optical model and Hauser - Feshbach theory.

The optical model calculations used a local potential with average parameters. These parameters were obtained from a systematic study of the elastic

scattering of polarized protons and from 14-Mev neutron elastic scattering data. The resulting potential contained six parameters, and was composed of a real and imaginary central potential and a spin orbit potential of the Thomas type. Compound elastic scattering was determined by using Hauser-Feshbach theory, wherever energy levels were known below the incident neutron energy.

Since such calculations are not generally valid for very light or very heavy nuclides, the authors (Agee and Rosen) indicate that these calculations were presented in an attempt to satisfy demands for cross sections which can be used where a high degree of accuracy is not required. Where possible, comparisons were made with experimental data, so as to give some insight as to the reliability of the calculated information.

Where a total elastic cross section was presented as obtained from a summation of shape elastic plus compound elastic scattering, this was used in the present analysis. Above ~5 or 6 Mev, the compound elastic scattering becomes negligible; so that, in this region, only data for shape elastic scattering were presented. The differential cross sections were presented as a function of angle, both in tabular and graphical form. In order to make this theoretical information more readily useful to those using neutronic codes, these angular distribution data have been analyzed in terms of Legendre polynomial expansions.

The calculated results for isotopes with mass numbers below 20 were not expanded in Legendre polynomials, since these were included by Agee and Rosen only to indicate trends that angular distributions might follow. All other nuclides were analyzed. A complete listing of nuclides is given in Table 3, along with the incident neutron energies yielding these distributions. Thirty-six isotopes ranging in mass from sodium to plutonium-240 were analyzed. The resulting Legendre expansion coefficients have been forwarded to Brookhaven National Laboratory and are available from the National Neutron Data Center (NNDC) at BNL. A report describing the results of the analysis has been distributed.[13]

3. α^{49}

The uncertainties in $\alpha = \sigma_c/\sigma_f$ for Pu-239 currently contribute large undertainties to the economic and safety parameters of fast breeder reactors. Recently, α^{49} in the energy range 0.2 to 15 kev was measured using improved

TABLE 3

SUMMARY OF DATA ANALYZED

Isotope	Incident Neutron Energies* (Mev)	Isotope	Incident Neutron Energies* (Mev)
Na^{23}	3.97, 4.0-16.0	Nb^{93}	1.0, 1.2, 2.0-16.0
Mg^{24}	5.0-16.0	Mo^{98}	6.04
Al^{27}	5.0-16.0, 14.7	Rh^{103}	6.04
Si^{28}	1.0, 2.0, 3.0, 3.5, 3.8, 4.0, 4.2, 4.5, 4.8, 5.0-16.0	Cd^{114}	4.0, 6.04
Cl^{35}	0.5, 1.0-16.0	In^{115}	4.0
K^{39}	0.5, 1.0-3.0, 3.7, 4.0-16.0	Sn^{118}	4.0, 6.04
Ca^{40}	6.0	I^{127}	4.0
Ti^{48}	3.0-16.0	W^{184}	2.0, 3.0, 5.0-16.0
V^{51}	1.0-16.0	Pb^{208}	4.0-16.0
Cr^{52}	2.0, 2.35, 3.0-16.0	Bi^{209}	4.0, 6.04
Mn^{55}	0.5, 1.0, 2.0, 5.0-16.0	Th^{232}	1.0, 1.2, 1.5, 2.0, 5.0
Fe^{56}	5.0, 6.0, 6.04, 7.0-16.0	U^{234}	5.0-16.0
Ni^{58}	1.0-16.0	U^{235}	5.0-16.0
Co^{59}	4.0	U^{236}	5.0-16.0
Ni^{62}	4.0	U^{237}	5.0-16.0
Ga^{69}	1.0, 5.0-16.0	U^{238}	5.0-16.0
Se^{80}	4.0	Pu^{239}	5.0-16.0
Y^{89}	6.0, 6.04, 7.0-16.0	Pu^{240}	5.0-16.0

*Where energies are given as 5.0-16.0, for example, data have been computed at 1.0-Mev intervals.

techniques by Schomberg, Sowerby, and Evans of A.E.R.E., Harwell.[14] Most new values are markedly higher than previous ones and, consequently, are of great concern to fast reactor designers.

In the experiment of Schomberg, et al, the values of α were obtained by using a calibration to "known" values of α for low energy resonances of Pu-239. The known values were calculated from the resonance parameters of a single level analysis of measured fission and total cross sections by Derrien et al.[15]

More recently, a multilevel analysis of the Pu-239 fission cross section from the Petrel event has been reported by J. A. Farrell of Los Alamos.[16]

In the present work, the multilevel parameters of Farrell were used to calculate the values of α for the calibration resonances of the Schomberg experiment under their conditions. The results are compared with the single-level based results in Figure 7. Considerable disagreement exists between the two sets of points, with several multilevel points implying lower α values than the single-level calibration predicts.

Some of the scatter in the multilevel based points may be due to the assumption of a constant capture width of 40 mv in Farrell's work.

The effect of using a constant Γ_γ of 40 mv was studied by using the Γ_γ values of Derrien for the multilevel analysis and reanalyzing the data for Γ_f. A better variance for the calibration is obtained and the implied α values are between the older values and those of Schomberg.

The main import of the results of this work are that the α values of the low energy resonances of ^{239}Pu are not sufficiently well known to provide a normalization having the desired degree of accuracy. A secondary implication is that

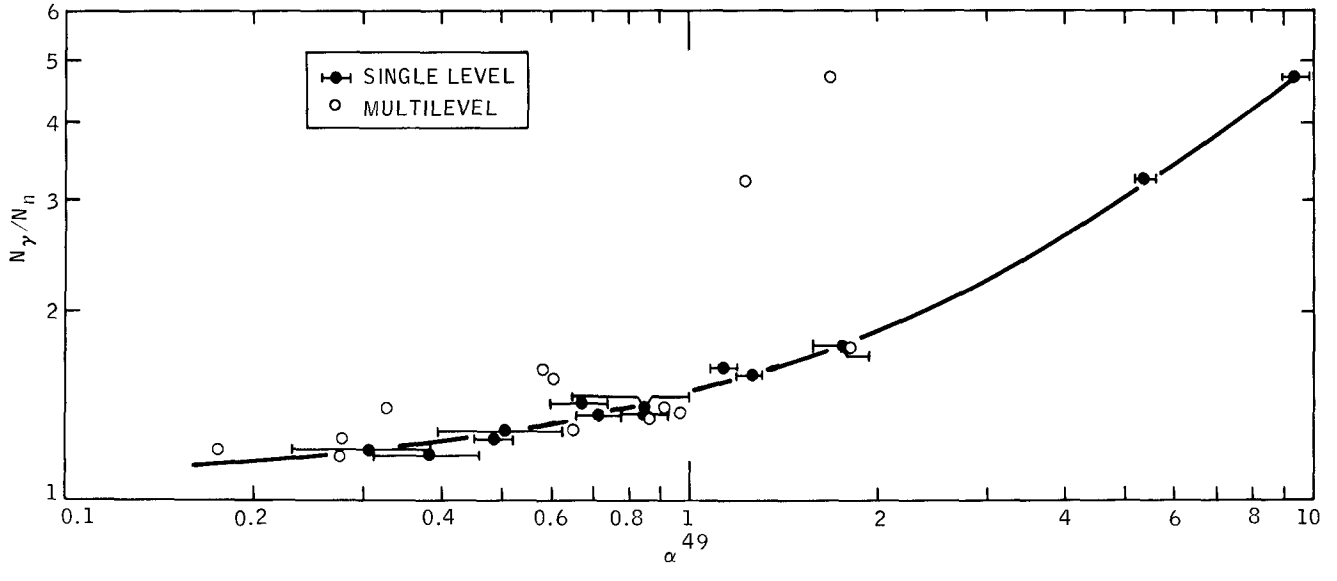

8-A26-069-1

Figure 7. Comparison of Calibration Curves Based on Single-Level and Multilevel Analyses of the Pu^{239} Fission Cross Section

the Schomberg provisional results lie near the upper limit of the range of results that current resonance parameters infer. A more complete description of this work has been submitted as a technical note to the editor of Nuclear Science and Engineering.

D. OPTICAL MODEL ANALYSIS AND DEVELOPMENT

In the process of converting the deformed nucleus optical model Code 2 PLUS from FORTRAN II to FORTRAN H for use with the IBM-360, Model 50, several modifications and extensions were incorporated. One of the original restrictions in 2 PLUS was that the potential V(r), coupling the ground level to the first excited level was real. Such an assumption, however, may not be valid and the imaginary well depth W(r), may depend strongly on whether or not a complex coupling is allowed. A complex coupling option, therefore, has been added to 2 PLUS. The code was further modified to calculate and print the neutron wavefunctions for all values of the angular momentum quantum numbers and both the ground state and first excited level of the nucleus.

Since a spherical model is widely used in the analysis of light and intermediate weight nuclide scattering, the computer code OPTIC was chosen as the basic spherical optical model code for cross section analysis use. This code, as originally written at Knolls Atomic Power Laboratory, included an R-matrix calculation permitting the possibility of analyzing intermediate structure, the capability of calculating Legendre moments of angular distributions analytically, and an improved automatic parameter search. This code was converted from FORTRAN II to FORTRAN H, a Hauser-Feshbach calculation added in order to analyze lower incident neutron energies. A punch option for NEARREX II was added so that a full compound nucleus calculation can now be carried out.

Consistent with the project objectives of development and testing of improved optical models, the evaluation of the heavy even-even rotor nuclide fast neutron cross sections by appropriate comprehensive nuclear models was continued. Major emphasis has been placed onthe nuclides Th-232 and U-238 which were analyzed together. Since it was shown by Moldauer that the most appropriate energy regime for fixing optical model parameters is that below 1 Mev, considerable attention has been given to parametric searching of the real well depth, the imaginary well depth, and the nuclear deformation parameter under the

requirements that models reproduce, at 10 kev, the experimentally observed total neutron cross section, the s-wave neutron wave strength function, and a reasonable value for the p-wave neutron strength function. These requirements are sufficiently rigorous that, under the restrictions of a minimum number of energy dependent free variables, a unique set of low energy parameters is produced. Not only are the optimum parameters similar for both Th-232 and U-238, but these values are not markedly different from commonly used optical model potentials.

In the consideration of the nuclear deformation, however, those values of deformation required for consistency are lower than those calculated and tabulated by Stelson and Grodzins[17] on the basis of the reduced electric quadrupole moment transition probabilities. It is found that this situation obtains generally not only for Th-232 and U-238, but for other heavy even-even nuclides as well. The deformations obtained upon searching are generally found to be consistent with the equilibrium deformations of the single particle potential obtained from projected wave functions in the BCS theory.[18] It is noted that for heavy nuclides, for most values of the deformation, the density deformations are overlapping with the deformations of the potential.

From 10 kev, the analyses proceeded at those energies for which experimental information, regarding total cross section, elastic cross section, angular distributions (and at low energies, the cross section for the excitation of the first 2+ excited state at 50 kev) was available. Information was generated and evaluated at the following energies: U-239 (0.01, 0.075, 0.157, 0.250, 0.450, 0.550, 0.800, 0.10, 2.0, 3.0, 4.0, 7.0, 15.0); Th-232 (0.01, 0.57, 0.70, 1.0, 1.25, 1.5, 2.0, 3.0, 4.0, 7.0, 15.0). All energies are in Mev. At each of these energies above 0.010 Mev, parametric search of the real and imaginary well depths was employed to obtain the best fit to the experimental information with the deformation remaining fixed and not taken as a function of energy. Best fit analyses for U-238 and Th-232 show that the energy variation of the well depths, real and imaginary, is similar for both nuclides. Moreover, as the real Saxon well decreases sharply, in the region of 1-3 Mev, the imaginary well shows a corresponding energy dependent increase in the same region.

The average neutron strength functions for 58 heavy, even-even, rotor nuclides from Ra 220 to (104) 262 were calculated with a deformed nucleus model

using single particle potential equilibrium deformations and an independent particle model approximation. The optical model potentials employed were corrected for both the symmetry number and the charge. In comparisons to existing experimental strength function data, it is found that, for s-waves, the general agreement is better for those model variants which include a coulomb term in the potential, whereas, for p-waves, with the exception of thorium, agreement favors variants not including a charge term.

Calculations performed on the basis of single-article potential equilibrium deformations yield neutron strength functions generally in better agreement with experiment that those obtained on the basis of deformations of the nuclear surface given by reduced electric quadruple transition probabilities.

The theory for a statistical treatment of decay of a compound nucleus state by gamma ray cascades followed by a particle (s) emission has been formulated. This theory should provide the basis for an improved treatment of compound nucleus phenomena at energies above a few Mev.

E. DOCUMENTATION

The following papers were presented at technical meetings during fiscal year 1968.

H. Alter, R. F. Berlund, C. L. Dunford, R. J. Creasy and G. D. Joanou, "Use of Computer Graphics in an Automated Neutron Cross Section Evaluation System," 14th Nuclear Science Symposium, IEEE, Los Angeles, California (October 1967)

R. G. Berland, C. L. Dunford, and R. J. Creasy, "Computer Graphics for Automated Neutron Cross Section Evaluation," American Nuclear Society, Chicago, Illinois (November 1967)

H. Alter, "Automated Evaluation of Experimental Data," Invited Paper, Second Conference on Neutron Cross Sections and Technology, Washington, D. C. (March 1968)

The following reports were issued during fiscal year 1968.

"A Technique for Computing the Inverse Differential Cross Section Transformation Matrix T^{-1}," NAA-SR-MEMO-12484 (July 1967)

"Conversion and Modification of 2 PLUS," NAA-SR-TDR-12532 (September 1967)

"OPTIC II, A Spherical Optical Model Code," NAA-SR-TDR-12531 (October 1967)

"NEARREX II, A Code for Compound Nucleus Calculations," NAA-SR-TDR-12530 (October 1967)

"Calculations of Pu-239 Resonance Cross Sections Using Fission Widths from Channel Fission Theory," NAA-SR-12515 (October 1967)

"Influence of Nuclear Deformation on Neutron Wave Strength Functions of Heavy Even-Even Rotor Nuclides," NAA-SR-MEMO-12538 (October 1967)

"Discrete Ordinates Representations of the Scattering Kernal," NAA-SR-12493 (November 1967)

"EDIT, A Fortran IV Senel H Program to Punch, Print, and Plot Selected Portions of an ENDF/B Data Tape," NAA-SR-12525 (November 1967)

"SCORE, An Automated Cross Section Evaluation System," NAA-SR-MEMO-12529 (January 1968)

"Availability of ENDF/B Neutron Cross Section Data," AI-AEC-TDR-12639 (January 1968)

"Lengendre Expansion Coefficients for Theoretical Angular Distributions of Elastically Scattered Neutrons," NAA-SR-12533 (March 1968)

"Neutron Wave Strength Functions from Model Equilibrium Deformations for Transuranic Nuclei," AI-AEC-MEMO-12652 (April 1968)

"Storage of Microscopic Cross Section Data in the AIENDF," NAA-SR-11980, Vol II (June 1968)

III. EVALUATION OF EFFORT DURING FISCAL YEAR 1968

A large fraction of the time required to produce an evaluated cross section library may be classified as nonproductive. A considerable portion of any evaluation is concerned with purely mechanical operations; consequently, not only is there often insufficient time for extensive data evaluation, but there are also long delays between the reporting of measured data and its availability for use in neutronic calculations. To help alleviate some of the problems associated with current data evaluation methods, a comprehensive automated data evaluation system, SCORE, is being developed which will encompass all the operations from the generation of theoretical data to the final evaluated cross section libraries. Such an extensive undertaking has been made possible by major technological advances in the new generation of computers. In particular, these advances are represented by new devices which permit on-line communication between man and a high-speed digital computer.

Man-computer interaction during the execution of a data evaluation problem can now be economically accomplished by the use of a graphic display console as a high-speed input-output device. The economy of this mode of operation is based on its time-sharing capability and its convenient output form (namely, graphic displays). The data evaluator, using the input device on a display console, can direct the processing and evaluating of experimental data by monitoring intermediate results; errors may be corrected easily, before a large amount of computer time is consumed. In addition, the evaluator may inject his analysis of partial results (which otherwise might be very difficult or expensive to approximate, by the computer program) during execution of the program. This interaction can save computer time and turn-around time, and provides insight into the problem being solved.

The range and capability of optical model calculations to predict neutron cross section data has been extended through modification of first generation computer codes. Results of the analyses for thorium-232 and uranium-238 show that the optical model is a useful cross section evaluation .

REFERENCES

1. R. F. Berland, C. L. Dunford, and R. J. Creasy, "Computer Graphics for Automated Neutron Cross-Section Evaluation," presented at the American Nuclear Society, 1967 Winter Meeting at Chicago, Illinois (November 1967)

2. C. L. Dunford, R. F. Berland, and R. J. Creasy, "SCORE, An Automated Cross Section Evaluation System," NAA-SR-MEMO-12529, ENDF 106 (January 1968)

3. M. J. D. Powell, "Curve Fitting by Cubic Splines," TP-307 (September 1967)

4. H. Alter, "Automated Evaluation of Experimental Data," presented at the Second Conference on Neutron Cross Sections and Technology, Washington, D. C. (March 1968)

5. R. S. Hubner, "EDIT, A Fortran IV Level H Program to Punch, Print, and Plot Selected Portions of an ENDF/B Data Tape," NAA-SR-12525 (November 1967)

6. B. J. Toppel, A. L. Rago, and D. M. O'Shea, "MC**2, A Code to Calculate Multigroup Cross Sections," ANL-7318 (June 1967)

7. NAA-SR-12570, Quarterly Technical Progress Report, AEC Unclassified Programs, July-September 1967

8. J. M. Otter, "The TRIX-I Code, An Improved Analytic Calculation of Resonance Integrals," NAA-SR-MEMO-11538 (July 1965)

9. J. M. Otter, "UNICORN, A Program to Calculate Point Cross Sections from Resonance Parameters," NAA-SR-11980, Vol VI (June 1966)

10. S. M. Offord and K. Parker, "Neutron Cross Sections of Copper in the Energy Range 0.0001 ev to 15 Mev," AWRE 0-63/67 (December 1967)

11. A. B. Smith, C. A. Englebrecht, and D. Reitman, "Elastic and Inelastic Scattering of Fast Neutrons from Co, Cu, and Ni, Physical Review," Vol 135 B, p 76 (July 1964)

12. B. Holmquist and T. Wiedling, "An Optical Model Study of Neutrons Elastically Scattered by Iron, Nickel, Cobolt, and Copper in the Energy Region 1.5 to 4.6 Mev," Conference Proceedings Nuclear Data for Reactors, Vol I, p 409, Paris 17-21 (October 1966)

13. P. W. Campbell, H. Alter, R. F. Berland, and V. Luco, "Legendre Expansion Coefficients for Theoretical Angular Distributions of Elastically Scattered Neutrons," NAA-SR-12533 (March 1968)

14. M. G. Schomberg, M. G. Sowerby, and F. W. Evans, "A New Method of Measuring Alpha (E) for ^{239}Pu," Paper SM-101/41, IAEA Symposium on Fast Reactor Physics and Related Safety Problems, Karlsruhe (November 1967)

15. H. Derrien, J. Blons, C. Eggermann, A. Michaudon, D. Paya, and R. Ribon, "Sections Efficaces Totale et de Fission du ^{239}Pu," Nuclear Data for Reactors, 2, 195 IAEA, Vienna (1967)

16. J. A. Farrell, "Multilevel Analysis of the ^{239}Pu Fission Cross Section from 14 to 90 ev," Phys. Rev., 165, 1371 (1968)

17. P. H. Stelson and L. Grodzins, Nuclear Data, Section A, 21, (December 1965)

18. A. Sobiczewski, "Equilibrium Deformations of Heavy Nuclei Calculated with Projected Wave Functions," Nuclear Physics, A-96, 258 (1967)

PAGE 28 is blank

Program: Civilian Power, LMFBR
AEC Task: 5-B, Reactor Physics, Fast Spectrum Doppler Measurements
Project Manager: H. A. Morewitz
Reporting Period: Fiscal Year 1968
General Order: 7701 Subaccount: 14610 AEC Category: 04-01-61-02.1

Principal Investigators: T. H. Springer, R. J. Tuttle, H. N. Royden

I. PROJECT OBJECTIVES

The objectives of this project are to (a) refine further the techniques originally developed at this laboratory for measuring Doppler reactivity coefficients, (b) investigate the Doppler coefficients of various fuel and fertile materials in a variety of fast spectra, (c) provide better understanding of temperature-induced reactivity changes by analytically and experimentally investigating these changes at cryogenic as well as very high temperatures, and (d) investigate resonance-overlap and interference effects, and the effect of varying the surface-to-mass ratio.

II. TECHNICAL PROGRESS DURING FISCAL YEAR 1968

Four different test regions in the ECEL have been studied during this period. These have provided spectra ranging from relatively soft, in Core 14, to a simulation of the spectrum in an LMFBR. Some of the characteristics of these test regions are listed in Table 1. The spectral changes were achieved by simple changes: Core 15 was built by replacing some of the carbon in Core 14 with

TABLE 1
TEST REGION CHARACTERISTICS

Core	Median Energies (kev)			Atom Densities (atom/barn-cm)							
	Fission	Absorption	Flux	U^{235}	U^{238}	C	Na	Al	Fe	Cr	Ni
14	3 87	2.66	84 46	0.00075	0 00244	0 04727	0.0	0 00945	0 00834	0.00203	0.00090
15	17.85	10 89	124 76	0 00075	0 00244	0 02626	0.0	0.01608	0 00834	0.00203	0.00090
16	66 35	37.99	149.71	0 00138	0.00870	0 01902	0 0	0.01682	0 01487	0 00388	0 00206
17	93 82	49 84	173.80	0.00138	0 00870	0 01427	0.00546	0 00983	0.01279	0.00334	0 00178

aluminum; Core 17 was built by replacing some of the aluminum in Core 16 with sodium.

A. REACTOR CALCULATIONS

The calculated CAESAR spectra of these four test regions are shown on Figures 1a, b, c, and d, along with some experimental results that will be discussed later. These graphs show the hardening of the spectrum caused by the substitution of aluminum for carbon, and the change in the flux near 3 kev caused by the presence of sodium in Core 17. In the course of designing these cores, it was discovered that significant differences in the calculated flux spectra in the vicinity of the sodium scattering resonance (2.85 kev) can be caused by the location of the group boundaries. This problem and its implications in the calculation of Doppler and sodium-void reactivity effects are now being examined under another project.

B. HEATED-BLANKET DOPPLER EFFECT

A preliminary trial of a new kind of Doppler effect measurement was undertaken in Core 14. This measurement consists of determining the Doppler effect of a sample within a room-temperature blanket, and again with the blanket heated. The "heated-blanket" experiment is of interest in relating the results of small-sample Doppler effect measurements in a cold critical assembly to the Doppler effect in a hot reactor. These first measurements indicated a resonance interference effect, when the sample and blanket were of the same material, that was verified by further measurements in Core 15.

The measurements in Core 15 used thorium and uranium-238 samples in blankets of thorium and uranium-238. The blankets were either at room-temperature or heated to an average temperature of 400°C. The results of these measurements are shown in Figures 2 and 3.

A significant change in the Doppler effect is caused by heating a blanket of similar material; no significant change is caused by heating a blanket of dissimilar material. While the observed changes are significant, they are sufficiently small to support the validity of the normal small-sample measurements.

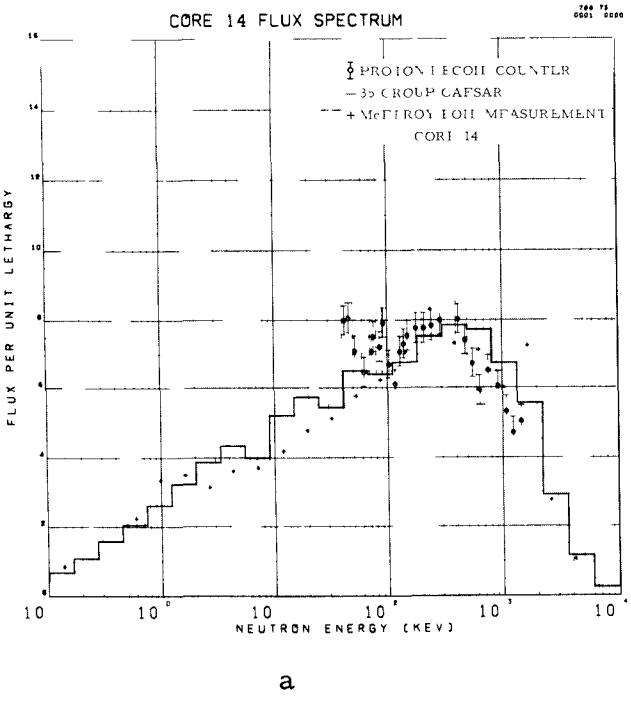

a

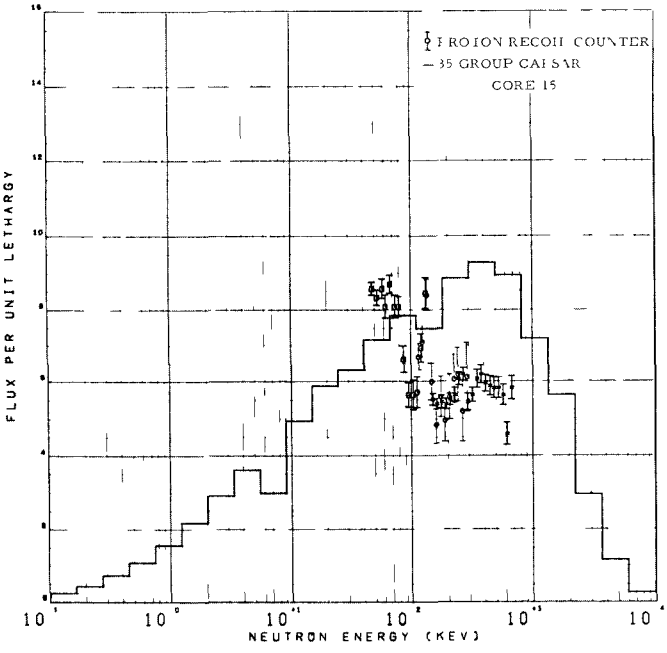

b

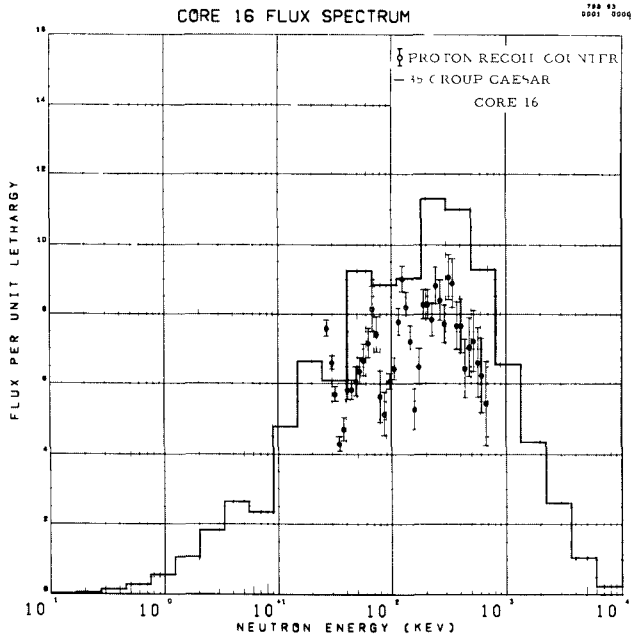

c

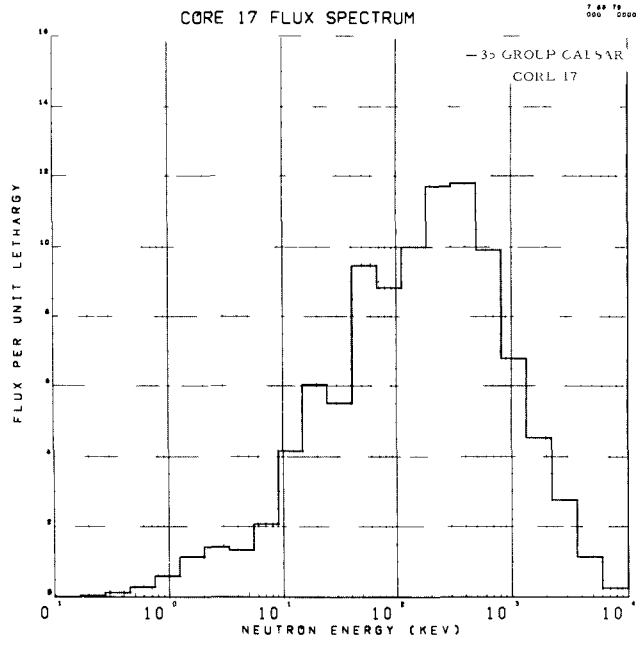

d

6-24-68 UNCL 7701-46106

Figure 1. Flux Spectra of Cores 14, 15, 16, and 17

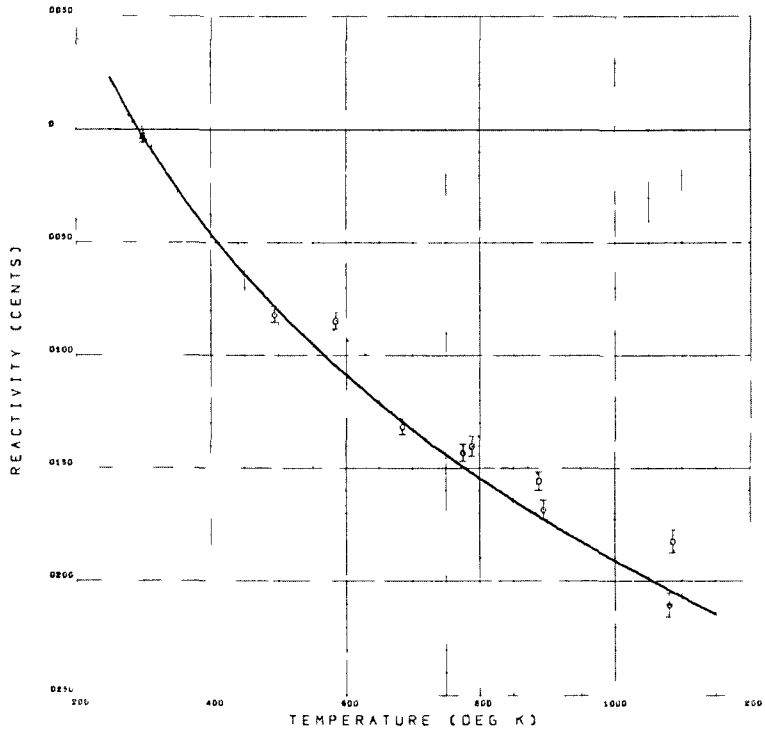

6-24-68 UNCL 7701-46107

Figure 2. Doppler Effect of Th in Blanket

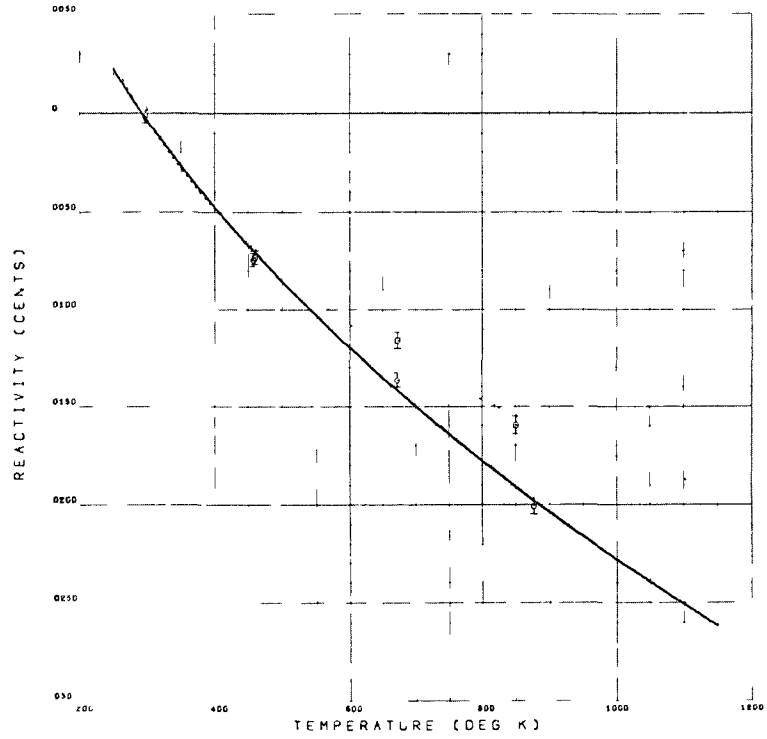

6-24-68 UNCL 7701-46108

Figure 3. Doppler Effect of U-238 in Blanket

Additional measurements have been made in Core 17; however, the data have not yet been analyzed.

Because resonance overlap effects between a sample and its immediate surroundings are strongly localized in energy, the usual broad-group methods for calculating the Doppler effect are inadequate for this situation. A program, RABBLE, specifically formulated at ANL for such problems is being converted to the IBM System/360 to permit calculations for these experiments.

C. SPECTRUM MEASUREMENTS

Measurements of the central flux spectrum of each of the four cores have been undertaken by use of proton-recoil proportional counters. The results for some of these cores are shown superimposed on the 35-group CAESAR calculated spectra shown in Figure 1. Smoothing of the calculated fine-group spectra by a gaussian resolution function reduces the complexity of the calculated spectra to that obtained experimentally, permitting a realistic comparison of the two. The comparison of the structure in the calculated and measured spectra can be used to supplement the internal energy calibration of the detectors.

The proton-recoil results for Core 16 are further compared with a portion of the theoretical spectrum (see Figure 4). The experimental values have been normalized to the calculation to permit more accurate comparison. A gaussian resolution function with full width at half maximum of 20% was used to smooth the AILMOE spectrum. The distinct dips in the smoothed spectrum at low energies are easily identified with the scattering resonances causing them; the dips at higher energies are the result of overlapping resonances in several of the elements present. This comparison shows the close correlation between peaks and dips in the measured spectrum with those calculated from basic nuclear data.

Additional information on the flux spectra of Cores 14 and 16 were provided by extensive activation measurements conducted under the coordination of W. N. McElroy, now at Battelle Memorial Institute, Pacific Northwest Laboratory. The results of the Core 14 measurements are shown in Figure 1; results for Core 16 are not yet complete. Preliminary results, however, indicate general agreement with the calculation.

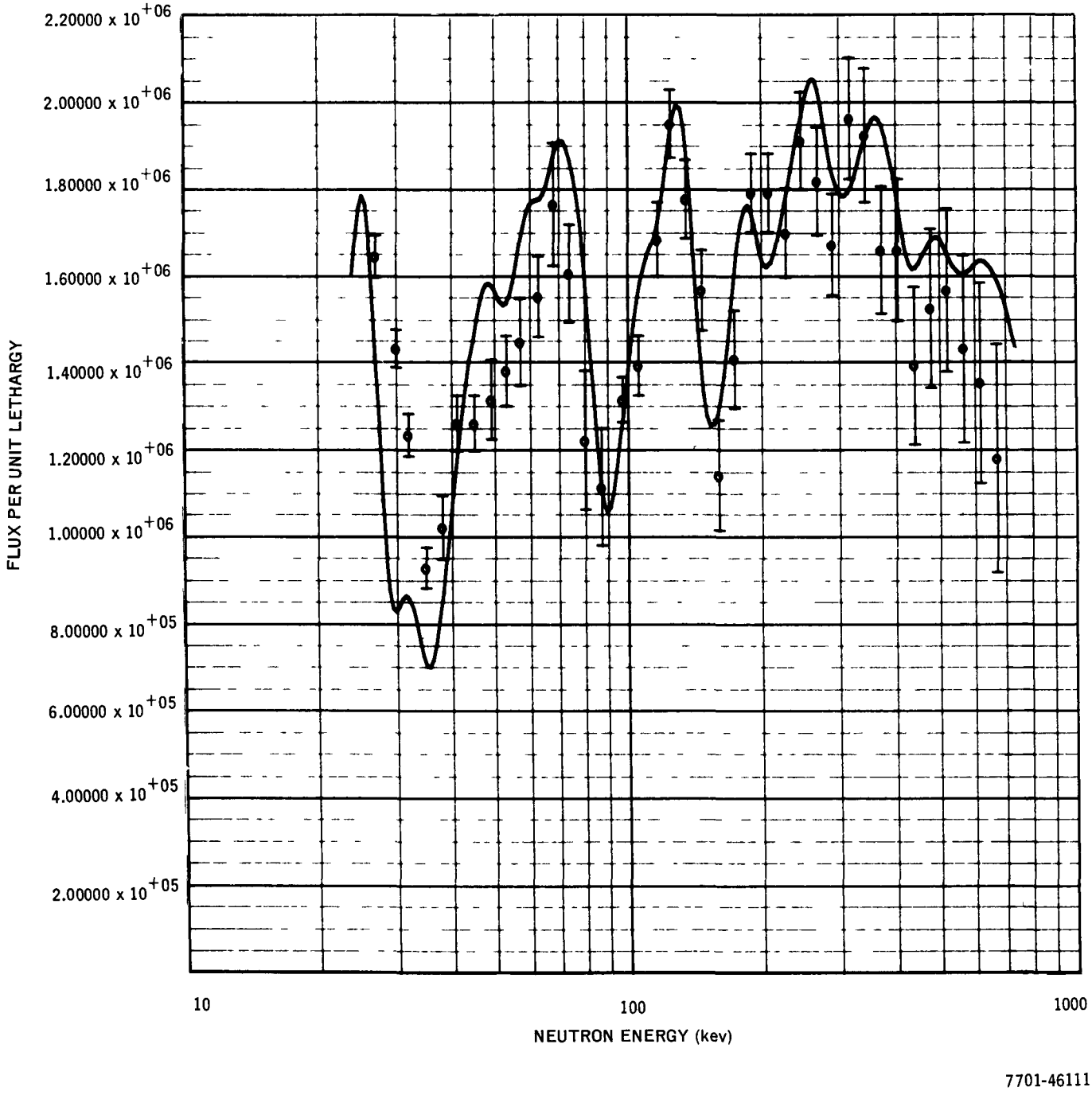

Figure 4. Core 16 Smoothed AILMOE Spectrum

D. FISSION RATES

Fission rate measurements were made in the four cores studied to insure that the flux is spatially flat over the region used for central reactivity measurements. Examples of these fission rate traverses, made in Core 16, are shown in Figure 5. Except where indicated, the statistical errors are equal to, or smaller than, the plotting symbols. The flatness of the flux as determined by these traverses is indicated in Table 2 where the observed deviations of the central four points (-5, 0, 5, and 10 cm) from the average are compared with the deviations expected from the statistical accuracy of the data. These results indicate that the flux below the Np^{237} fission threshold at 250 kev is flat within about 1.6%; and above this energy, is flat within about 0.3%.

Calibration of these fission counters is normally provided by alpha-spectrometry. The silicon diode in the plutonium counter became very noisy due to irradiation in the reactor; therefore, only an approximate calibration has been provided in the Core 16 data. A cross calibration, however, with a new detector in Core 17 will permit an accurate normalization of the previous data.

E. REACTIVITY MEASUREMENTS

Reactivity measurements have been made with a great variety of materials in these four cores. Some of the more interesting samples are summarized in Table 3. Although the results for Core 14 have been reported previously, they are included here for completeness. The results for Core 17 have not yet been analyzed.

F. DOPPLER EFFECT

Doppler-effect measurements have also been made with a great variety of materials. The results of the most significant materials are shown in Table 4. Correction for the expansion effect in the fissile materials was provided by similar samples with slightly different surface-to-mass ratios. (This method was not possible for the two samples of plutonium oxide, Samples No. 6 and 9.) Data from Core 17 have not yet been analyzed.

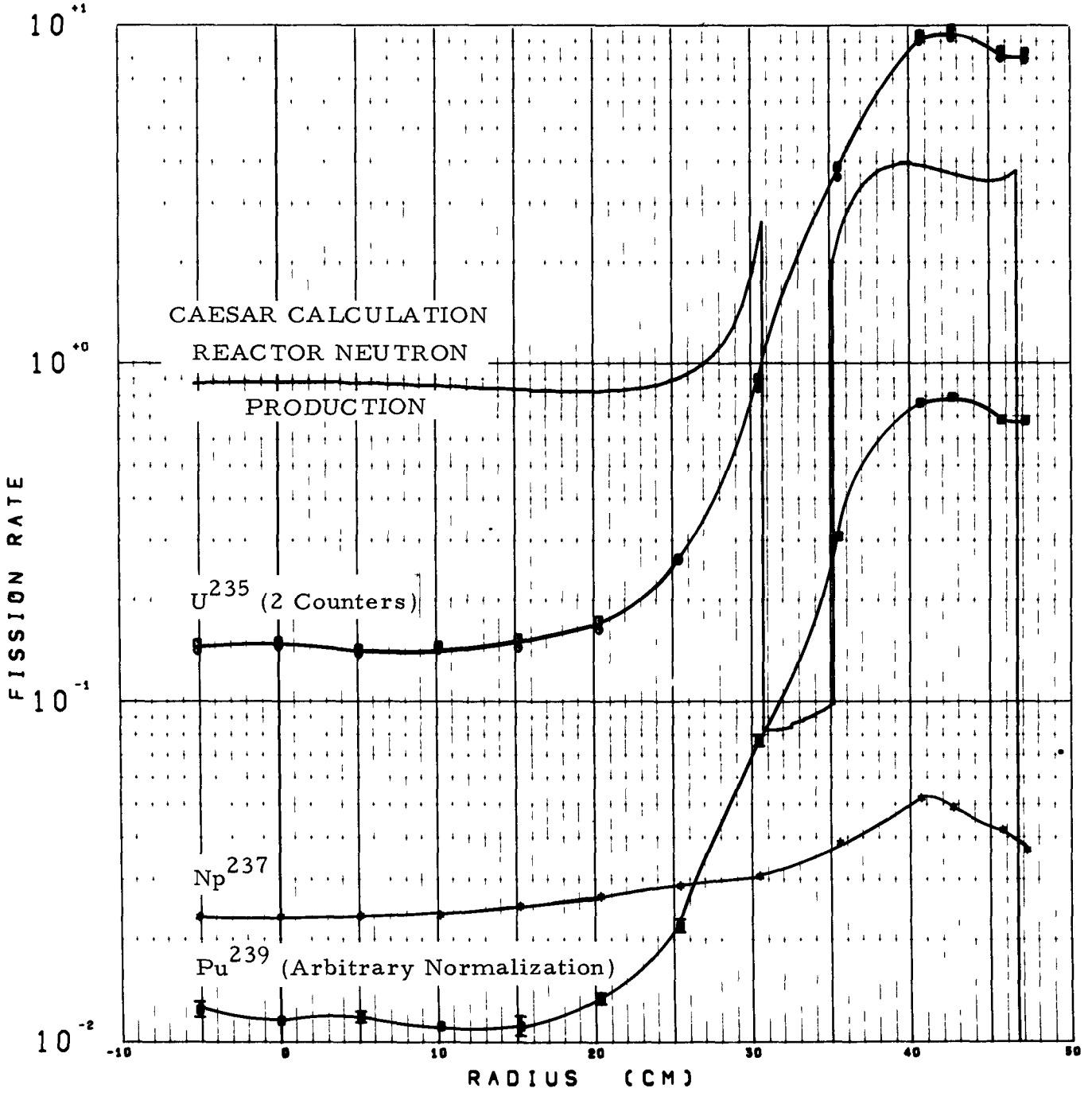

Figure 5. Core 16 Fission Distribution

TABLE 2

DEVIATIONS OF CENTRAL FISSION RATES

Counter	Observed Deviation (%)	Expected Deviation (%)
U^{235}	±1.8	±1.0
Np^{237}	±0.6	±0.5
Pu^{239}	±3.8	±3.4

TABLE 3

REACTIVITY MEASUREMENTS

Sample	Mass (gm)	Specific Reactivity (millicent/gram)		
		Core 14	Core 15	Core 16
U^{235}	182	+11.7	+10.6	+10.7
	59	+13.1	+10.8	+10.5
	15	+13.9	+11.1	+9.5
U^{238}	185	-1.51	-1.04	-0.87
Th	114	-2.89	-1.87	-1.61
Ta	164	-7.76	-5.18	-3.79
W	190	-2.84	-1.78	-1.33
PuO_2 No. 2 (91, 8, 1, 0)*	66	+-	+14.4	+12.7
PuO_2 No. 6 (58, 32, 7, 3)*	62	+9.95	-	+9.21
PuO_2 No. 9 (41, 42, 10, 7)*	62	+8.59	-	+7.81
$Pu^{241}O_2$ (1, 4, 94, 1)*	10	+18.9	-	+13.9

*Percentages of Pu^{239}, Pu^{240}, Pu^{241}, and Pu^{242} respectively

TABLE 4

DOPPLER-EFFECT MEASUREMENTS

Sample	Mass (gm)	Core Number					
		14		15		16	
		$(20\text{-}600)\frac{1}{\rho}\frac{dp}{dT}$		$(20\text{-}600)\frac{1}{\rho}\frac{dp}{dT}$		$(20\text{-}600)\frac{1}{\rho}\frac{d\rho}{dT}$	
		(m cent)	(10^{-6}/°C)	(m cent)	(10^{-6}/°C)	(m cent)	(10^{-6}/°C)
U^{235}	193	11.0	8.9	7.8	7.38	4.7†	-6
$U^{235}O_2$	101	3.1	4.7	2.2	4.28	-	-
PuO_2 No. 1 (91, 8, 1, 0)*	67	-7.7	-14.3	-6.6	-12.5	-	-
PuO_2 No. 6 (58, 32, 7, 3)*	62	-10.8†	†	-5.5†	†	-	-
PuO_2 No. 9 (41, 42, 10, 7)*	62	-11.2†	†	-7.7†	†	-	-
U^{238}	179	-35.4	-218	-21.9	-199	-11.0	-122
Th	114	-37.8	-198	-22.1	179	-11.0	-103

*Percentage of Pu^{239}, Pu^{240}, Pu^{241}, and Pu^{242} respectively
†No expansion effect correction made

G. EXPANSION EFFECT

Depending on the real and adjoint flux spectra, the expansion effect may be a large or predominant fraction of the temperature reactivity effect. As mentioned above, the method currently used to determine the expansion effect is to measure the variation of specific reactivity with surface-to-mass ratio and to relate this variation to temperature-induced dimensional changes by means of the thermal expansion coefficients of the material. The specific reactivity of different samples is calculated by means of perturbation theory, by using cross sections modified by escape probabilities. The modified cross sections include

both the self-multiplication effect (fissions caused by neutrons born in the sample) and the self-shielding effect (flux depression in the sample). Agreement between the calculated and observed reactivity variations for U^{235} has been good in these cores; agreement is less good for plutonium, but the comparison is somewhat hampered by the small number of plutonium samples.

H. EFFECTIVE CAPTURE-TO-FISSION RATIO

In view of the recent intense interest in the value of the effective capture-to-fission ratio, $\bar{\alpha}$, for Pu^{239} in a fast reactor spectrum, an analysis was begun to determine if values of this parameter could be calculated from previously obtained data. The method used incorporates the calculated value of $\bar{\alpha}$ for U^{235}, and uses the measured reactivities and fission rates of Pu^{239} and U^{235}. Significant corrections based on the calculated neutron flux and importance spectra are required, as is true of all the integral methods used to date.

The calculated value of $\bar{\alpha}$ for U^{235} in Core 15 is 0.255. The calculated value for Pu^{239} is 0.307. By using measured reactivities and fission rates the derived value of $\bar{\alpha}$ Pu^{239} is 0.05; in severe disagreement. There are, however, indications that the experimentally determined fission rate of Pu^{239} in this core is in error. When the experimental Pu^{239}/U^{235} fission ratio is replaced by the calculated ratio, the resulting value of $\bar{\alpha}$ for Pu^{239} is 0.316; in much better agreement. The measurements associated with the Pu^{239} fission rate determination are currently being investigated in order to eliminate the source of error.

The results of measurements made in earlier cores in this program and also in the Advanced Epithermal Thorium Reactor (AETR) program have been analyzed in the same manner. The values of $\bar{\alpha}$ derived from these measurements are compared with the calculated values in Figure 6. A major source of systematic error (generally small, but emphasized by the present method of analysis) is the extrapolation of reactivities with small samples to samples of effectively zero mass. This problem has been solved for recent cores but the solution has not been applied to the earlier measurements discussed here.

Because of the heavy reliance on calculated factors in this and similar methods, and their relatively large contribution to the final uncertainty, an alternate method of determining $\bar{\alpha}$ has been proposed by S. G. Carpenter.

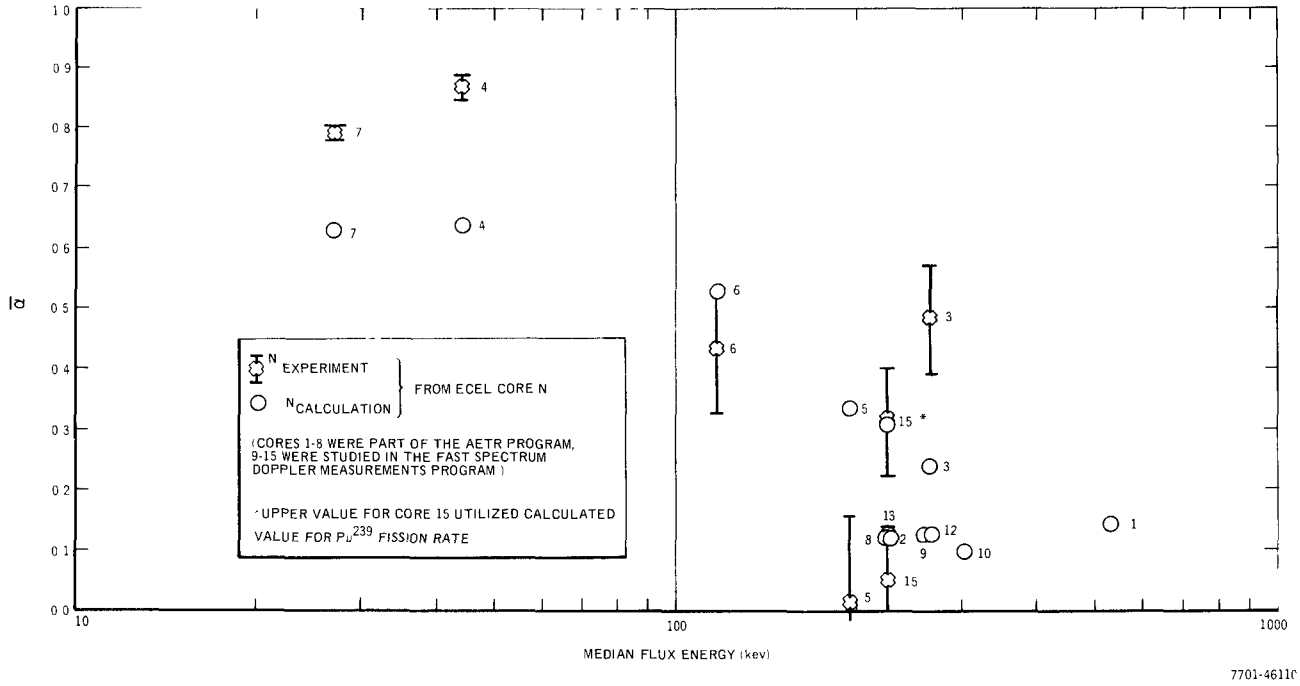

Figure 6. Alpha Values of Pu^{239} from Results Obtained in AETR Program Using Calculated Value of α for U^{235}

This method is based on the experimental determination of the various terms in the perturbation theory expression for the reactivity of a sample, neglecting scattering. The major difference in this method is the determination of the reactor importance production rate by a combination of neutron source and fission counter measurements as developed in the AETR program. The sources proposed for this method are a Cf^{252} fission source and several photoneutron sources to measure the low-energy importance.

I. ULTRA-HIGH TEMPERATURE OVEN

Difficulties with vacuum seals, electrical insulation, and heater coil supports have prevented successful measurements with the ultra-high temperature oven at its design temperature (2000°C) in the reactor. Trials made with the oven at 950°C in the reactor indicated no unforeseen problems in operation or data acquisition, and validated the planned method for data analysis. Since this oven design has achieved 1950°C in bench-top tests, the basic principle appears satisfactory and further improvement of the materials in use will be attempted.

J. PUBLICATIONS

Results obtained with these cores have been presented in the following reports:

"Measurements of the Temperature Coefficient of Reactivity of U^{235}, Pu^{239}, and Higher Pu Isotopes," presented at the American Nuclear Society Winter Meeting, Chicago, November 1967

"Variations in the Fast Spectrum Doppler Coefficients of Th and U^{238} as a Function of the Type and Temperature of the Environment," presented at the American Nuclear Society Annual Meeting, Toronto, June 1968

"Doppler and Related Measurements in a Soft Fast-Reactor Spectrum," AI-AEC-12705

III. EVALUATION OF EFFORT DURING FISCAL YEAR 1968

Measurements have been made in a significant range of flux spectra, including representative LMFBR spectra. Calculational artifacts due to group-boundary location, of general interest in the design of sodium-cooled reactors, have been found. Spectrum measurements by two distinct methods, foil activation and proton-recoil spectrometry, have been made and compared. Considerable progress in the development of the proton-recoil method has been made. The interaction between heated material in the reactor and a small heated sample has been measured systematically, and detailed analysis of the results has been started. Fission rate measurements verify the flatness of the flux in the central region of the cores. Reactivity and Doppler-effect measurements have been made with a variety of fissile, fertile, structural, and control materials. A successful method for calculating the expansion effect of fissile isotopes has been developed. Previously obtained data have been analyzed to determine the effective capture-to-fission ratio; and a new, more accurate method has been devised. The ultra-high temperature heater has not yet been completely successfully operated in the reactor; however, the concept has been proven.

PAGE 42 is blank

Program: Reactor Development
AEC Task: 5-C Basic Theory Calculation, Region Dependent Flux Spectra
Project Manager: H. A. Morewitz
Reporting Period: Fiscal Year 1968
General Order: 7701 Subaccount: 13310 AEC Category: 04-40-01-01.1

Principal Scientist: F. L. Fillmore

I. PROJECT OBJECTIVES

The general objective of this project is to develop and extend fast reactor physics analysis methods which are efficient, of adequate accuracy, and of sufficient scope to meet fast breeder reactor nuclear design and safety requirements. This objective is to be realized by development and extension of methods for accurately determining the energy and spatial distribution of direct and adjoint spectra required for realistic evaluation of the safety and economic characteristics of fast reactors and the development and extension of physics methods to provide accurate information with regard to fast reactor fuel cycle requirements, safety design requirements, and accident conditions.

II. TECHNICAL PROGRESS DURING FISCAL YEAR 1968

The required code development to permit a complete region-dependent weighting spectrum calculation in a single computer run, (the linking of CAESAR, AILMOE, and GRISM) was completed. Modifications to CAESAR include in-computer core transmission of region-dependent bucklings to AILMOE, in-computer core reception from GRISM of the region-dependent cross section libraries, and removal of the requirement for loading a hexadecimal cross section library each time the code is called by the system. Subroutines for calculating fission and capture traverses were incorporated, and the input of the cross sections used in the perturbation theory calculation of central reactivity coefficients was automated.

Modifications to AILMOE include the automated reception of the region-dependent bucklings from CAESAR and the automated transmission to GRISM of the weighting spectrum which is calculated for each region.

To permit more than one CAESAR library to be made in the same run, it was necessary to introduce a multiple case option in GRISM. Cross sections for the perturbation theory calculation of central reactivity coefficients are transmitted to CAESAR through internal computer manipulation.

The checkout of the above code modifications was completed and a simplified test problem was run to check for successful interaction among the several codes in making a complete region-dependent calculation.

A 25-group, one-iteration calculation was made for the ZPR-3-34 critical assembly. There are 7 core isotopes and 4 blanket isotopes in this calculation; about 60 min of 360/50 computer time was required. The analysis of the results from the zeroth and first iterations showed only small differences between corresponding quantities.

A 25-group, one-iteration calculation was made for the ZPR-3-48 assembly. The results of this calculation along with those from a 5 group ZPR-3-48 calculation were analyzed. In both cases, there were small differences between the zeroth and first iterations results. However, these differences were usually less than the corresponding differences due to the variation in group structure of the 25-group and the 5-group calculations. The conclusion drawn is that in assessing criticality for critical assemblies of the ZPR-3-48 type, it is more important to use an adequate number of groups than to employ region dependent weighting spectra. This conclusion has not been verified for large fast reactors and for quantities such as the sodium void coefficient, the Doppler coefficient, and the breeding ratio.

A fundamental mode weighting calculation was performed for a typical 3000-liter LMFBR. An important objective of this calculation is to determine the effect of region dependent weighting spectra on the sodium void and Doppler coefficients of LMFBR reactors of this size.

III. EVALUATION OF EFFORT DURING FISCAL YEAR

A highly automated computerized method was developed to permit a complete region-dependent weighting spectrum neutronic calculation in a single pass through an IBM system 360/50 computer. The necessary code linkage was completed and checked out. As a result of these developments, considerable savings, both in manpower and computer cost, for using this reactor evaluation tool have been achieved.

The newly linked system of computer codes was tested on calculations for the two critical assemblies ZPR-3-34 and ZPR-3-48 whose blanket regions are similar. Both of these assemblies had been analyzed previously by using the various individual links of the computer code. The reanalysis was used as the basis to show that the linked code calculation did indeed give the same results as the unlinked calculation. The differences in k_{eff} obtained with the fundamental weighting spectrum and the region-dependent weighting spectra for these assemblies do not appear to be significant. The effect, however, of spatial weighting on Doppler, sodium void, and reactivity coefficients has yet to be determined.

Similar effects for the 3000-liter LMFBR case remain to be studied.

PAGE 46 is blank

Program:	General Reactor Technology			
AEC Task:	5-D Reactor Physics, Integral Experiments			
Project Manager:	H. A. Morewitz			
Reporting Period:	Fiscal Year 1968			
General Order:	7701	Subaccount:	13210	AEC Category: 04-40-01-02.1

Principal Investigator: R. K. Paschall

I. PROJECT OBJECTIVES

The purpose of the fast reactor physics program is to supply data pertinent to both the safe and economic design and operation of fast power reactors. Safety and economics often compete in good reactor design and very conservative estimates are usually made in the area of safety because of the paucity of precise physics data. This program is designed to study these specific areas and confirm the nuclear parameters and calculational methods used on conceptual evaluation and preliminary design.

The large volume of coolant (50%) and structural material (15%) in current fast reactor designs make increasingly important the accurate knowledge of light element scattering cross sections which affect the magnitude of both the Doppler and sodium-void effects. Also of concern is the resonance shielding for various mixtures of the light elements.

A series of integral experiments are being performed using coolant material (sodium) and the predominant structural material (iron). The measurements seek to determine the differential neutron spectrum in large volumes of sodium, in a large quantity of pure iron, and in appropriate mixtures of these materials, for both isotopic and reactor neutron sources. The resulting neutron spectra will be compared to predictions based on Monte Carlo calculations in order to check the scattering cross sections presently used. The use of a reactor as a neutron source will allow, in addition, reactivity measurements of the sodium void as well as direct studies of spectral changes occurring during this voiding.

The techniques for measuring the neutron spectra over a wide range of energies are quite limited. The recent development of the proton-recoil

spectrometer using hydrogen or methane filled detectors is one of the most promising. Resolution of approximately 20% is obtained over energies of 20 to 500 kev. The energy range can be extended with much worse resolution (such as 60% at 1.0 kev). With Li^6 and He^3 spectrometers; measurements can be made from 500 kev to about 5 Mev (up to about 14 Mev with very expensive electronics and many corrections to the measurements).

II. TECHNICAL PROGRESS DURING FISCAL YEAR 1968

A. PROTON RECOIL SPECTRA IN SODIUM

A new series of proton recoil neutron spectrum measurements in the large volume of sodium was completed. Figure 1 shows the experimental arrangement. Ten slabs of sodium, each 12.5-in. thick (12-in. of Na between 0.25-in.

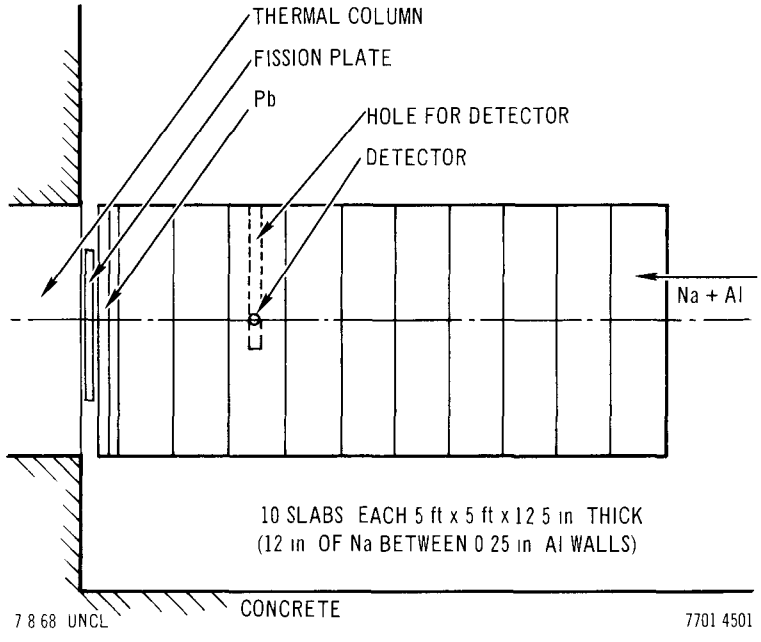

Figure 1. Experimental Arrangement for Neutron Spectrum Measurements in Sodium

Al walls) by 5-ft^2 were stacked together to give a volume 125-in. thick by 5-ft^2. A 24-in. diameter fission plate between the 5-ft^2 graphite thermal column of the STIR reactor and sodium provided the fission neutrons. Two lead plates 1-in. thick by 5-ft^2 were placed between the fission plate and the sodium. This attenuated the gamma flux without changing the neutron spectrum by any measurable amount. The spectrometer detectors were located in the center of one of the slabs which has a 2-in. diameter by 36-in. deep hole in it. This slab was interchanged with the others to allow the detectors to be placed with 15.9, 79.4, 142.9, 206.4, and 269.9 cm of sodium and aluminum between them and the fission plate.

Some analysis of the data has been completed. Results of the measurements at 79.4 cm have been analyzed in detail and are shown in Figure 2. The histogram is an ANISN calculation for sodium only. The continuous curve is an AILMOE calculation in sodium and aluminum with negative buckling and 20% curve smoothing. The measurements and ANISN calculations are normalized to the AILMOE calculations.

Dips in both the measured spectrum and AILMOE calculation at 35 and 90 kev show that aluminum should be included in the ANISN calculations in order to properly predict the neutron spectrum. The large peak between 100 and 400 kev in the ANISN calculation is not observed in the measurements. Including aluminum in the calculation may eliminate this discrepancy. AILMOE calculations are only useful near the source. They show the energy separation and relative magnitudes of the peaks and valleys but do not reflect correct changes with distance into the sodium volume. ANISN calculations are made for each specific distance but, at present, do not include the aluminum and have too coarse an energy grid to show much detail.

Figures 3, 4, 5, 6 and 7 show the measured results from approximately 30 kev to 300 kev. These measurements used detectors filled with 0.5 and 1.0 atm of hydrogen. No gamma discrimination was used for these data. The results above and below this energy range are still being analyzed. Figures 3, 4, 5, and 6 also show the ANISN calculations from 1.0 to 1.0 Mev. Experimental and calculated spectra are compared directly in the following manner. Absolute flux per unit lethargy at a particular detector location is determined by the

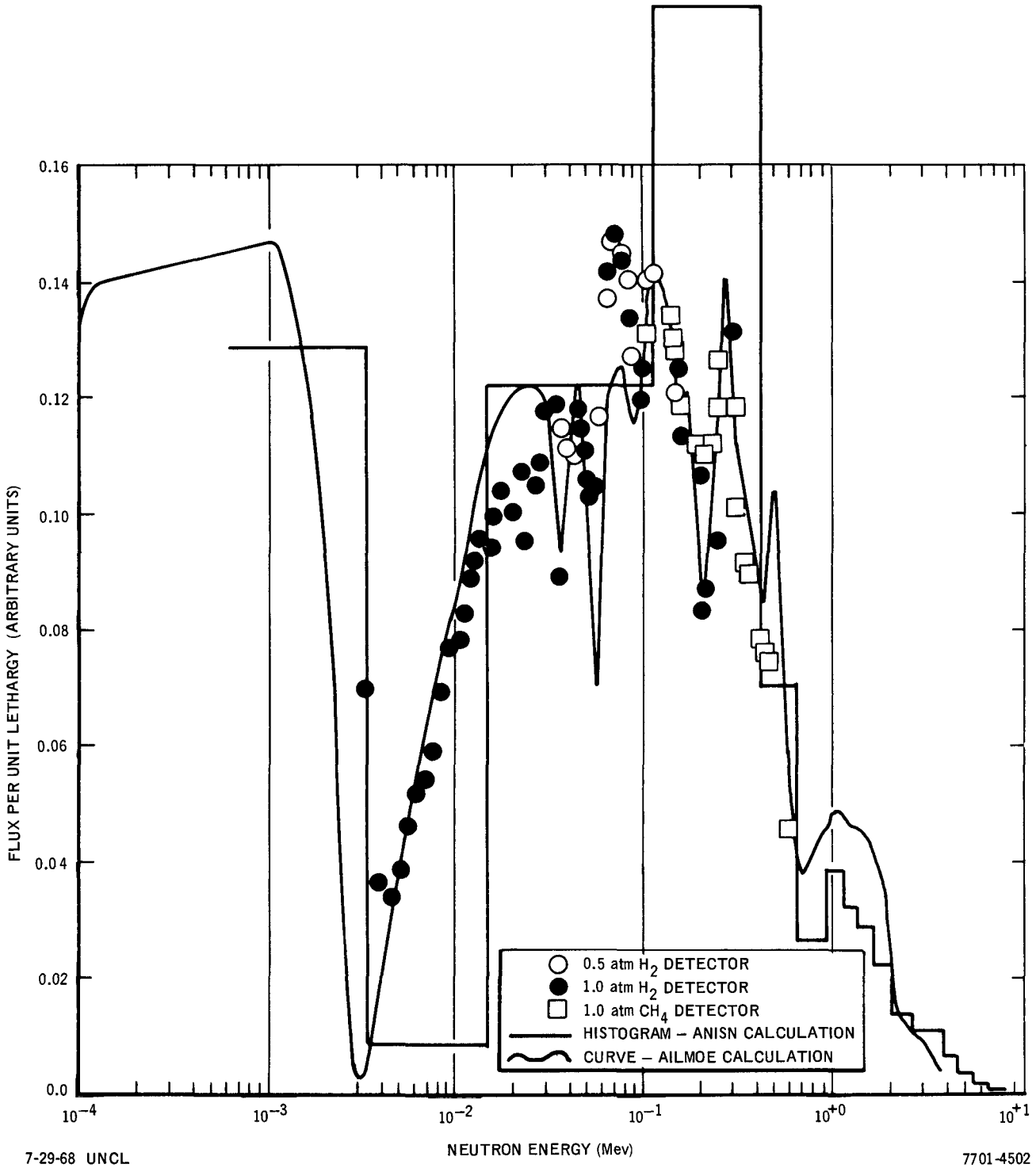

Figure 2. Neutron Spectrum in Na + Al, 79.4 cm (31.25 in.) of Na + Al Between Detector and Fission Plate

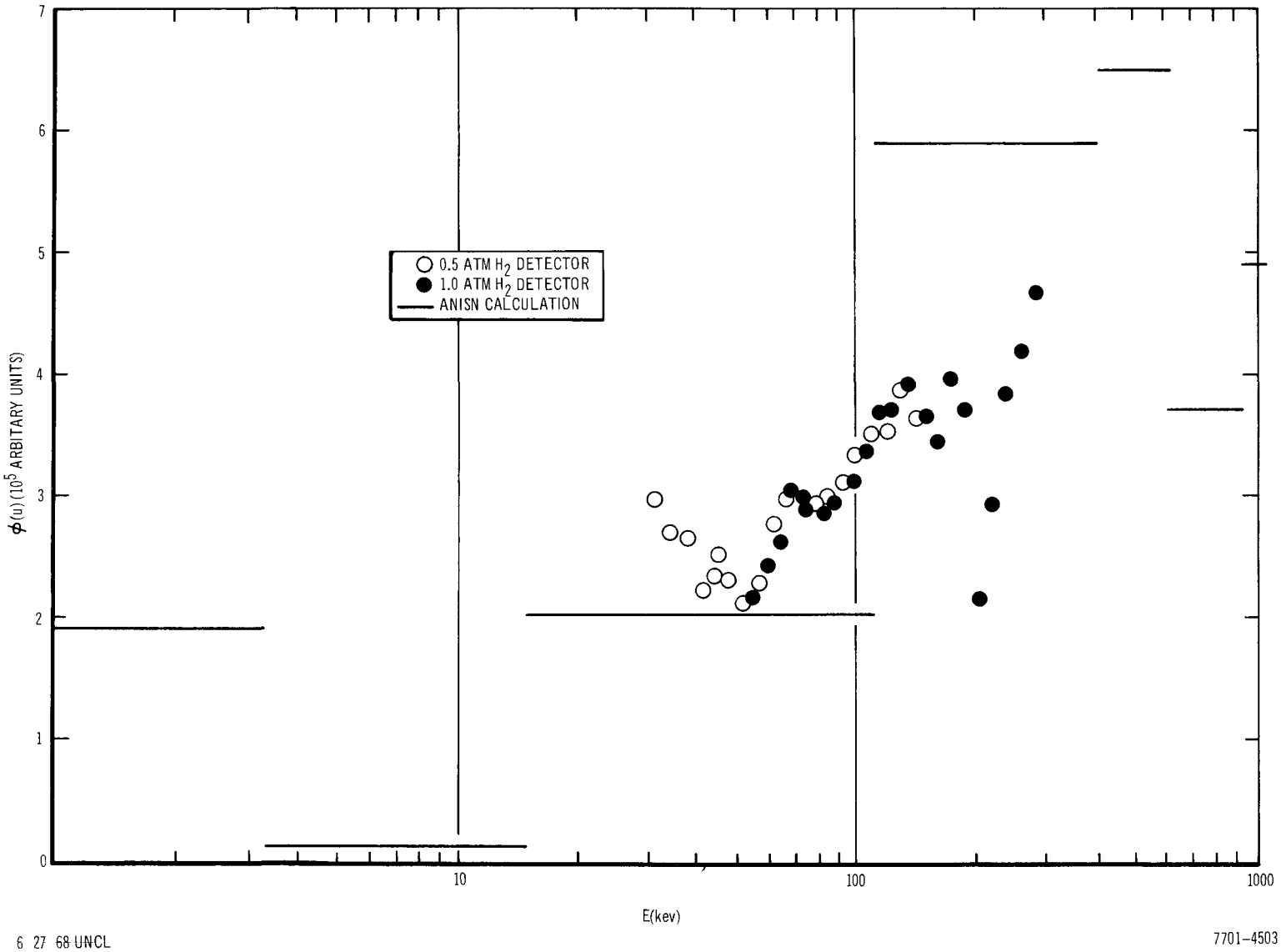

Figure 3. Neutron Spectrum at 15.9 cm in Na + Al

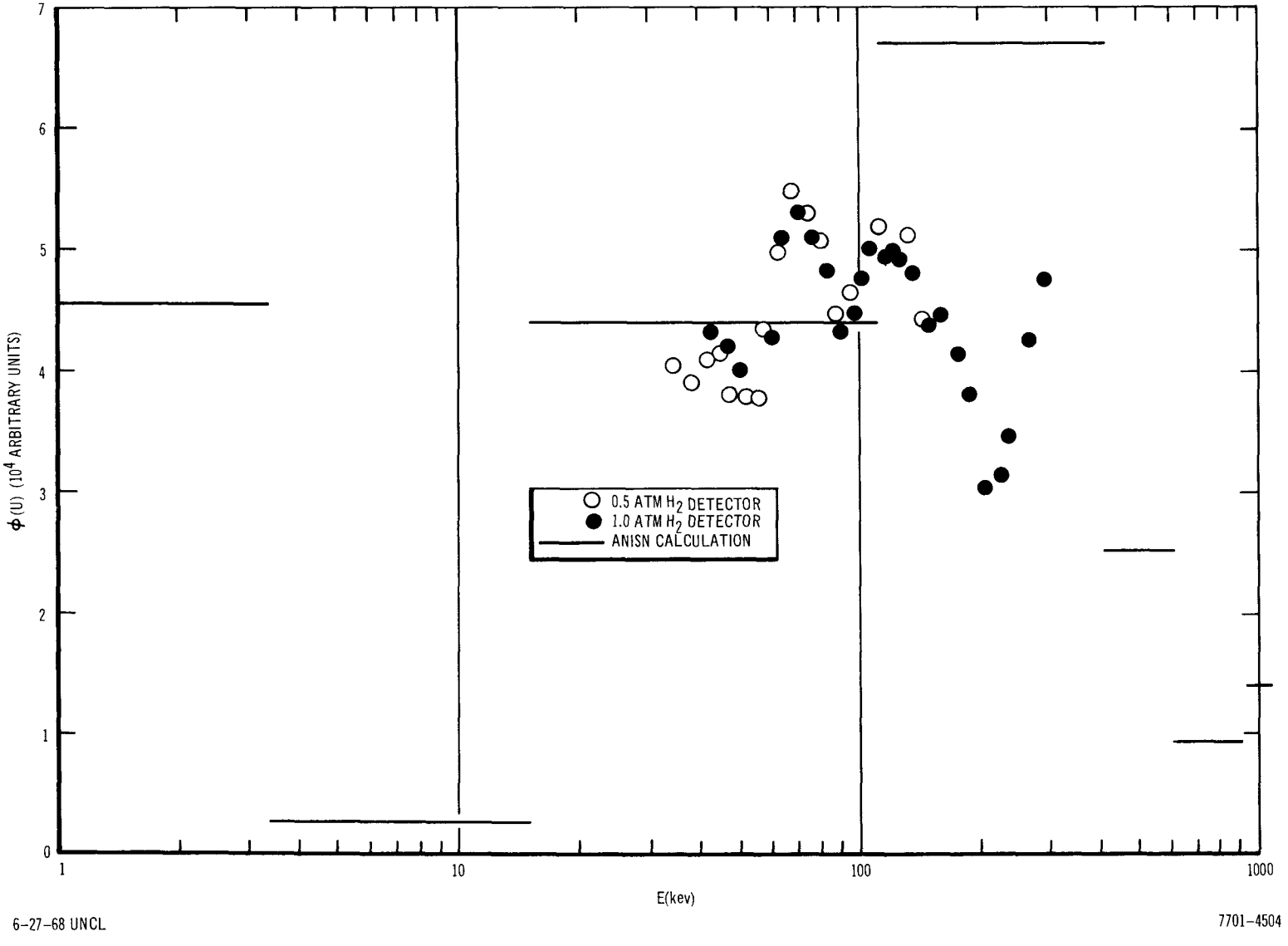

Figure 4. Neutron Spectrum at 79.4 cm in Na + Al

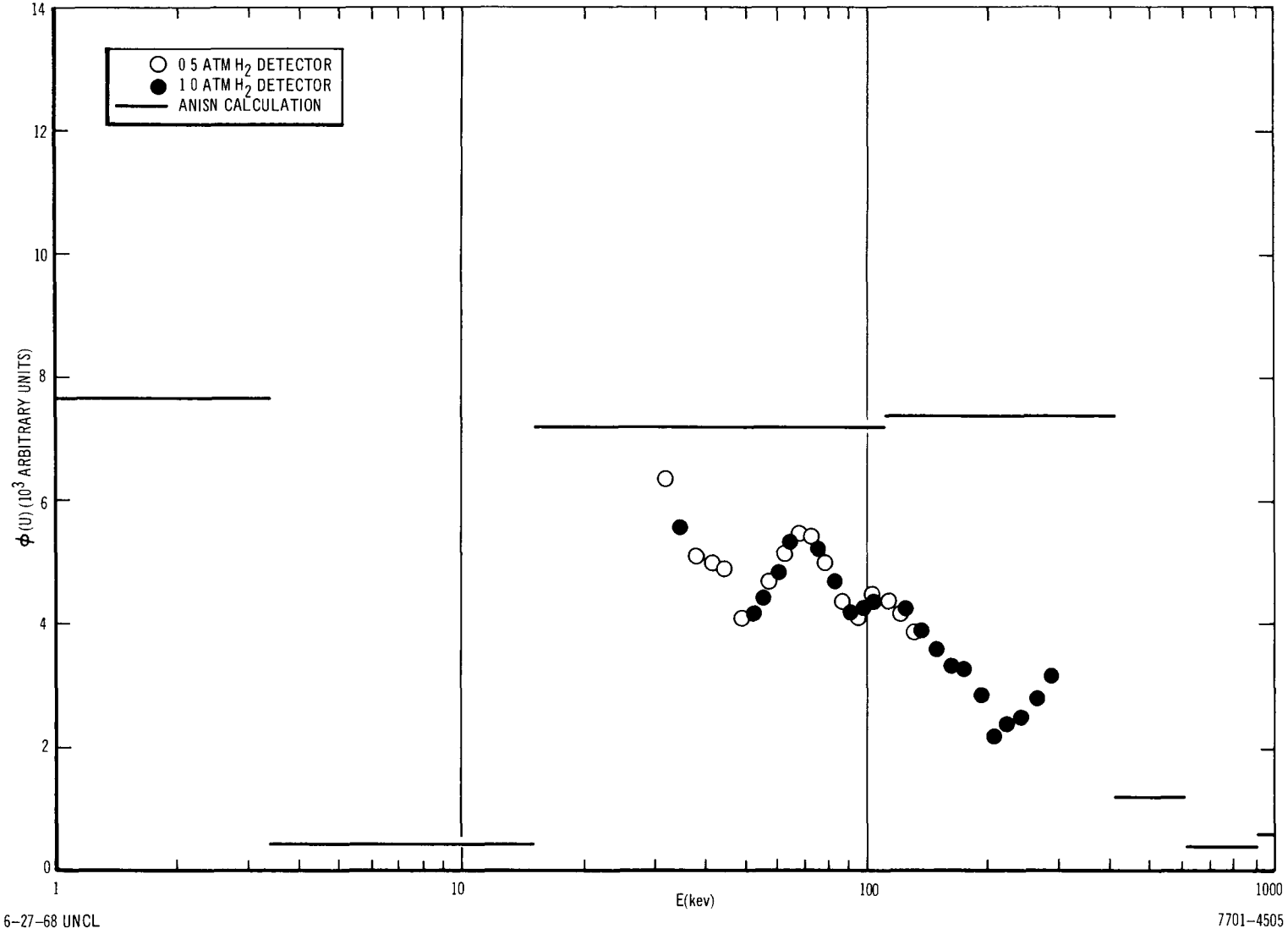

Figure 5. Neutron Spectrum at 142.9 cm in Na + Al

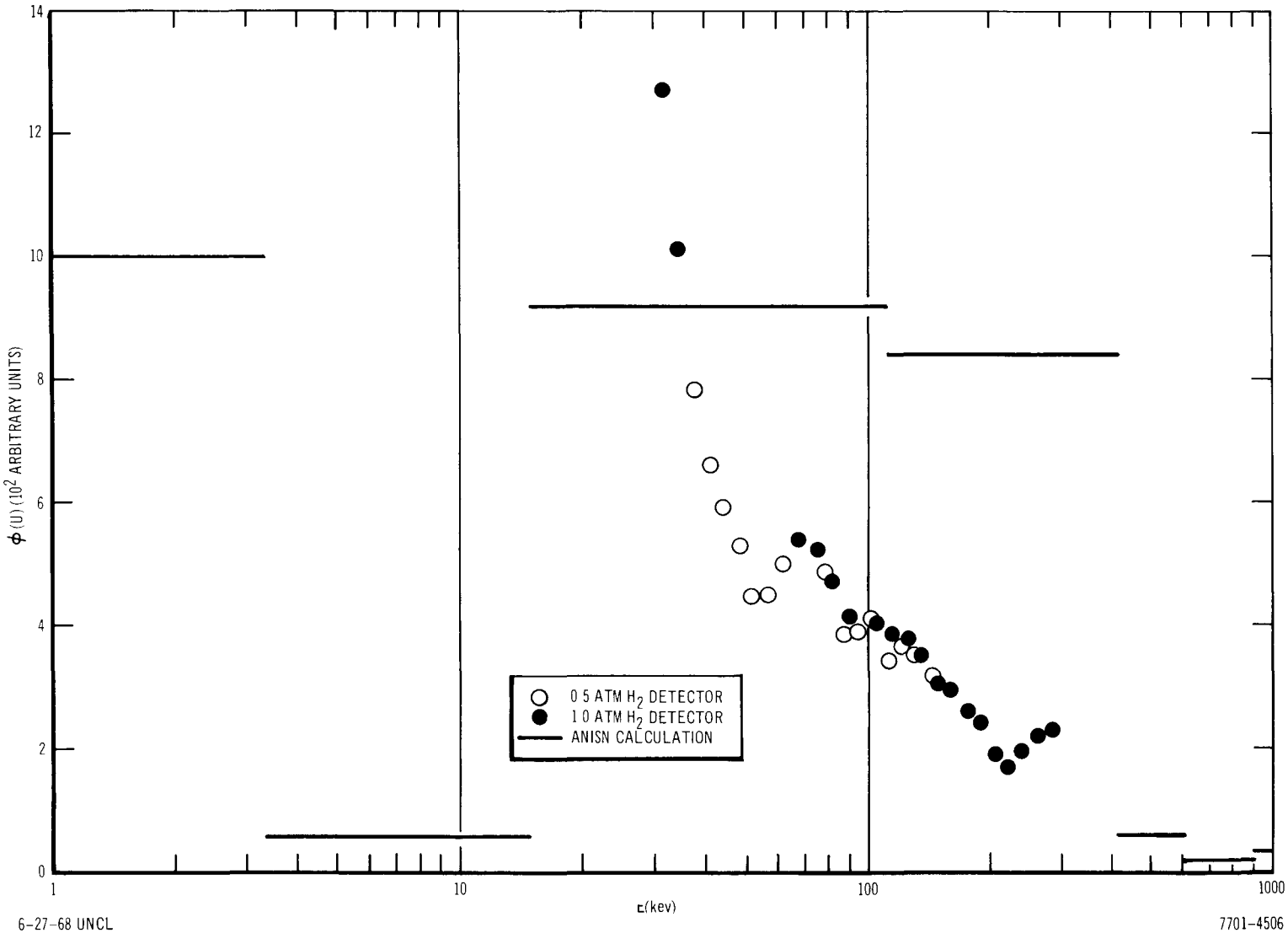

Figure 6. Neutron Spectrum at 206.4 cm in Na + Al

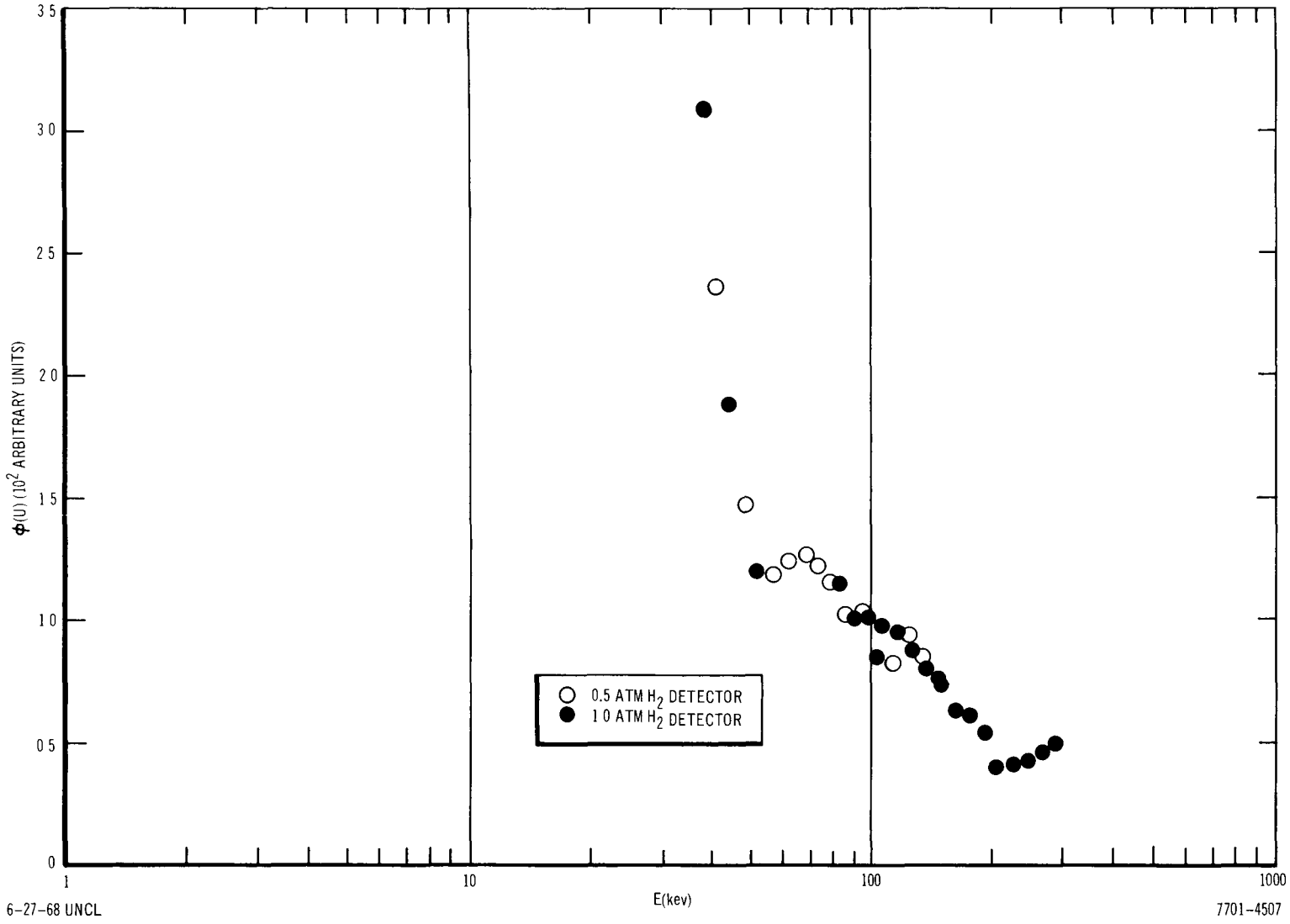

Figure 7. Neutron Spectrum at 269.9 cm in Na + Al

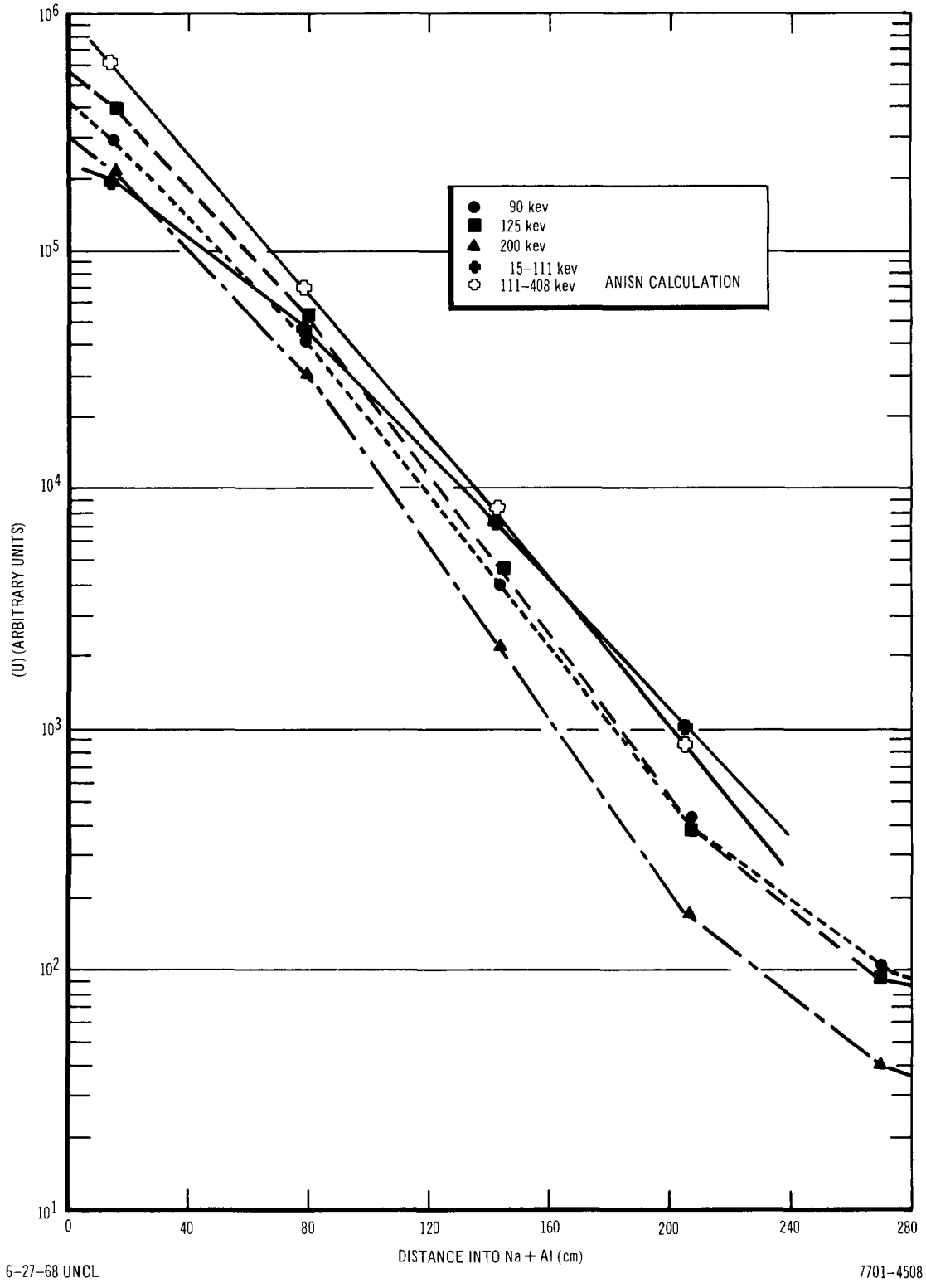

Figure 8. Neutron Attenuation in Na + Al

data-analysis code, from counts per unit energy (collected by the pulse-height analyzer), data-collection time, number of hydrogen atoms in the detector, detector volume, and the (n, p) cross section for hydrogen.

To calculate the flux at that location, the reactor power level (determined by a calibrated ionization chamber) is recorded. For any reactor power level, the fission-neutron flux from the fission plate is known from previous inter-calibration measurements made by the staff at the STIR facility. The calculated flux distribution throughout the sodium volume is then based on a known initial fission-neutron flux from the fission plate. At any reactor power level, therefore, and any location within the sodium, the flux per unit lethargy can be calculated and directly compared with the measured results. To maintain a high counting rate, the reactor power is increased as the distrance between the fission plate and detectors is increased; the measured and calculated fluxes are then divided by the reactor power to compare the results at all locations. Figure 8 compares the measured attenuation of 90, 125, and 200 kev neutrons in sodium and aluminum with that calculated for two energy groups in sodium.

B. GAMMA SHIELDING STUDIES

Spectrum studies were also made in the ECEL reactor in order to evaluate the affect of lead shielding on proton recoil counter performance. Comparison with runs made without the lead showed that no measurable effect on the neutron spectrum could be attributed to the lead shield.

An attempt was made to detect neutrons originating in the core center, with a detector located outside the reactor but looking down the empty central drawer to the core center. Different shielding and collimation arrangements indicated partial success; however, more hydrogeneous material is needed around the detector to eliminate neutrons scattering off the room walls and iron shield near the detector as well as from the other reactor parts.

C. ELECTRONIC CIRCUIT DEVELOPMENT

Modifications were made to the pulse shaper to improve the dynamic range and count rate capabilities. It was completely reconstructed in a NIM module. The diode pump to the sample capacitor was direct coupled. Previously, a 10 second RC time constant was included in the circuit at this point. The

nuvistor vacuum tube diode was replaced with a thin film silicon diode which has just recently been made available. This diode [Isofilm (1BB13)] has a very low reverse leakage, a forward voltage drop of 0.2 volt at 1.0 ma forward current, and a reverse recovery time of 2 nanoseconds. A gain-of-2 amplifier was then added before the diode pump. This increased the peak voltage to the sample-end-hold circuit to 20 volts. The increased gain also enabled integration and a much faster secondary clip at the output. This produces a pulse shape more compatible with the ADC of the Nuclear DATA pulse height analyzer. The forward voltage drop of the silicon diode is now only 1% of full scale and the dynamic range of the instrument is now better than 100 to 1. A diode limiter was placed before the trigger amplifier to prevent it from going into saturation. This improved bias stability of the Schmitt trigger. Twenty-five-times overload pulses had occurred in the trigger amplifier from saturated delay line amplifier pulses. These pulses become numerous when the system gain is increased to observe low energy pulses. The diode limiter completely eliminated any effects caused by high rates of overload pulses. The principle reason for this modification was to have the pulse shaper release its output pulse (recovery of Schmitt trigger) at the zero-crossing of the delay line amplifier. The pulse shaper was modified from the original design so that the energy and risetime information to the multichannel analyzer are in coincidence. Timing the analyzer pulses at the zero crossover of the energy pulse will allow the addition of auxiliary coincidence gating to the counting system. A window discriminator can now easily be added to the system. Inspection for pulse pileup can be incorporated and the time-to-height converter that is in the risetime channel can be gated without affecting the 150 nsec coincidence requirement of the dual parameter analyzer.

III. EVALUATION OF EFFORT DURING FISCAL YEAR 1968

The proton recoil neutron spectrometer was reconstructed with major improvements in the electronic circuitry. These improvements extended the dynamic range and count rate capabilities of the spectrometer, so that it is now possible to obtain good spectral information down to 4 kev in neutron energy, with good separation from the gamma-ray background.

A complete series of spectrum measurements was made in a large volume of sodium (with some aluminum) out to 269.9 cm from a fission neutron source.

The measurements at one location near the source were compared with an AILMOE calculation. The relative agreement of the peaks and valleys in the flux vs energy is very good. A dramatic improvement in the spectral detail was obtained. The effects of the resonances and dips in the sodium and aluminum cross sections were very visible and compared favorably with AILMOE predictions. The measured neutron attenuation as a function of distance from the source was compared with an ANISN calculation in sodium and showed fair agreement. It is clear from these comparisons that the calculation should be made with the aluminum included and with a finer energy grid. Also, a Monte Carlo calculation should be made to exactly account for the leakage from the sides of the finite sodium volume.

PAGE 60 is blank

Program: Reactor Development
AEC Task: 5-E, Monte Carlo Methods
Project Manager: H. A. Morewitz
Reporting Period: Fiscal Year 1968
General Order: 7701 Subaccount: 13320 AEC Category: 04-01-61-02.1

Principal Scientist: L. B. Levitt

I. PROJECT OBJECTIVES

The basic objective of this project is to advance the state of the art of Monte Carlo applications to the analysis of fast reactors and fast critical assemblies. This development is needed so that experimental programs and design studies may be optimized through the use of computer programs capable of describing complicated geometric configurations while calculating the effects of localized perturbations. These objectives will manifest themselves in the ultimate development of third generation Monte Carlo fast reactor criticality codes which will treat perturbations due to changes in temperature, density, and material composition. These codes will have rapid convergence and will make efficient use of the new generation of computers.

II. TECHNICAL PROGRESS DURING FISCAL YEAR 1968

The most significant development in fiscal year 1968 was the establishment, in detail, of adjoint Monte Carlo sampling schemes required to implement the third generation Monte Carlo codes. These schemes eliminate the need to do adjoint Monte Carlo with multigroup data. They permit identical cross section libraries to be used for direct and adjoint Monte Carlo calculations. They will permit development of importance sampling schemes to handle anisotropic elastic scattering which will be equally applicable in both direct and adjoint Monte Carlo codes.

A mathematical basis for the combined use of adjoint and direct techniques has been established and documented in NAA-SR-12494. The TRAFE resonance integral code has been used as a tool to verify techniques which will be used in the next generation fast reactor criticality code. These techniques include the use of:

1) Statistical estimation in the adjoint portion of the calculation, permitting the rigorous use of stratified sampling of the source energies resulting in improved energy source sampling.

2) "Naive" correlation (starting each corresponding history of two correlated runs with the same random number), and

3) "Nearly Complete" correlation. This has been introduced into the normal mode calculation in order to improve the correlation between the infinitely dilute and experimental sample portions of the calculation. This is the same technique which will be most useful in an investigation of dimensional, density, and Doppler broadening perturbations.

Calculations using the modified version of the TRAFE code indicate a remarkable improvement in the ability to determine the cadmium cutoff as a result of the "Naive" and "Nearly Complete" correlation techniques which were incorporated. Significant reduction in computer costs have been made possible through the optimization of the sequencing of the adjoint and normal portions of the neutron history.

In an adjoint simulation of elastic scattering, a statistical weight factor arises because the scattering kernel is unnormalized. Transformations have been developed to help reduce the spread of the statistical weight factors thereby leading to a considerable reduction in the variance of the estimate.

Direct and adjoint versions of the code (STRIFE) which calculates the resonance escape probability for a two slab lattice were written. Direct mode calculations were compared with various adjoint formulations in order to determine which adjoint sampling techniques result in estimates of lowest variance. The normalization factors and methods of sampling required by the transformed adjoint equation are different from those used in conventional multigroup adjoint representations. The STRIFE code was used as an experimental tool to develop proper methods both for source weighting, final tallying, and for comparison of variance in the estimates.

The adjoint simulation of the test problem setup in the STRIFE code produced results in complete agreement with direct Monte Carlo calculations on

the same problem. This agreement is for both constant and highly resonant absorber regions over an extremely wide range of resonance escape probabilities (0.3 to 0.996). Inspection of these results has enabled us to define quantitatively the conditions which require an adjoint Monte Carlo treatment; and conversely, those problems for which the adjoint approach would be less efficient than the direct Monte Carlo simulation. The new features introduced into this investigation (namely, the transformation of the adjoint Boltzmann integral transport equation and the use of a scattering kernel which is inherently normalized for elastic scattering while preserving the angular distribution) have been thoroughly tested and their usefulness is clearly indicated by the results obtained.

Several adjoint tallying procedures were compared and their performance in the test problem carefully evaluated. The terminal tallying procedure appears considerably better than the collision-by-collision tallying procedure. Ultimately, however, the best result will be obtained from an optimized linear combination of both procedures.

Work has begun on the study of source settling problems in reactor criticality calculations through the use of the reactor analysis version of the SAFE code (NAA-SR-MEMO-12490).

A detailed analysis of a 20,000-history Monte Carlo Criticality calculation previously performed on the SAFE code was initiated in an attempt to observe source settling and other potential problems which will have to be faced in the development of the fast reactor analysis code VIM. The settling down of the power distribution (Figure 1) indicates that the presently used method of source selection, which avoids the use of a preliminary set of neutron histories to fix the neutron source, does in fact lead to the asymptotic source distribution necessary for eigenvalue problems. Thus, the expenditure of computer time for running neutron histories prior to achieving the settled distribution can be minimized or even eliminated. In addition, the excellent behavior of thin region fluxes speaks well for the procedure presently used in the SAFE code. Few-group cross sections obtained by Monte Carlo in this run show satisfactory convergence for engineering purposes at the end of the 20,000 histories. The results of this analysis indicate that a fast reactor analysis code can be expected to procedure satisfactory flux convergence in the same time necessary to accurately determine k_{eff}.

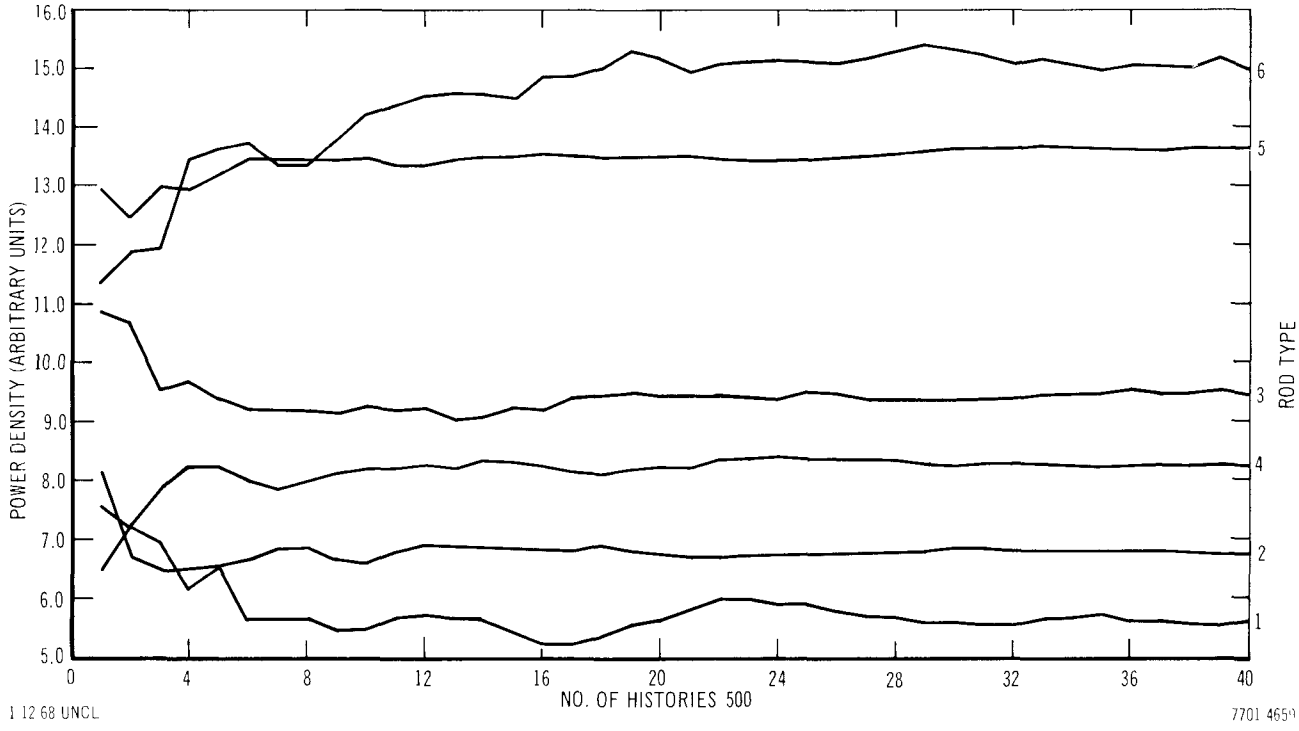

Figure 1. Power Distribution Settling

Importance sampling schemes are now being investigated for the purpose of simplifying the selection of scattering angles in those energy regions where the elastic scattering is anisotropic. This will be useful when applied to fast reactor problems where the angular distributions may change with energy. While the motivation for this investigation was the improvement in efficiency of adjoint selection procedures, this particular simplification will also serve the same purpose on direct mode fast reactor criticality calculations.

DOCUMENTATION

The following papers were presented at technical meetings during fiscal year 1968.

L. B. Levitt, "Some Applications of Monte Carlo to Particle Transport Problems," SHARE XXX Meeting, Houston, February 1968 (Invited Paper)

L. B. Levitt, "Applications of Monte Carlo to Problems in Reactor Design and Experimental Analysis," ANS Meeting, Toronto, Canada, June 1968 (Invited Paper)

L. B. Levitt, A seminar titled "A Non-Multigroup Adjoint Monte Carlo Approach to Problems in Reactor Design and Experimental Analysis" was presented to the Nuclear Engineering Department of the University of Washington in Seattle on May 22, 1968

The following reports and papers were published during fiscal year 1968.

SAFE – A Three-Dimensional Monte Carlo Code for Nuclear Safety Studies, NAA-SR-MEMO-12490 (July 1967)
A New Use of Adjoint in the Monte Carlo Estimation of Resonance Integrals, NAA-SR-12494 (September 1967)
The Use of Self-Optimized Exponential Biasing in Obtaining Monte Carlo Estimates of Transmission Probabilities, Nuc. Sci. and Eng. 31, 500-504 (1968)

III. EVALUATION OF EFFORT DURING FISCAL YEAR

The use of adjoint Monte Carlo is essential to the solution of any neutronics problem involving local effects such as small experimental detecting regions, hot spots, etc. As of this writing, no adjoint Monte Carlo code using detailed point cross-section data has been written. The most significant development of the present fiscal year in the Monte Carlo program, therefore, is the establishment, in detail, of adjoint Monte Carlo sampling schemes compatible with the demands of the next generation of Fast Reactor Monte Carlo Codes (VIM, VIGOR).

These schemes eliminate the need to do adjoint Monte Carlo with multigroup data, and permit identical cross-section libraries to be used for direct and adjoint Monte Carlo calculations. This means that the VIM code system can use a master cross section library in both modes (adjoint and direct). They also permit future development of importance sampling schemes to handle anisotropic elastic scattering which will be equally applicable in both direct and adjoint Monte Carlo codes. In addition, these schemes eliminate much of the inherently high variance encountered in previous multigroup treatments.

An investigation of the detailed simulation procedures needed in a Monte Carlo adjoint mode transport calculation has been performed. It was felt that this is essential to permit proper application of adjoint Monte Carlo techniques to Doppler coefficient and dimensional perturbation problems. The techniques developed and incorporated into the TRAFE code involve a superposition of adjoint mode neutron histories to determine a normal mode source for that portion of the neutron history subsequent to the 1st encountered with the perturbed region. Extension of this technique to reactor problems in which some of the idealizations properly utilized in TRAFE no longer apply is not a straightforward

procedure. One of the more significant problems is how to account for the non-normalized scattering kernel which must be brought to bear on the statistical weight of the adjoint particle in tracking its history upward in energy.

Some work has been published on the adjoint transport equation and Monte Carlo applications of it, but few, if any, realistic problems have been solved involving fast neutrons. Some of these analyses have used multigroup cross-section libraries. The use of such libraries is open to question. Simulation of the adjoint transport equation using point cross-sections and detailed anisotropic scattering models is the essential goal of the present investigation, since the ultimate substitution of Monte Carlo calculations for experiments must be based on physical models which are as realistic as can practicably be contained in a digital computer code.

Calculations using the modified version of the TRAFE code indicate a remarkable improvement in the ability to determine the cadmium cutoff as a result of the "Naive" and "Nearly Complete" correlation techniques which were incorporated. The success of the correlation techniques has been quite encouraging and promises to yield equal success in fast reactor criticality calculations. There are problems of a nature similar to those for which TRAFE was developed; however, where one cannot avoid the complexities of a complete adjoint solution, the more generally applicable techniques incorporated into the STRIFE code were developed.

It is interesting to note that in problems in which the absorption was extremely small and taking place in an extremely small region, that the adjoint simulation produced nearly zero variance. Three-figure convergence on (1 - p) was obtained in one second of CDC-6600 computer time. In other words, in problems involving a very small detector and a large source, the adjoint procedure is not only far superior to the direct Monte Carlo calculation but compares quite favorably with any analytic or numerical treatment.

Importance sampling in the adjoint source energies greatly reduced the variance for the highly resonant absorbing detector problem. Since the importance sampling employed was deliberately lacking in detail over the energy range involved, it is clearly indicated that any analytic scheme, however crude,

could be effectively utilized in spectrum calculations employing the adjoint simulation procedures.

As a result of the successful development of nonmultigroup adjoint sampling techniques, work can now proceed on the direct development of the VIM code system. VIM can now contain the capability for solving neutronics problems involving local effects, in a highly efficient manner.

PAGE 68 is blank

Program: Nuclear Safety		
AEC Task: 6A, Reactor Dynamics Simulator Development		
Project Manager: H. A. Morewitz		
Reporting Period: Fiscal Year 1968		
General Order: 7702	Subaccount: 29110	AEC Category: 04-60-01-09.1

Principal Scientist: E. U. Vaughan

I. PROJECT OBJECTIVES

The basic objective of this project is to improve the present state of kinetics codes for use in fast reactor safety calculations. Improved codes and methods to study the kinetics of fast breeder reactors are needed in order to remove some of the existing uncertainties in conceivable FBR accidents. These improvements will produce a space dependent calculational scheme capable of giving a reasonably accurate picture of the complexities of space-time-energy dependent fluxes at computation costs lower than those obtained by the "exact" solution.

II. TECHNICAL PROGRESS DURING FISCAL YEAR 1968

Effort has been concentrated on exploring the use of the synthesis method to represent space-dependent spectra in fast reactors. Before attempting the general kinetics cases ultimately intended, the spectrum synthesis method in the one-dimensional static case was explored and tested by comparison with multigroup diffusion theory. The equations of the latter theory are

$$-D_g(z)\,\Phi_g''(z) + \Sigma_g(z)\,\Phi_g(z) - \sum_{g'=1}^{g-1} \Sigma_{g',g}(z)\,\Phi_{g'}(z) = \frac{1}{\lambda} S_g(z) \qquad \ldots(1)$$

and

$$S_g(z) = X_g(z) \sum_{g'=1}^{G} \nu\Sigma_{fg}(z)\,\Phi_g(z) \qquad \ldots(2)$$

$$\Bigg\} \; g = 1, \ldots, G$$

where:

$D_g(z)$ = diffusion constant in group g for region containing point z,

$\Sigma_g(z)$ = removal cross section in group g for region containing z,

$\Sigma_{g',g}(z)$ = cross section for transfer from group g′ to group g in region containing z,

$X_g(z)$ = fission spectrum in group g for region containing z,

$\nu\Sigma_{fg}(z)$ = neutron production cross section in group g for region containing z,

$\Phi_g(z)$ = neutron flux in group g at point z, and

λ = effective multiplication factor of the system.

In spectrum synthesis, the flux, $\Phi_g(z)$, is approximated by a linear combination of a limited number, I, of known spectra

$$\varphi_{ig},\ g = 1, \ldots, G;\ i = 1, \ldots, I;$$

in the form

$$\Phi_g(z) \approx \sum_{i=1}^{I} u_i(z)\,\varphi_{ig} \quad . \qquad \ldots(3)$$

The set, φ_{ig}, for a given value of i is called the i^{th} basis spectrum, and the coefficient, $u_i(z)$, is called the i^{th} mixing function.

Equations to determine the mixing functions, $u_i(z)$, are obtained by the "method of weighted residuals," in which I weight functions are introduced:

$$W_{kg},\ g = 1, \ldots, G \text{ and } k = 1, \ldots, I. \qquad \ldots(4)$$

After substituting Equation 3 into Equations 1 and 2, Equations 1 and 2 are multiplied by W_{kg} and summed over g. The result is

$$\sum_{i=1}^{I}\left[-D_{ki}(z)\,u_i''(z) + H_{ki}(z)\,u_i(z)\right] = \frac{1}{\lambda}S_k(z) \quad , \qquad \ldots(5)$$

and

$$S_k(z) = X_k(z)\sum_{i=1}^{I}\nu\Sigma_{fi}(z)\,u_i(z) \quad , \qquad \ldots(6)$$

where the coefficients are:

$$D_{ki}(z) = \sum_{g=1}^{G} W_{kg}\,D_g(z)\,\varphi_{ig} \quad , \qquad \ldots(7)$$

$$H_{ki}(z) = \sum_{g=1}^{G} W_{kg}\left[\Sigma_g(z)\varphi_{ig} - \sum_{g'=1}^{g-1}\Sigma_{g'g}(z)\varphi_{ig}\right] \quad , \qquad \ldots(8)$$

$$X_k(z) = \sum_{g=1}^{G} W_{kg} X_g(z) \quad , \qquad \ldots(9)$$

and

$$\nu\Sigma_{fi}(z) = \sum_{g=1}^{G} \nu\Sigma_{fg}(z)\, \varphi_{ig} \quad . \qquad \ldots(10)$$

The weights, W_{kg}, usually used at present are obtained by defining I coarse groups, and assigning

$$\left.\begin{aligned} W_{kg} &= 1, \text{ if g is in the } k^{th} \text{ coarse group} \\ &= 0 \text{ otherwise,} \end{aligned}\right\} \quad k = 1, \ldots, I. \qquad \ldots(11)$$

This is the "group balance" form of the method of weighted residuals. The alternative "Galerkin" method in which the weight functions, W_{kg}, are the same as the basis spectra, φ_{ig}, has also received some attention.

The goal of the present effort is to compare fluxes (3) synthesized from solutions of the system (5), (6) with fluxes obtained directly from the system (1), (2). For this purpose, 25 groups (G = 25) are used, and the multigroup diffusion code CAESAR[1] supplies the solution of (1), (2). The system (5) (6) however, though simpler than (1) (2) because I < G, also has a new complication because the transfer matrix H_{ki} of (5), unlike the transfer matrix $\Sigma_{g'g}$ of (1) is not necessarily triangular. Consequently, the code, RAUM,[2] solves the system (5), (6) even for nontriangular matrices H_{ki}, was acquired and converted to operate on the IBM System 360 Model 50, and is used to compute the mixing functions, $u_i(z)$, of Equation 3.

A code, XMAS, has been written that computes the coefficient-matrices (7), (8), (9), and (10) from a CAESAR library, given the boundaries of the I coarse groups for W_{kg}, and the I basis spectra, φ_{ig}. Another code, PLEASER, has been written that uses the basis spectra, φ_{ig}, and the output, $u_i(z)$, of a RAUM calculation to compute the synthesized flux of Equation 3, and to produce CRT plots of the resulting spectra at various points, z, together with the spectra computed by CAESAR at those points.

Calculations were made with the XMAS-RAUM-PLEASER system on the two-region (core and blanket) fast critical assembly ZPR-III-48.[3] Table 1 presents some of the results obtained for integral quantities, while CRT plots of

TABLE 1

RESULTS FOR INTEGRAL QUANTITIES

Calculation Method	Multiplication Factor	Power Fraction in Blanket
Conventional 25-group	1.0176	0.094
Conventional 2-group	1.0223	0.232
Synthesis, two CAESAR spectra, group balance	1.0187	0.083
Synthesis, two infinite-medium spectra, group balance	1.0227	0.094
Synthesis, two infinite-medium spectra, Galerkin	1.0493	0.104

the corresponding spectra at representative core and blanket points appear in Figures 1 through 8. In these calculations, only two basis spectra were used in the synthesis, typical of the core and the blanket respectively; they were obtained either as the CAESAR spectra at typical core and blanket points, or as 25-group infinite-medium zero-buckling spectra for core and blanket compositions. With two basis spectra, the running time for RAUM was about 20 sec per case, in contrast to running times of about 4 min per case for CAESAR with 25 groups.

The table shows that the two-group calculation gave far too much power in the blanket, while the Galerkin synthesis gave the multiplication factor 3% too high; the group-balance synthesis is more satisfactory in these respects. The figures show that better spectra were obtained by using CAESAR basis spectra than by using infinite-medium basis spectra, in concordance with the better multiplication factor in the table; while the Galerkin method gave better spectra than the group-balance method, in contrast to the results in the table.

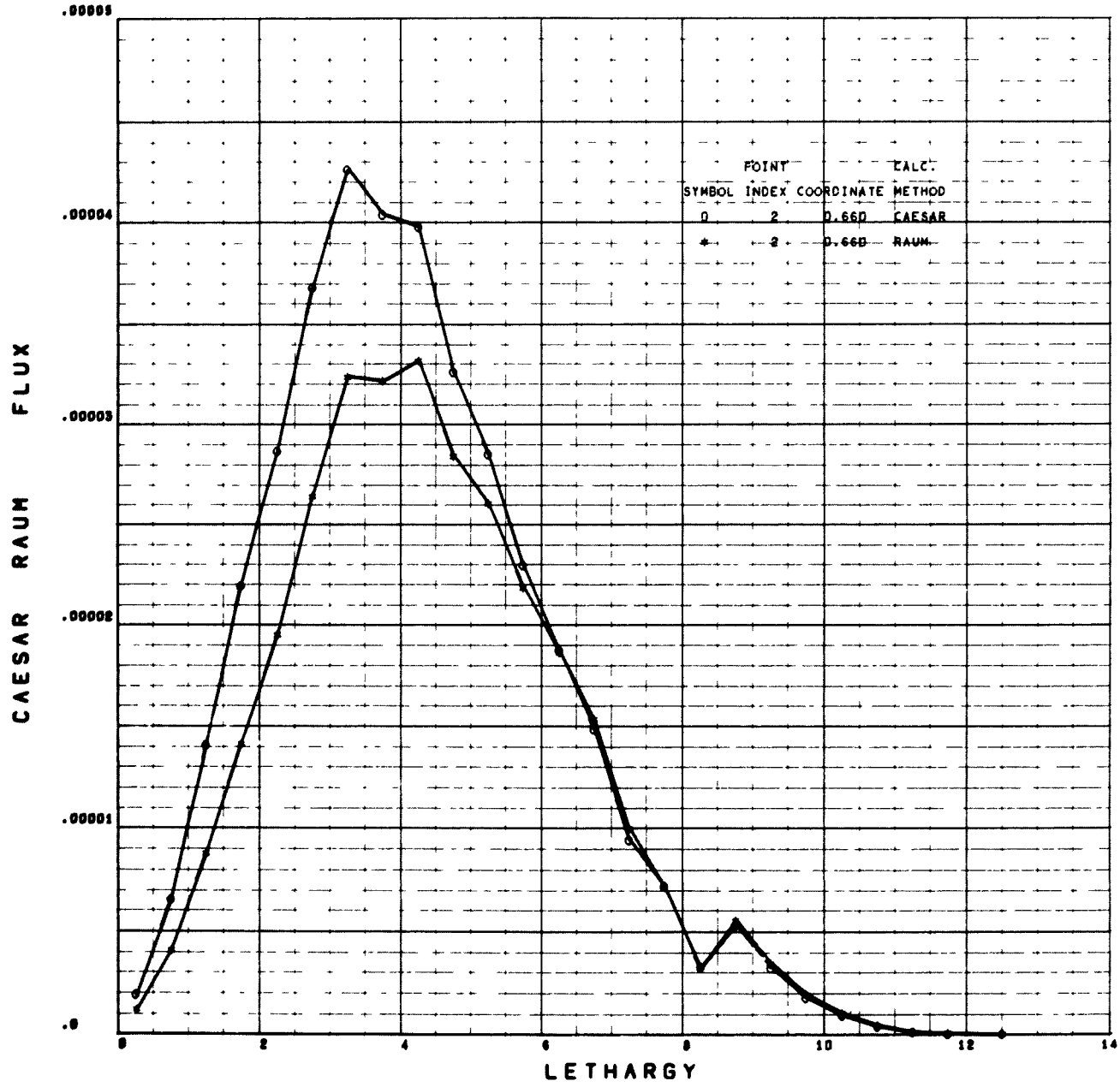

Figure 1. Spectra at Center of ZPR-III-48 Core Given by 2-Group Diffusion Theory and by 25-Group Diffusion Theory

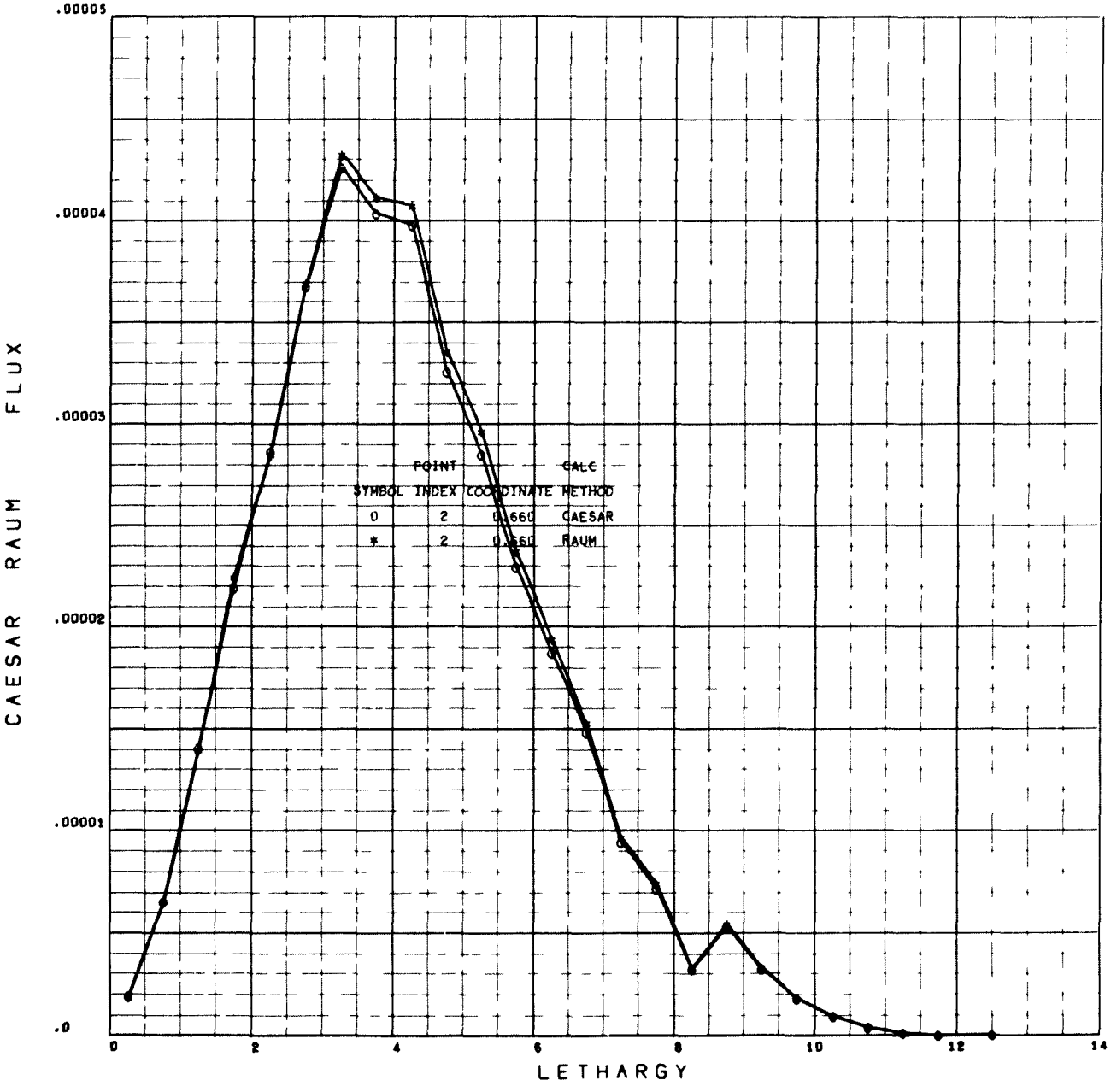

Figure 2. Spectra at Center of ZPR-III-48 Core Given by 2-Spectrum Synthesis Using CAESAR Basis Spectra and Group-Balance Method, and by 25-Group Diffusion Theory

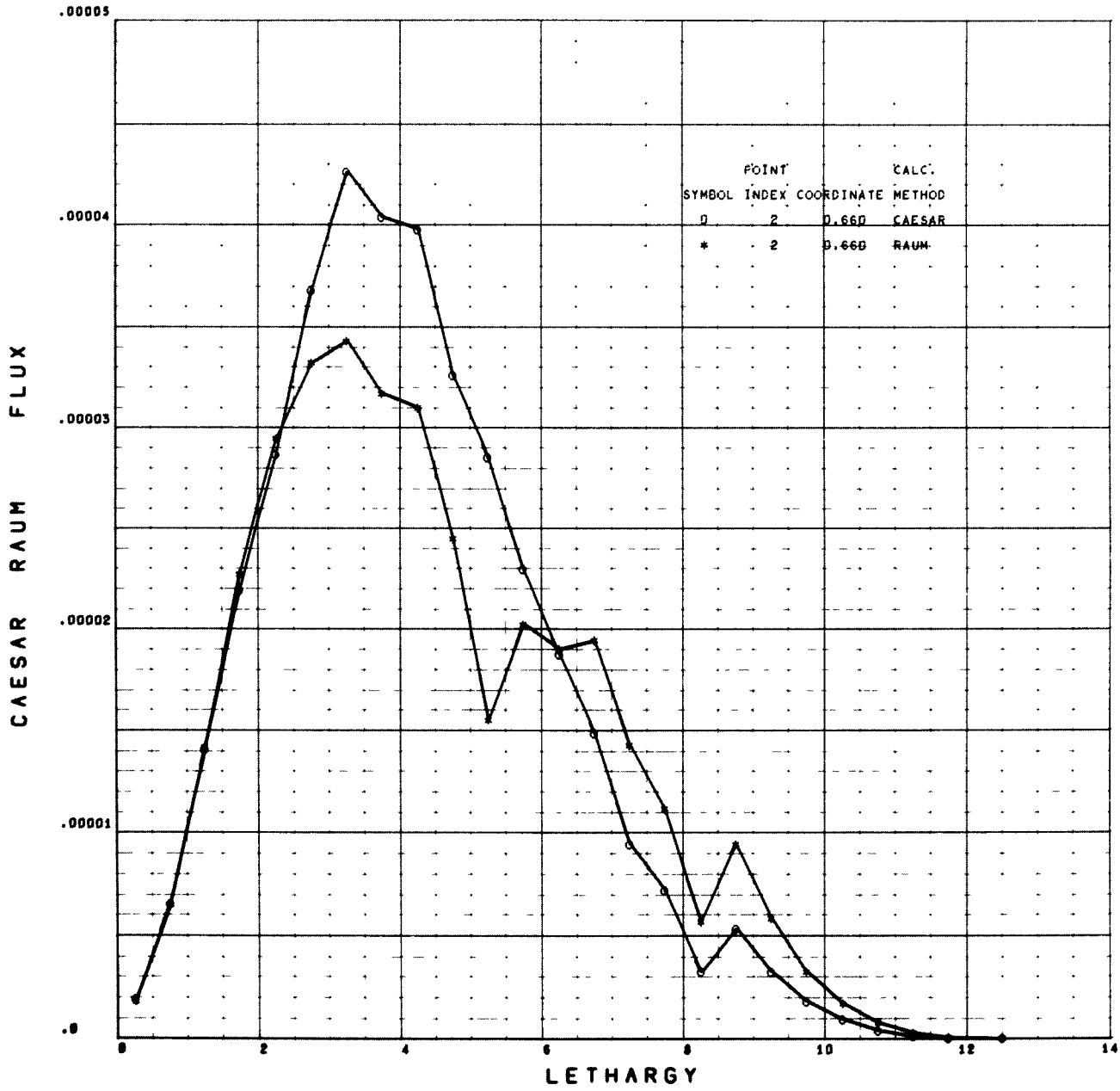

Figure 3. Spectra at Center of ZPR-III-48 Core Given by 2-Spectrum Synthesis Using Infinite-Medium Basis Spectra and Group-Balance Method, and by 25-Group Diffusion Theory

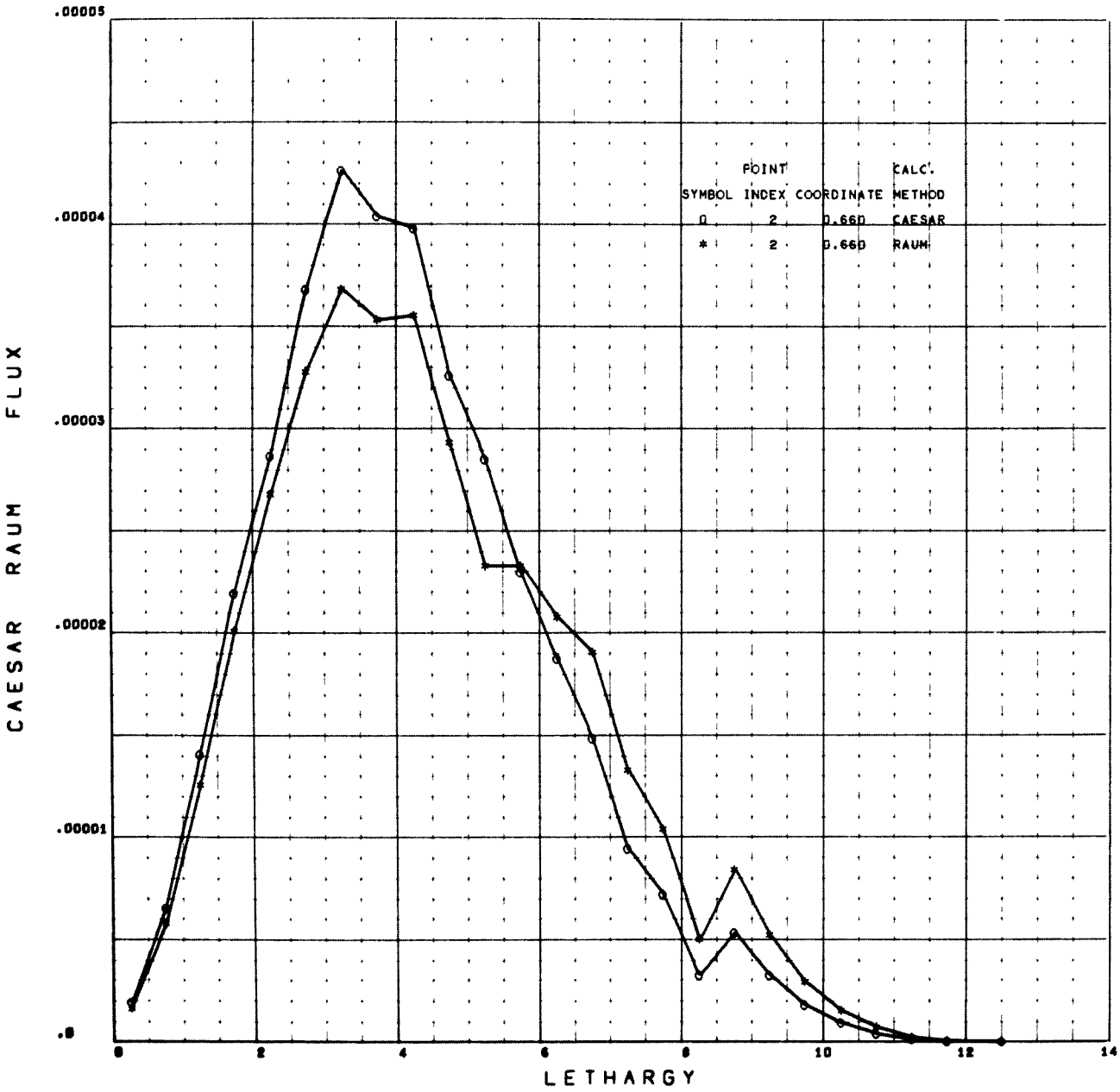

Figure 4. Spectra at Center of ZPR-III-48 Core Given by 2-Spectrum Synthesis Using Infinite-Medium Basis Spectra and Galerkin Method, and by 25-Group Diffusion Theory

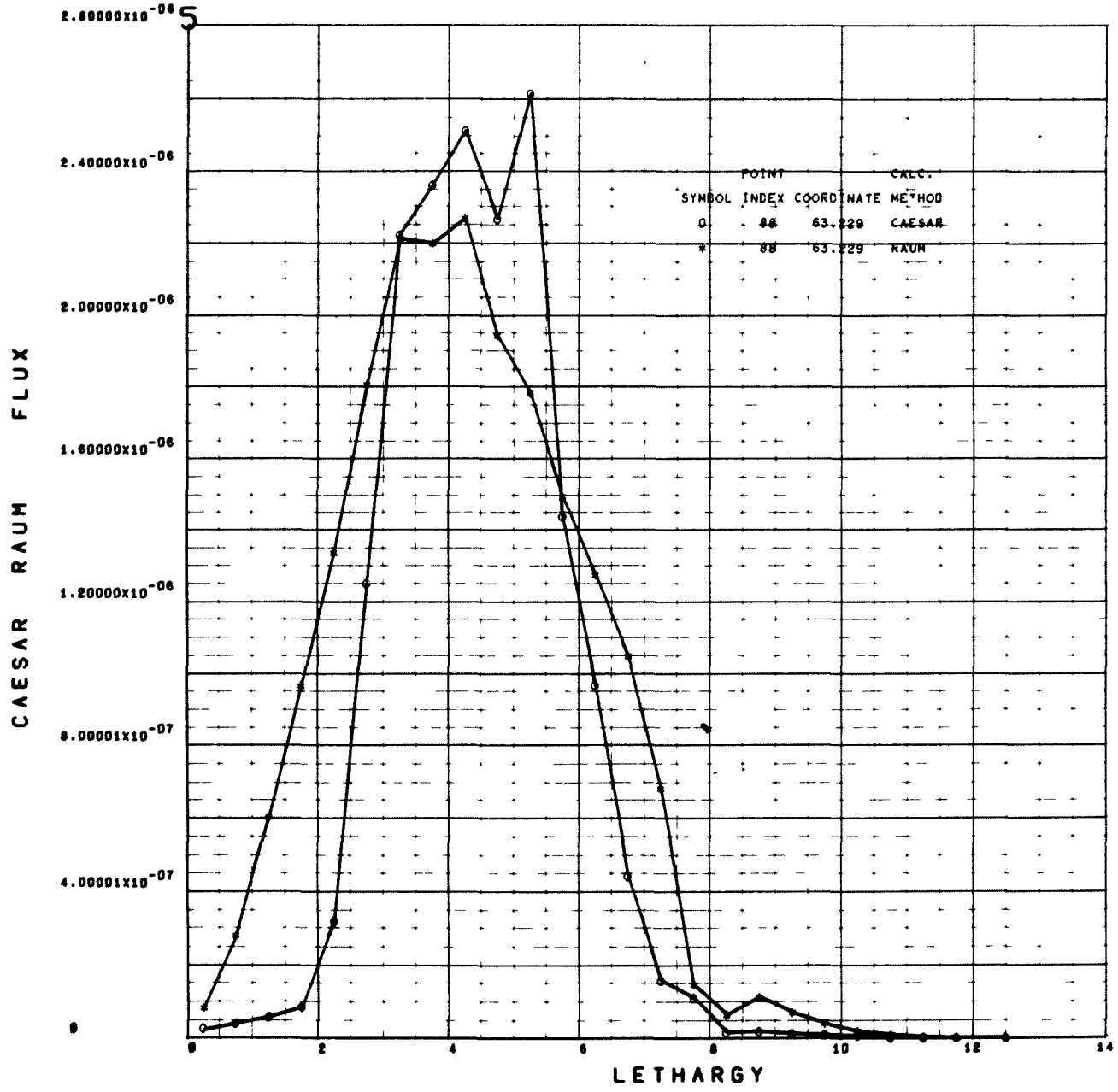

Figure 5. Spectra at Center of ZPR-III-48 Blanket Given by 2-Group Diffusion Theory and by 25-Group Diffusion Theory

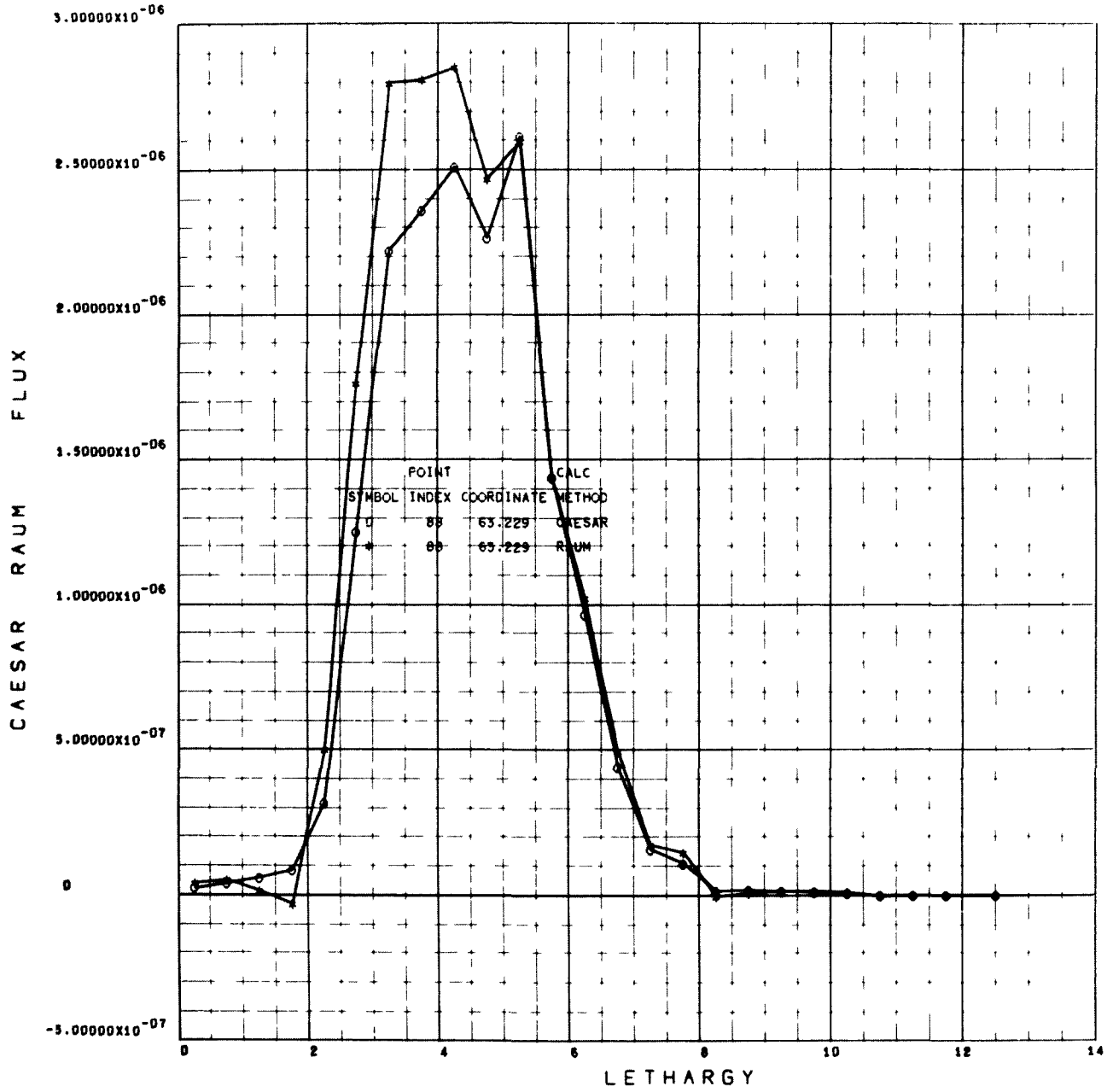

Figure 6. Spectra at Center of ZPR-III-48 Blanket Given by 2-Spectrum Synthesis Using CAESAR Basis Spectra and Group-Balance Method, and by 25-Group Diffusion Theory

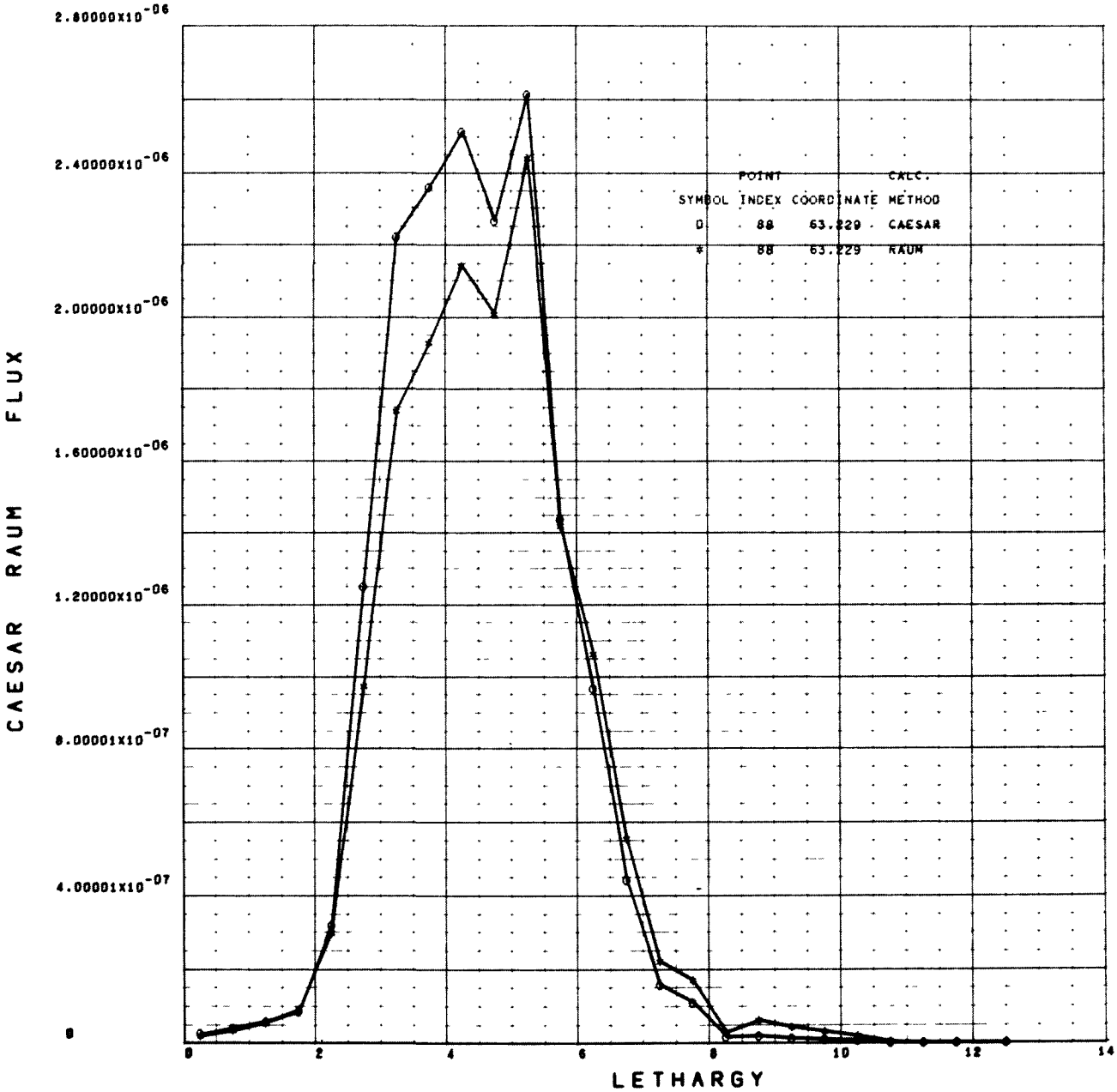

Figure 7. Spectra at Center of ZPR-III-48 Blanket Given by 2-Spectrum Synthesis Using Infinite-Medium Basis Spectra and Group-Balance Method, and by 25-Group Diffusion Theory

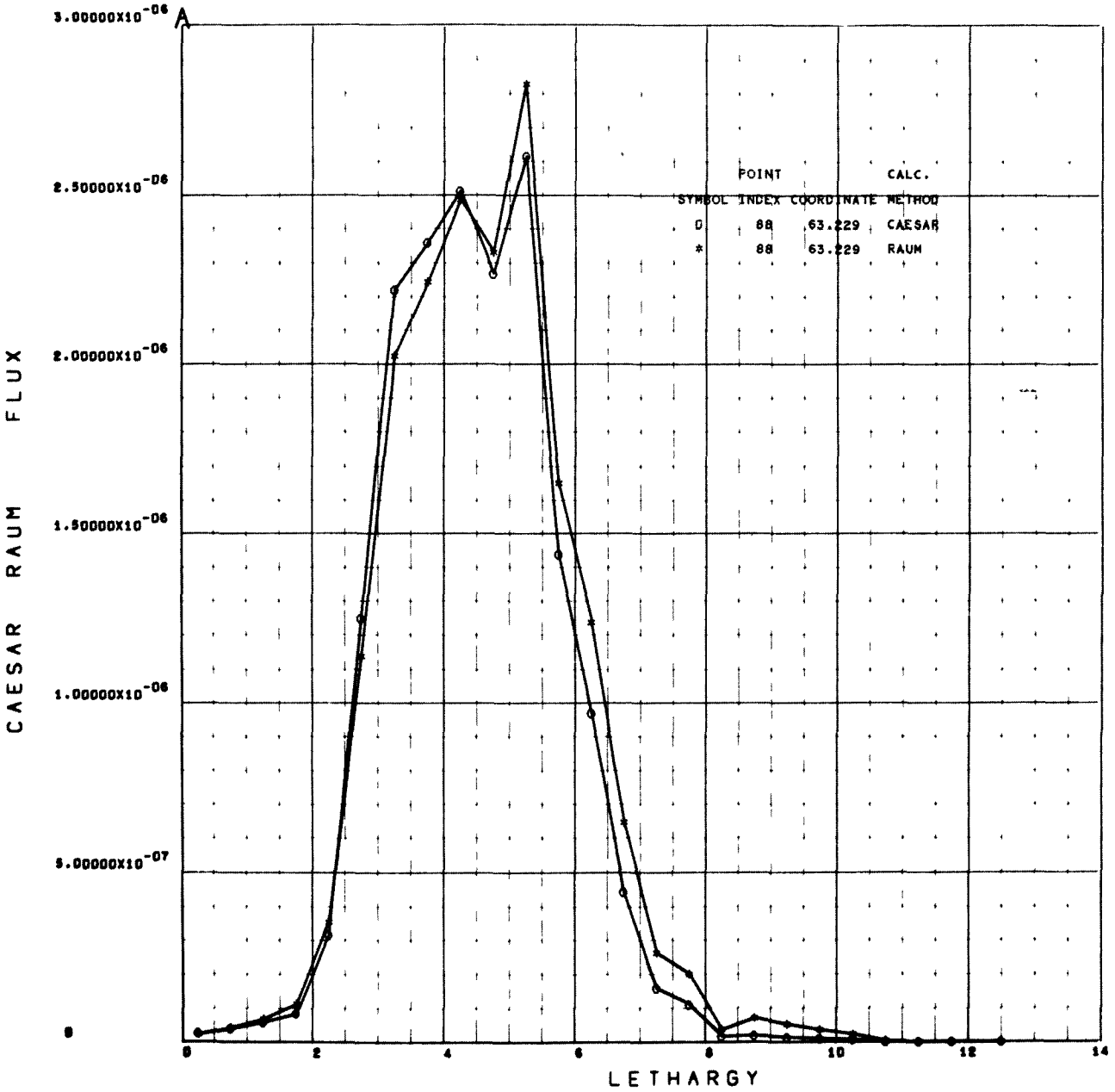

Figure 8. Spectra at Center of ZPR-III-48 Blanket Given by 2-Spectrum Synthesis Using Infinite-Medium Basis Spectra and Galerkin Method, and by 25-Group Diffusion Theory

III. EVALUATION OF EFFORT DURING FISCAL YEAR 1968

It was intended originally to use a multigroup formulation of the kinetics problem in order to ensure the spectral detail needed in treating fast reactors. As a result of further study, however, it was recognized that the principal applications of the synthesis method have been to water-moderated systems, and that the success of the method in these applications is to be ascribed to its separation of neutron distributions into two parts. One part is held fixed during the calculation and thus can be very detailed; while the other part, which is not fixed and must be calculated, is kept free of these details, thereby reducing the computing effort. Now in fast reactors, though there is a great deal of spectral detail, spatial distributions are relatively smooth; hence, the appropriate way to apply the synthesis method to fast reactors is by synthesizing the spectrum. For this reason, it was decided to use spectrum synthesis rather than the multigroup method.

Results obtained thus far indicate that the expected simplification, and consequent acceleration, of the calculations is indeed possible and that the accompanying loss of accuracy can be encouragingly small. In particular, the spectrum synthesis method is seen as more reliable than the group method having the same complexity of spectral representation. Subsidiary results are indications that infinite-medium spectra are not fully satisfactory, and that the group-balance method is at least as reliable as the Galerkin method.

An important question is the stability of the results of calculations with the group-balance method against changes in the location of the boundary between the groups. While this question requires further study, experience now available indicates that there are substantial ranges of lethargy within which this boundary location can be varied without serious adverse effect on the results, but that there is also a range of lethargy that must be avoided or very unphysical results will be obtained. This corresponds to the possibility of breakdown of the variational and Galerkin synthesis methods recently reported by Yasinsky and Kaplan.[4]

REFERENCES

1. D.C. Baller, "CAESAR, A Multigroup, Multiregion, One-Dimensional Diffusion Equation Code," AI-66-MEMO-167 (December 1966)
2. F. D. Federighi, "RAUM - Solution of One Dimensional Coupled Diffusion-Type Equations on the Philco-2000," KAPL-M-FDF-1 (February 1962)
3. A. M. Broomfield et al., "ZPR-3 Assembly 48: Studies of a Dilute Plutonium-Fueled Assembly," ANL-7320, pp 205-215 (1966)
4. Yasinsky and Kaplan, Nuclear Science and Engineering 31, 354 (1968)

PAGE 82 IS BLANK

Program:	Reactor Development
AEC Task:	6C Nuclear Safety, Fission Product Contamination and Control Studies
Project Manager:	J. L. Ballif III
Reporting Period:	Fiscal Year 1968
General Order: 7702	Subaccount: 29410 AEC Category: 04-60-10-01.1

Principal Investigators: M. Silberberg, J. Guon, G. Zwetzig

I. PROJECT OBJECTIVES

The objective of this program is to elucidate the behavior of fission products released to the coolant in a fast, sodium-cooled, LMFBR reactor during normal operation, in order to provide information necessary for the development of fission product trapping techniques in such systems. The disposition of fission products during normal operation must also be known in order to assess the consequences of potential accidents. Information is required on the extent of fission product retention in sodium coolant, the rate and extent of release to the cover gas, and the rate and extent of plate-out on surfaces.

II. TECHNICAL PROGRESS DURING FISCAL YEAR 1968

A. PUBLICATIONS

A topical report entitled, "LMFBR Fission Product Contamination and Control Studies — A Status Report," AI-AEC-12687 was prepared and published.

B. SOURCE TERM CHARACTERIZATION

1. Typical Fast Breeder Reactor Characteristics

In order to provide a realistic and consistent basis for calculation of activation and fission product behavior under various conditions, a tentative set of design characteristics for a "typical" LMFBR were formulated. These are shown in Table 1. Although it is recognized that many of these characteristics will require revision, they will be used as an interim basis for calculations until more detailed information is available on the system configuration of a specific reactor.

TABLE 1

DESIGN CHARACTERISTICS OF REFERENCE LMFBR

Rated Core Power (Mwt)	2120
Sodium Inventory in Tank, Total (lb)	1.1×10^6
Flux, Estimated (n/cm^2-sec)	5×10^{15}
Coolant Mean Circuit Time Through Primary (sec)	120
Velocity of Coolant Through Core (ft/sec)	11.1
Active Length of Core (ft)	2
Surface to Volume Ratio, Primary Coolant System (ft^{-1})	1.5

2. Radioisotope Flow Chart

Because of the number and complexity of the processes occurring in a typical LMFBR with regard to the behavior of fission and corrosion products released into the coolant, the possible paths were delineated by which these products are injected, transported, and depleted. A block diagram summarizing these various paths and processes is shown in Figure 1.

This flow chart has been used as a guide in initial formulation of the source term model computer program which is described in a later section.

3. Radiological Hazards Index

A radiological hazards index was developed to indicate which fission products would present the greatest radiological hazard should they escape from the reactor fuel and primary system, and become airborne in the reactor environment. This index would, thus also provide guidance to R&D efforts by indicating which fission products required the greatest analytical and experimental study. As presently formulated, the index for a given isotope, i, is proportional to its total inventory in the fuel, $(Ci)_i$; its fractional release from the fuel, f_i; its volatility or fugacity, v_i (assuming it escapes from the primary system via the cover gas); and its relative toxicity, as given by the reciprocal of its Maximum Permissible Concentration in Air, $(MPC_a)_i$. Normalized to Kr^{85}, the radiological hazard index is then given by:

$$RHI(t,i) = \frac{(Ci)_i}{(Ci)_{Kr^{85}}} \times \frac{(MPC_a)_{Kr^{85}}}{(MPC_a)_i} \times \frac{f_i}{f_{Kr^{85}}} \times \frac{v_i}{v_{Kr^{85}}} .$$

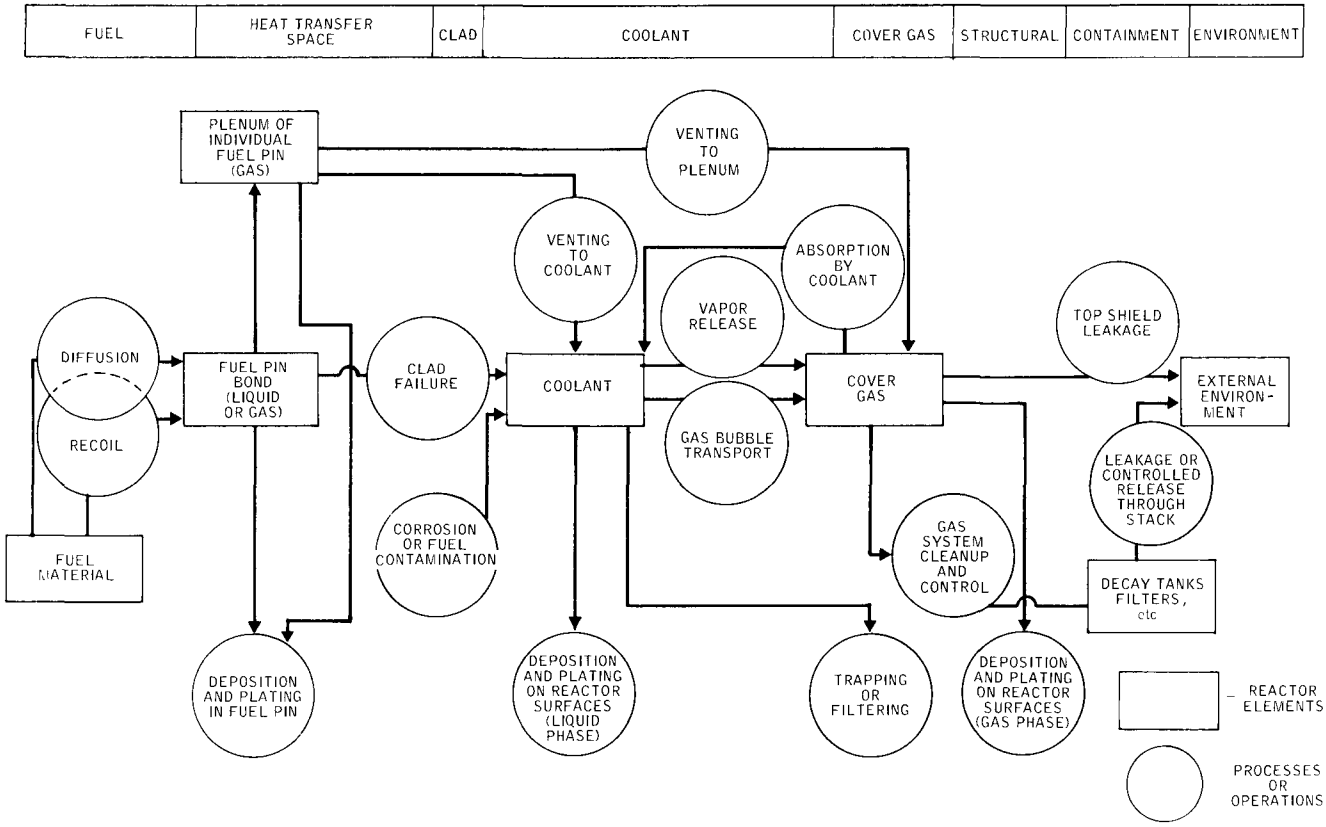

Figure 1. Radioisotope Flow Chart

The inventory of each isotope in the fuel was calculated by using the CURIE-DOSE-THUNDERHEAD digital computer program. An operating period of one year and a reactor thermal power of 2120 Mwt were also assumed, to provide an initial estimate of the RHI. The choice of Kr^{85} as a normalization point was prompted by its long half life, its high release fraction from the fuel, and by its volatility which implies a high release fraction to the cover gas. Due to the lack of all of the necessary information at this time, the release fractions and fugacities of all isotopes were assumed to be equal to the corresponding values for Kr^{85}; i.e., $f_i = f_{Kr^{85}}$ and $v_i = v_{Kr^{85}}$. With this simplifying assumption,

$$RHI(t,i) = \frac{(Ci)_i}{(Ci)_{i_{Kr^{85}}}} \times \frac{(MPC_a)_{Kr^{85}}}{(MPC_a)_i} .$$

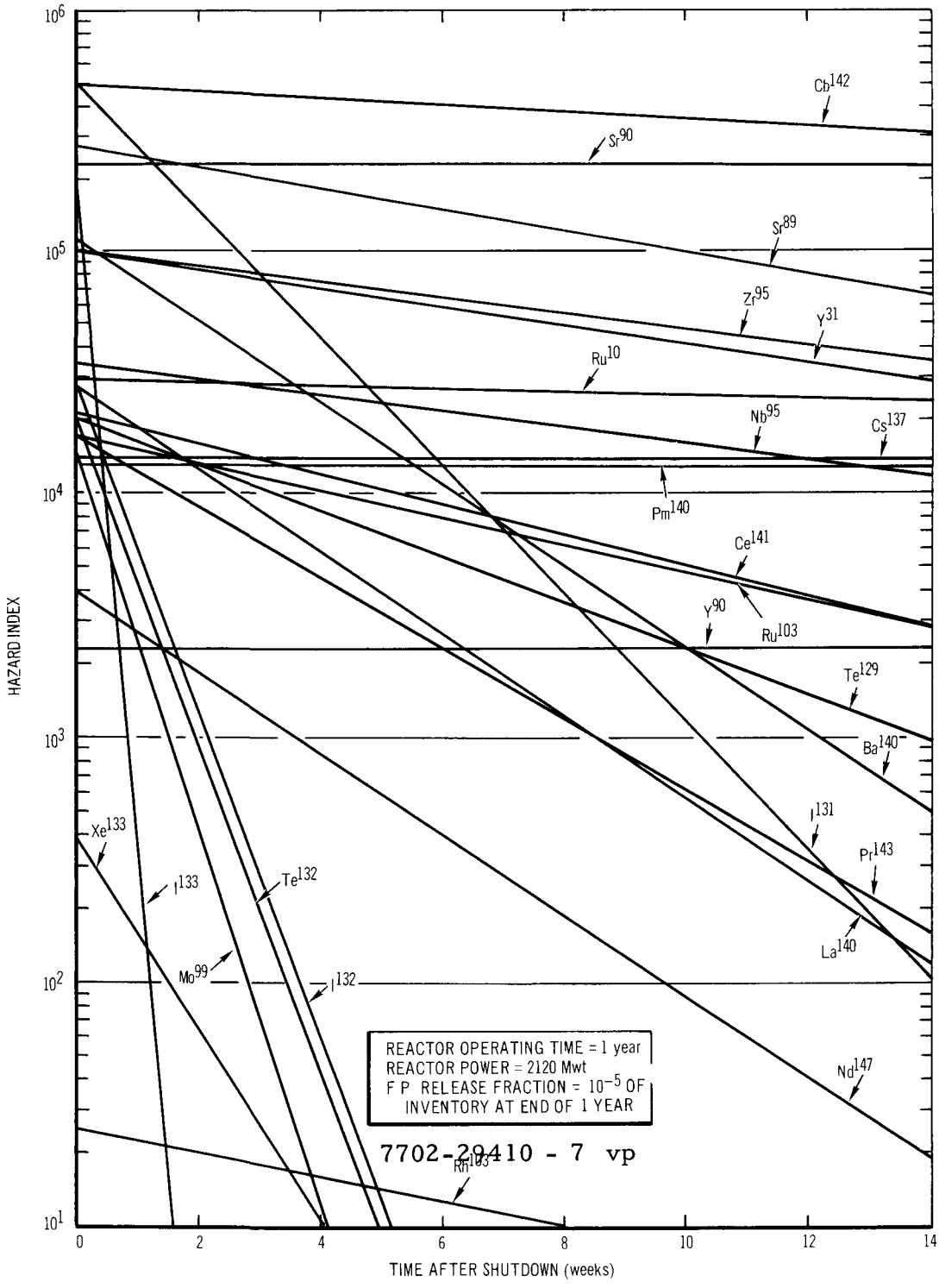

Figure 2. Radiological Hazard Index vs Time after Shutdown

The results are shown as a function of time after shutdown in Figure 2. Here it is seen that during reactor operation and immediately thereafter the most important isotopes are ^{144}Ce, ^{90}Sr, ^{89}Sr, ^{95}Zr, ^{91}Y, ^{106}Ru, ^{131}I, ^{133}I, and ^{140}Ba. If, however, the radiological release occurred two or three months after shutdown, Figure 2 shows that the list would be the same except for the removal by decay of ^{131}I, ^{133}I, and ^{140}Ba.

It is to be noted that the above radiological hazard index is of extremely limited value at the present time because of the simplifying assumptions which were employed relative to the release fraction from the fuel and the relative volatility. Another factor which is completely neglected in the index is that of the differing tendencies for removal of isotopes from the coolant stream by plating or deposition. Thus, when all of these factors are taken into account, the relatively volatile isotopes such as Cs, I and Xe would probably move sharply upward in the index while the refractory materials would move sharply upward in the index while the refractory materials would move sharply downward. Present efforts in the development of the source term model and in the performance of fundamental experiments using the fission product behavior loop, and vaporization data now available for Cs and I, however, should remove a number of these deficiencies.

4. Radiation Index

A second evaluation was performed to determine those fission product isotopes whose inventory, half-life, and gamma energy would provide the major contributions to the after-shutdown radiation levels which, in turn, would affect maintenance and repair of the LMFBR system. Again, no standard quantitative basis is presently in use. Therefore, to minimize subjective aspects of the evaluation, dose rates were based on an assumed unshielded point source. By using the above assumption, a dose rate was calculated for each isotope considered, based on the inventory of the isotope per unit volume of sodium. The resulting values were then normalized by dividing by the corresponding ^{22}Na dose rate. This isotope was selected as a normalization base because of its long half life and because it will obviously remain with the sodium regardless of the volatility or deposition of fission products.

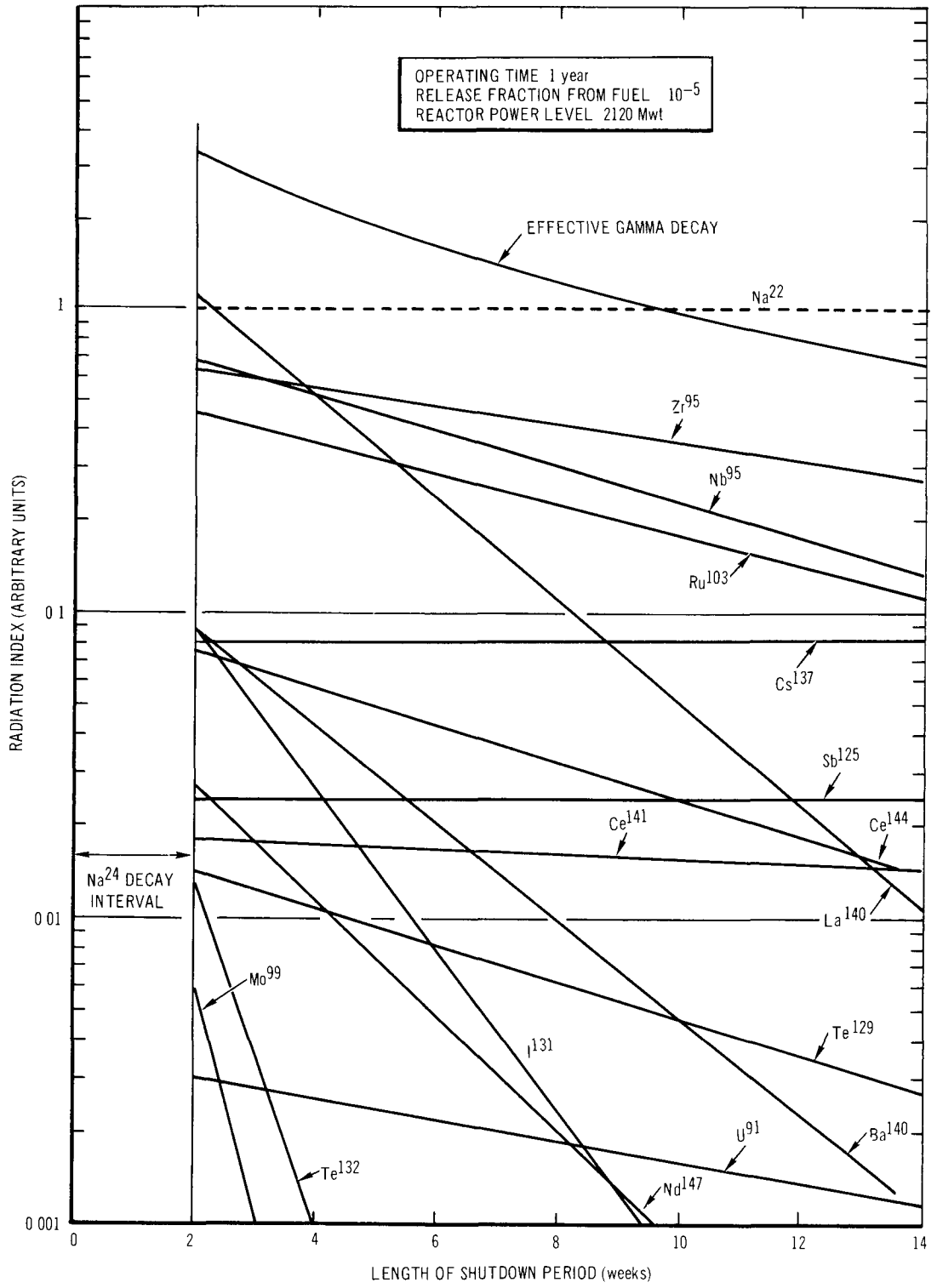

Figure 3. Radiation Index vs Time after Shutdown

Thus,

$$RI(t,i) = \frac{D_i}{D_{Na^{22}}} = \frac{(Ci)_i \times E_i}{(Ci)_{Na^{22}} \times E_{Na^{22}}} ,$$

where:

$RI(t,i)$ = radiation index for the i^{th} isotope at time t,

$D_i, D_{Na^{22}}$ = dose rate at a distance of 1 ft from 1 cm^3 of sodium containing isotope i and Na^{22} respectively,

$(Ci)_i, (Ci)_{Na^{22}}$ = inventory of i^{th} and Na^{22} in coolant respectively (curies), and

$E_i, E_{Na^{22}}$ = energy of equivalent photons emitted from i^{th} isotope and Na^{22} respectively.

The results are shown in Figure 3, where the Radiation Index for each isotope is presented as a function of the time after shutdown. Since many LMFBR operating plans may include a waiting period, following shutdown, of about two weeks for ^{24}Na decay before contact maintenance can be performed, this initial period is indicated in the figure.

Inspection of Figure 3, shows that the most important isotopes with respect to residual radiation levels are ^{95}Zr, ^{95}Nb, ^{103}Ru, and ^{137}Cs. Also relatively important immediately after shutdown is ^{140}La, but this isotope is seen to decay relatively rapidly. Figure 3 also shows that after about 10 weeks, ^{22}Na is the predominant source of gamma radiation.

Again, this index is of only limited value because it assumes equal fractional release of all isotopes from the fuel and neglects selective removal from the coolant stream by vaporization and deposition.

5. Relative Concentration of Fission Products and Corrosion-Activation Products

Another potential source of radiation in the coolant is that due to activation of core structural materials, such as fuel cladding, fuel element sheaths, etc., which subsequent to activation are corroded or eroded into the coolant stream.

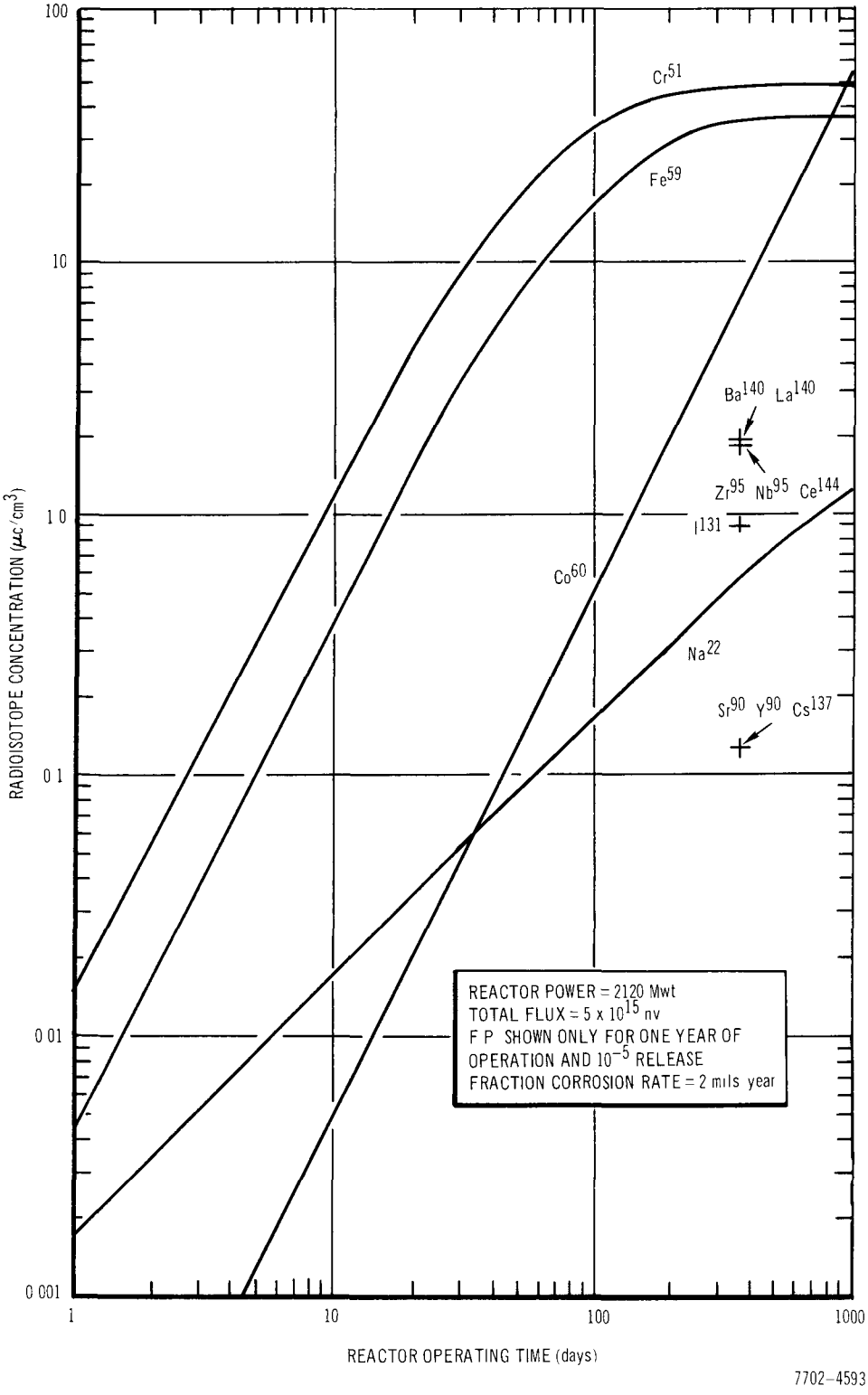

Figure 4. Activity Concentrations for Corrosion Products, Fission Products, and ^{22}Na vs Reactor Operating Time

While there will be corrosion products from other parts of the primary loop which are activated as they pass through the core, the primary source of corrosion-activation products will be core structural materials. This is because materials located in the core are subjected to the highest continuous neutron flux, and because they are also subjected to the highest temperatures, thus leading to higher corrosion rates.

The effect of corrosion of activated core materials was estimated by considering the corrosion of the fuel cladding at a rate of 2 mils per year,[1] in a reactor operating at 2120 Mwt and a total neutron flux of 5×10^{15} nv. The reactions considered important were

$$^{58}Fe(n,\gamma)^{59}Fe ,$$

$$^{50}Cr(n,\gamma)^{51}Cr, \text{ and}$$

$$^{59}Co(n,\gamma)^{60}Co ,$$

where the cobalt reaction is included and is based on an assumed cobalt impurity in stainless steel of 0.05%. In performing the calculations, the resonance integral for each isotope was evaluated over the flux spectrum of a typical LMFBR.

The results are shown in Figure 4. Also shown in Figure 4 is the growth of ^{22}Na activity concentration (assuming fresh sodium) and the concentration of some of the more important fission products (assuming one year of reactor operation, 10^{-5} release fraction at the end of one year, and no decay or depletion).

Inspection of Figure 4 indicates that for the assumed corrosion rate and the assumed fission product release fraction, the activity of corrosion products, if not depleted by some mechanisms such as plating, will predominate over all of the other activities. Moreover, since the corrosion product activity is directly proportional to the corrosion rate, Figure 4 shows that even if the corrosion rate were one tenth the assumed value, the corrosion product activity, if not depleted, would still be dominant. Figure 4 also shows that after about 2-1/2 years, ^{60}Co will become the most important corrosion product activity.

The ^{22}Na activity is also of interest since it is seen to build up to significant concentrations rapidly and cannot be selectively removed from the coolant.

6. Source Term Model Formulation

Development of a source term model which will reduce or eliminate some of the limitations presently associated with the radiological hazard index and radiation index was initiated. It is planned that this model will be programmed for digital computer solution. The objective of this model is to provide a quantitative, flexible accounting of all of the important processes which affect the radioactivity of the sodium coolant of an LMFBR; the radioactivity of the cover gas; and the contamination-induced, residual radiation levels of equipment for which contact maintenance may be required. Many of the constants and functional relationships for some of the processes in the model remain to be determined; however, such a model will be of considerable value in assessing the relative importance of the various processes which are known and in establishing limits of importance for the processes under study.

With respect to the coolant, a general equation of the following form is being employed as a starting point for use in the computer code:

$$N_i = \sum_j R_{ij} - N_i \sum_k \alpha_{ik} \ ,$$

where:

N_i = number of atoms of isotope i in coolant,

R_{ij} = rate of introduction of isotope i into coolant by process j, and

α_{ik} = fraction of i removed from coolant per unit time by process k.

The production term, $\sum_j R_{ij}$, includes all important processes by which radioactivity is introduced into the coolant; the removal term includes all removal processes, including radioactive decay, vaporization, and deposition on surfaces.

The following decisions were made concerning the computer code.

a) The code will consider the following sources of radioactivity:

1) Fission products,

2) ^{22}Na and ^{24}Na,

3) Activated core structural materials (clad, etc.) which enter the coolant stream by corrosion,

4) Primary loop corrosion products which are activated in the core,

5) Fuel contamination in the coolant, and

6) Fission products arising from fuel contamination in the coolant.

b) The fission product inventory will be calculated by using an adaptation of the CURIE code. This adaptation will include the use of Pu fast fission yields and variable reactor power level.

c) The rate of release of fission products to the coolant and the fraction of each isotope released will be specified by the user.

d) Corrosion rates are specified by the user.

e) Removal of isotopes will occur by radioactive decay, by vaporization to cover gas spaces, and by first-order sorption processes on primary system component surfaces.

f) The code will account for isotope inventories in the cover gas, in the coolant, and on surfaces.

Equations for use in the computer program covering the following quantities and processes were derived and are being studied:

a) Change in coolant concentration of a given isotope as a result of a first order sorption reaction at a pipe surface,

b) Change in surface concentration of a given isotope as a result of the above process,

c) Effect of surface corrosion on both of the above quantities,

d) Quantity of a given isotope in cover gas spaces, and

e) Effect of decay of radioactive isotope A on coolant concentration of daughter isotope B.

In addition to the above, the effect of cladding failure history on coolant and deposition inventories of a hypothetical radioactive fission product isotope in a system having a depletion constant, α, was analyzed for three cases:

1) Long reactor operation with no cladding failures followed by simultaneous clad failure in a fraction, f_1, of the fuel pins and coincident reactor shutdown at time, T,

2) Long reactor operation with failed cladding in a constant fraction, f_1, of the fuel pins, with shutdown after a time, T, and

3) Reactor operation with progressive fuel cladding failure (fraction of fuel pins having failed cladding = at), with shutdown at time, T.

Analytical expressions were derived for the coolant and deposition inventories for each of the three cases listed above. With respect to the coolant radioactivity, the results show that the ratio of radioactivity levels for Case 1/Case 2 = $(\lambda + \alpha)/\lambda$, and for Case 3/Case 2 =

$$\frac{at}{f_1}\left[\frac{1}{1 - e^{-(\lambda+\alpha)t}} - \frac{1}{(\lambda+\alpha)t}\right],$$

where:

λ = decay constant of hypothetical isotope (sec^{-1}),

α = system depletion constant for hypothetical isotope (sec^{-1}),

a = fractional rate of cladding failures for Case 3 (sec^{-1}),

f_1 = fraction of fuel pins having cladding failures (Cases 1 and 2), and

t = duration of reactor operation (sec^{-1}).

The above analysis assumes a simple $(1 - e^{-\lambda t})$ generation rate for the hypothetical isotope. This is sufficiently rigorous for initial trend analysis. For the proposed computer code, however, the derived relationships will be modified to accept fission product inventories as generated more rigorously by an adaptation of the CURIE code.

C. FUNDAMENTAL STUDIES

1. Vaporization Experiments

The extent of vaporization of a given isotope or its partial pressure in the cover gas is a function of its volatility compared to sodium. The relative volatility or distribution coefficient, K_d, of a fission product specie between gas and liquid phases can be expressed as

$$K_d = \frac{\gamma_i P_i^o}{P_{Na}^o} , \qquad \ldots(1)$$

where:

P_i^o = vapor pressure of pure fission product specie i,

P_{Na}^o = vapor pressure of pure sodium, and

γ_i = activity coefficient of fission product specie i in sodium solution.

The distribution coefficient can also be expressed as the ratio of the specific activities (curies/gram Na) of the f. p. specie in the gas and liquid phases.

Vaporization equilibria experiments were conducted to obtain relative volatility data for two volatile and radiologically important fission products in sodium, namely cesium and iodine (present as NaI). The data were obtained by using a transpiration apparatus and tracer techniques. The relative volatility of cesium in sodium (containing 125 ppm oxygen) was determined over a concentration range of 1×10^{-5} to 8×10^{-5} mole fraction Cs (with Cs^{134} tracer), from 680 to 900°K. The experimental data, see Figure 5, for the relative volatility of Cs in sodium were correlated by the relationship

$$\log K_d = 987/T + 0.490 , \qquad \ldots(2)$$

where

T = absolute temperature, °K.

The data also clearly show that the Cs-Na system obeys Henry's Law in the concentration region investigated.

The relative volatility of sodium iodide in sodium (containing 25 ppm oxygen) was determined at a concentration of 1×10^{-6} mole fraction NaI (with NaI^{131} tracer), from 695 to 860°K, see Figure 6. The experimental correlation for the relative volatility of NaI in sodium was found to be

$$\log K_d = 1840/T - 2.34 \ . \qquad \ldots(3)$$

In examining the data for the two systems, it is convenient to compare the experimentally derived activity coefficients with those predicted. These values are given for 605 and 900°K in Table 2.

TABLE 2
ACTIVITY COEFFICIENTS

Temperature (°K)	Cs-Na		NaI-Na	
	Calculated	Experimental	Calculated	Experimental
650	4.4	1.9	1.2×10^6	3×10^5
900	2.9	3.5	140	420

The experimental values of activity coefficient were obtained from the defining Equation 1 and by using the experimental data from Figures 5 and 6. The calculated activity coefficients were obtained from Equations 9 and 12 of AI-AEC-12687.

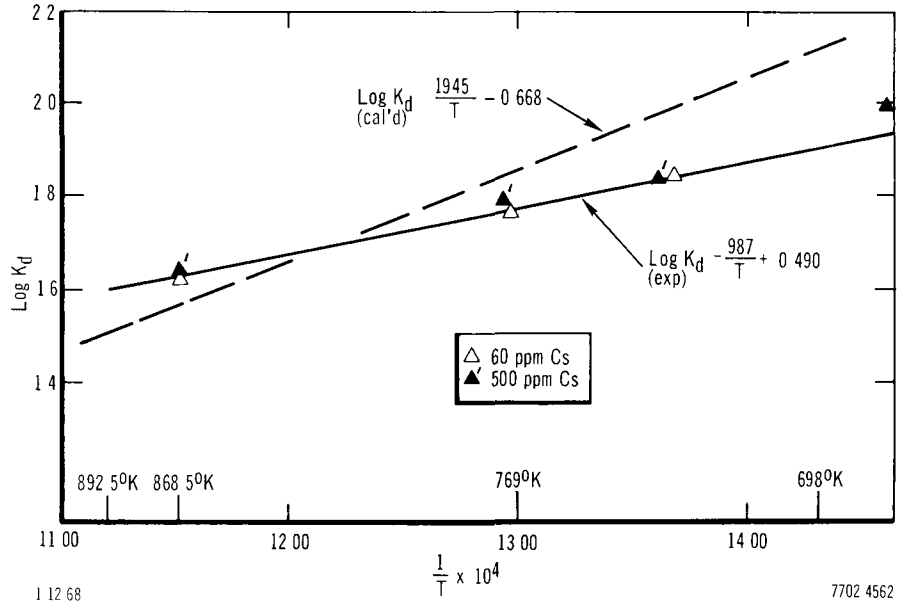

Figure 5. Calculated and Experimental Relative Volatility for the NaI-Na System

The data for cesium show a discrepancy; in that, ordinarily, the activity coefficients would tend toward unity with an increase in temperature, as is the case for the sodium iodide. One possible explanation for this trend may be due to the level of oxygen (e.g. 125 ppm) in the sodium for the cesium runs. That there does seem to be some kind of interaction between cesium and oxygen in sodium has been observed in the cold trapping studies, Section II-C-2. Additional data on Cs vaporization with sodium at low oxygen levels (e.g. 5 ppm) could confirm this effect.

The data for sodium iodide, although of somewhat lower temperature dependence than predicted, does seem to be quite reasonable and in fair agreement with work of Saroul,[2] Clough,[3] and with sodium aerosol work at AI.[4] The data for the sodium-iodide:sodium system is not in agreement with the experimental and theoretical work of Castleman.[5] As shown in Figure 6, the curve derived from Reference 5 (for region 940 to 1200°K) has a considerably different temperature dependence for K_d, and although agreement with the present work is obtained at ~1000°K, the departure between the two investigations is considerable when the BNL curve based on Reference 5 is extrapolated to 700°K. The experimental equilibrium vaporization data of Castleman[6] for the NaI-Na system was obtained with carrier-free NaI^{131} system; whereas, in the AI work, 6 ppm of NaI carrier was employed. The difference between the results of the two investigations may be due to the fact that the present study was conducted at concentrations approaching the NaI solubility in sodium at the lower temperatures. At the lowest temperature studied (700°K), however, the reported solubility of NaI in Na is $\sim 1.2 \times 10^{-5}$ mole fraction compared with the 1×10^{-6} mole fraction of NaI employed in the present studies. Thus, it is not apparent that solubility limitations have affected the results; however, it is possible that at the lower temperatures, the activity coefficient is not concentration independent at these concentration levels, e.g. ~0.1 saturation.

2. Deposition and Trapping Studies

A number of screening experiments were performed to determine the effectiveness of cold trapping as a means for removal of cesium contamination from a sodium coolant stream. The experiments also attempted to determine the

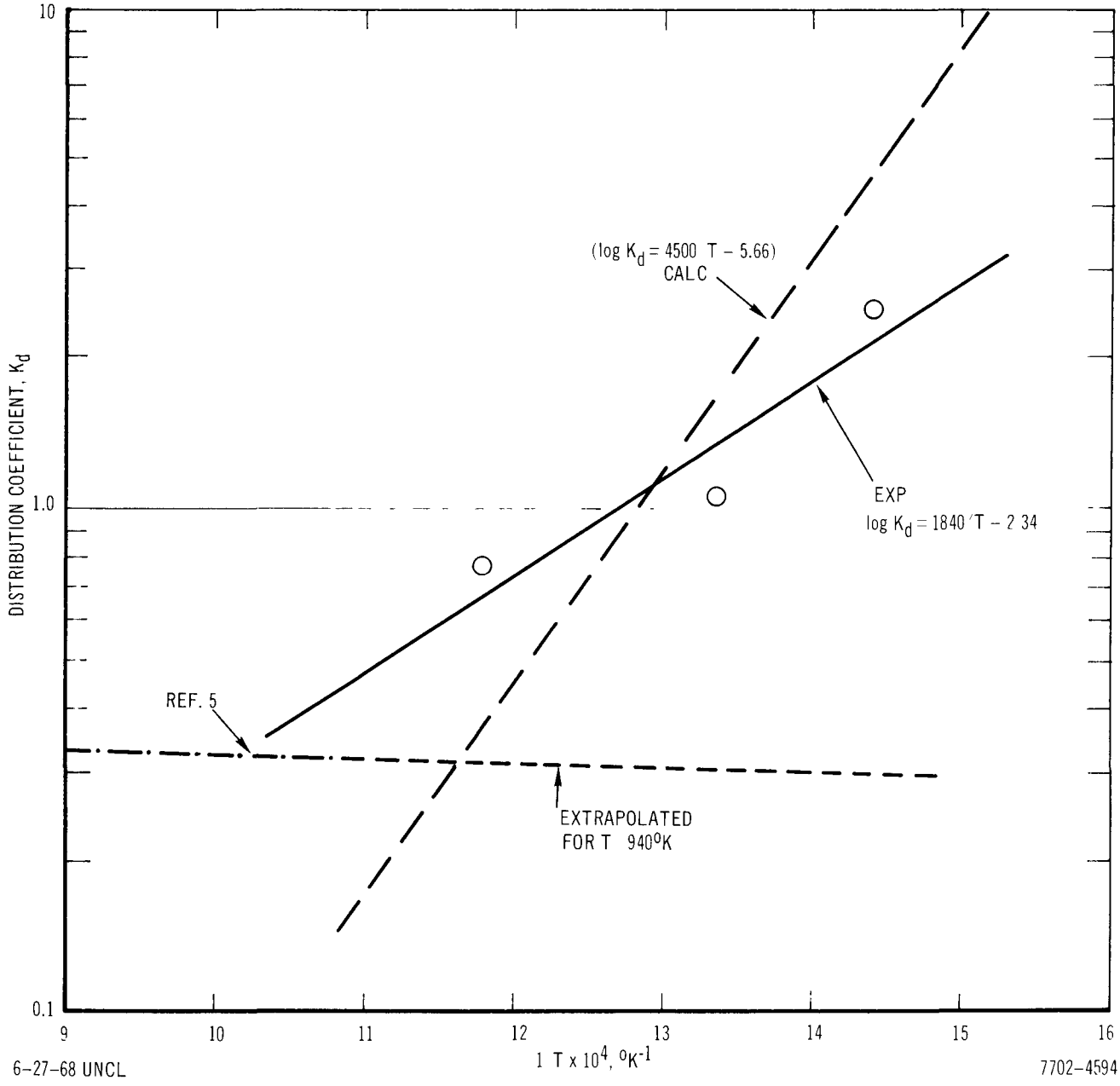

Figure 6. Calculated and Experimental Relative Volatility for the NaI-Na System

nature of the trapping mechanism and the parameters affecting its efficiency. The apparatus used in these experiments consisted of a small loop of stainless steel tubing having a capacity of 98 ml.[7]

The results of the initial experiments conducted in Fiscal Year 1967, while showing correlation between temperature and radiation, were only of partial use in determining the correlation between amounts of cesium and sodium oxide trapped. To investigate the effect of adsorption on cesium deposition, the effect of sodium oxide concentration (at various starting concentrations) was also required.

In the next series of experiments, the first run was performed by using sodium with the lowest oxygen concentration (5 ppm) available. Upon completion, a sufficient quantity of oxide was added to raise the level to 25 ppm. This was repeated in 25 ppm increments until cesium trapping had been observed in sodium containing up to 150 ppm of additional oxygen. The results for 5 to 105 ppm of oxide are shown in Figures 7 and 8. The data in Figure 8 were obtained by increasing the amount of stable cesium carrier in the loop after the 155 ppm oxygen run from 65 to 330 ppm. These data indicate, to some extent at least, a probable exchange or dilution phenomenon between the radioactive cesium removed by the cold trap and the additional stable cesium added.

A third series of experiments was performed to verify the effects and trends observed in the other two. For example, the flow rate was varied for the low oxygen concentration run, and produced little change in the results. A "blank" run was also made with no radioactivity in the sodium to verify that the temperature variations of the cold trap had not been affecting the detector response.

The results of these studies indicate at least an observable relationship between cesium trapping efficiency and the oxygen concentration in the sodium. These experiments indicate a trapping mechanism which is operative even at temperatures at which the Na_2O would presumably be in solution and, thus, further indicate that deposited Na_2O in the cold trap is probably not the primary mechanism related to cesium trapping. One can then speculate that this may imply a mechanism related to a reaction of oxygen with steel constituents with this combination having an effect on cesium trapping characteristics. The

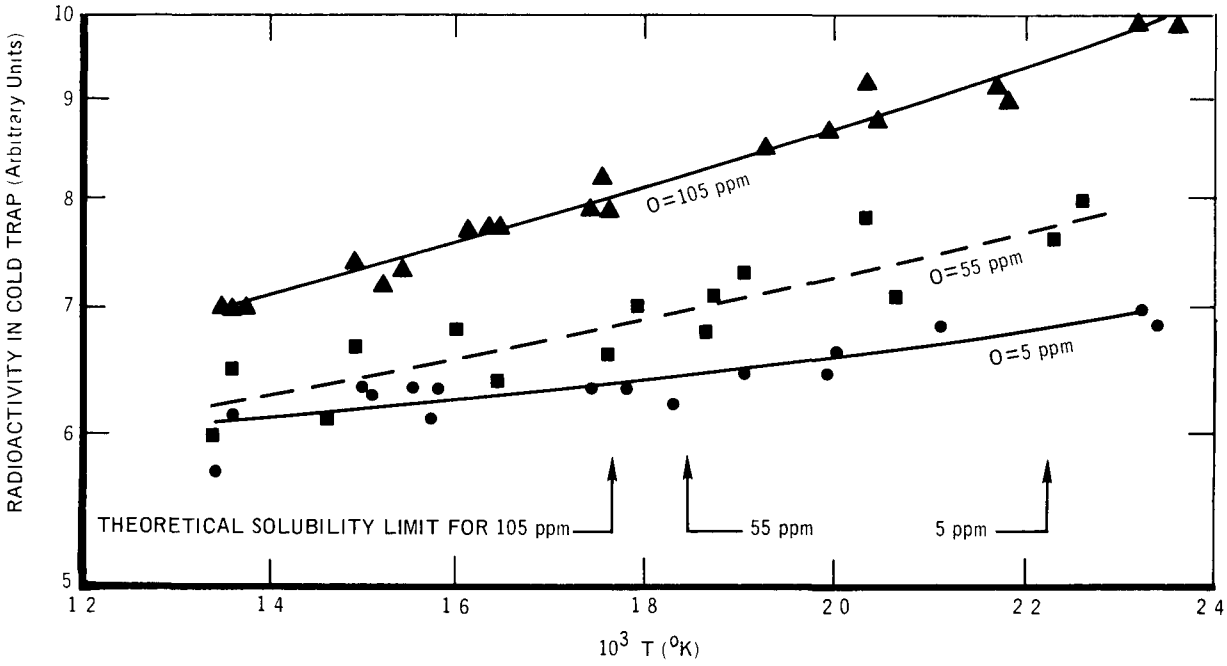

Figure 7. Radioactivity in Cold Trap

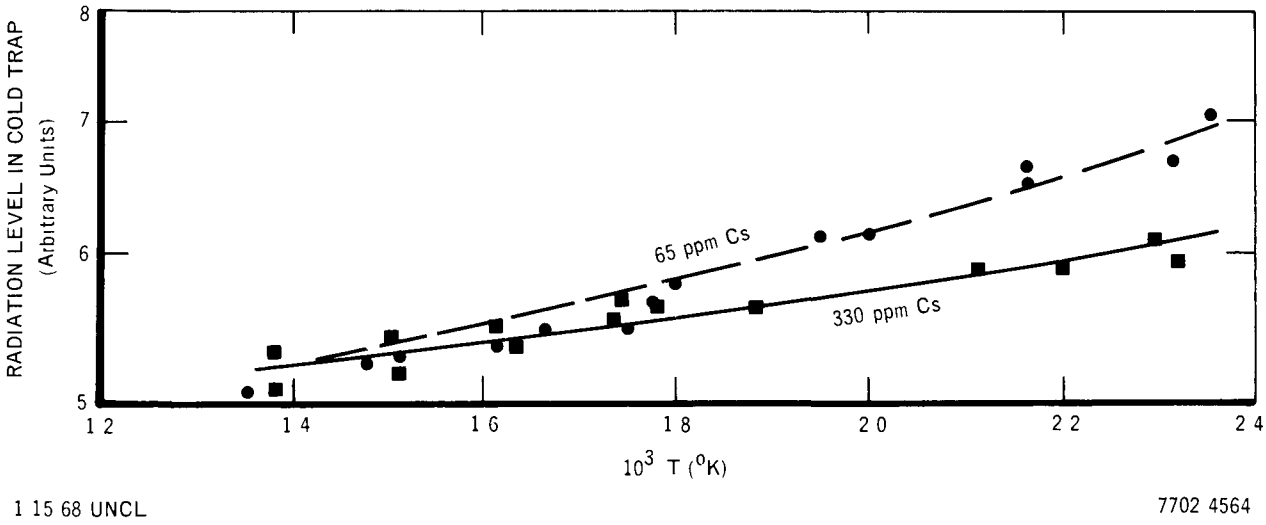

Figure 8. Radiation Level in Cold Trap

experimental data obtained for the two cesium concentrations are too limited to allow a conclusive evaluation. The data, however, do indicate that the introduction of stable Cs provides a possible mechanism for exchange of stable cesium with radioactive cesium, thus possibly explaining the apparent decrease in trapping efficiency as measured by the scintillation detector.

3. Fission Product Behavior Loop

In order to provide a facility with greater flexibility than the small (100 gm) sodium loop described above, a larger loop (2000 gm) has been placed in service. By providing several by-pass legs and two traps in series, sodium can be conditioned before and during a run, and deposition tendencies can be better defined than with the smaller loop. Figure 9 shows the Fission Product Behavior Loop (FPBL) prior to the final assembly phase. Missing from the loop in this figure are heaters, thermocouples, insulation, and three by-pass legs. Figure 10 is the P and I diagram for the FPBL. Table 3 lists the design parameters for the loop.

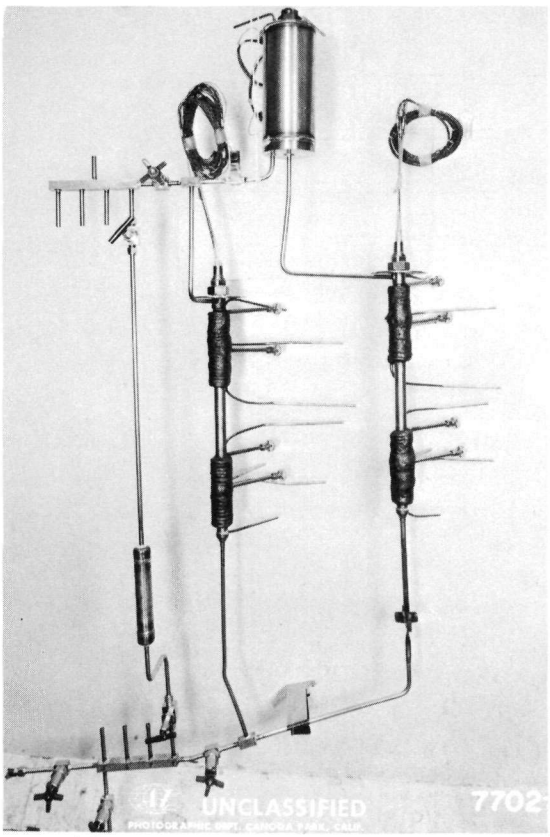

5-2-68 UNCL 7702-4065

Figure 9. Fission Product Behavior Loop Prior to Assembly

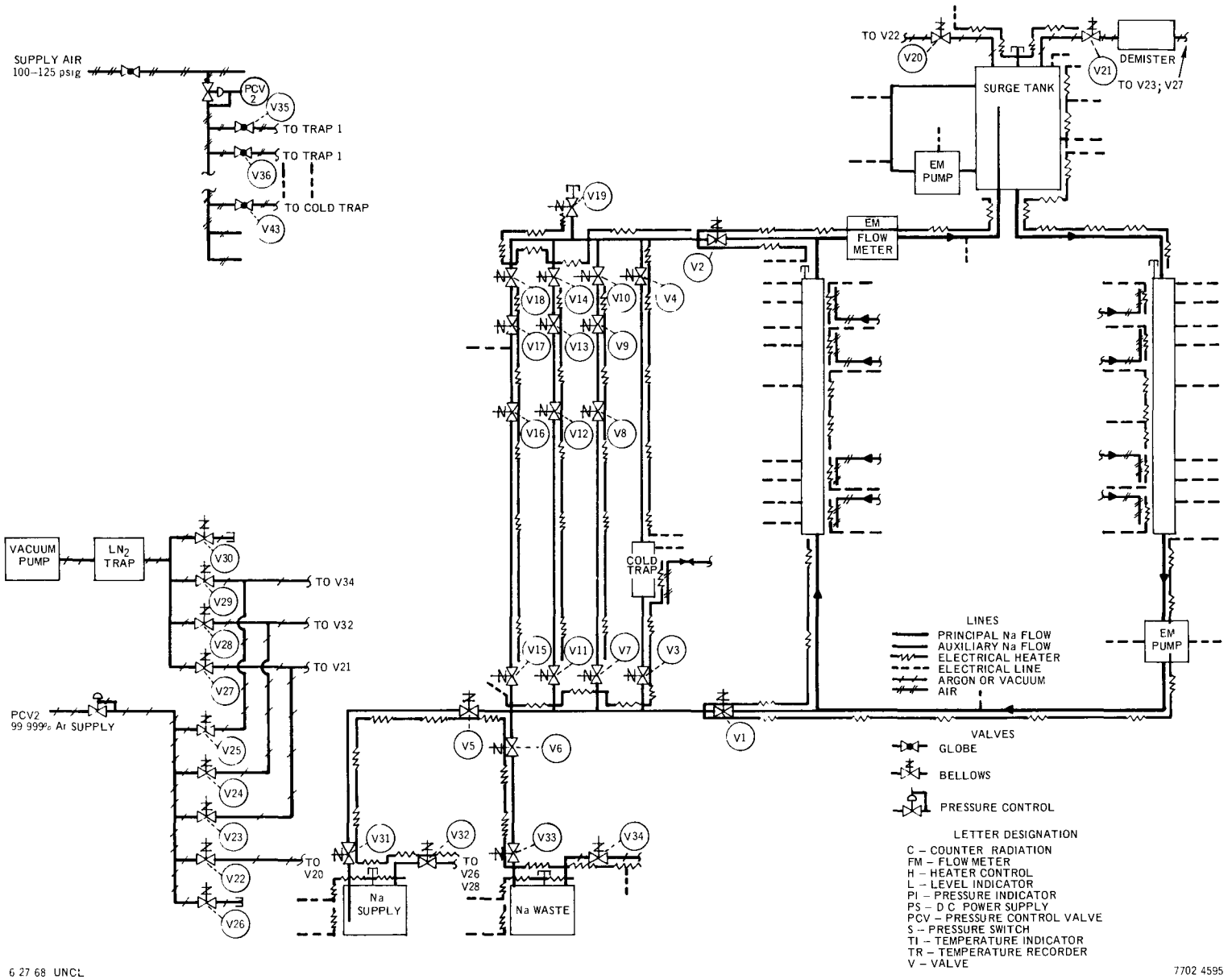

Figure 10. Fission Product Behavior Loop P&I Diagram

TABLE 3

DESIGN PARAMETERS FOR FISSION PRODUCT BEHAVIOR LOOP

Loop Temperature (°F)	300 to 1200
Trap Temperature* (°F)	300 to 1200
Sodium Volume (cc)	2000
Sodium Flow Rate (ft/sec)	
Loop Tubing	0.3 to 3.0
Annular Section of Trap	0.3 to 2.6
Unpacked Trap Section	0.04 to 0.4
Pump Throat	0.7 to 6.2
Material of Construction†	304 stainless steel

*Independently variable
†Except valves, 316 stainless steel

The objectives of making tests in the FPBL are to provide information on:

a) The plating tendencies of various fission products on 304 stainless steel,

b) The effect of fission product and oxygen concentration on deposition, and

c) Suitable materials and conditions for the trapping of fission products.

It is believed that the greatest chance for experimental success lies in the study of individual fission product elements first; then, through analytic as well as experimental procedures to determine if synergisms exist. To this end, the experimental program is divided into four phases, the first of which has started:

Phase I, Loop characterization,

Phase II, Deposition tests (including the effect of oxygen) in an all stainless steel system,

Phase III, Trapping studies using a variety of trapping materials and surfaces, and

Phase IV, Interaction studies.

In order to minimize the analytic and experimental effort, fission products have been grouped as to their predicted chemical behavior in sodium. The following considerations were made in organizing these analogue groups:

a) Similarity of behavior of these elements in solvent systems other than sodium,

b) Tendency of the elements to form oxides that are stable relative to sodium oxide,

c) Tendency of these elements to form intermetallic compounds with the major constituents of 304 stainless steel,

d) Volatility of the elements, and

e) Extent of solubility of the elements in sodium.

In selecting a representative radioisotope from each analogue group, the following criteria were used:

a) The isotope was to be a gamma emitter,

b) The isotope should not decay to gamma emitting isotopes which might confuse data interpretation,

c) (n,γ) production reactions were preferred, no interferring radioisotopes being generated, and

d) If no suitable radioisotope of the element was found, a suitable radioisotope was to be selected from a chemical analogue.

Table 4 lists the analogue grouping, selected representative radioisotope, and expected fate in Phase II tests. The only fission product experimentally studied to date relative to deposition, cesium, does not behave as predicted from the chemical-physical data used in the grouping of the elements.

Calculations have been made relative to the specific activity of the radioisotopes required for various detection levels. Based on presently anticipated handling procedures, the lower limit on radioisotope concentration in the sodium for adequate counting statistics is 100 ppb. Because of several simplifying, pessimistic assumptions used in these calculations, the actual lower limit may

TABLE 4

ANALOGUE-GROUPING AND EXPECTED FATE OF VARIOUS FISSION PRODUCTS

Analogue Grouping	Representative Radioisotope	Expected Fate in Stainless Steel System
Cs	Cs-134	Volatilization or deposition as complex oxide
Ba, Sr	Ba-133	Deposition as oxide
Mo, Ru, Sb, Ag*	Ru-103 Sb-124	Diffusion into stainless steel
Ce, La, Nd, Y, Zr	Ce-141	Deposition as oxide or diffusion into stainless steel
Nb	Ta-182	Deposition as oxide or diffusion into stainless steel
H^3, I, Te	Se-75	Vaporization or diffusion into stainless steel

*May not be a successful analogue grouping.

be 10 ppb, not substantially different than that level corresponding to the release to the coolant of 10^{-5} of the fission product inventory in the fuel of a 100 Mwe LMFBR after one year operation. Requests for quotation from various radioisotope suppliers are being processed relative to the procurement of the required radioisotopes.

D. SYSTEM STUDIES, (LMFBR SYSTEM BEHAVIOR)

The system depletion factor concept which has been described in previous reports[8,9] was applied to a typical LMFBR to determine the range of radiation levels that might be encountered three feet from the surface of an intermediate heat exchanger. Calculations were performed for the case where the heat exchanger contained sodium but had been isolated from the main coolant stream, and for the case where the heat exchanger had been drained. The assumptions and analytical model employed in the calculations are described in AI-AEC-12687.

The results of these studies are as shown in Table 5. The data in Table 5 also show that in either instance, primary responsibility for the high radiation levels must be assigned to the plated fission products. The explanation for this is the huge surface area provided by the heat exchanger so that over 30% of all of the plated fission products were deposited in this heat exchanger (the rest of the plated fission products were deposited in this heat exchanger (the rest of the plated fission products were deposited in the other two heat exchangers and the piping). Also contributing to the high dose provided by the plated fission products was the fact that over 80% of the listed fission products had plated-out. The low Na dose rates in the case of the filled heat exchanger were due to the ^{24}Na decay which had taken place since shutdown and the low equilibrium activity of ^{22}Na.

TABLE 5

DOSE RATES THREE FEET FROM SURFACE OF HEAT EXCHANGER
(TEN DAYS AFTER SHUTDOWN FOLLOWING
30 YEARS OF REACTOR OPERATION)

Isotope	Dose Rates (R/hr)					
	Exchanger Full of Sodium			Exchanger Drained		
	Plated Fission Products	Activity in Na	Total	Plated Fission Products	Activity in Na*	Total
^{95}Zr-^{95}Nb	23	0.9	23.9	42	†	42
^{140}Ba-^{140}La	26	1.4	27.4	48	†	48
^{137}Cs-^{137m}Ba	8	0.02	8.0	14	†	14
^{24}Na	-	7.0	7.0	-	†	-
^{22}Na	-	3.0	3.0	-	†	-
Total			69.3			104

*Activity in Na adhering to walls of heat exchanger; assumed uniform thickness equivalent to 0.017 lb/ft^2.
†Negligible

The limitations of the above example should be stressed. It was performed primarily to illustrate the application of the depletion factor concept, but also illustrated the potential importance of fission product plating in restricting access to primary system components. Insofar as accuracy is concerned, this is undoubtedly very low at the present time because the depletion constants, α, were based on very limited data from two reactor systems (SRE and FERMI) which bear little detailed resemblance to projected LMFBR's. Further, the assumption of uniform plating is highly questionable, since some preferential plating in either the cold or hot legs of the loop or in cold traps or other parts of the system would be expected. Finally, the question of corrosion product activities has been neglected and, as shown in an earlier section, these activities might ultimately be dominant. The principal conclusion to be drawn from these results is that extremely high radiation levels would be present in the vicinity of heat exchangers, and that these levels would prevent all but the most limited personnel occupancy. Accordingly, no contact maintenance except of the most superficial sort could be performed until the radiation levels had been materially reduced. The study results also indicated that reliance upon natural decay would be extremely time-consuming since after decay of the ^{24}Na activity, the residual levels decreased with an effective half-life of only 20 to 40 days.

III. EVALUATION OF EFFORT DURING FY 1968

The completion of a topical report providing an up-to-date summary of the technical status of this project is considered a major milestone. Preparation of this report has required the compilation of data from a number of past experiments and studies, and its organization into a single coordinated document. This is particularly timely insofar as it provides a good starting point for initial efforts involved in preparation of the source term model computer program and initial operation of the fission product behavior loop.

With respect to efforts involved in source term characterization, the preparation of the radioisotope flow chart and the definition of design characteristics for a Reference LMFBR are important preliminaries to the preparation of the source term model computer program, though the reference design characteristics will undoubtedly require considerable refinement and expansion before the

computer program is developed. The radiological hazard index and the radiation index, while initially useful for very preliminary screening purposes are now clearly of limited value insofar as providing program guidance is concerned. Their primary value may be in indicating the need for development of the source term model computer program and for the development of experimental data using the fission product behavior loop. The study leading to analogue grouping of important fission products may also be of considerable value by providing a more efficient experimental program with the FPBL; however, at least a limited number of tests should be performed to confirm the validity of at least some of the more questionable analogue assignments.

The study of the effect of the corrosion of activated fuel cladding is considered particularly significant in that it indicates that under some conditions these products may overshadow many of the fission products in importance, at least in terms of radiation levels if not in terms of radiological hazard. It is planned that provisions for further investigation of this problem will be included in the source term model computer program.

As regards the source term model computer program, the effort in this area has been underway for only a short time so that it is difficult to evaluate its significance. Almost all of the other studies performed, however, point to the need for a program of this type. One difficulty, nevertheless, is apparent from the outset. This is, that the model will only be useful to the extent that reasonably accurate experimental data are available either for use directly in the code or for adjusting code parameters. This, of course, emphasizes the importance of the FPBL experiments.

The cold-trapping studies involving cesium provided useful experience in using radiometric techniques for the study of isotope deposition and also provided some limited data bearing on the possible mechanisms involved in cesium trapping. Both of these results will be of value in the operation of the FPBL.

The system study involving application of the depletion factor concept to an LMFBR demonstrated the potentially great importance of plated fission products in restricting access to primary system components for maintenance operations. While there are many uncertainties and approximations involved in the calculations,

the results further underline the need for development of a reasonably accurate quantitative understanding of fission and corrosion product plating.

The delay in construction and operation of the FPBL (scheduled for operation in February) has permitted detailed planning of the experimental program. Starting with no plans to expand the deposition experimental work beyond cesium, a plan has been evolved in which fission products have been grouped as to anticipated behavior, analyses completed relative to radioisotope requirements, an experimental approach completed, and a loop designed, fabricated and testing begun. As a result, data acquisition and analysis should proceed smoothly.

REFERENCES

1. Private communication, Dr. J. Colby, USAEC-DRDT
2. J. Saroul, "Investigation of the Behavior of Fission Products in Sodium and Argon – PIRANA Experiments," Int. Conf. on the Safety of Fast Reactors, Aix-en-Provence, September 1967
3. W. S. Clough in "A Summary of Research and Development Work Carried Out in 1966 in Health and Safety Departments of UKAEA," AHSB (RP) M 46 September 1967
4. Private communication, R. L. Koontz, Atomics International
5. A. W. Castleman, Jr., and I. N. Tang, "Thermodynamics of Fission Product-Sodium Solutions," BNL-11611, November 1967
6. Private communication, A. W. Castleman, Jr., Brookhaven National Laboratory
7. Atomics International, "Annual Technical Progress Report – AEC Unclassified Projects, Fiscal Year 1967," p. 80, NAA-SR-12492, August 1967
8. Atomics International, "Quarterly Technical Progress Report – AEC Unclassified Projects, January-March 1967," Task 6C; NAA-SR-12395, May 1967
9. Reference 7, page 68

PAGE 110 is blank

Program:	Reactor Development
AEC Task:	6-D & E, Nuclear Safety, Gaseous Effluents, Sodium Fires
Project Manager:	H. A. Morewitz
Reporting Period:	Fiscal Year 1968
General Order: 7702	Subaccount: 31111 AEC Category: 04-60-40-04.1

Principal Investigators: R. Koontz, C. Nelson, L. Baurmash, R. Johnson, M. Greenfield, J. Hopenfeld, M. Silberberg, D. Hausknecht

I. PROJECT OBJECTIVES

The general objective of this project is to develop experimental information and analytical methods which characterize the release and transport of effluents and energy generated during a primary-coolant-sodium accident. The source of energy generation may be from the escaping coolant by rapid thermal energy transfer and/or by combustion of the sodium coolant. The effluents are sodium (as Na 24) or its oxide, in particulate form, and selected fission products available as potentially serious dispersions of radioactivity. The information to be developed is required for the design and safeguards analysis of economical, sodium-cooled, fast reactors.

II. TECHNICAL PROGRESS DURING FISCAL YEAR 1968

A. PRESENTATIONS

The following presentations were made during this fiscal year.

Three papers were presented at the 1967 ANS Winter Meeting on November 5-9, 1967.

1) D. F. Hausknecht and M. A. Greenfield, "A Model Describing the Behavior of the Aerosol Produced by a Sodium Fire"
2) R. L. Koontz, C. T. Nelson, and L. Baurmash, "Characteristics of Aerosols Generated During Sodium Fires"
3) R. L. Koontz, C. T. Nelson, and L. Baurmash, "Characteristics of Vaporizing UO_2 in Air"

Two papers were presented at the International Conference on the Safety of fast reactors at Aix-en-Provence, France in September 1967.

4) "Sodium Burning, Aerosol Generation, and Control of Fission Product Release During an Accident" – Part I, "Sodium Burning"; Part II, "Aerosol Generation and Control of Fission Product Release"

5) The experimental and analytical work performed at AI on the study of the effect of aerosol agglomeration on the reduction of the radiological source term following a design basis accident (DBA) in a liquid metal fast breeder reactor was presented on May 13 and 14, 1968 in Washington, D.C. to members of the (a) Environmental and Sanitary Engineering Branch and the R&D Branch of Nuclear Safety, RDT, and (b) The Division of Licensing and Regulation of the AEC.

B. FUNDAMENTAL EXPERIMENTS

1. Laboratory Test Chamber Studies of Na and UO_2

a. Floor Deposition

Experimental studies of the oxidization of liquid sodium and the arc-vaporization of UO_2 in air in the laboratory test chamber (LTC) have led to an empirical observation of the relation between the maximum median particle radius produced by agglomeration and the mass concentration ρ_R (μgm/cc) which is introduced into the chamber. The general form is such that

$$r_{50} = a(\rho_R)^{0.4} \qquad \ldots(1)$$

where

a = 0.7 for U_3O_8 and Fe_3O_4 aerosol mixtures, and

a = 1.0 for Na_2O aerosols.

r_{50} = the mass mean radius of the total distribution* when agglomeration has proceeded for a time long enough for 1/2 of the released mass to settle on the floor.

Figure 1 is a plot of the observed relationship between the released mass concentration $M_R/V = \rho_R$(μgm/cc) and T_{50} (min) for all of the experiments which have been performed to date. The empirical observations between T_{50} and ρ_R can be related to the aerodynamic radius ($\sqrt{d}\,r$), the mass median radius (r_{50}) and to the chamber dimensions. The experimental observations can be used to predict the settling characteristics of the two aerosols which have been studied.

The observations of T_{50}, if normalized for the true density d(gm/cc) of the released aerosol and the height H(cm) of the LTC, can be expressed as

*r_{50} is obtained from experimental observations of the time (T_{50}) to accumulate 1/2 of the mass which settles on the floor.

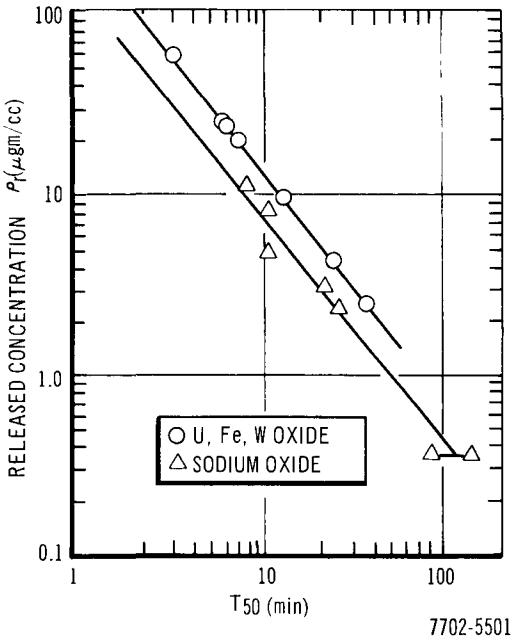

Figure 1.

Released Material vs Floor Deposition Half-Time in the LTC

$$T_{50} = \frac{52.5H}{d \cdot (\rho_R)^{0.8}} \quad \text{for } Na_2O \; ; \; d = 2.27 \text{ gm/cc}, \qquad \ldots(2)$$

and

$$T_{50} = \frac{115H}{d \cdot (\rho_R)^{0.8}} \quad \text{for } U_3O_8\text{-}Fe_3O_4 \; ; \; \bar{d} = 7.0 \text{ gm/cc}. \qquad \ldots(3)$$

However, Na_2O forms "spherical" aerosols; whereas, U_3O_8 and Fe_3O_4 form branched-chain aerosols. Therefore, the true density is only applicable in the case of the Na_2O; a reduced effective density is appropriate in the case of the U_3O_8-Fe_3O_4 aerosol. If the density of the chain-like aerosol is chosen to be ~3.2 gm/cc (a not unreasonable value based on the electron micrographs of these aerosols), both expressions for T_{50} reduce to Equation 2. This equation is close to the theoretical expression derived from the solution of the equation for stirred settling of a log normal distribution for spheres where the mass mean radius (mmr) is equal to r_{50} and where the geometric standard deviation, σ = 1 - 2.5; i.e.,

$$T_{50} = \frac{50H}{d \cdot (\rho_R)^{0.8}} \quad . \qquad \ldots(4)$$

Solutions of the equation represented by various values of r_{50} and σ can be used to determine the concentration vs time history of any aerosol with a known r_{50} and σ, which is postulated to exist following its release and agglomeration to a known size.

b. Wall Deposition

The wall plating characteristic of sodium oxide aerosols in the LTC chamber was found to be a function of the released concentration. The empirical observation is T_{50} (wall) = $77/(\rho_R)^{0.6}$ (min). Additionally, the fraction of released material which plated on the wall decreased as ρ_R increased. The deposition velocity on the wall, v_w, can be expressed as v_w (cm/sec) = $1.67 \times 10^{-3} (\rho_R)^{0.6}$, thus implying an increasing deposition velocity with increased concentration. Since ρ_R increases with the fire area, burn time, or temperature, a possible explanation has been sought by looking at thermophoretic forces and the influence of the observed temperature gradients on the wall plating rate.*

For Na_2O particles larger than 1.2μ in diameter (the approximate mass median diameter of the initially released oxide), the deposition due to thermophoresis is constant and equal to 0.08 cm/min-°C-cm. The temperature gradients to the wall increase as ρ_R increases; thus, a reasonable explanation for the observed relation is that $v_w \sim \Delta T/\Delta X \sim \rho_R$. The heat liberated and available for loss to the walls is the product of the heat of combustion and the mass of sodium burned, M_{oxide}; thus, $\rho_R = M_R/V = fM_{oxide}/V$, where f, the release fraction of the oxidized sodium, equals 0.2 for Na oxidized in air.

The fractions of material partitioned between the floor and walls, based on the empirical observations (on sodium oxide aerosols) between the initial wall and floor deposition rate, $v_{50}(w)$ and $v_{50}(f)$ respectively, are such that, for a given initial concentration, v_{50} (floor) increases more than v_{50} (wall). (This is consistent with our observations that as ρ_R increases, the fraction on the floor increases.)

Unlike the sodium oxide aerosols experiments, the fraction of material deposited on the walls for the arc-vaporized UO_2 experiments seems to be independent of the released mass concentration; i.e., a constant fraction of the released mass is deposited on the walls. At the present time, it appears that neither diffusion of the long chain-like aerosol nor thermophoresis is a likely explanation of this effort.

An aerosol mixture composed of oxidized Na and UO_2-stainless steel was generated in the LTC. The materials combined and settled as one aggregate.†

*See AI-AEC-12680, Task 6D.
†See NAA-SR-12570, pp 43-49.

The concentration of each constituent Na_2O, U_3O_8, and Fe_3O_4 decreased at the same rate even though the density of Na_2O is 1/3 that of U_3O_8 or Fe_3O_4. It was noted that the observed half time for the floor deposition of the mixture fits that of the vaporized UO_2 aerosol of Figure 1 even though the relative concentration of Na_2O was 86% of the total. The effective radius of the mixture was noted to be much larger than either that of Na_2O or U_3O_8 alone;* this may account for the increased settling rate.

2. Spray Fires

Two experiments have been performed in the Spray Test Vessel (STV). The first test was preliminary and scoping in nature. Rather large droplets were formed in the spray similar to those in the jet spray from a pinhole leak in a high pressure pipe. The spray lasted for a period of 2.0 sec, and 93% of the liquid Na which was released fell on the floor during the spray time. During the spray period (probably due to the large droplet size and the resultant rapid fallout), 0.35% of the initial 4% oxygen was consumed (10% of the available oxygen).

Since the pressure, temperature, and O_2 concentration are monitored as a function of time, some attempt at an energy balance was made for both tests.

Table 1 shows the pertinent data obtained for the two tests. Row 10 shows that the computed ΔP, based on the heat balance obtained from the ΔO_2 measurement Row 6 (assuming that Na_2O_2, rather than Na_2O was formed, because of excess available oxygen), agreed with Row 9, the measured ΔP. (If one assumes that Na_2O was formed, the heat balances cannot be made.) Row 12 shows that the spray nozzle droplet size was improved after the first test. The deposition rate decreased during the injection period.

Table 1 also gives the parameters necessary to characterize the aerosol which remains airborne after the initial fallout of the large droplets of Na. First, it is noted in Row 17 that fine sprays are almost completely oxidized in excess O_2. Oxygen, 10% by volume, will oxidize 183 gm of Na when forming Na_2O_2 in the STV. Note also that the oxidized Na in Test 2 is nearly equal to that which remains airborne, see Row 18. This would follow from the fact that oxidation of sodium produces fine particles, and small sodium particles are easier to oxidize completely than coarse particles. Row 13 of Table 1 gives T_{50}, the time

*See NAA-SR-12492, p 101

TABLE 1

SPRAY TEST RESULTS

Row No.	Parameter	Test No.		Comment
		1	2	
1	Na released (gm)	68	24	
2	Spray time (sec)	2	20	
3	Initial O_2 (%)	4	10	
4	Initial Na temperature (°F)	600	1000	
5	Spray size	coarse	finer	See fallout rate during spray (Row 12)
6	O_2 consumed (% oxygen)	0.35	0.92	During spray
7	Na oxidized, from ΔO_2 (μgm/cc)	9.5	25	During spray, Na in Na_2O_2 is computed.
8	Time to consume O_2 (sec)	2.6	26	
9	Measured pressure change (psi)	2.8	9.5	
10	Computed, ΔP (psi)	3.0	9.0	From ΔO_2 forming Na_2O_2
11	Na_2O_2 produced (gm)	14.5	38	During spray
12	Spray, fallout rate (gm Na/sec)	18	0.1	During spray
13	Aerosol deposition, T_{50} (min)	6	3	d = density gm/cc
14	Equivalent size of Row 13	6.8	9.8	Aerodynamic radius, d = density gm/cc
15	Measured concentration of aerosol after spray of Na (μgm/cc)	5-6	24	Na in Na_2O_2 is measured.
16	Fraction of released spray on floor (%)	60	67	
	wall	37	33	
	wall and ceiling	40		
17	Released Na oxidized during spray time (%)	12.5	93	Row 7/Row 1
18	Fraction of Na remaining airborne	0.58	0.92	Row 15/Row 7
19	Row 15 converted to Na_2O_2 (gm)	9.4	41	

for 50% of the mass to settle, after the spray has stopped. Thus Row 13 can be used to determine the effective size of the aerosol which is being deposited. This size has been computed from T_{50} and is shown in Row 14 in terms of the aerodynamic radius, $\sqrt{d} \cdot r$. The true density of the airborne material is not known as yet, but is believed to be close to that of Na_2O_2. Since the initial size of the spray is not known, it is not possible to relate this computation of the size to any growth or agglomeration phenomenon. However, it is clear that the initial concentration of sodium remaining airborne for Test 2 was larger than that of Test I, Row 15, and that the fallout half time was shorter. It is also clear that the initial spray from Test 2 was finer than that of Test 1 (see Row 12), and thus would not settle faster unless the particles had grown rapidly to be larger (see Row 13). Thus, the same general picture of the behavior of the aerosol from sodium spray fires as that from pool fires emerges, although the present results must be considered to be preliminary.

3. Phase I – Large Fundamental Fires

The Phase I Large Fundamental Fires experiments included studies of the characteristics of sodium fires by controlling such parameters as sodium temperature, oxygen concentration of the gas mixture within the reaction chamber and gas mixture flowrate (see Figure 2). Six (2-ft diameter) fires were conducted during the year to study the effects of the above parameters on the burning rate of sodium (lb/ft^2-hr) and the release fraction of sodium combustion products. A summary of the experimental parameters used during the test series is given in Table 2.

The majority of the Phase I sodium fires were conducted with an inlet gas mixture oxygen concentration of 4 vol % while the effects of flowrate and sodium

TABLE 2
PHASE I TEST CONDITIONS

Inlet Gas Mixture (vol % O_2)	Gas Mixture Flowrate (scfm)	Sodium Temperature (°F)
4	18, 90, 150	590 - 1300
9.5	90	950 - 1300
21	90	850 - 1300

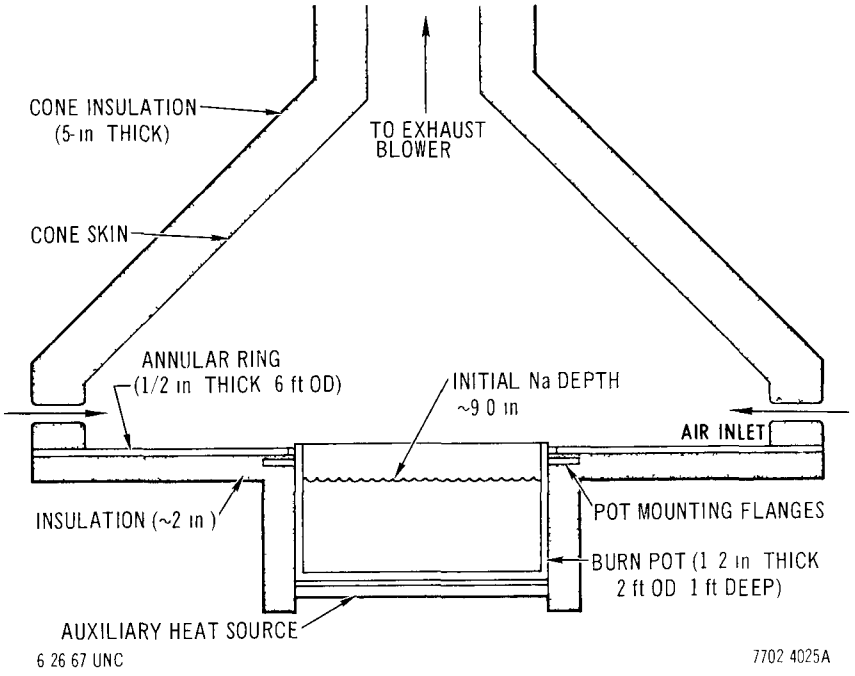

Figure 2. Large Fires Apparatus, Revised Burn Chamber

TABLE 3

PHASE I, 4 vol % O_2 BURNING AND RELEASE RATE

Inlet Gas Mix Flowrate (scfm)	Average Na Temperature (°F)	Burn Rate (lb/ft^2-hr)	Release Rate (lb/ft^2-hr)
19	595	0.91	0.091
19	900	0.98 ± 0.02	0.285
18	945	1.17 ± 0.06	0.262
18.1	950 to 1030	1.0 to 1.4	0.2 to 1.33
18.1	1250	2.1	1.22
87	590	0.985	0.156
86.5	970	1.85 ± 0.096	0.570
150	610	1.15	0.165
142	960	1.55 ± 0.07	0.534
155	1300	2.7	2.00

temperature were studied. Three standard gas mixture flowrates were established for the test series (see Table 2). Nominal steady state sodium temperatures of approximately 600, 900, and 1200°F were established at the above gas mixtures and flowrates.

Sodium burning rates and combustion product release rates were determined for each fire. For the Phase I tests which maintained a 4 vol % oxygen concentration, burning rates in the atmosphere from 0.91 to 2.7 lb/ft^2-hr were observed. This included observations at all gas mixture flowrates. Specific burning rates of 0.91 to 2.1 lb/ft^2-hr were observed at flowrates of 18 scfm and average sodium temperatures of 600 to 1250°F. Table 3 summarizes the sodium burning and release rate data for the 4 vol % oxygen Phase I tests. It was calculated that the release rates at the low flows were proportional to the vapor pressure at the test temperature.

At a constant flowrate of 90 scfm, additional experiments were performed to determine sodium burning and release rates at increased gas mixture oxygen concentrations. These tests were conducted with gas mixtures having a 9.5 and 21 vol % oxygen concentration and were initiated with an average sodium temperature of approximately 850 and 950°F, respectively. Maximum burning rates observed for the 9.5 and 21 vol % oxygen tests were 5.9 and 9.0 lb/ft^2-hr, respectively. The observed burning rate for tests conducted with a gas mixture flowrate of 90 scfm are summarized as a function of average sodium temperature, see Figure 3. The release fraction of sodium oxide for this test series is shown on Figure 4. It is interesting to note that the 21 vol % oxygen test was completely self-sustaining (i.e., no electrical heat input was required to maintain or increase the bulk sodium temperature), the 9.5 vol % oxygen test represents the approximate threshold of being self-sustaining, and the 4 vol % oxygen tests required electrical heat input to maintain equilibrium sodium temperatures, particularly at the lower sodium temperatures.

During the Phase I test series, an overall system heat balance was developed to account for the heat flow from the sodium combustion region to the system. Time dependent values of bulk sodium temperature, gas mixture temperatures, and system component temperatures were compiled for each test and used as input to the Phase I heat balance code (PHASE I HTBAL). This code calculates the heat transfer throughout the system (see Figure 5). A simplified

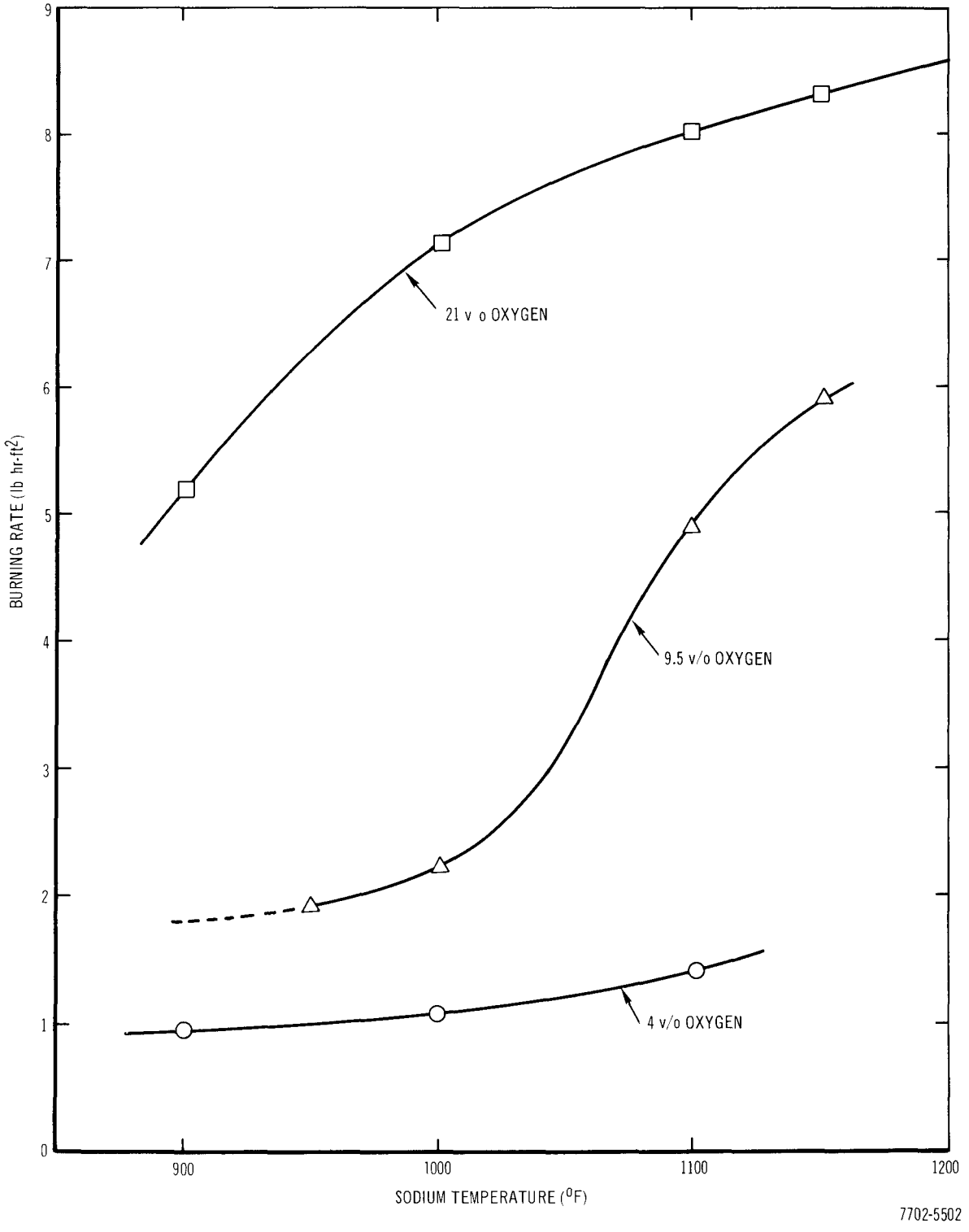

Figure 3. Phase I Experiments, Burning Rate vs Sodium Temperature for 4, 9.5, and 21 v/o O_2 (gas flow rate = 90 SCFM)

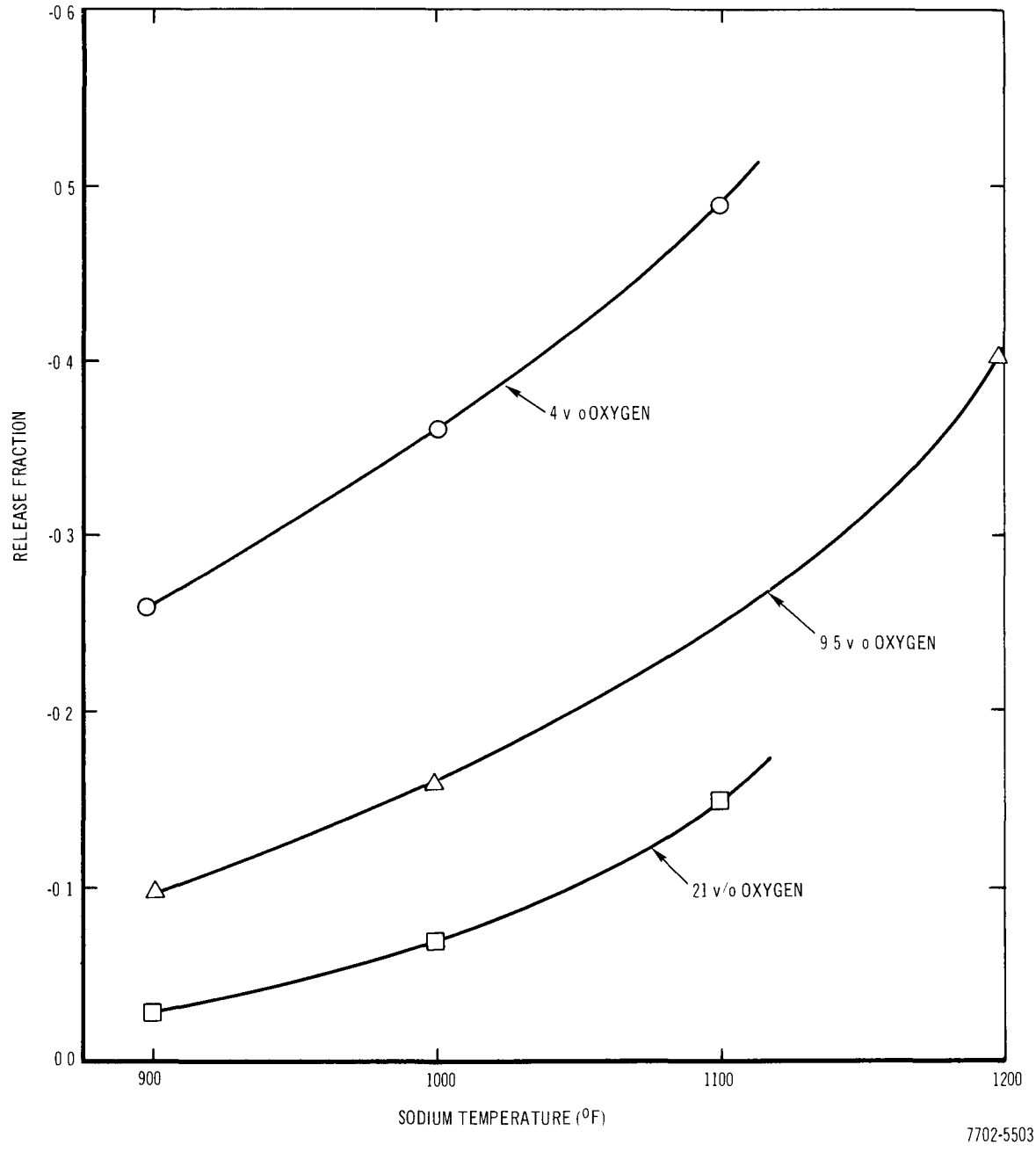

Figure 4. Phase I Experiments, Oxide Release Fraction vs Sodium Temperature for 4, 9.5, and 21 v/o O_2 (gas flow rate = 90 SCFM)

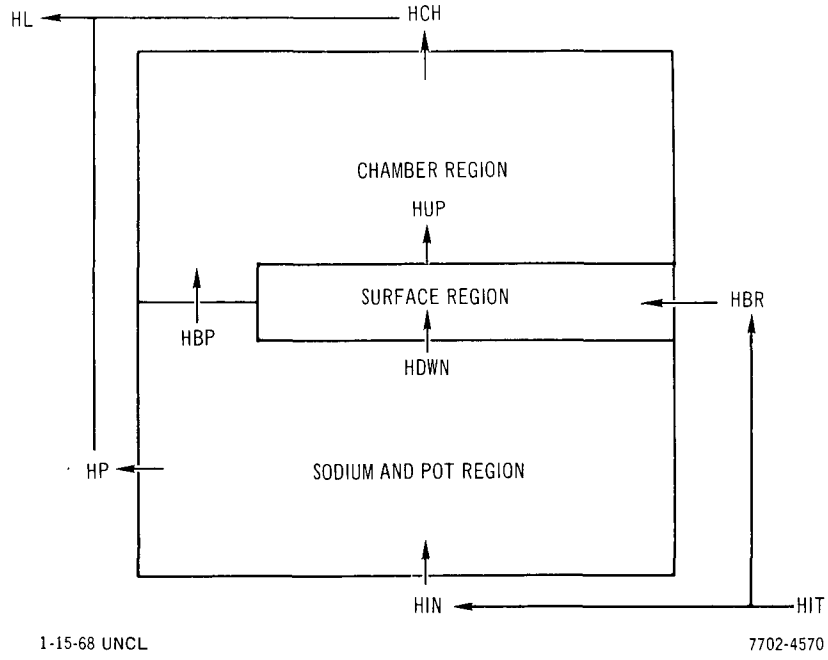

Figure 5.

Large Fires Apparatus, Heat Transfer Scheme

heat balance equation is written around the sodium surface region or reaction zone to determine the respective heat flow.

$$q_{down} + H_C R_B = q_{up} \quad ,$$

where

HDWN = q_{down} = the heat transferred to or from the sodium,

HUP = q_{up} = the heat transferred to region above the surface region,

HBR = H_C = the heat of combustion, and

R_B = the observed burning rate.

The heat transferred to the region above the sodium (q_{up}) is calculated from the components of (1) the enthalpy change of the gas in the system, (2) the enthalpy change of flowing gas from the inlet to outlet, (3) the enthalpy change of the enclosure cone metal, insulation, and protrusions, (4) the enthalpy change of the burnpot support flange metal and insulation, (5) the heat conducted through the enclosure cone and support flange insulation, and (6) the enthalpy change of the sodium oxide released. The heat transferred between the surface region and the sodium is calculated from the components of (1) the enthalpy change of the sodium, (2) the enthalpy change of the burnpot metal and insulation, and (3) the heat transferred through the burnpot metal and insulation by conduction.

Specific heat transfer values of interest calculated in the Heat Balance Code are (1) the heat transferred from the reaction zone (HUP), (2) the heat transferred to the sodium to the reaction zone (HDWN), (3) the total heat loss from the Phase I system (HL), and (4) the system and reaction region heat balance accountability terms. Comparison of data on the heat transferred from the reaction zone to surroundings (HUP) with the sodium burning rate, release rate, and sodium inventory data, has led to an empirical determination of the heat contributions resulting from combinations of the oxide (Na_2O) and peroxide (Na_2O_2) end-product reactions. Consequently, an improved accountability of system and surface region heat balances was made for tests at 9.5 and 21 vol % oxygen concentration. Contributions to the combustion heat due to the peroxide reaction has been shown to be more predominant at high oxygen concentration atmospheres. Figure 6 shows a review of the combustion energy distribution as a function of sodium temperature for the 4, 9.5, and 21 vol % air mixture tests. The combustion energy distribution comprises heat transferred to the system from the reaction zone HUP, and the directional heat contribution from the sodium, HDWN. Positive HDWN indicates that heat is being transferred to the system and – HDWN indicates that heat is being transferred to the sodium. Although the system heat losses are directly proportional to system temperature, the heat which is transferred from the reaction zone to the sodium becomes predominant for gas mixtures greater than 9.5 vol % as shown in Figure 7. Current analytical models have also shown that heat losses from a sodium pool are essentially matched by the increased contribution of heat transferred from the reaction zone to the sodium, due to the higher burning rates at this gas mixture concentration.

C. PHASE II LARGE MODELING FIRE EXPERIMENTS

Fabrication of the Phase II test chamber was completed and the unit installed at the Sodium Fires Test Installation. The Phase II test chamber consists of a 2500 ft^3 cylindrical vessel, 10 ft in diameter and 30 ft high. The vessel comprises a lower reaction cell, two secondary or top sections, and a removable ellipsoidal head section. Existing atmosphere control, discharge effluent, and sodium fill lines which service the Phase I experimental system also service the Phase II system.

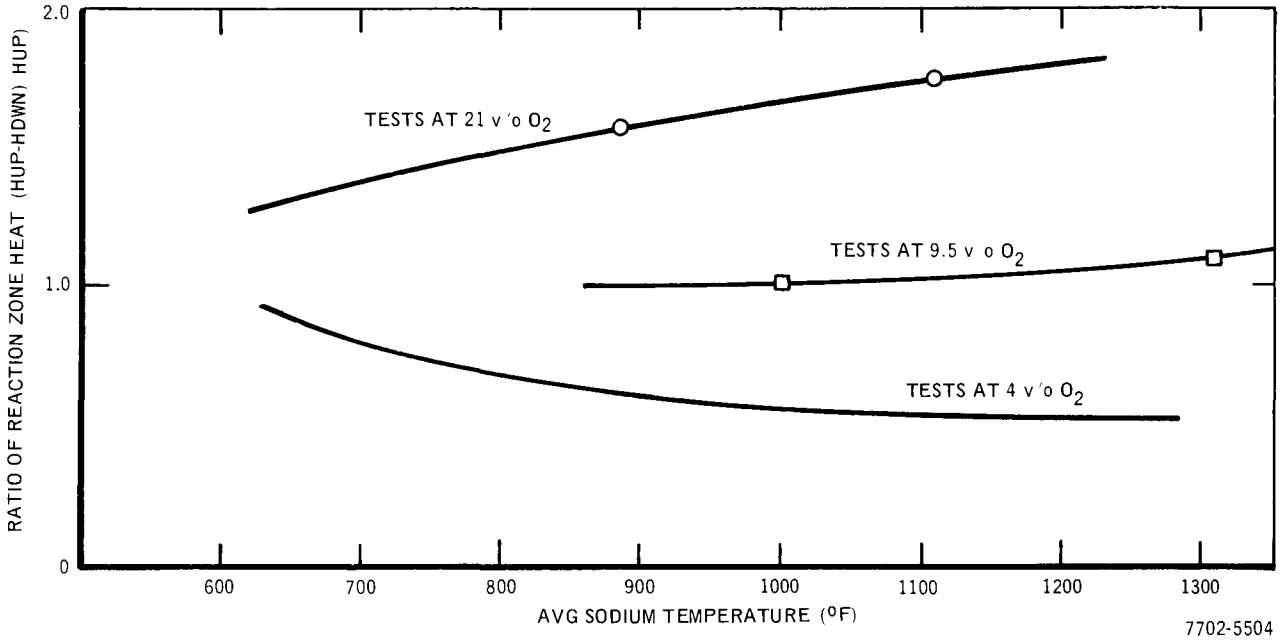

Figure 6. Ratio of Reaction Zone Heat Transfer (HUP-HDWN/HUP) vs Average Na Temperature (TNA)

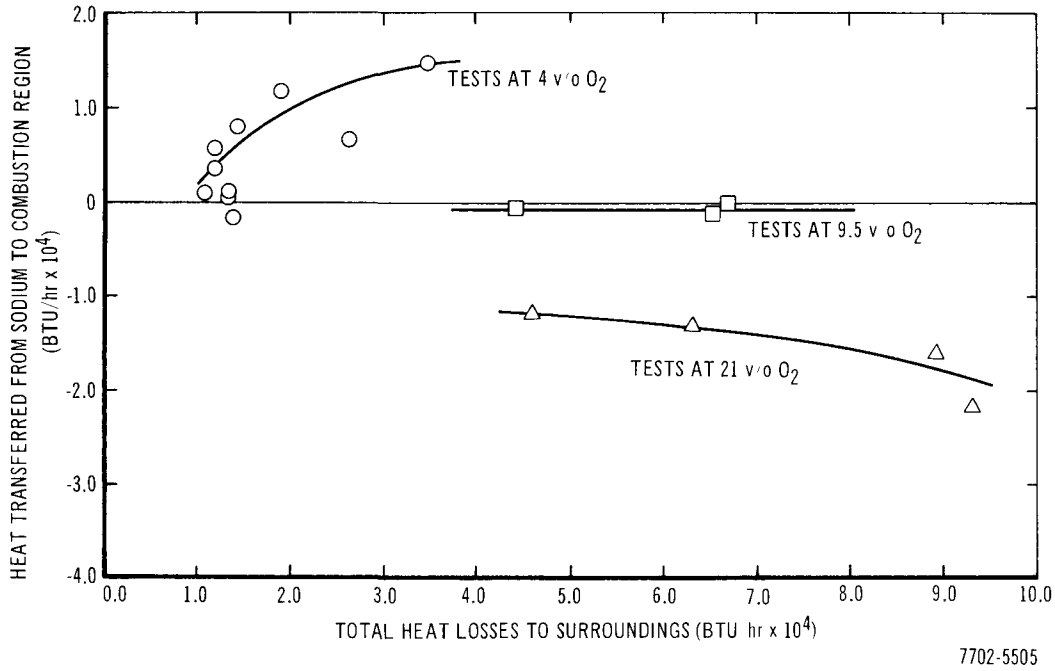

Figure 7. Heat Transfer from Sodium to Combustion Region (HDWN) vs Total System Heat Losses (HL)

In the Phase II test chamber, the large fire modeling capability is maintained by providing a removable interface donut section between the reaction cell and the secondary volume. The interface section is constructed in the shape of a donut to allow determination of the effects of a variable diameter opening (simulating an open primary equipment cell in an LMFBR) on the oxygen transport mechanism. Initial atmospheric conditions are established within the reaction cell and secondary volumes through separate gas lines which are connected to the Phase I gas mixing manifold system. Effluent gases from the Phase II test chamber may be directed through the Phase I gas scrubber and effluent gas stack discharge pump. An extension line from the existing Phase I sodium storage and transfer system is connected to the Phase II reaction cell and is directed to the sodium spill pan which is located on the reaction cell floor. The Phase II test system is shown in Figure 8.

The general criteria under which the initial Phase II calibration-aerosol modeling test will be conducted have been established. These criteria include an initial sodium temperature of 1000° F, a burning area of 6 ft^2, a 25 lb sodium spill, and an air atmosphere. Fabrication of test components required for the first test has been initiated and is nearing completion. These test components include an auxiliary sodium preheat and transfer system, a burn pan and burn pan heater system, a burn pan lifting spider assembly, and an aerosol sampling system.

D. ANALYTICAL DEVELOPMENT

1. Data Reduction Codes

A data reduction code which provides the fundamental conversion from millivolt sensor output into engineering units has been written for both sodium fire burning experiments, Phases I and II. The Phase I data reduction code was used to provide engineering unit input to the Phase I heat balance code for each test conducted. Initial checkout of the Phase II data reduction code has been made. Both heat balance codes utilize standard heat transfer equations to account for the heat losses occurring within the test chamber during a test and differ only by specific geometry requirements. Volume and area weighted enthalpy change and conduction equations are used to calculate the respective heat losses as a function of time. A summation of the weighted heat loss terms

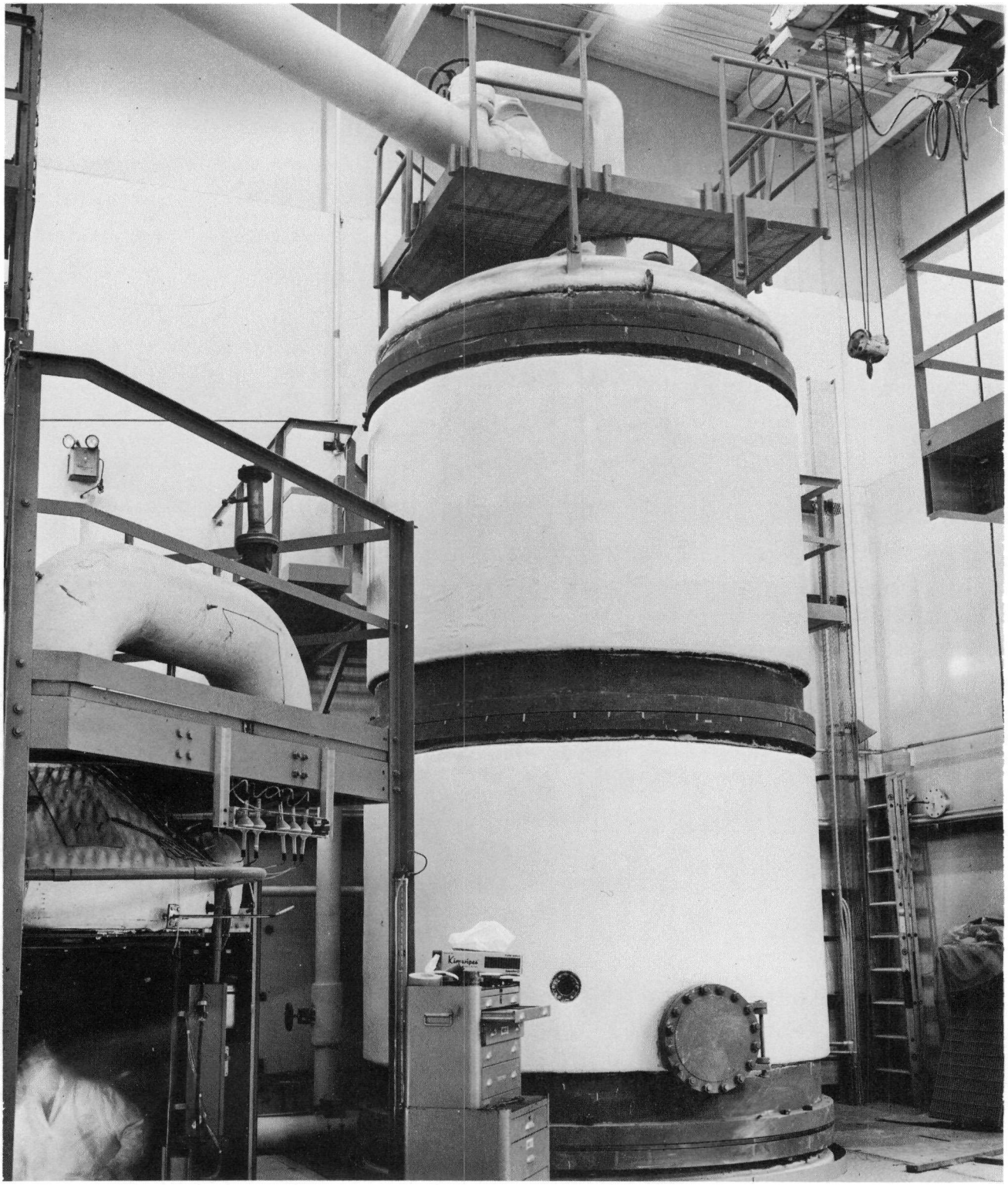

00-102207

Figure 8. Phase II Test System

is compared with the heat generated by the sodium fire (and electrical heat input where applicable) to determine a continuous heat balance accountability. The Phase I heat balance code determines a heat balance around the reaction region and the entire system, whereas the Phase II heat balance code breaks down the system heat balance into geometric regions similar to that used in the analytical burning models. Although the Phase I heat balance code was used extensively during the testing program, the Phase II heat balance code requires final compilation and checkout prior to use on the initial calibration-aerosol Phase II test.

2. Transient Sodium Burning Model

Preliminary use of the transient sodium burning code has been for model checkout only during this report period. The theoretical sodium burning rates and reaction zone flame temperatures were determined for typical large scale fast reactor facility geometries for sodium spill temperatures up to 1300°F. These calculations assume that the reacting cell is completely inerted at the initiation of a sodium fire and that the cell is fully ventilated to a secondary volume after initiation. The cases studied therefore reflect only the limiting case when the sodium burning rate is limited by the rate at which oxygen can be drawn through the cell opening. Preliminary results obtained from the transient sodium burning model, indicate that a burning rate which is considerably smaller than that from Phase I experiment is obtained (0.3 lb/hr-ft^2 at 940°F and 21 vol % oxygen calculated, versus 0.9 to 1.5 lb/hr-ft^2 at 4 vol % oxygen by experiment). This is due essentially to the small cell opening (9 ft^2) used in the model. Figure 9 shows the dependence of burning rate and flame temperature as a function of time and the sodium pool temperature for a typical geometry case.

3. SOFIRE Sodium Burning Code

The SOFIRE code has been used extensively during this report period. The code was used to predict the consequences resulting from various sodium pool fire configurations on other sponsored programs (FFTF, AI-FBR, and LMFBR programs). Also the code was used to predict consequences of the initial Phase II fires.

Improvements to the SOFIRE code includes additional format efficiencies and the addition of alternate heat sink equations which allow the user more flexibility in geometries assumed for the fire configuration.

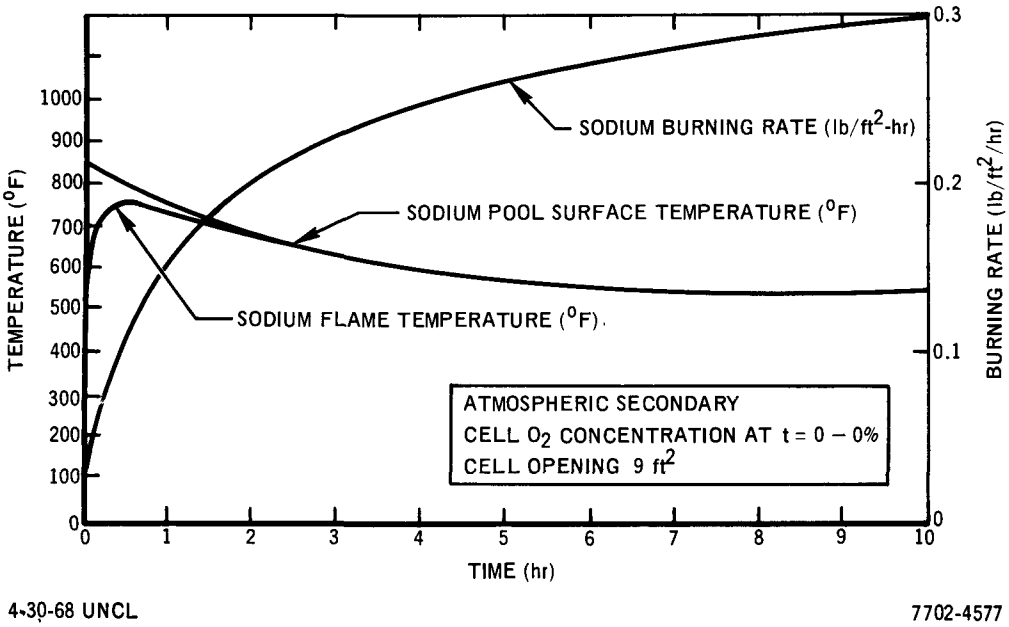

Figure 9. Transient Sodium Burning Code

4. Aerosol Behavior

The heterogeneous agglomeration code (HAC) with agglomeration mechanisms for Brownian and gravitational motion was reprogrammed for the purpose of improving the efficiency of problem solving in terms of cost and time. Debugging of this revised code is now in progress.

A faster running code which utilizes an empirical mass model, EMM code, has been developed which predicts the behavior of the LTC experiments in a satisfactory manner. The EMM code is inexpensive to use and predicts the LTC experimental results for high concentrations.

III. EVALUATION OF EFFORT TO DATE

The design and installation of the Phase II test vessel met the desired schedule requirements of the program. The design and fabrication of special test components required for initial system calibration and aerosol tests has been completed. The installation of these components and the required instrumentation is also progressing per schedule.

A number of Phase I large fire tests were run during this fiscal year. Initial analysis of the Phase I test data has been completed. The HTBAL code was developed and provided increased ability to calculate the time dependent energy distribution. Increased knowledge was obtained of the contribution of the sodium burning reaction to the overall energy released during fires with various gas mixtures. Data were accumulated in the required form to evaluate the radiative and convective heat transfer coefficient values for various fire configurations. The temperature dependence of sodium burning and release rate values at low oxygen concentration was investigated.

Development of the transient burning model, TRANBURN, the Phase I heat balance code, HTBAL I, and the Phase II heat balance code, HTBAL II, and associated subroutines has progressed so that engineering calculations and evaluations can be made.

The initial spray fire experiments seem to validate all analytical models which predict reaction and energy release as a function of particle size. As the particle size decreases, the fraction of its mass which is oxidized increases. These particles remain airborne where they agglomerate and fall out.

The experimental information and analytical models developed for this project can now be used for LMFBR safeguards analysis. This new information leads to improved accuracy in the predictions of the hazards resulting from major reactor accidents. When credit is taken for agglomeration of the aerosols produced at the time of the accident, with the resultant prompt growth to large particle sizes, there is a considerable reduction in the potential radiological source term for reactor site dose calculations. The economic implications of the reduction in site boundary distances are substantial.

PAGE 130 is blank

Program:	Fast Reactor Development
AEC Task:	6-G, Nuclear Safety (Kinetics), Boiling Studies for Sodium Reactor Safety
Project Manager:	H. A. Morewitz
Reporting Period:	Fiscal Year 1968
General Order: 7702	Subaccount: 13410 AEC Category: 04-60-01-09.1

Principal Investigators: D. Logan, J. Landoni, and C. Baroczy

I. PROJECT OBJECTIVES

The general objective of this project is to develop basic information on two-phase flow and boiling required in the safety evaluation of LMFBR design. This information is important because of the key role that sodium boiling plays in reactor dynamics, in fuel meltdown accidents, and in the ultimate shutdown mechanism of the reactor. Specific objectives of the experimental program include the development of reliable high-flux heaters, and the measurements of boiling heat transfer characteristics, two-phase pressure drop, void fraction, liquid superheating, transient voiding rates and pressures in single channels, and hydrodynamic instabilities. Specific objectives of the theoretical study, in addition to any analyses required to support the experimental work, are: the development of digital computer codes which will predict transient void fraction, flow rate, and heat transfer for single and multichannel sodium flow; and the incorporation of these codes into a general reactor kinetics code.

II. TECHNICAL PROGRESS DURING FISCAL YEAR 1968

During FY 1968, a major experimental effort was expended in development and application of high heat flux heaters. Major accomplishments include: (1) successful completion of 276 transient boiling tests to obtain data on superheating of liquid sodium (266 tests were made with a 15 in. heater and 10 were made with a newly developed 30 in. heater), (2) successful development of a constant heat flux 30 in. long by 1/4 in. OD stainless steel sheath heater, (3) successful development of an axially shaped heat flux 36 in. long by 1/4 in. OD stainless steel sheath heater, (4) link-up of important instrumentation output directly with the data reduction center (this allows direct readout of data in engineering units on equipment that has traceable calibration back to NBS standards, and

(5) upgrading of boiling detection methods so that more positive identification of incipient boiling can be made.

The major analytical effort resulted in: (1) successful development and documentation of TRANSFUGUE IIa, a single channel two-phase transient code for use with sodium, (2) conversion of a steady state two-phase multichannel steam code for use with sodium (SODIFAZE code), and (3) conversion of a transient two-phase multichannel steam code for use with sodium (TRANSODIFAZE code).

A. SODIUM LIQUID SUPERHEATING

Four hundred and ninety-five sodium liquid superheat tests have been performed at pressure levels up to 12.5 psia (276 of these tests have been performed during FY 1968). These tests are being done to determine the extent of liquid superheating required to initiate boiling in a single LMFBR coolant channel as influenced by parameters such as velocity, heat flux, inlet subcooling, coolant purity, pressure, heater surface finish, etc. Two testing methods have been used: (1) the pressure, inlet temperature, and flow are established; then, heater power is gradually increased until incipient boiling occurs, or (2) the heater power, inlet temperature, and flow are established; then, test section pressure is gradually decreased until incipient boiling occurs. The temperatures are measured by multiple thermocouples which probe through the test section wall 1/16 in. into the 1/8-in. sodium annulus surrounding the heater. The saturation temperature is determined from a sodium saturation curve by using pressures measured with a Barton absolute pressure gage.

One hundred and thirty-one runs have been made during this last quarter and are shown in Table 1. All of the K runs (K1-42) and run L1 were made by Test Method 2 (decreasing pressure to cause boiling). The remainder of the 131 runs were made with Test Method 1 (increasing heat flux to cause boiling). Runs L1-10 were made with the newly developed 30 in. heater.

Figure 1 shows a plot of the maximum measured liquid superheat vs pressure as obtained to data for various heat flux levels. Figure 2 shows a different perspective of the heat flux effect on maximum obtainable superheats. With few

TABLE 1

SODIUM LIQUID SUPERHEAT TEST RESULTS
(Sheet 1 of 3)

Run No.	Condenser (psia)	Test Section (psia)	Maximum Test Section (psia)	Time at Maximum Pressure (min)	Inlet Temperature (°F)	Heat Flux (Btu/hr-ft^2)	Flow (ft/sec)	Bulk Superheat (°F)
JB-1	5.00	7.91			1399		3.26	
JB-2	5.00	7.95			1404	0.266×10^6	3.30	19
JB-3	5.00	7.93			1405	0.236×10^6	3.28	5
JB-4	5.00	7.88			1404	0.288×10^6	3.30	26
JB-5	5.00	7.97			1400	0.291×10^6	3.30	25
JB-6	5.00	7.98			1399	0.256×10^6	3.32	-3
JB-7	5.00	8.00			1399	0.255×10^6	3.30	6
JB-8	5.00	7.99			1408	0.317×10^6	3.20	41
JB-9	5.00	7.92			1404	0.297×10^6	3.22	26
JB-10	5.00	8.10			1400	0.346×10^6	3.20	41
JB-11	5.00	7.95			1398	0.327×10^6	3.22	31
JB-12	5.00	7.80	15.0	5.0	1403	0.354×10^6	3.17	35
JB-13	5.00	8.04			1397	0.304×10^6	3.15	20
JB-14	5.00	7.90			1397	0.319×10^6	3.20	24
JB-15	5.00	7.93	15.0	5.0	1408	0.310×10^6	3.13	42
JB-16	5.00	8.01			1404	0.340×10^6	3.20	41
JB-17	5.00	7.88			1402	0.303×10^6	3.13	29
JB-18	5.00	7.92	15.0	5.0	1412	0.235×10^6	3.20	3
JB-19	5.00	7.96			1409	0.264×10^6	3.11	14
JB-20	5.00	8.14			1406	0.333×10^6	3.11	41
JB-21	5.00	7.82			1404	0.324×10^6	3.24	37
JB-22	5.00	8.11			1404	0.344×10^6	3.20	44
JB-23	5.00	8.15			1404	0.339×10^6	3.13	36
JB-24	5.00	8.15			1404	0.341×10^6	3.13	40
JB-25	5.00	7.89			1403	0.325×10^6	3.24	37
JB-26	5.00	8.19			1398	0.360×10^6	3.26	39
JB-27	5.00	8.04			1399	0.326×10^6	3.15	31
JB-28	5.00	7.88	15.0	5.0	1410	0.328×10^6	3.26	44
JB-29	5.00	8.11			1407	0.342×10^6	3.13	41
JB-30	5.00	8.05			1403	0.353×10^6	3.13	40
JB-31	5.00	7.89			1402	0.347×10^6	3.26	46
JC-1	5.00	7.78			1337	0.393×10^6	3.22	3
JC-2	5.00	8.00			1333	0.460×10^6	3.17	26
JC-3	5.00	7.83			1324	0.441×10^6	3.15	17
JC-4	5.00	7.97			1320	0.431×10^6	3.15	12
JC-5	5.00	8.10			1317	0.469×10^6	3.17	30
JC-6	5.00	7.81	15.0	5.0	1318	0.393×10^6	3.15	-3
JC-7	5.00	7.86			1313	0.385×10^6	3.17	-14
JC-8	5.00	7.93			1310	0.502×10^6	3.15	43
JC-9	5.00	7.92			1308	0.511×10^6	3.13	44
JC-10	5.00	7.91	15.0	5.0	1313	0.503×10^6	3.11	48
JC-11	5.00	8.00			1308	0.539×10^6	3.17	60
JC-12	5.00	7.83			1304	0.520×10^6	3.20	49
JC-13	5.00	7.92			1304	0.518×10^6	3.20	40
JC-14	5.00	7.98	10.0	18 hr	1217	0.758×10^6	3.20	95

(continued)

TABLE 1

SODIUM LIQUID SUPERHEAT TEST RESULTS
(Sheet 2 of 3)

Run No.	Condenser (psia)	Test Section (psia)	Maximum Test Section (psia)	Time at Maximum Pressure (min)	Inlet Temperature (°F)	Heat Flux (Btu/hr-ft^2)	Flow (ft/sec)	Bulk Superheat (°F)
JC-15	5.00	7.74			1214	0.588×10^6	3.20	0
JC-16	5.00	8.11			1216	0.661×10^6	3.15	34
JC-17	5.00	7.98			1218	0.552×10^6	3.11	-30
JC-18	5.00	7.61			1223	0.676×10^6	3.11	57
JC-19	5.00	7.76			1223	0.627×10^6	3.20	12
JC-20	5.00	7.40	15.0	5.0	1216	0.740×10^6	3.20	66
JC-21	5.00	6.39			1210	0.688×10^6	3.20	72
JC-22	5.00	8.47			1209	0.763×10^6	3.22	68
JC-23	5.00	7.72			1211	0.593×10^6	3.15	-18
JC-24	5.00	6.45	15.0	5.0	1212	0.505×10^6	3.26	-33
JC-25	5.00	7.93			1207	0.680×10^6	3.22	11
JC-26	5.00	7.86			1204	0.629×10^6	3.22	-14
JC-27	5.00	7.80			1207	0.654×10^6	3.24	-2
JC-28	5.00	7.95	15.0	5.0	1212	0.790×10^6	3.24	90
JC-29	5.00	7.95			1208	0.739×10^6	3.13	56
JC-30	5.00	7.92			1209	0.711×10^6	3.20	38
JC-31	5.00	7.89			1212	0.731×10^6	3.22	53
JD-1	5.00	5.45			1137	0.813×10^6	3.20	8
JD-2	5.00	5.09			1138	0.792×10^6	3.20	59
JD-3	5.00	5.08			1148	0.727×10^6	3.24	30
JD-4	5.00	4.98			1149	0.588×10^6	3.20	-24
JD-5	5.00	5.13	15.0	5.0	1158	0.716×10^6	3.20	36
JD-6	5.00	5.05			1148	0.807×10^6	3.17	78
JD-7	5.00	5.26			1146	0.716×10^6	3.17	21
JD-8	5.00	4.95			1147	0.705×10^6	3.15	24
JD-9	5.00	4.86	15.0	5.0	1140	0.752×10^6	3.20	37
JD-10	5.00	5.10			1229	0.520×10^6	3.17	2
JD-11	5.00	5.03			1229	0.438×10^6	3.17	-9
JD-12	5.00	5.12			1232	0.551×10^6	3.20	27
JD-13	5.00	5.19			1294	0.381×10^6	3.15	15
JD-14	5.00	5.15			1291	0.388×10^6	3.17	18
JD-15	5.00	5.06	15.0	5.0	1291	0.378×10^6	3.20	19
JD-16	5.00	5.06			1285	0.394×10^6	3.15	20
JD-17	5.00	5.10			1287	0.359×10^6	3.22	2
K-1	5.00	11.34	15.0	3.0	1308	0.485×10^6	3.00	15
K-2	5.00	9.63	12.0	3.0	1305	0.496×10^6	3.28	20
K-3	5.00	8.07	12.0	3.0	1302	0.537×10^6	3.39	62
K-4	5.00	8.35	10.0	3.0	1300	0.496×10^6	3.39	50
K-5	5.00	9.65	10.0	3.0	1302	0.538×10^6	3.20	36
K-6	5.00	9.45	10.0	3.0	1308	0.538×10^6	3.17	44
K-7	5.00	10.00	11.0	3.0	1312	0.539×10^6	3.17	21
K-8	5.00	9.75	11.0	3.0	1315	0.542×10^6	3.20	36
K-9	5.00	9.70	11.0	3.0	1311	0.538×10^6	3.20	36
K-10	5.00	9.50	10.0	3.0	1306	0.536×10^6	3.22	33

(continued)

TABLE 1

SODIUM LIQUID SUPERHEAT TEST RESULTS
(Sheet 3 of 3)

Run No.	Condenser (psia)	Test Section (psia)	Maximum Test Section (psia)	Time at Maximum Pressure (min)	Inlet Temperature (°F)	Heat Flux (Btu/hr/ft^2)	Flow (ft/sec)	Bulk Superheat (°F)
K-11	5.00	8.40	10.0	3.0	1305	0.541×10^6	3.20	56
K-12	5.00	9.62	10.0	3.0	1302	0.536×10^6	3.17	29
K-13	5.00	9.30	10.0	3.0	1300	0.548×10^6	3.20	40
K-14	5.00	8.28	10.0	3.0	1302	0.538×10^6	3.24	33
K-15	5.00	8.29	10.0	3.0	1302	0.536×10^6	3.22	31
K-16	5.00	7.05	10.0	3.0	1304	0.536×10^6	3.30	79
K-17	5.00	8.79	10.0	3.0	1304	0.540×10^6	3.26	44
K-18	5.00	10.73	11.0	3.0	1215	0.719×10^6	3.24	25
K-19	5.00	9.00	11.0	3.0	1213	0.712×10^6	3.34	39
K-20	5.00	8.78	12.0	3.0	1214	0.721×10^6	3.26	47
K-21	5.00	7.91	13.0	3.0	1219	0.728×10^6	3.34	75
K-22	5.00	8.70	12.0	3.0	1221	0.730×10^6	3.28	59
K-23	5.00	7.88	12.0	3.0	1225	0.731×10^6	3.34	76
K-24	5.00	7.70	12.0	3.0	1226	0.731×10^6	3.37	80
K-25	5.00	9.12	12.0	3.0	1225	0.741×10^6	3.30	56
K-26	5.00	8.22	11.0	3.0	1219	0.745×10^6	3.30	74
K-27	5.00	10.06	12.0	3.0	1217	0.738×10^6	3.26	-2
K-28	5.00	9.70	13.0	3.0	1218	0.759×10^6	3.30	45
K-29	5.00	10.18	12.0	3.0	1216	0.683×10^6	3.26	-27
K-30	5.00	11.27	12.0	3.0	1216	0.743×10^6	3.28	-12
K-31	5.00	10.46	12.0	3.0	1216	0.719×10^6	3.24	-7
K-32	5.00	12.45	12.0	3.0	1216	0.766×10^6	3.15	-9
K-33	5.00	11.19	12.0	3.0	1214	0.729×10^6	3.11	31
K-34	5.00	10.35	16.0	3.0	1213	0.737×10^6	3.28	26
K-35	5.00	9.54	12.0	3.0	1215	0.737×10^6	3.29	54
K-36	5.00	9.89	12.0	3.0	1218	0.740×10^6	3.30	48
K-37	5.00	9.30	12.0	3.0	1222	0.739×10^6	3.24	73
K-38	5.00	6.84	11.0	3.0	1230	0.538×10^6	3.28	22
K-39	5.00	6.69	10.0	3.0	1225	0.541×10^6	3.37	25
K-40	5.00	5.85	10.0	3.0	1227	0.550×10^6	3.30	44
K-41	5.00	6.41	8.0	3.0	1226	0.547×10^6	3.37	34
K-42	5.00	6.56	8.0	3.0	1219	0.546×10^6	3.37	21
L-1	5.00	10.71	12.0	3.0	1157	0.429×10^6	3.07	-21
L-2	8.00	7.93			1168	0.398×10^6	3.26	21
L-3	8.00	7.94			1162	0.402×10^6	3.24	10
L-4	8.00	8.04			1162	0.402×10^6	3.24	3
L-5	8.00	7.99			1163	0.424×10^6	3.26	47
L-6	8.00	8.00			1168	0.393×10^6	3.24	29
L-7	8.00	8.00			1165	0.382×10^6	3.26	-4
L-8	8.00	8.00			1164	0.363×10^6	3.22	-6
L-9	8.00	7.79			1162	0.408×10^6	3.22	25
L-10	8.00	8.04			1163	0.412×10^6	3.20	30

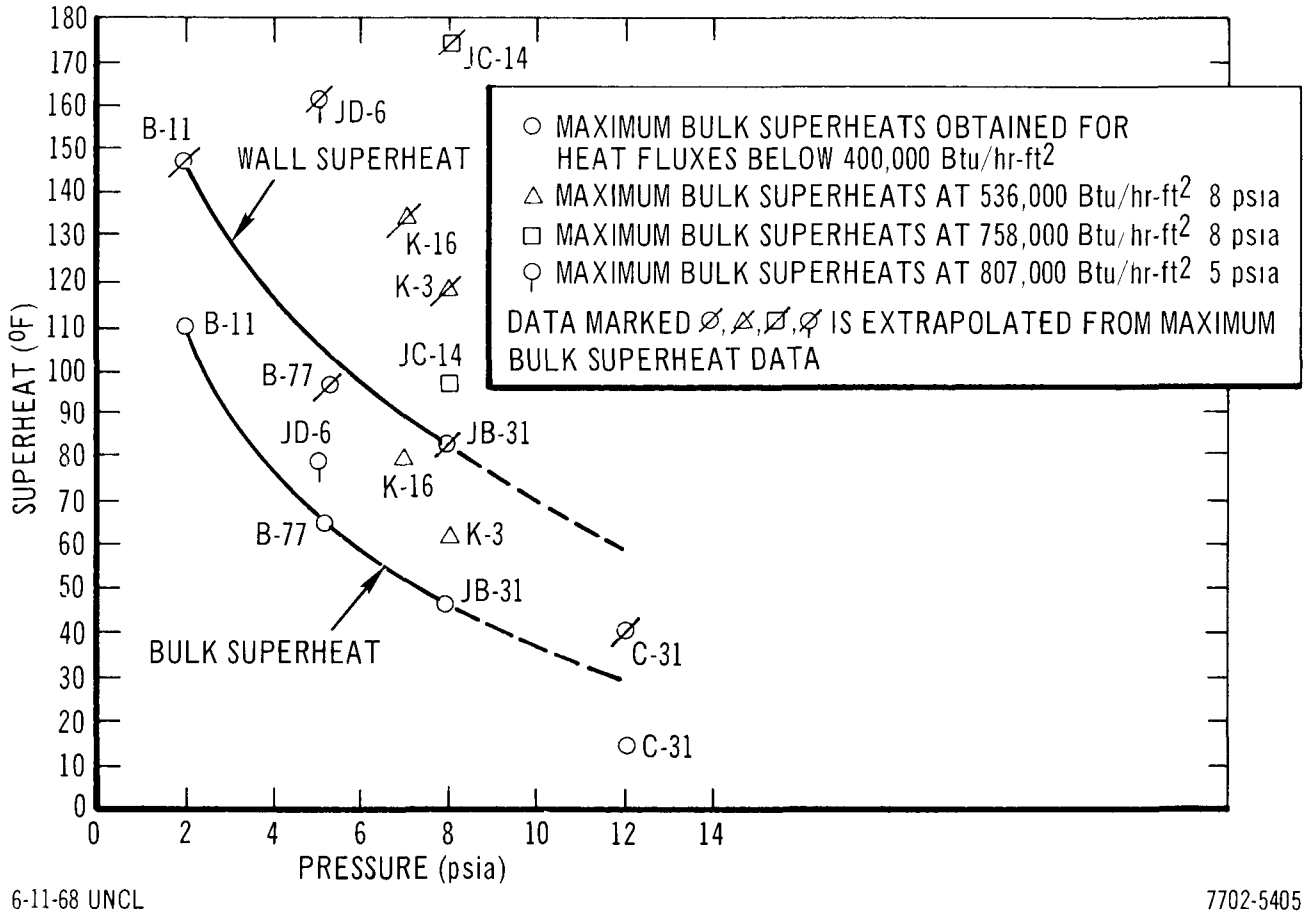

Figure 1. Maximum Measured Superheats vs Pressure

exceptions, the experimental data prior to the last quarter of FY 1968 were taken at heat fluxes of less than 400,000 Btu/hr-ft^2. Probably because of the random nature of incipient boiling, as demonstrated by a histogram (AI-AEC-12638, page 74) of superheat data as obtained from identically controlled parameters which showed the scatter to have a bell-shaped distribution,* those few experimental points with high heat fluxes did not indicate any heat flux dependence. The experimental work performed during the last quarter of FY 1968, however, was planned so as to examine heat flux effects principally at 8 psia. This was done when using Test Method 1 (increasing heat flux to produce boiling) by reducing the inlet temperature (increasing inlet subcooling), thus forcing the

*Similar distributions have been found by K. H. Spiller, et al, "Superheating and Single Bubble Ejection in the Vaporization of Stagnating Liquid Metal," ATOMkern Energie, 12, 111-114, (1967); Translated in AERE-Trans-1078 (1967)

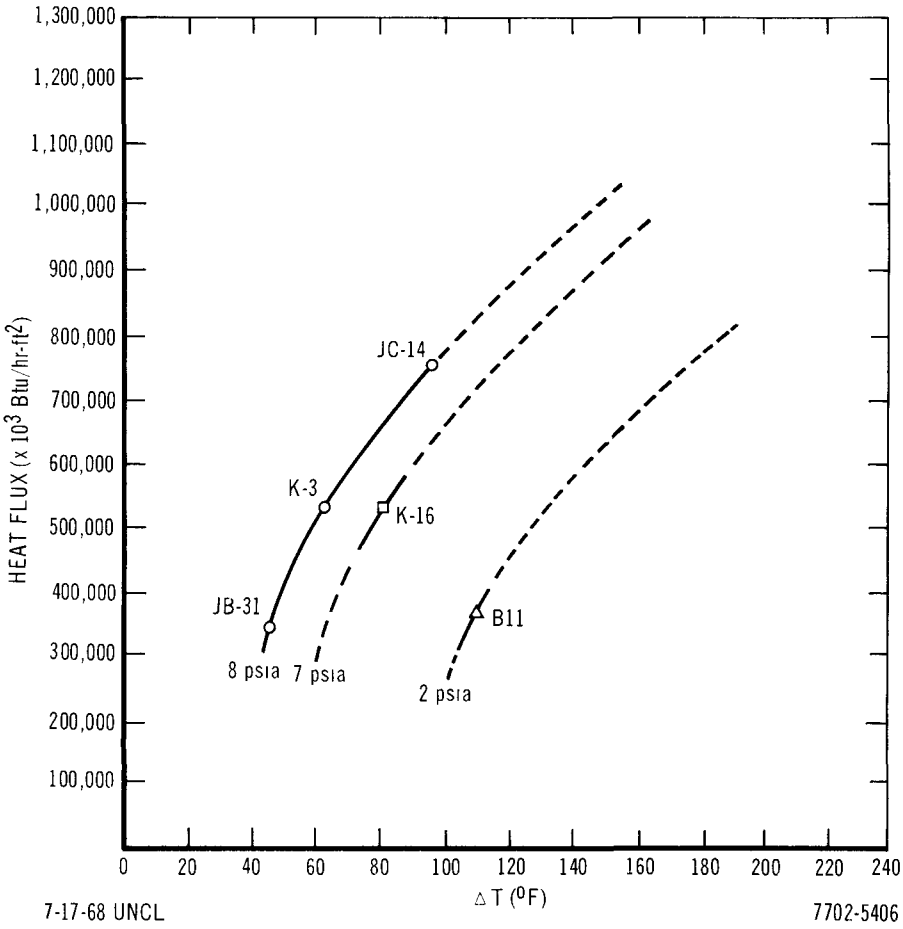

Figure 2. Heat Flux vs Single Channel Maximum Bulk Superheat

heater to a higher total heat output; i.e., higher heat flux, to heat the sodium to saturation temperature and when using Test Method 2 (decreasing pressure to produce boiling) by simply setting the heat flux to a high value. The maximum measured bulk superheats as obtained by both methods are given in Table 2. With the high heat fluxes examined at 8 psia, the experiments show an increase in the maximum measured bulk superheat of 51°F (run JC-14) or from 44 to 95°F and an increase in the wall superheat of 71°F or from 102 to 173°F. The curves of Figure 2 show that both wall and bulk superheats increase linearly with heat flux; i.e., a doubling of heat flux results in a doubling of superheat. This

TABLE 2

MAXIMUM BULK SUPERHEAT DATA

Run No.	Heat Flux (Btu/hr-ft^2)	Pressure (psia)	Maximum Bulk Superheat (°F)	Test Method
JB-31	347,000	7.89	46	1
K-3	537,000	8.07	62	2
K-16	536,000	7.05	79	2
JC-11	539,000	8.00	60	1
K-24	731,000	7.70	80	2
JC-14	758,000	7.98	95	1
JD-6*	807,000	5.05	78	1
B-11	370,000	1.91	109	1
B-77	310,000	5.23	64	1
C-31	250,000	12.00	14	1

*It is estimated, using the general shape of the curves in Figure 1, that the maximum bulk superheat that will be obtained, when several runs have been made, will be ~130°F.

effect is anticipated strictly on the basis of heat balance. The reduction in superheat with pressure is noted as expected; a reduction in bulk superheat has been noted previously with increasing coolant velocity. A few high heat flux runs were made at pressures other than 8 psia; however, they are again inconclusive, probably because of the randomness of incipient boiling.

Superheating is greatly influenced by phenomena which are not normally controlled nor readily measured. For example, the K1 to K17 runs were made by using Testing Method 2 at heat fluxes of approximately 540,000 Btu/hr-ft^2. The superheating that was obtained had a random scatter from 15 to 79°F bulk superheat. Runs K18 to K32 were made two days later, again using Testing Method 2 at heat fluxes of approximately 740,000 Btu/hr-ft^2. The superheating that was obtained had a random scatter from 25 to 80°F bulk superheat for the first 9 runs; and then, without any variation in test method or change in controllable parameters, the superheating dropped to -2°F bulk superheat, attempted to return on the next run to the normal scatter range with a 45°F bulk

superheat, then dropped to negative bulk superheats for all following runs. The heater was left for the next 12 days in the flowing sodium in the loop at a sodium temperature of approximately 700°F. Ten additional runs, K33-42, were then made with control parameters as close as possible to those of runs K1-32. The random superheat scatter was back to normal with a range of 21 to 73°F bulk superheat. Whatever phenomenon had occurred with runs K27 to 32 had ceased to exist during the 700°F storage for the 12-day interim between tests.

B. HEATER DEVELOPMENT

Successful development of a 15-in. long by 1/4-in. OD heater was made in FY 1967 with additional improvements made throughout FY 1968. Two of the more important improvements were: (1) development of a method for spring loading the boron nitride insulator sleeves so that gaps are prevented from occurring between the sleeves due to thermal expansion difference and ratcheting of sleeves during repeated thermal expansion transients, and (2) use of a rhenium wafer inserted at the molybdenum-graphite interface and has eliminated pitting and any visually observable deterioration of this joint.

A 30-in. long by 1/4-in. OD stainless steel sheath, constant heat flux heater has also been developed. The heat flux capabilities of the 30-in. heater are not known as an adequate power supply is not available for testing beyond 39 kw total power. The heater has, however, been tested to 812,000 Btu/hr-ft^2 in sodium at an exit temperature of 1335°F. The heater has been at fluxes in excess of 700,000 Btu/hr-ft^2 several times with the sodium exit temperature over 1200°F; also, it has been used for the superheat runs L1-10 in this report. It has over 35 min of transient operating time and is still operational. The successful heater was made possible by a development improvement which allowed the previously limiting voltage ($\sim$150) to be exceeded. (The operating voltage at the 812,000 Btu/hr-ft^2 heat flux level was 195 volts.)

A 36-in. long by 1/4-in. OD stainless steel sheathed, shaped heat flux heater has also been developed. This development will lead to heaters with chopped cosine axial heat flux distributions similar to the distribution in LMFBR fuel pins. Again, the maximum heat flux capabilities of the 36-in. shaped heat flux heater is not known, as adequate power was not available for testing. The center 11 in. was at a heat flux of 722,000 Btu/hr-ft^2 in sodium at an exit temperature of 1345°F. The upper 12-1/2 in. was at a heat flux of 625,000 Btu/hr-ft^2.

The bottom 12-1/2 in. was composed of two types of graphite; a 7-1/2-in. piece next to the center 11-in. section, which had a heat flux of 625,000 Btu/hr-ft^2; and a 5-in. piece at the tip, which had a heat flux of 475,000 Btu/hr-ft^2. The maximum operating voltage imposed on the heater was 202 volts. The heater has 15 min of operating time and is still operational.

C. INSTRUMENT IMPROVEMENT

Incipient boiling detection has been greatly improved by a development combining both an EM flowmeter detection system and an acoustic detection system modified to operate from an integrated signal to eliminate shutdown from spurious extraneous noises.

The major instrumentation outputs have been tied directly into the Santa Susana data reduction center. The data is read out in engineering units on equipment that has traceable calibration back to NBS standards. Up to 25 inputs can be connected at any one time. The data is presently being read on a line printer at the rate of 4 channels per second. The more important data is connected to several of the 25 input channels allowing a higher rate of scan. The scan time can be changed to 8 channels per second by recording on magnetic tape; however, the higher scan rate has not been required yet.

D. THEORY: TRANSFUGUE IIa DEVELOPMENT

A topical report, NAA-SR-12503, describing TRANSFUGUE IIa, its use, and a hypothetical LMFBR accident (loss-of-pressure) solution was published March 15, 1968.

The code was developed to analyze a single heating element (fuel pin) in an annular flow channel corresponding to the present experimental test section. Within this restriction, any axial variance may be accounted for. In addition, the heat generating element is represented by three cylindrical coaxial shells in each axial node. The code can analyze any heat transfer and fluid flow condition in the turbulent flow regime.

Code development has continued since publication of the topical report. The code presently accounts for variable heat transfer and friction factor coefficients for the all-liquid metal and two-phase flow regime. The code can also extend a transient into the dry vapor condition (superheated), although at present

this portion of the code is not completely checked out. At present, the code is being modified to handle convergent and divergent flow within a node.

E. THEORY: CODE CONVERSION

In order to provide a method for analyzing two-phase flow behavior in interconnected flow channels (such as those existing in the LMFBR) in the event of an accident in which the sodium coolant boils, two codes which were originally developed for steam have been converted for use with sodium. The two-phase sodium characteristics, void fraction, and friction multipliers, were obtained from general correlations[1,2] which have shown good correspondence with a very wide range of data. As used in the codes, the two-phase characteristics encompass the following ranges: boiling temperature, 1600 to 2000°F; quality, 0 to 10%; and mass velocity, 0.25×10^6 to 3×10^6 lb/hr-ft^2.

a. SODIFAZE

The steady state, multichannel boiling steam code[3] was converted to use with sodium and, in this form, is known as SODIFAZE.

A typical set of results is shown in Figure 3 for three geometrically identical laterally interconnected vertical channels, numbered 1, 2, and 3, for which the heat inputs are 16,000, 13,000, and 10,000 Btu/hr-ft, respectively. The total flow rate is constant, and crossflow between channels takes place in the two-phase region. The boiling temperature is 1800°F with 200°F subcooling at the entrance to the heated section.

Figure 3 shows the variation of pressure with length. It can be seen that the pressure gradient successively increases as each of the three channels attains boiling conditions. The variation of flow rate with length, for each of the channels, is also shown. As a result of having the greatest heat input, Channel 1 attains boiling first with an attendant, large reduction in its flow rate and a corresponding increase in the flow rates of Channels 2 and 3. A similar condition occurs when Channel 2 boils (length = 1.75 ft) and Channel 3 boils (length = 2.25 ft). Once all three channels are boiling, the flow rates become constant. Quality and void fraction, as a function of length, are shown for each of the three channels. As expected, Channel 1 has the highest quality and greatest void fraction at any given location in the boiling region. The extremely rapid increase of void fraction with quality is shown for Channel 1 where, at the

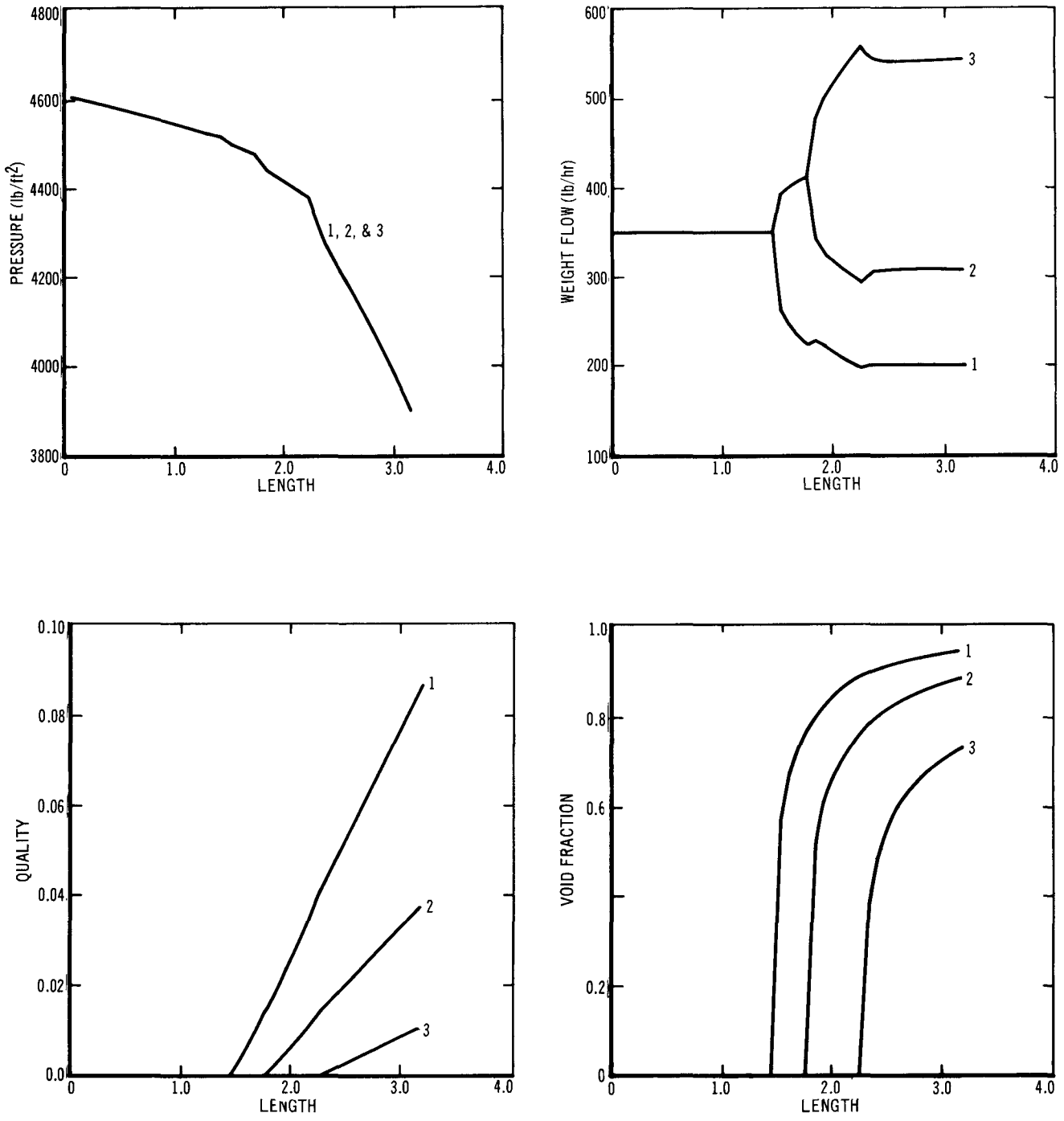

9-28-67 UNCL

7702-5403A

Figure 3. Pressure Drop, Flow, Quality, and Void Fraction for Sodium Boiling in Three Interconnected Channels

initiation of boiling (quality = 0.003), the void fraction is already equal to 0.57. While this characteristic is most pronounced for sodium, similar behavior would be expected for other alkali liquid metals at the same reduced temperature (same value of property index).

By using the results of a series of runs similar to that described above, pressure drop as a function of flow rate, at fixed heat inputs, was determined and is shown as the middle curve (three channels) in Figure 4. Note that in contrast to the typical check curves for single channels (Channel 1 or 3 alone), in which the pressure drop rises rapidly with reduced flow rate as soon as the two-phase region is entered, the three-channel curve shows a broad, essentially constant pressure drop region during the period when each of the channels is successively attaining boiling. Only when the last channel achieves boiling, does the pressure drop rise rapidly. The unusual, flat region may be of importance in the evaluation of average core void fraction.

To verify the unusual check curve (pressure drop vs flow rate at constant power) previously indicated (Figure 4) for three interconnected channels, additional runs were made with the SODIFAZE code. Moreover, a second check curve, for channel heat inputs different from those of the first case, was calculated and was shown to have characteristics similar to those of the first case. The check curves are shown in Figure 5; Curve A has a hot-to-cold-channel heat input ratio of 1.6 and Curve B, a ratio of 1.2. In each case, the heat input to the hot channel is identical. Both curves show similar characteristics in that a small increase in pressure drop occurs, as a channel attains boiling; then, as flow is decreased, the pressure drop decreases slightly until the next channel starts boiling. Because of the higher heat input for Curve B, Channels 2 and 3 start boiling at higher flow rates than in the case of Curve A. As a result, the flow rate span over which the three channels achieve boiling conditions and the attendant essentially constant pressure drop region, is less for Curve B than for Curve A. Each curve shows the steeply rising pressure drop characteristic typical of a single channel, only when all three channels have reached boiling conditions.

b. TRANSODIFAZE

A transient multichannel boiling code[4] was converted for use with sodium by incorporating the two-phase characteristics previously described. In this

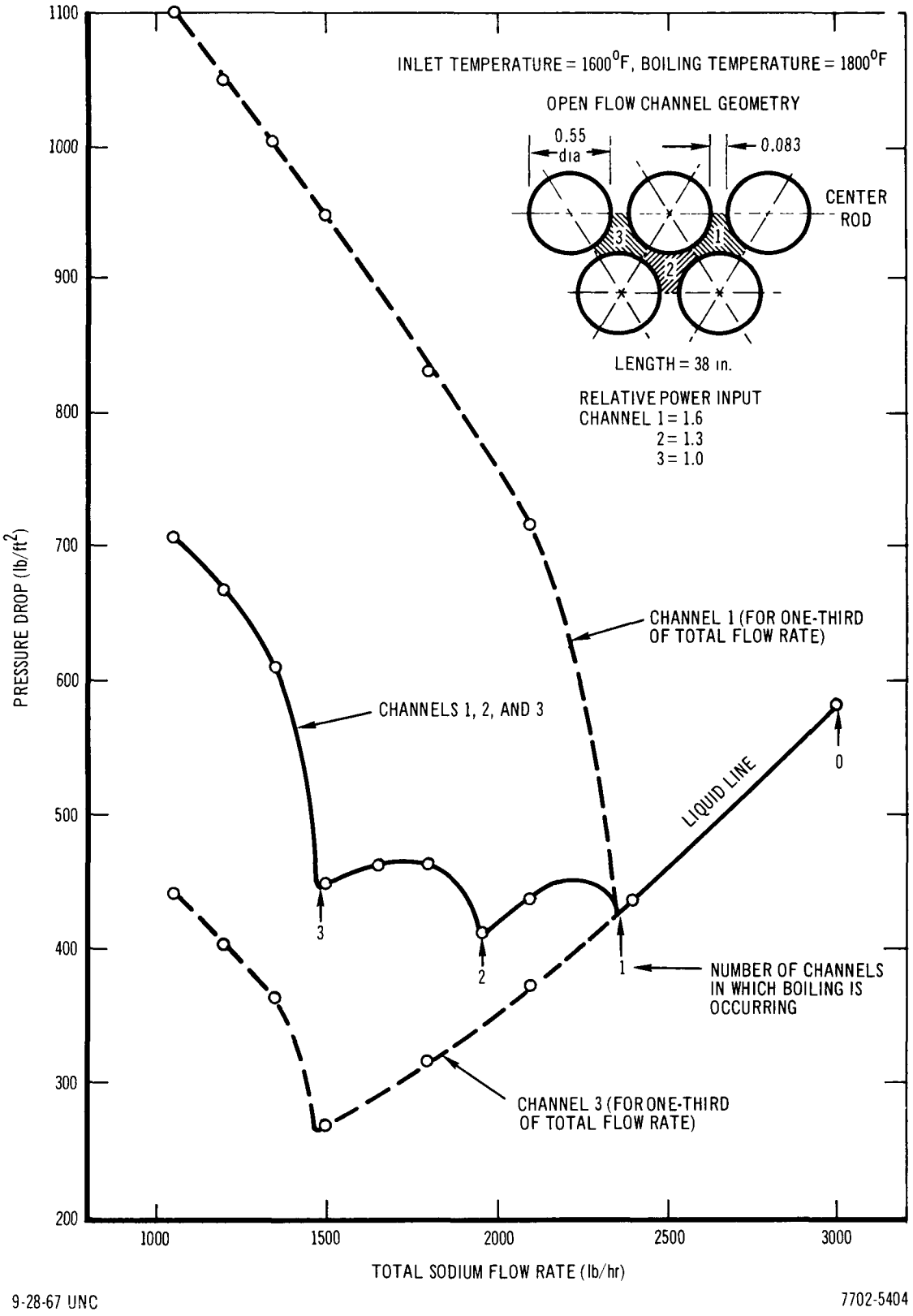

Figure 4. Pressure Drop vs Flow Rate for Three Interstices (channels) with Fixed Power Input

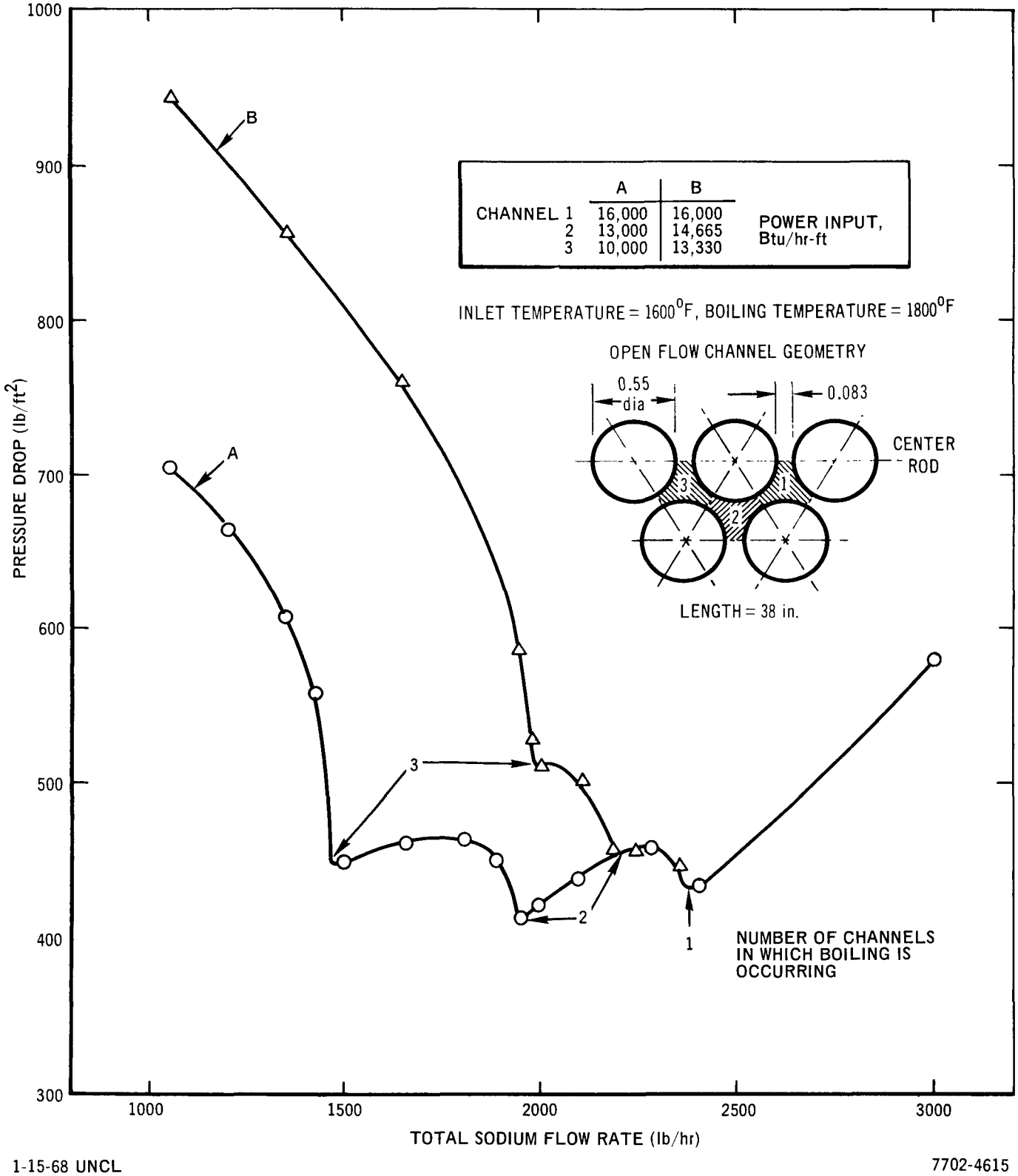

Figure 5. Pressure Drop vs Flow Rate for Three Interstices

form, the code is known as TRANSODIFAZE. To check out this code, comparison was made with a steady state case previously computed by SODIFAZE; Figure 6 shows the steady state results of TRANSODIFAZE and the previously shown results (Curve A, Figure 5) from SODIFAZE. It can be seen that both codes produce unique check curves which are very similar. The greatest difference, about 23% in pressure drop, occurs at the lowest flow rate when all three channels are boiling. This discrepancy is believed to stem from the different methods employed by each code to evaluate the quality of crossflow, and results in a lessening of the mixture quality differences between channels in the case of TRANSODIFAZE. This, in turn, produces a smaller pressure drop.

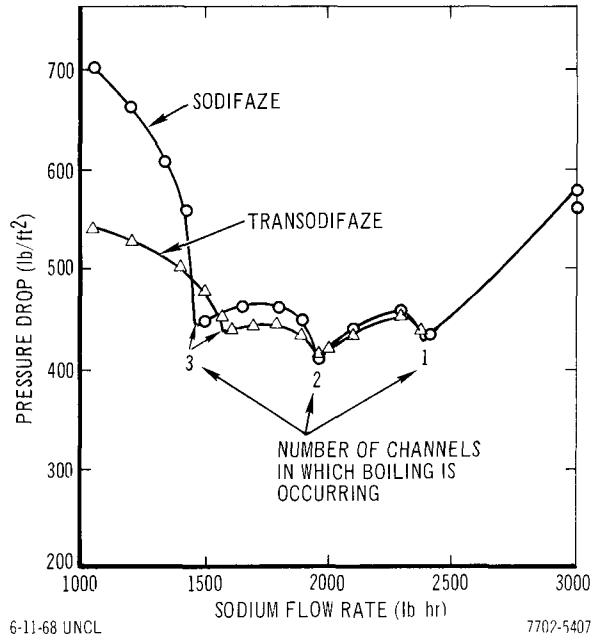

Figure 6. Comparison of Pressure-Drop Flow Results from Two Codes

III. EVALUATION OF EFFORT DURING FISCAL YEAR 1968

Overall progress in both the experimental and analytical phase of the project is considered excellent. Major accomplishments for the year include: (1) completion of 276 transient liquid superheat tests, (2) improvement of an in-performance proven 15-in. heater (485 tests have been made with 5-15-in. heaters and Heater B was still operational after 170 tests when it was retired for

surface examinations, and Heater K is operational with additional testing scheduled as soon as its surface has been refinished), (3) successful developments and improvements in fabrication techniques have apparently solved the voltage breakdown problem allowing successful test of two long stainless steel sheathed heaters, a constant heat flux 30-in. long by 1/4-in. OD heater, and a shaped heat flux 36-in. long by 1/4-in. OD heater, (4) improvements in data acquisition (direct tie-up of instrumentation with the data reduction center and improvements in the boiling detector), (5) development and documentation of TRANSFUGUE IIa, a single channel two-phase transient code for use with sodium, (6) conversion and checkout of two steam codes for use with sodium (SODIFAZE — a steady state two-phase multichannel code and TRANSODIFAZE — a transient two-phase multichannel code). Both codes show that the pressure drop-flow curve, at constant heat input, for a group of three interconnected channels is markedly different from that of a single channel operating alone. Experimental verification of this unusual pressure-drop flow characteristic for a group of flow channels is indicated, since it is clear that this characteristic will reduce the maximum superheat from that observed in studies of single channels.

REFERENCES

1. C. J. Baroczy, "Correlation of Liquid Fraction in Two-Phase Flow with Application to Liquid Metals," Chemical Engineering Progress Symposium Series, No. 57, Vol 61 (1965)

2. C. J. Baroczy, "A Systematic Correlation for Two-Phase Pressure Drop," Chemical Engineering Progress Symposium Series, No. 64, Vol 62 (1966)

3. D. E. Schramm and R. F. Berland, "A Multi-Channel, Two-Dimensional, Two-Phase Flow Model and IBM 7090 Code," NAA-SR-9444, December 31, 1963

4. L. R. Steele and R. F. Berland, "A Transient Multichannel Two-Phase Hydraulic Code," NAA-SR-9425, December 1, 1964

PAGE 148 is blank

Program:	Liquid Metal Fast Breeder Reactor Technology			
AEC Task:	8, Sodium Reactor Experiment			
Project Manager:	C. W. Wheelock			
Reporting Period:	Fiscal Year 1968			
General Order:	7704	Subaccount:	All	AEC Category: 04-01-61-07, 3

Project Engineer: W. C. Sturtevant

I. PROJECT OBJECTIVES

In April 1967, plan TI-599-19-001 was approved for the deactivation of the SRE facility to a "store-in-place" condition so that components would not be damaged and costs would be minimized during an undefined period of storage.

In September 1967, direction was received to prepare plans to dispose of the plant, render the site safe from hazards, protect equipment until transferred, and dispose of unsalvageable scrap. Components were to be made available to other AEC programs, with priority to LMEC, FFTF, EBR-II, ZPPR, and AARR. Prior to receipt of this directive, the plant was being prepared to be "stored-in-place".

II. TECHNICAL PROGRESS DURING FISCAL YEAR 1968

Four alternate plans for plant disposition were prepared and submitted as Engineering Document TI-599-19-101. Later, a less extensive plan was written and submitted to AEC, on November 17, 1967. The plan described in TI-599-19-003 defines the activities and schedule for deactivating SRE so that its final disposal can be carried out at a later date. This plan was approved and deactivation proceeded accordingly.

The sodium in the heat transfer systems was drained to hold tanks. The secondary sodium was drained to 55-gallon drums and stored. The reactor and all sodium systems were cooled to ambient, and shift operation was terminated. Deactivation of the kerosene cooling systems, sodium systems, inert gas systems, R/A liquid and gaseous waste systems, hot cells, contaminated support facilities, component handling machines, and core components was completed and responsibility for surveillance was transferred from Nuclear Operations to Facilities and Industrial Engineering.

The unirradiated SRE Core III fuel was moved to fuel storage building 064 and responsibility for it was transferred to Nuclear Materials and Waste Management.

III. EVALUATION OF EFFORT DURING FISCAL YEAR 1968

During July and August, operation of the sodium heat transfer systems, at 350°F was maintained. Sodium circulation was terminated in August 1967 after an elapsed time of 21,477 hours since initiation in May 1965. The sodium systems were drained to hold tanks, per deactivation procedure PR-599-31-001. Operating time for various system components since completion of the SRE-PEP modifications to the plant is as follows.

System Component(s)	Operating Time (hr)	
	Primary Systems	Secondary Systems
Main Pumps, total	17,582	11,442
Auxiliary Pumps, total	15,241	17,881
Main Pumps, @> 690°F	2,141	1,645
Auxiliary Pumps, @> 690°F	2,245	2,253
Hot Traps	7,105	994
Cold Traps	5,629	3,912
	Critical	At Power
Reactor	0	0

Upon completion of draining the secondary sodium to 55 gallon drums for storage, the reactor and heat transfer systems were cooled to ambient. The secondary hold tank contains approximately a 5 to 15 ft^3 heel of clean sodium which could not be drained.

Temperature controllers, recorders, and one EM pump for the primary hold tank have not been removed because of possible use during final plant disposition. The primary tank is filled with 1000 ft^3 of frozen sodium containing low level contamination (3×10^{-3} μ Ci/cm^3. Responsibility for the sodium systems was transferred from Nuclear Operations to Facilities and Industrial Engineering.

The inert gas systems deactivation was completed and responsibility was transferred to Facilities and Industril Enginnering per deactivation procedure PR-599-69-001. The two SRE inert gas systems normally supplied helium to

the sodium systems and nitrogen to the kerosene systems; both systems will remain in service to provide cover gas for the sodium and kerosene systems. Corrosion in these systems will thus be limited. To reduce the cost of make-up gas, the helium system was converted to nitrogen.

Under the "stored-in-place" objective, NaK bubblers were installed in series in the inert system supply line. These were to remove trace amounts of oxygen and water from the supply gas in order to minimize corrosion damage to the sodium systems during an extended period of storage. Until January 1968, the bubblers functioned normally. Plugging then occurred intermittenly in the upstream unit. This continued until the sparger holes were cleared by heating the bubler to $\sim$ 180°F and rapping it sharply with a mallet. Because plant re-start capability then no longer was a requirement, the bubblers were removed from service in order to reduce surveillance costs.

Deactivation of the R/A liquid and gaseous waste systems has been completed per deactivation procedures PR-599-63-001 and PR-599-63-002, and responsibility has been transferred to Facilities and Industrial Engineering.

In deactivating the R/A liquid waste system, the fuel wash cells were flushed with a solution of sodium dichromate. This was done to inhibit corrosion in the black iron portions of the system. The R/A sump tanks were then drained and the liquid was shipped for disposal.

The system for treating the wash cell effluent contained fission and activated corrosion products which resulted in radiation levels ranging from 40 to 100 mr/hr at the exterior of the piping and components. This source of contamination was easily removed because the system was constructed as a package on a steel pallet. Unions connecting the system to the R/A liquid and gaseous waste systems, kerosene system, and the water and steam supplies were disconnected. The pallet was lifted from its pit, and after capping all lines, the system was boxed and shipped for disposal.

Unirradiated core III fuel elements were removed from SRE storage cells. As required in deactivation procedure PR-599-28-001, the fuel bundles were separated from hanger-rod/shield-plug-assemblies, decontaminated to less than 100 d/m-cm^2, doubly encapsulated in plastic, and stored in the New Fuel Storage Vault (Bldg. 064). This action completed removal of all fuel from the

SRE. Except for the Core III hanger-rod/shield-plug-assemblies, which are relatively free of radioactive contamination, all components were removed from the SRE fuel, moderator, and pump storage cells. Particulates were removed from the cells by using a 7.5 hp industrial vacuum cleaner with roughing and absolute filters. During the operation, the radioactive level at the collection pot increased from 25 to 500 mr/hr. After completion, the vacuum was decontaminated to less than 25 mr/hr. A contamination survey of the cells was completed in accordance with directives received in CPAO letter CP-68-6145; the results are included in a final report, NAA-SR-12572, "Retirement of SRE," to be published in July 1968. Contaminated Support Facilities final survey data also are included in this report.

Components removed from the storage cells will not be useful in the ultimate disposal of the SRE. These components were placed in two oil bath tanks which were removed from the sodium cleaning facility. Because decontamination of the tanks would be prohibitive, they were boxed for disposal as R/A waste.

Deactivation of the sodium cleaning facility and other contaminated support facilities per PR-599-93-002 was completed and responsibility for them was transferred to Facilities and Industrial Engineering.

Equipment requested by AEC-RDT-designated priority groups was deleted from the SRE inventory which was then submitted by AEC-CP to other RDT contractors. The secondary sodium system pumps and expansion tanks were removed and shipped to maintain gas integrity of the pumps and the remaining sodium systems. The secondary pump motors, variable-speed couplings, and dynamic oil seal housings were removed for use with the pumps. The secondary pumps were removed with their adjoining tank as a unit by use of a mobile crane. The overhead 2-ton crane and monorail plus some structure steel were removed to provide access to the pump.

The sodium system vault and gallery nitrogen dehumidification (DH) systems also were removed and shipped to BNW for use on the FFTF program. Other SRE equipment, predominantly instrumentation, was removed and shipped to AEC-DRT designated program.

Southern California Edison Company (SCE) provided the principal heat sink for the SRE in the form of a 6-Mwe steam electrical plant. The system has been separated from the AEC-owned portion of the main secondary sodium system,

the lines have been capped, and a nitrogen atmosphere is being maintained on the systems. This now permits SCE to remove their equipment and they are examining approaches and schedules for this removal. At SCE's request, information on sodium handling and site renovation was provided for use in preparing specifications for this effort.

Consolidation of the SRE records including: prints, bibliographies, log books, manuals, monthly progress reports, weekly reports, plant data sheets, test procedures, photographs, slides, movies, technical information, administrative information, and correspondence was completed.

III. EVALUATION OF EFFORT DURING FISCAL YEAR 1968

Deactivation of the SRE for "storage-in-place" proceeded during July and August as scheduled except for some delay in draining the sodium systems due to last minute reviews of the following: (1) potential problems in cooling the reactor vessel, (2) evaluation of the feasibility of taking precooldown photographs of the inside of the reactor vessel, and (3) the need for a NaK bubbler to the inert gas supply to assure that accumulation of moisutre and/or oxygen over a long period of storage could not cause damage. Shortly after concluding that cooling the reactor vessel would not introduce serious problems, that photographs would not be taken, and that a NaK bubbler would be installed; direction was received to dispose of the plant. This change of objective necessitiated the revision of most of the specifications and procedures, and caused deactivation work to be suspended in some areas. After studying alternate plans for disposal of the plant, a plan was agreed upon in November. The remaining deactivation work was completed as planned with a gradually decreasing work force. Equipment requested by first- and second-priority AEC programs was removed during the last half of the year for less than the estimated costs. The small amount of deactivation, equipment removal work, and the publishing activities on the final report which remain to be done in GFY 1969 are at approximately the level anticipated during the planning phase.

PAGE 154 is blank

Program:	FBR Fuel Cladding and Structural Materials
AEC Task:	10-A Coolant Chemistry
Project Manager:	J. L. Ballif/J. J. Gill Principal Investigator: E. W. Murbach
Reporting Period:	Fiscal Year 1968
General Order: 7706	Subaccount: 29510 AEC Category: 04-01-61-01.1

I. TASK OBJECTIVES

The objectives of this task are to (1) define, prepare, and manage a source of stock "systems quality" sodium for the program, (2) develop sampling and transfer procedures for handling sodium without contamination, and (3) monitor the compositions of sodium and of gas atmospheres in use on all the tasks in this program; and provide a management system for insuring the use of proper procedures in sampling, transferring, and analyzing of sodium.

II. TECHNICAL PROGRESS DURING FISCAL YEAR 1968

A. SODIUM SUPPLY LOOP

The sodium supply loop was operated continuously during the year except for the shutdowns to replace oxygen meter electrodes. The first shutdown was in July 1967 to install a calibrated electrode. The electrode which had been in service broke during the shutdown and removal process so that some delay was entailed in removing the broken ceramic. The calibrated electrode broke during loop startup necessitating a second shutdown for removal of this electrode and the broken ceramic. Installation of the second calibrated electrode and startup of the loop was accomplished without further incident.

In April 1968, the calibrated oxygen meter ceased to function. The loop was shutdown and the oxygen meter electrode removed. It had apparently broken during operation. The piping in the immediate vicinity of the oxygen meter housing was cut out of the loop in order to effectively remove bits of the broken ceramic. At this time, the hot trap discharge valve which had become inoperative was also cut out of the loop and replaced with a new valve. After cleaning and reassembly, the loop was started up in order to replace sodium in the void sections; then it was shutdown briefly for installation of a new (uncalibrated) oxygen meter electrode.

No problems were encountered after either shutdown. The oxygen contamination which was introduced during the shutdown was rapidly removed by the cold trap. Plugging runs made shortly after both shutdowns did not show plugging until the freezing point of sodium was reached.

The loop was operated at a nominal temperature of 500°F with the cold trap temperature at 260°F and the hot trap temperature at 1200°F, except for a brief period when temperature coefficient studies were being carried out with the oxygen meter.

The loop operated with oxygen and carbon levels of less than 10 ppm. Measured values were generally in the range of 5-10 ppm, although the concentrations are thought to have been less than 5 ppm as the sampling and analysis techniques are uncertain below the 5 ppm level.

B. SODIUM DISPENSING

Loading of retorts for Task 10-C was continued on a routine basis. During the fiscal year, 24 biaxial type retorts were loaded (~420 gms of sodium, each) and 23 uniaxial type retorts were loaded (~125 gms of sodium, each).

Approximately five gallons of sodium were dispensed to the Sodium Chemistry Project (Task 12). This sodium contained 6 ppm carbon and 8 ppm oxygen compared to the 35 ppm carbon and the 15 ppm oxygen present in the first batch dispensed in August 1966.

The supply tank for the new fission product behavior loop was filled after connecting it to one of the dispensing stations and circulating sodium through the tank for four days.

All sodium loadings have been accomplished without difficulty. The only problem is that outgassing of the retorts is slow because the small fill tube restricts the pumping speed; however, this is only a minor inconvenience.

C. SODIUM SAMPLING

Sampling of the loops and retorts in use in the Cladding Program was continued on a routine basis. The loops were sampled with the flow-through sampler using a nickel sampling tubing and the retorts were sampled into an evacuated section of nickel tubing. No problems were encountered during sampling.

Studies on the sampling blanks initiated during the previous fiscal year were completed. The blank for the flow-through sample was measured by contacting sections of tubing with oxygen free amalgam, and determining the gain in oxygen by the amalgam. The retort sample blank was determined by sampling the supply loop with flow-through and retort samplers simultaneously. The final results were, 3.2 ± 0.8 ppm oxygen for stainless steel tubing, 2.0 ± 1.0 ppm oxygen for nickel tubing, and 7.4 ± 1.5 ppm oxygen for the retort sampler, as blank corrections.

Oxygen analyses of the retort sampler were usually in the range 5-20 ppm. There were some questions regarding the higher values, but it has been found that the atmosphere in the inert gas glove box has been deteriorating. A new circulating pump was recently installed, and the gettering units were fully regenerated so that the atmosphere in the box is now much improved.

The Task-D loop was sampled approximately weekly during operations. Oxygen and carbon analyses were both less than 10 ppm for all samples.

One set of carburization tabs was exposed to the Task-D loop sodium for 976 hours at 1200°F. After removal of the tabs, photomicrographs were prepared and microhardness traverses were taken. No evidence of carburization of the tabs was observed which indicates that the loop is operating at equilibrium conditions with reference to carbon transport.

D. OXYGEN METER STUDIES

As mentioned in Section A, a calibrated oxygen meter electrode was installed in the supply loop early in the fiscal year. It remained in operation until April 1968, at which time the ceramic apparently broke. The total operating time for this electrode was 5909 hours.

The behavior of this electrode during its period of operation is shown in the figure. It can be seen that the emf output of this electrode was quite stable. One oxygen addition was made by adding oxygen to the cover gas of the surge tank. The addition was calculated to increase the oxygen level by 25 ppm. Even though there was a shar p drop in emf, chemical analysis failed to show an increase in oxygen level.

The added oxygen was removed by cold-trapping. An interesting point which can be seen in the figure is the slow return of the emf level after the

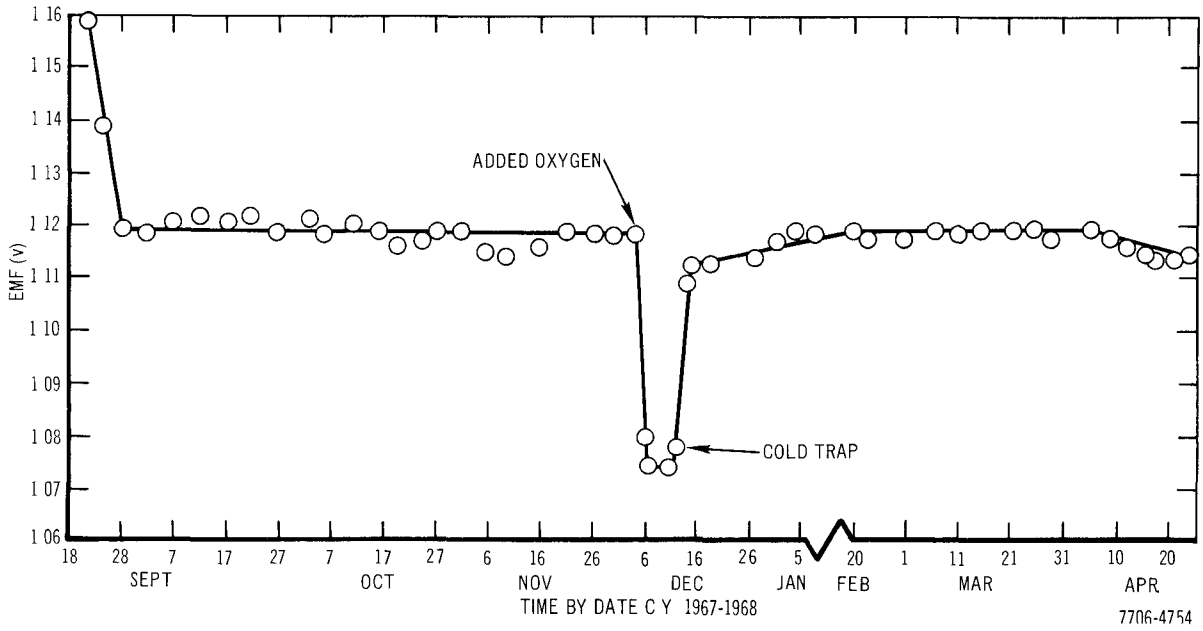

Results on Second Oxygen Meter Electrode

addition. This is another indication of the buffering of oxygen by the stainless steel. The oxygen gettered by the steel is slowly released during cold-trapping.

Another series of experiments was conducted to determine the temperature coefficient of the electrode. Both the loop and electrode temperatures were varied. The cold and hot traps were valved out of the system during these tests.

The data are divided into two groups to illustrate the temperature effects. Table 1 shows the results when the loop temperature is essentially constant and the electrode temperature is varied. Table 2 shows the results when the loop temperature was also varied.

TABLE I

OXYGEN METER OUTPUT AS A FUNCTION OF TEMPERATURE

(Constant Loop Temperature)

Temperature (°F)		Emf
Electrode	Loop	(volts)
571	524-530	1.134
551	520-522	1.132
575	521-530	1.135
527	520-521	1.131

TABLE II

OXYGEN METER OUTPUT AS A FUNCTION OF TEMPERATURE

(Loop Temperature nominally equal to Electrode Temperature)

Temperature (°F)		Emf
Electrode	Loop	(volts)
575	568-569	1.155
552	547-550	1.146
527	520-521	1.131

The data in Table 2, which were taken with the loop and the electrode at essentially the same temperature, give an apparent temperature coefficient of approximately + 0.5 mv/°F. The data in Table 1, however, for a constant loop temperature condition, show a temperature coefficient that is practically zero. It is believed, therefore, that the apparent temperature coefficient for Table 2 data is primarily caused by the temperature dependence of the stainless-steel – oxygen-sodium equilibrium. In a sodium solution saturated with oxygen, the theoretical temperature coefficient is - 0.225 mv/°F at approximately 500°F. Since these solutions are very much unsaturated, one would not necessarily expect to find a negative temperature coefficient. The reasons for this are discussed in some detail in report, AI-AEC-12700.

The new electrode installed in May stabilized within a few days, and its emf has varied between 1.170 and 1.175 volts. This is quite close to the theoretical emf vs oxygen concentration curve. Based on the Los Alamos solubility data, a 1.170 volt reading is equivalent to 3 ppm oxygen at 500°F.

E. PUBLICATIONS AND PAPERS

The report, "Sampling Blanks for the LMFBR Cladding Program," NAA-SR-12616, by E. W. Murbach, was issued January 30, 1968.

The report, "Evaluation of an Electrochemical Oxygen Meter," AI-AEC-12700, by E. W. Murbach and N. W. Heath, was issued.

The paper, "Dispensing and Sampling Sodium for the LMFBR Cladding Project," by E. W. Murbach and J. E. Bodine, was presented at the November (1967) meeting of the American Nuclear Society.

The paper, "Experience with the UNC Oxygen Meter at Atomics International," by E. W. Murbach, was presented at the AEC Oxygen Meter Working group in April (1968) in Germantown.

III. EVALUATION OF EFFORT DURING FISCAL YEAR 1968

The operation of the sodium supply loop has been quite satisfactory, and the dispensing and sampling of the sodium have been reduced to routine operations. The sodium analysis has been within specification at all times except during those periods when oxygen has deliberately been added to the loop in a test sequence.

The operation of the oxygen meters is routine, and it has been found that the amount of sampling required to confirm that the oxygen level is being maintained can be markedly reduced because of the reliability of the meter reading during steady state loop operations; however, the removal and the replacement of an oxygen meter probe is not an easy task. It usually amounts to a two-day (or more) operation, particularly if there are many pieces of broken ceramic to be removed. Our experience with the service life of an electrode is limited to the one 5900 hours' life unit. The failures of the other units is attributed to causes other than aging in service.

The oxygen addition tests have given rather definite evidence that the oxygen meter is indeed responsive to changes in oxygen content of the sodium, even though the amounts of oxygen added were not indicated by the meter emf change. It was rather clearly shown from these studies, that type 304 stainless steel exerts a strong buffering effect on the oxygen concentration in sodium. This finding is in good agreement with the results of others who have also examined the behavior of the oxygen meter.

Program: FBR Fuel Cladding & Structural Materials
AEC Task: 10-B, Materials Management
Project Manager: J. L. Ballif
Reporting Period: Fiscal Year 1968
General Order: 7706 Subaccount: 29520 AEC Category: 04-01-61-01.1

Principal Investigator: D. F. Atkins

I. PROJECT OBJECTIVES

The objectives of this task are to: (1) procure and characterize a supply of the selected material required by the program (304SS, 316SS, Incoloy-800, and Inconel-625), and (2) mange, store and issue to authorized persons, the supply of selected material.

II. TECHNICAL PROGRESS DURING FISCAL YEAR 1968

Annealed 304SS tubing and annealed 316SS tubing have been added to the supply of characterized, as-received tubing of reference heats of 304SS and 316SS. This annealed material will be used for comparison with the as-received material containing 10 to 15% cold work. Time, temperature parameter studies were performed so as to insure that the same grain size was maintained during the annealing operation. For 304SS, the annealing treatment consisted of 30 min at 1900°F in a dry hydrogen environment. The 316SS tubing was annealed at 1950°F for 30 min in the same environment.

The reference heat of Incoloy-800 was fabricated into thin-walled tubing to meet the requirements of the Program. The size and quantity of this tubing is tabulated below.

Item	Size (in.)	Amount Ordered (ft)	Amount Received (ft)
1	0.275 ID x 0.010 wall	500	474
2	0.275 ID x 0.020 wall	200	149
3	0.315 ID x 0.020 wall	100	101
4	0.210 ID x 0.008 wall	400	213
5	0.145 ID x 0.035 wall	50	57
6	0.230 ID x 0.010 wall	50	56

This tubing was from a heat in which the aluminum and titanium contents were 0.1 and 0.2%, respectively. The normal commerical composition for Incoloy-800 contains about 0.4% each of aluminum and titanium. The low Al and Ti content was selected, in cooperation with Battelle Northwest Laboratores (PNL), to reduce the aging effects associated with these two elements.

The tubing supplier experienced difficulty in meeting the specified mechanical properties and in producing a product of acceptable grain structure. The tubing mill was visited in late August, 1967 to discuss these fabrication problems. All of the six sizes ordered were found to have a duplex grain structure unsuited for the project and not in accordance with the specification. There were thin layers on both sides of the tube wall where the grain size was ASTM 9 to 10 compared to ASTM 6-1/2 to 7-1/2 grain size in the main portion of the wall. The thickness of the fine grain on the inside surface was 0.0010 to 0.0025-in.; the thickness on the outside surface was about half that on the inside. The cause of this condition was uncertain. It may be due to the small amount of contamination observed on the raw stock, nitrogen contamination in annealing, or a combination of reductions and annealing treatments employed. It was decided to chem-mill 0.003 to 0.004 in. from each surface of the redraw stock before proceeding with the drawing operations. This treatment would remove any surface contamination that might be responsible for the duplex structure.

This procedure eliminated the problem on all finished tubing except Items 2 and 4 in the table above. The 0.275-in. I. D. x 0.020-in. wall material was found to possess a small grain structure (ASTM 9) on the I. D. to a depth of 0.0006-in. The 0.210-in. O. D. x 0.008-in. wall material, requested by PNL, had this small grain structure on both the I. D. (0.0008-in. depth) and O.D. (0.0004-in. depth). The manufacturer was able to remove this fine grain structure by chemical milling the final product and still achieve the specifications for the tubing. The mechanical properties requirements had to be relaxed on all tubing sizes. It was concluded that the lower Al and Ti content was responsible for the slightly lower strength encountered with this heat.

Two-hundred feet of 0.275-in. I. D. by 0.010-in. wall Incoloy-800 tubing was purchased from a normal composition heat (0.34% Al and 0.43% Ti). This material will be used for comparison studies with the low Al + Ti reference heat. About 460 ft of pressure tubing (0.126-in. O. D. x 0.063-in. I. D.) was

also fabricated from this commerical composition heat for stress rupture retort fabrication.

Cold finished strip of 0.062-in. thickness was prepared with 11 and 38% cold work for uniaxial-creep/stress-rupture studies. This material was prepared from the reference heats of both 304SS and 316SS.

Characterized tubing (190 ft, 0.210-in. O. D. x 0.0008-in. wall) of reference heat 316SS was issued to Battelle Northwest Laboratories for development studies. A short length of tubing from both the 304SS and 316SS reference heats was supplied to Brookhaven National Laboratory for heat transfer studies in sodium.

III. EVALUATION OF EFFORT DURING FISCAL YEAR 1968

The problem of producing thin-walled tubing of uniform grain structure from the reference heat of Incoloy-800 may be related to the lack of process metallurgy technology on this material. This material has a low aluminum (0.10%) and low titanium (0.20%) content as compared to the normal commercial alloy. The apparent absence of this problem with the tubing made from the commerical heat of this alloy supports this theory.

As a general observation, our tubing supplier has encountered many more problems with both heats of Incoloy-800 than they did with the 304SS or the 316SS. These problems are to be expected whenever a manufacturer undertakes the fabrication of a high quality product with an alloy in which there is not an extensive background of fabrication experience and technology.

The low titanium and aluminum content of the reference heat of Incoloy-800 must be studied to determine the importance of these elements on mechanical behavior and fabrication processes. This feature must be resolved before an extensive mechanical testing program can be started on the tubing of this heat.

PAGE 164 is blank

Program: FBR Fuel Cladding and Structural Materials
AEC Task: 10-C Mechanical Properties
Project Manager: J. L. Ballif/ J. J. Gill
Reporting Period: FY 1968
General Order: 7706 Subaccount: 29530 AEC Category: 04-01-61-01.1

Principal Investigator: D. F. Atkins

I. PROJECT OBJECTIVES

The objectives are to determine the individual and combined effects of environment (sodium and helium), strain rate (10^{-7} to 10^{-3}/hr) and stress condition (uniaxial and biaxial) on the creep, stress rupture, and fatigue characteristics of selected cladding alloys. The alloys selected for study will be those which have greatest potential for fast reactor applications.

II. TECHNICAL PROGRESS DURING FISCAL YEAR 1968

A. SUMMARY

Scoping tests to provide early biaxial stress rupture information on the behavior of 304 stainless steel and 316 stainless steel in system quality sodium were completed. These tests defined the 100- to 1000-hr stress rupture properties at temperatures of 1000 to 1400°F, and provided data for selection of appropriate stress levels for long-term tests. These tests also served to study the influence of cold work on the stress rupture properties of the alloys.

By using the specially designed sodium retorts which test twelve specimens simultaneously, the long-term stress rupture properties of the reference heats of 304 stainless steel and 316 stainless steel thin-walled tubing (0.010-in. wall) were studied in a high purity sodium environment. Specimens were placed on test under a biaxial stress mode (1/2:1) with stress levels selected to give rupture times over the 100- to 10,000-hr range. A total of 28 retorts containing 336 specimens of 304 stainless steel and 316 stainless steel were placed on test during FY 1968. Most of these tests were in a high purity static sodium environment where the oxygen impurity level ranged from 8 to 15 ppm and the carbon level was about 15 ppm. Sodium chemistry results were verified by extracting

TABLE 1

BIAXIAL STRESS RUPTURE TESTS, LMFBR CLADDING PROGRAM

Retort No.	Test Temp (°F)	SS Alloy	Clad Condition*	Environment	Life Span (hr)	Status		Remarks	Date(s) Start/Completed
						Test	Examine		
1	1300	304	AR	Na + Zr	100-700	Complete	Complete	Scoping test	2-11066/3-13
2	1400	304	AR	Na + Zr	100-400	Complete	Complete	Scoping test	2-6-67/2-22
3	1400	304	AR	He	100-800	Complete	Complete	Effect of sodium	3-18-67/4-21
4	1200	304	AR	Na + Zr	100-2600	Complete	Complete	Scoping test	3-27-67/7-14
5	950	304	AR	Na + Cu	100-3000	Complete	Complete	Effect of copper	4-21-67/9-18
6	1400	304	AR	Na	100-900	Complete	Complete	Scoping test	6-2-67/7-7
7	1100	304	AR	Na	100-3000	Complete	Complete	Scoping test	6-9-67/10-30
8	1400	304	Ann	Na	100-2000	Complete	Complete	Effect of cold work	6-15-67/9-12
9	1000	304	AR	Na	100-700	Complete	Complete	Scoping test	8-12-67/9-11
10	1400	304	AR	Na	1000-3000	Complete	Complete	Extension of data	8-10-67/12-18
11	1200	304	AR	Na	100-4000	Complete	Complete	Extension of data	8-12-67/1-10-68
12	1100	304	AR	Na + Cu	100-700	Complete	Complete	Effect of copper	8-18-67/9-18
13	1200	304	AR	He	100-5000	Complete	-	Effect of sodium	10-20-67/6-11-68
14	1200	304	AR + aged	Na	100-1000	Complete	-	Effect of thermal aging	11-2-67/3-6-68
15	1200	304	AR	Na	5000-10,000	1/4 Complete	-	Extension of data	11-9-67
16	1000	304	AR	Na	100-3000	Complete	-	Extension of data	11-22-67/3-31-68
17	1200	304	Ann	Na	5000-10,000	In progress	-	Extension of data	2-22-68
18	1200	304	Ann	Na	100-5000	3/4 Complete	-	Effect of cold work	1-25-68
19	1000	304	AR	Na	5000-10,000	In progress	-	Extension of data	4-2-68
20	900	304	AR + Ann	Na	100-5000	2/3 Complete	-	Scoping test	12-1-67
21	1000	304	Ann	Na	100-5000	Complete	-	Effect of cold work	2-15-68/5-20-68
22	1000	304	Ann	Na	5000-10,000	In progress	-	Extension of data	2-29-68
24	1300	304	AR	Na + Cu	100-1000	Complete	-	Effect of copper	3-26-68/5-15-68
101	1400	316	AR	Na	100-1000	Complete	Complete	Scoping test	8-10-67/9-21-67
102	1200	316	AR	Na	100-10,000	Complete	-	Extension of data	8-12-67/6-6-68
103	1000	316	AR	Na	100-4000	Complete	-	Scoping test	9-14-67/3-5-68
104	1400	316	AR	He	100-1600	Complete	Complete	Effect of sodium	8-31-67/11-15
105	1400	316	Ann	Na	100-800	Complete	Complete	Effect of cold work	10-19-67/11-27
106	1200	316	Ann	Na	100-2000	Complete	-	Effect of cold work	10-24-67/1-18-68
107	1000	316	Ann	Na	100-600	Complete	Complete	Effect of cold work	12-6-67/1-8-68
108	1000	316	AR	He	100-2000	Complete	-	Effect of sodium	1-12-68/4-9-68
109	1200	316	AR	Na	100-2000	Complete	-	Scoping test	2-9-68/4-25-68
110	1000	316	AR	Na	1000-10,000	In progress	-	Extension of data	4-23-68
111	1000	316	Ann	Na	1000-10,000	Discont.	-	Extension of data	5-10-68/6-4-68
112	900	316	Ann	Na	100-5000	In progress	-	Extension of data	6-20-68

*AR = As-received tubing containing 10-15% cold work
Ann = Annealed tubing

small sodium samples several times during each retort test. A number of tests were also conducted in high purity helium to assess the effects of sodium. Table 1 gives the status of all biaxial multispecimen retorts which have been assembled on this program.

Uniaxial creep rupture tests were conducted on 304 stainless steel sheet stock (0.062-in., reference heat) in 1200°F sodium. These tests provided information on the effect of stress mode and cold work. A total of twenty specimens in the annealed, 11%, and 38% cold worked conditions were tested. The results are summarized in Table 2.

Studies on the stress rupture behavior of 304 stainless steel in copper contaminated sodium were performed. This work provided information in support of EBR-II operations.

Two topical reports covering the work on this task were issued this fiscal year. Studies of the stress rupture behavior of austenitic stainless steel in zirconium-gettered sodium are reported in NAA-SR-12353. The biaxial test results of 304 stainless steel and 316 stainless steel in high purity sodium are discussed in detail in AI-AEC-12694.

B. COLD WORK EFFECTS

The specimens used on this program were taken from two highly characterized heats of thin-walled tubing (0.010-in. wall x 0.275-in. ID). Both the 304 stainless steel and the 316 stainless steel tubing contained 10 to 15% cold work introduced during the final drawing operation at the tube mill. Mill terminology for this material is "1/8 hard." The tubing was purchased in this condition because it was expected that the harder tubing would have better handling and assembly characteristics than material in the "dead-soft" annealed condition. Although it was recognized that the cold working would increase the strength and reduce the ductility slightly, the small degree of cold work was not considered to be of too much significance. It was learned, however, that if the test temperatures were sufficiently high to allow recovery, cold working significantly reduced the long-term stress rupture properties.

The stress rupture results obtained on 304 stainless steel in sodium are plotted in Figure 1. The cold worked alloy is initially stronger than annealed material from the same lot; however, the two curves converge with the annealed

TABLE 2

STATUS OF UNIAXIAL STRESS-RUPTURE TEST OF REFERENCE 304 SS SHEET IN 1200° F Na

Sample No.	Sample Condition	Stress (psi)	Rupture Time (hr)	Elongation (%)	Steady-State Creep Rate (in./in.-hr)
8A	Anneal	30,000	143*	44	1.15×10^{-3}
9A	Anneal	30,000	55	17	1.27×10^{-3}
12A	Anneal	30,000	69	-	-
4A	Anneal	25,000	421	40	2.4×10^{-4}
5A	Anneal	25,000	388†	33	3.4×10^{-4}
11A	Anneal	25,000	383	41.5	2.76×10^{-4}
6A	Anneal	21,000	1233	29	8.0×10^{-5}
7A	Anneal	21,000	1253	29	6.3×10^{-5}
1C3	38% Cold Work	35,000	46	3	2.9×10^{-4}
2C3	38% Cold Work	35,000	47	3	1.9×10^{-4}
3C3	38% Cold Work	30,000	66	3.5	1.9×10^{-4}
4C3	38% Cold Work	30,000	72	3	2.3×10^{-4}
5C3	38% Cold Work	20,000	187	6.5	1.2×10^{-4}
6C3	38% Cold Work	20,000	147	6	1.64×10^{-4}
2C1	11% Cold Work	39,000	Discontinued§	-	-
1C1	11% Cold Work	39,000	47	15	8.6×10^{-4}
4C1	11% Cold Work	35,000	105.6	10	2.0×10^{-4}
5C1	11% Cold Work	35,000	93	13	3.8×10^{-4}
3C1	11% Cold Work	27,000	1290	7	2.0×10^{-5}
7C1	11% Cold Work	27,000	897	11.5	-

*Specimen aged in 1200°F Na without load for 120 hr due to furnace controller problem

†Specimen failed at gage mark

§Test discontinued due to furnace controller problem

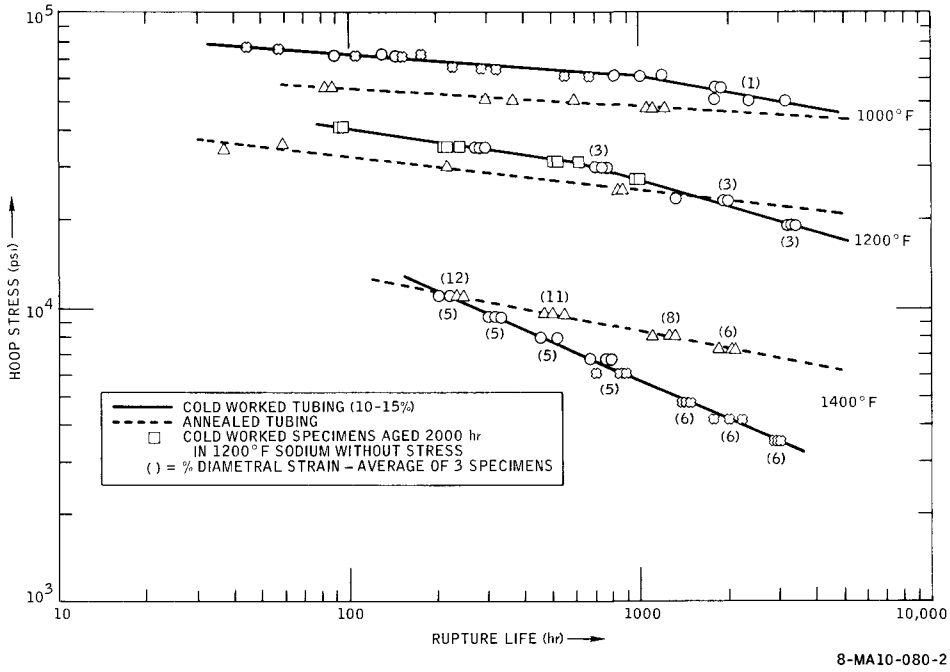

Figure 1. Biaxial Stress Rupture Properties of Cold-Worked and Annealed 304 SS in Sodium

material possessing superior long-term properties. The cold work benefits are especially short lived at 1400°F. At lower temperatures, the strength benefits of the cold work are retained longer, but still retain a rather strong dependence on temperature.

This temperature dependence indicates that the mechanism associated with the cold work behavior involves a time dependent, thermally activated process. A series of tests, therefore, were performed in which cold worked specimens were thermally aged for 2000 hr in 1200°F sodium. The specimens were unstressed during this aging step. If recovery processes were to occur, this thermal treatment should have produced changes in the stress rupture behavior. However, subsequent stress rupture tests produced no change in stress rupture properties as a result of the thermal soak (Figure 1). These observations indicate that if recovery processes do occur, they must be activated by stress or by a combination of temperature, time, and stress.

The reproducibility of the biaxial stress rupture test results from one sodium retort to the next is demonstrated by the data on the cold worked curves at 1400 and 1000°F in Figure 1.

The diametral strain observed in the ruptured specimens is given by the figures in parentheses in Figure 1. The 10 to 15% cold work greatly reduces the strain at rupture and the strain seems to be insensitive to stress levels.

The behavior of the cold worked 316 stainless steel alloy, shown in Figure 2, is similar to that of the 304 stainless steel, although the 316 stainless steel seems to be more resistant to the cold working effects. The strengthening benefits of cold work is retained probably beyond 10,000 hr at 1200°F. Again, the data on the 1200°F cold work curve indicate the reproducibility of the twelve specimen retorts. The reduction in strain due to cold work is especially pronounced at 1000°F. Only 1-2% strain was observed as compared to 12-16% for annealed material over the same stress range.

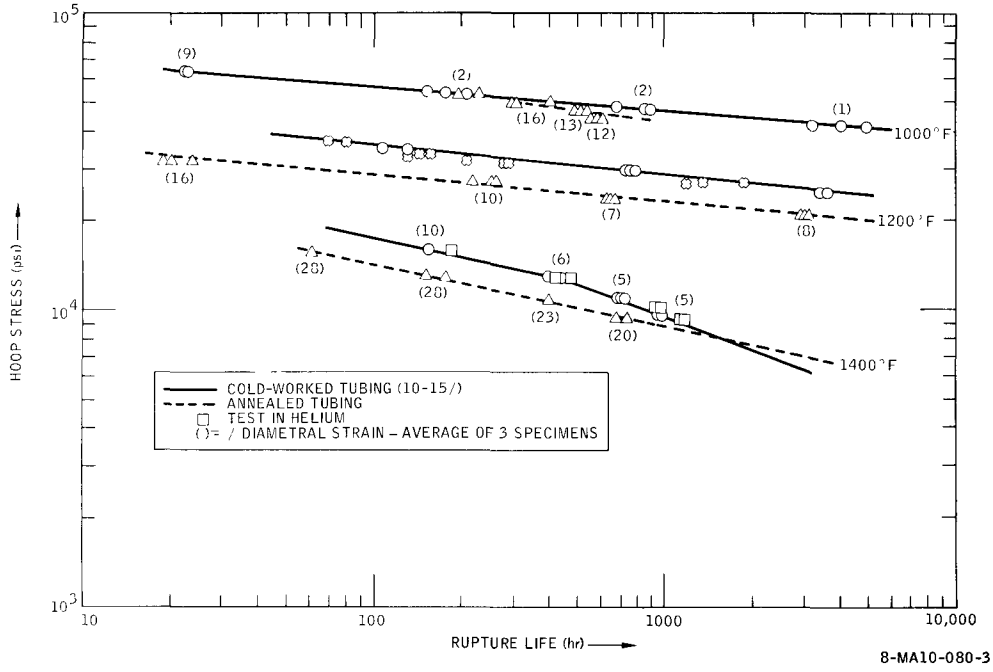

Figure 2. Biaxial Stress Rupture Properties of Cold-Worked and Annealed 316 SS in Sodium

A comparison of the strain rate behavior of the reference heats of 304 stainless steel and 316 stainless steel in 1400°F sodium is shown in Figure 3. Annealed 316 stainless steel has a strain rate comparable to that of annealed 304 stainless steel tubing; however, the rupture strain of the annealed 316 stainless steel was found to be almost double that of annealed 304 stainless steel in 1400°F sodium.

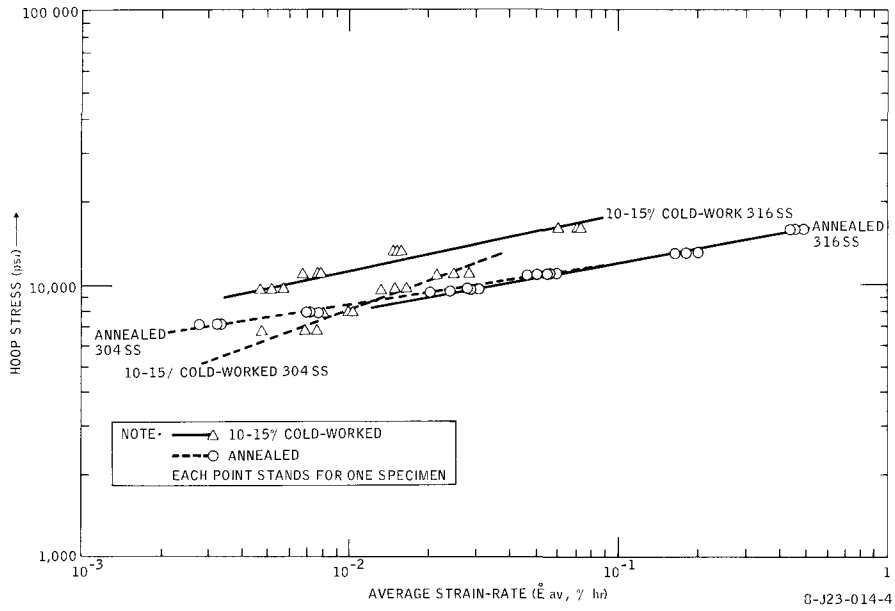

Figure 3. Strain-Rate Behavior of Reference-Type 304 SS and 316 SS Tubing in 1400°F Sodium

The maximum diametral strain at rupture for each of the two alloys in 1400°F sodium are compared in Figure 4. Both annealed alloys and the cold worked 316 stainless steel show the normal behavior of strain; i.e., a decrease with an increase in rupture time. The cold worked 304 stainless steel behaves abnormally, with the strain slightly increasing with time. This might be attributed to recovery occurring at 1400°F. The strain insensitivity exhibited by the cold worked 304 stainless steel alloy has also been reported for the British M-316 alloy containing about 20% cold work.*

The effect of increasing the level of cold work has been studied; and although the results are preliminary, it seems that the behavior of the 10 to 15% cold worked tubing is accentuated by higher cold work levels. Figure 5 shows data obtained under uniaxial stress on sheet stock of the 304 stainless steel reference heat in 1200°F sodium. The 38% cold worked alloy is very weak in stress rupture, weaker than the annealed material after about a 60-hr rupture life. In general, it has been found that an increase in cold work results in an increase

*H. K. Richardson and R. McDowell, "Elevated Temp. Stress Rupture Properties of M316, FV548, and Nimonic PE16 P.F.R.-Type Tube," TRG Report 1482(c), 1967

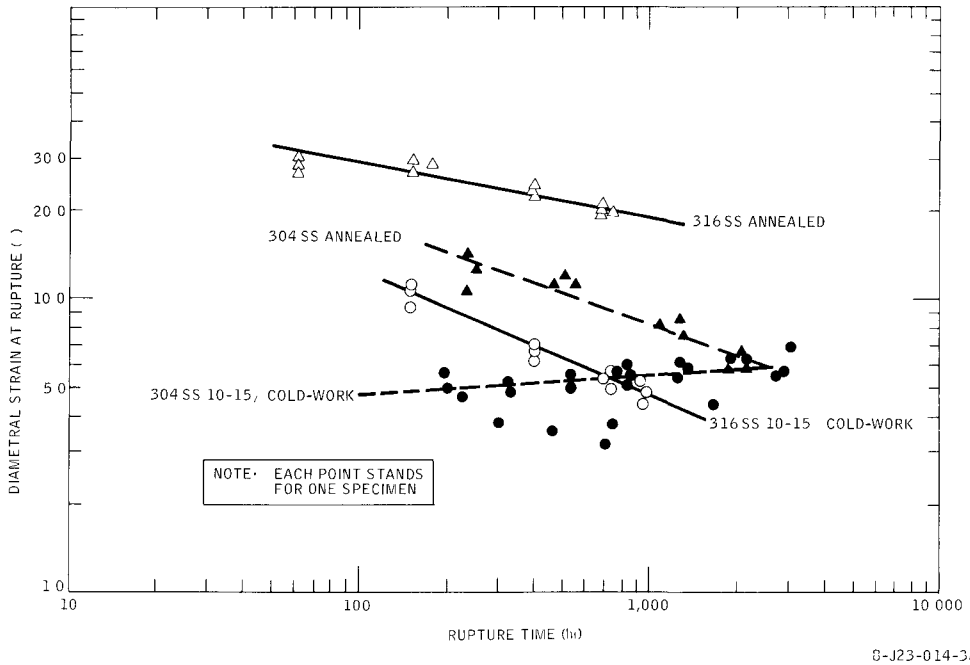

Figure 4. Variation of Strain With Rupture Time for 304 SS and 316 SS in 1400°F Na

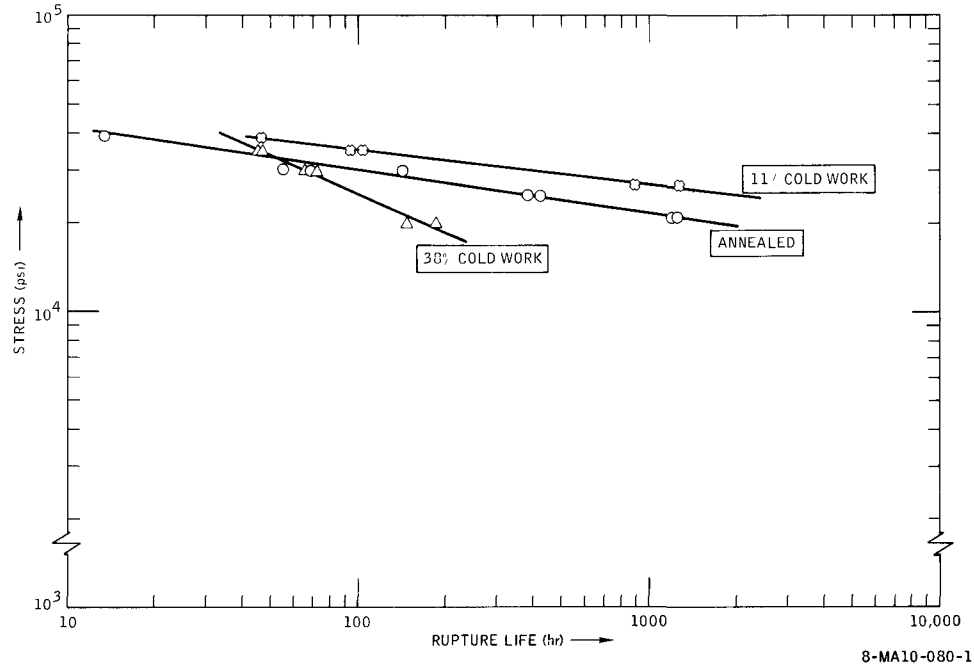

Figure 5. Uniaxial Stress Rupture Behavior of 304 SS in 1200°F Sodium 0.062 in. Sheet, Reference Heat (20013)

in the slope of the stress rupture curve and a shift in the cross-over-point of the annealed and cold work curves to shorter rupture times.

C. SODIUM EFFECTS

Concern about the influence of the static sodium environment on the stress rupture properties of the two alloys prompted tests in a high purity helium environment. It was found that the sodium did not change the stress rupture strength of the stainless steel. The results of one such test in 1400°F helium are plotted in Figure 2. The creep rate behavior in both sodium and helium is shown in Figure 6. From these observations and similar results on tests at lower temperatures on both alloys, it was concluded that the static sodium environment was not influencing the stress rupture properties of the two alloys.

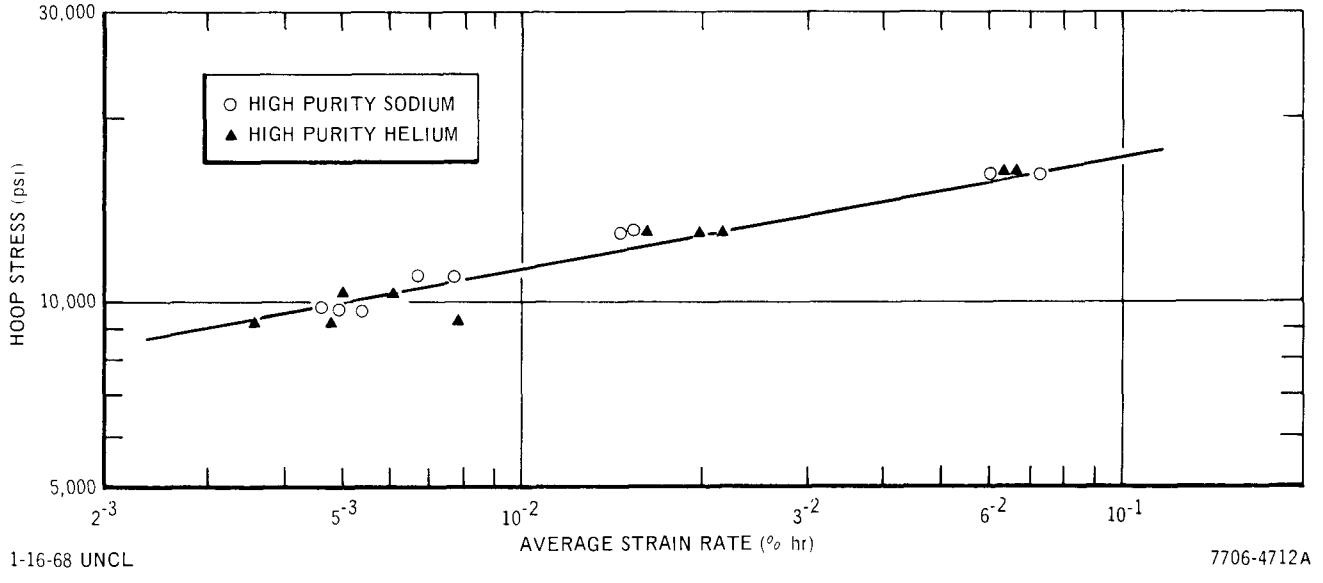

Figure 6. Strain Rate Comparison of 316 SS Tested in 1400°F Sodium and Helium

D. STATE OF STRESS

Studies on the effect of the stress mode on the stress rupture behavior of the cladding were initiated. Uniaxial tests in 1200°F sodium were performed on annealed, and on 11 and 38% cold-worked sheet stock of the reference heat of 304 stainless steel. The test results on twenty specimens are summarized in Table 2 and the stress rupture data are plotted in Figure 5. Although still very

preliminary at this time, a direct comparison of results on annealed material in both the uniaxial and biaxial (1/2:1) stress modes provides further insight into the influence of stress state on creep and stress rupture. As shown in Figure 7, the uniaxial stress state produces a large amount of ternary creep. As a result, the total strain at rupture is about 40%. Under a biaxial hoop stress, there is much less tertiary creep; and for an equivalent stress, the strain is only about one-fourth that found in the uniaxial stress state.

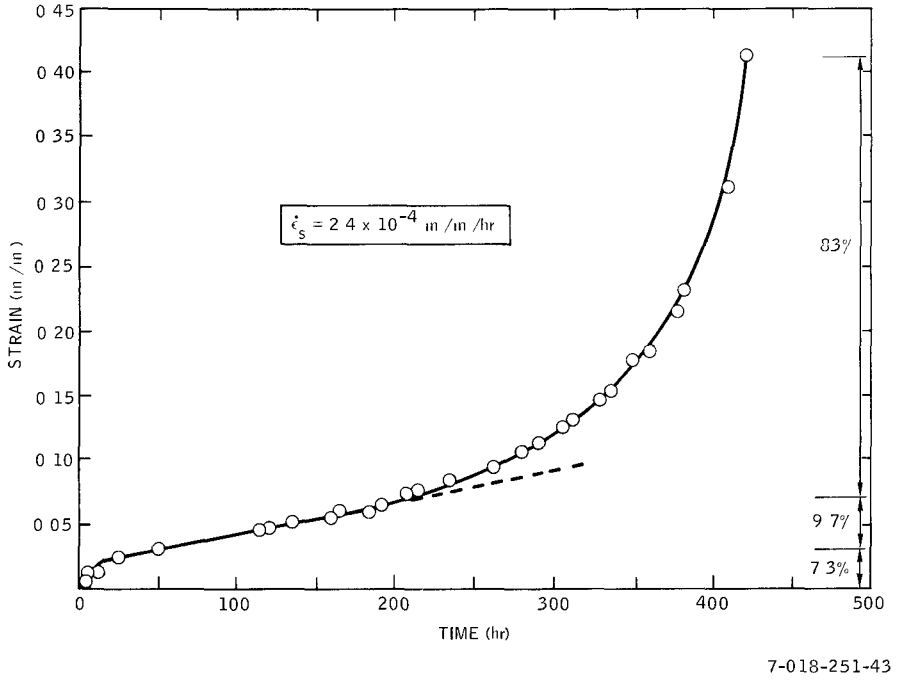

Figure 7. Uniaxial Creep Curve for 304 SS (Annealed) in 1200°F Sodium (Stress = 25,000 psi)

To provide additional information on the effects of stress mode, experimental studies on methods of imposing an equal hoop and axial stress (1:1 biaxial) on tubular cladding were conducted. In actual fuel element performance the cladding may be subjected to simultaneous hoop and axial stresses in the latter stages of life. To simulate this condition, a test was devised that uses a tubular specimen internally pressurized with gas while under axial tension. Conditions were chosen such that the tension and hoop stresses were equal (1:1 biaxiality). Figure 8 shows a photograph of the test assembly. The concept

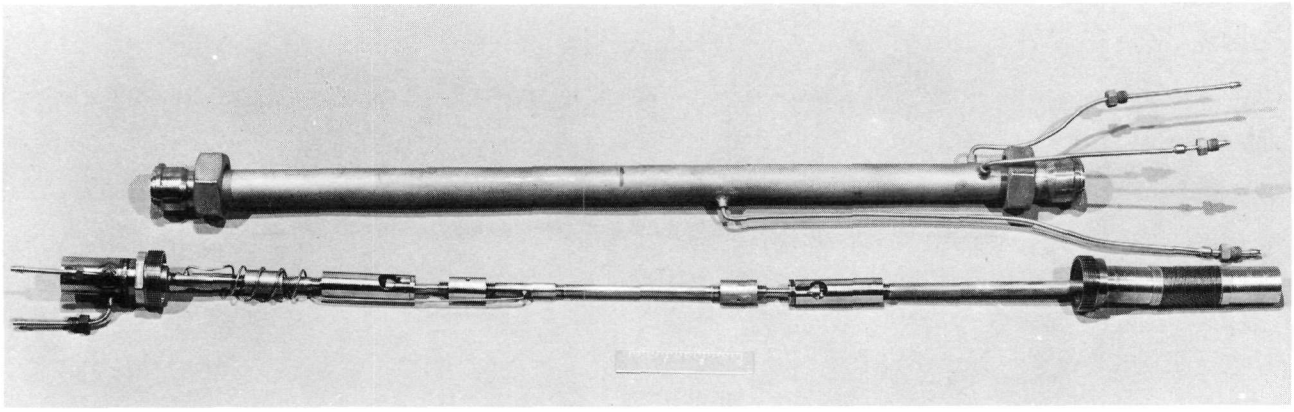

7706-4051

Figure 8. Test Assembly for 1:1 Biaxial Stress Rupture Tests

whereby a gage length is created by reducing the wall thickness between the welded end plugs, has been successfully demonstrated. A 0.020-in. wall tube was ground on the OD to produce a 0.010-in. wall in the central two inches of the specimen. After annealing, the specimen was tested in 1200°F helium with a 28,000 psi hoop stress and an equivalent axial stress. Failure was by a pin hole type crack, similar to those associated with the 1/2:1 biaxial stress mode. The rupture life was 220 hr, which is intermediate between that predicted for pure uniaxial and the 1/2:1 biaxial. Strain in tha axial direction was 10%, and in the hoop direction, 13%. The steady-state creep rate in the axial direction was 1.54×10^{-4}/hr. The use of chemical milling in place of grinding was evaluated and found to give a more uniform metal removal on the tubing wall. This technique has been adopted and several specimens of both 304 stainless steel and 316 stainless steel have been prepared and will be tested next fiscal year.

An alternative specimen design which eliminates the requirement for a reduced tubing wall section uses a compression ring to reduce stresses at the end plug welds. A specimen of cold worked (10 to 15%) 304 stainless steel tubing tested in 1200°F helium successfully demonstrated the feasibility of this design concept. The specimen was stressed to 30,000 psi in both the biaxial (1/2:1) and the uniaxial directions. Failure occurred in the 0.010-in. wall by a small longitudinal crack after 460 hr under test. Axial strain was 5.3%; the maximum diametral strain was 8%.

E. FRACTURE MODE

Metallographic examination of the stress rupture specimens tested in both sodium and helium revealed that all fractures were intergranular with fissuring along grain boundaries away from the rupture. No difference in fracture behavior was observed over the temperature range 1100 to 1400°F. Metallography on 1000°F specimens is incomplete.

Under a biaxial stress mode, the ruptures are generally small longitudinal cracks in the tubing wall. Below 1200°F and occasionally at 1200°F, failure sometimes occurred by an explosive-type rupture. The cause of this type of rupture has not been identified. The rupture is characterized by a large longitudinal crack, accompanied by localized distortion similar to that experienced on short term burst tests. The sudden release of high pressure gas apparently creates a shock wave which is transmitted through the sodium. This high energy wave results in bending and twisting of the pressure tubes connected to the specimens and a flattening of previously ruptured specimens which were no longer internally pressurized. To alleviate this problem, solid stainless steel slugs were placed inside the specimens to reduce the gas volume. This procedure was found to greatly reduce the extent of damage. While explosive-type ruptures still occurred, damage to neighboring specimens was eliminated. The unstressed control specimen (containing no internal slug or gas pressure) was also undamaged. Figure 9 compares the specimens from two retort tests, one with internal specimen slugs and the other without slugs. It is clear that the insertion of the solid slugs was effective in reducing damage to the specimens by the explosive force accompanying specimen rupture.

F. COPPER CONTAMINATION

Following observation of contamination of EBR-II primarysodium with copper per,* a series of tests were performed to determine whether or not there were pronounced effects of the copper on the mechanical behavior of Type 304 stainless steel thin-wall tubing. Many EBR-II components are made of this or closely related (304L) alloy and there was concern that copper in the sodium might penetrate grain boundaries or alloy with the stainless steel and reduce the mechanical strength of the reactor components.

---

*Albert V. Crewe, "Reactor Development Program Progress Report," Argonne National Laboratory Report ANL-7317, March 1967

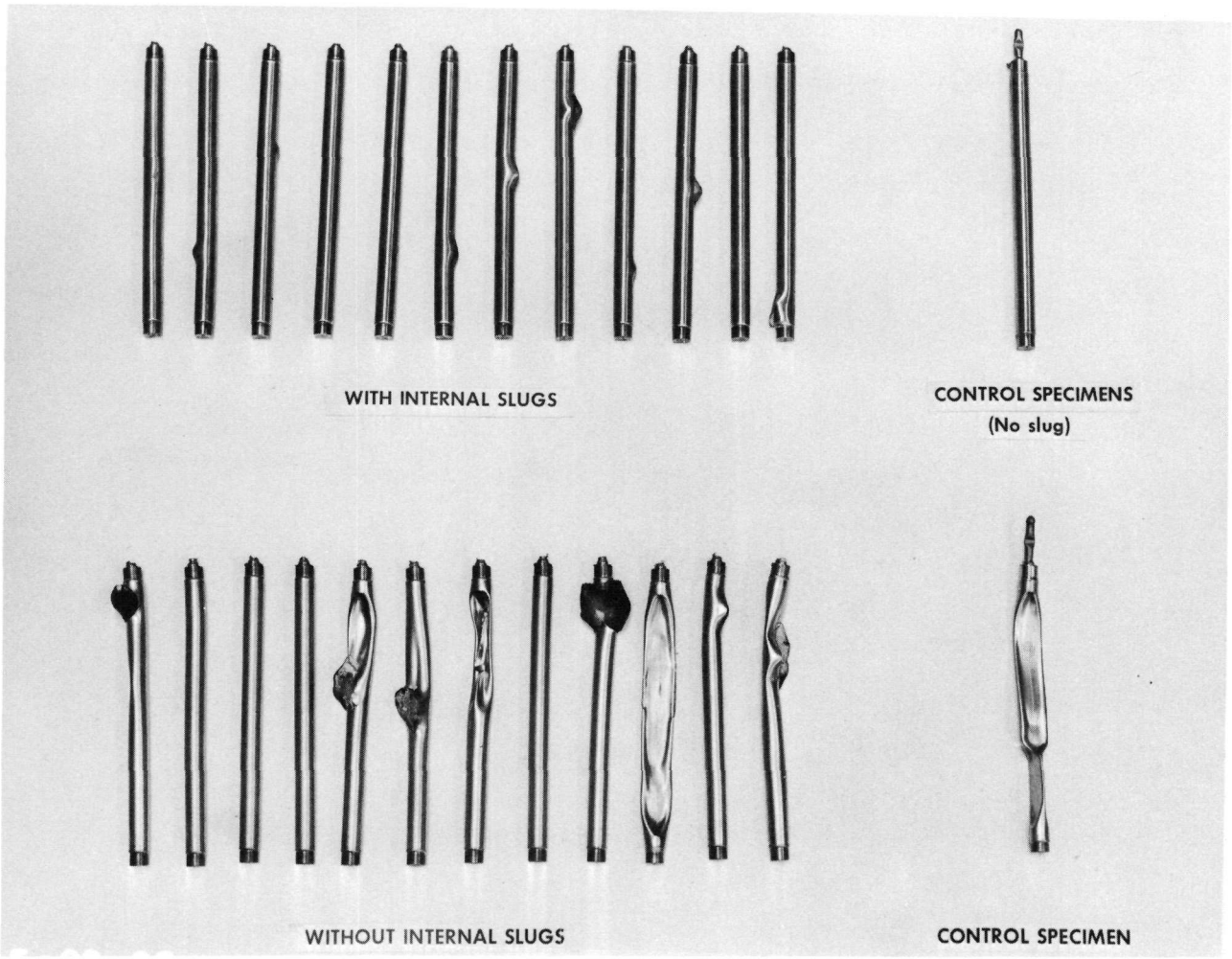

7706-4067

Figure 9. Influence of Internal Slugs on Specimens Tested in 1000°F Sodium

Three biaxial test retorts were assembled to test both copper plated and nonplated tube specimens in copper-saturated sodium at 950, 1100, and 1300°F. In addition to twelve stress rupture specimens, each retort contained four 304 stainless steel Charpy impact specimens and two pure copper corrosion tabs. The stress-rupture specimens were made from 304 stainless steel tubing (0.010-in. wall by 0.27-in. ID by 4-in. long) used in the current cladding program. The tubing contained 10 to 15% cold work. On some of the specimens, a copper plating (0.0002-in. and 0.0006-in.) was applied to the OD surfaces. Tests were conducted in static sodium retorts containing approximately 450 cc of sodium.

Results of the stress rupture tests are plotted in Figure 10. Both the copper-plated and the nonplated specimens gave essentially the same values.

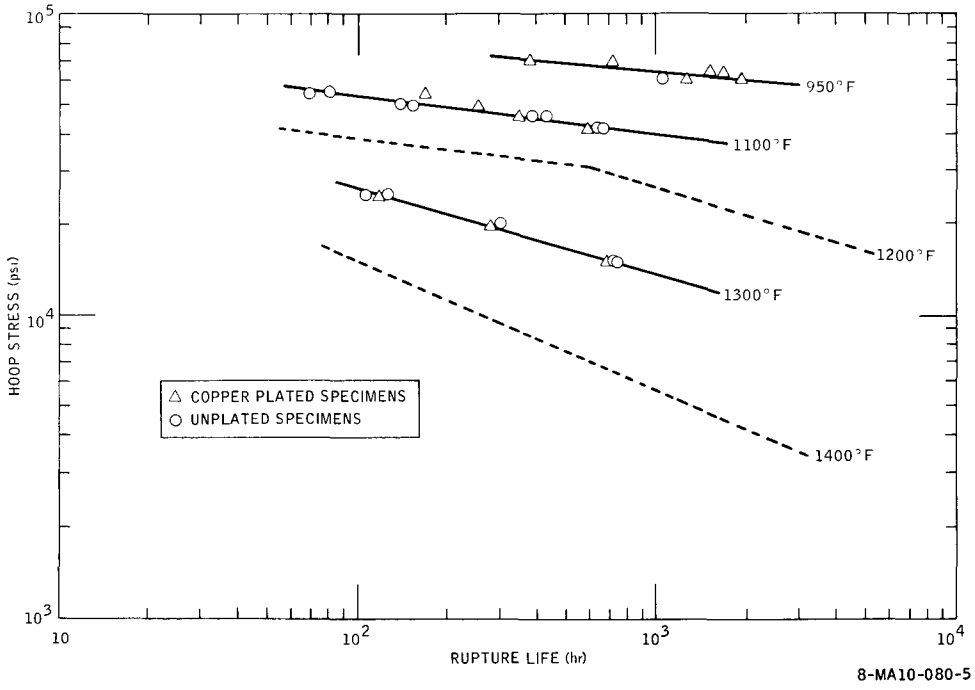

Figure 10. Biaxial Stress Rupture of 304 SS Tubing (10-15% Cold-Work) in Copper-Contaminated Sodium

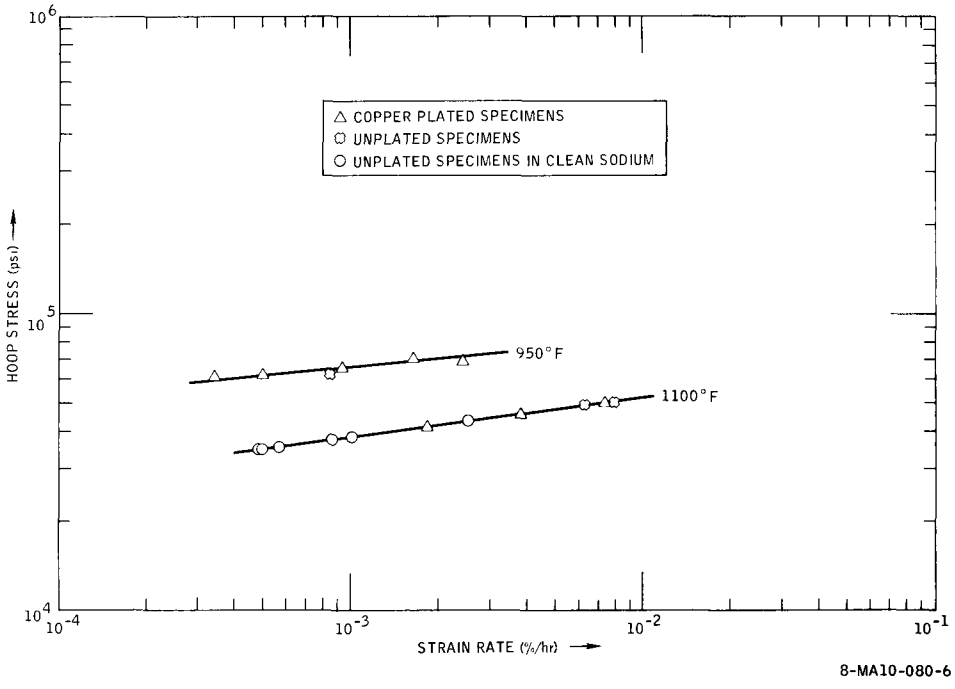

Figure 11. Strain-Rate Behavior of 304 SS Tubing (10-15% Cold-Work) in Copper-Contaminated Sodium

The 1100°F line was obtained from previous tests on the same 304 stainless steel heat in high purity (no copper contamination) sodium. The tests in copper saturated sodium lie on top of this high purity sodium curve. The dashed lines at 1200°F and 1400°F also represent stress rupture curves generated in high purity sodium. Based on these studies, it can be concluded that the presence of copper in sodium does not alter the stress rupture properties of the stainless steel under the test conditions imposed.

Strain measurements, taken on the diameter of the specimens after test, provided a comparison of the average strain-rate. As shown in Figure 11, the creep rate is the same for both copper plated and unplated specimens in copper saturated sodium. Specimens which were tested in high purity sodium at 1100°F also exhibit the same creep rate. Strain measurements on the 1300°F test are not complete.

Charpy impact tests on the exposed specimens are listed in Table 3. The reduction in impact strength of the exposed specimens is attributed to thermal aging effects. Metallographic examination did not show any copper penetration into the stainless steel. Again, tests on the specimens from the 1300°F retort are not complete.

The copper corrosion tabs in the retorts served a twofold purpose. Primarily they were placed in the sodium to provide a constant supply of copper. Weight change measurements on the copper tabs provided a qualitative indication of the corrosion of copper by sodium. Corrosion was observed to have a rather strong dependence on temperature.

TABLE 3

IMPACT-STRENGTH OF 304 SS CHARPY V-NOTCH SPECIMENS
(Impact test temperature = -75 ± 3°C)

Specimen Condition	Specimen Number	Cu-Thickness (in.)	Impact Strength (ft-lb)	Average Impact Strength (ft-lb)
As Received Annealed 304 SS	K7-1	0	125	123
	K7-1	0	124	
	K7-4	0	120	
Cu-Plated Annealed 304 SS	K7-10	0.0006	124	123
	K7-12	0.0002	122	
	K7-13	0.0002	115	
	K7-14	0.0002	131	
Cu-Plated, Annealed 304 SS Exposed to 950°F Na	K7-17	0.0006	102	108
	K7-18	0.0006	100	
	K7-19	0.0006	115	
	K7-20	0.0006	117	
Cu-Plated 304 SS (Annealed) Exposed to 1100°F Na	K7-6	0	82	81
	K7-7	0	84	
	K7-9	0.0006	84	
	K7-11	0.0006	78	

III. EVALUATION OF EFFORT DURING FISCAL YEAR 1968

The multiple specimen biaxial stress-rupture testing concept has produced accurate, consistant data with a high statistical confidence. The static sodium is sampled several times during each test, and the ability to maintain a high-purity sodium environment for the test specimens has been demonstrated.

The static sodium tests provide an important testing feature to the cladding program. With the multiple specimen testing capability, a large amount of data can be generated in the shortest possible time. The data has been demonstrated to be very reliable and, with the triplicate tests, a high statistical confidence in the data is obtained. The static sodium provides an environment which is consistent and reproducible for the many tests involved. It is ideally suited for definition of the effects of process and metallurgical variables, and for theoretical studies on state-of-stress and creep equations. The rigid control on test conditions and the large amount of data which must be generated on such studies makes the static sodium retort concept both technically and economically attractive. It is recognized that tests in static sodium will not provide adequate data for answers as to sodium corrosion allowance and corrosion effects (ferrite layer formation and mass transport). These studies, however, are currently in progress on another task (10-D) and preliminary results have demonstrated the complimentary relationship between the static and dynamic sodium tests.

Metallographic studies on the stress rupture specimens provide perhaps the best clues as to the mechanism leading to premature failure of the cold worked alloys. As shown in Figure 12, the cold worked alloy possesses extensive grain boundary voids as compared to annealed material in a similar test. This behavior is consistent at lower temperatures, different stress levels, and with the 316 stainless steel alloy.

The proposed model for the cold worked behavior is that in which cold working strengthens the grains of the metal by strain hardening, and by precipitation on slip bands and dislocation sites within the grains. Under stress, the grains resist deformation and the applied stress is concentrated at the weaker grain boundaries. This leads to grain boundary sliding, grain rotation, and eventual premature grain boundary cracking. By contract, the grains of the annealed alloy are ductile and deform under stress. This accounts for the higher strain observed on annealed material. With the accommodation of strain within the grains, stresses at the grain boundaries are reduced and grain boundary sliding is a less prominent factor.

Figure 12. Effect of Cold-Work on Microstructure and Void Density of Type 304 Stainless Steel in 1400° F Na

One of the objectives of performing tests in both the uniaxial and biaxial stress mode is to establish a correlation between state-of-stress and stress-rupture strength. Based on the studies to date, the data seem to obey Von Mises' distortion-energy yield theory. For thin-walled tubes subjected to an axial load and internal hydrostatic pressure, the theory can be expressed mathematically by

$$\sigma_1^2 + \sigma_2^2 - \sigma_1\sigma_2 = \sigma_0^2 \quad ,$$

where there is a large ΔT,

σ_1 = axial stress,

σ_2 = hoop stress, and

σ_0 = effective stress.

Using this relationship, uniaxial and biaxial test results obtained in 1200°F sodium on annealed 304 stainless steel were compared. Figure 13 shows the excellent correlation that was obtained by using Von Mises' yield criterion. A good correlation was also found when the results of biaxial annealed 304 stainless steel in 1400°F sodium were compared with uniaxial test in vacuum data generated under Task 10-E.

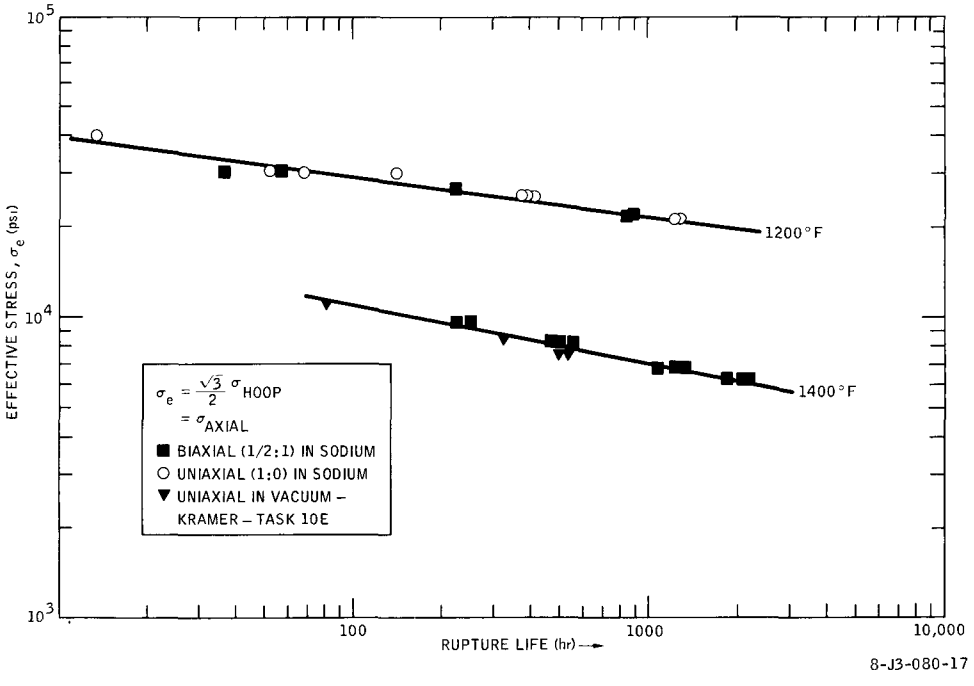

Figure 13. The Application of Von Mises' Yield Theory for Comparison of Biaxial With Uniaxial Stress Rupture Data (Annealed 304 stainless steel – HT. 20013)

The work on copper contaminated sodium has shown that the presence of copper in sodium is not detrimental to the impact strength or the creep/stress-rupture properties of 304 stainless steel at temperatures up to 1300°F. Although the duration of the tests were only around 1000 hr, examination of the specimens indicates that considerably longer exposures could be tolerated. The work did reveal a potential problem of copper deposits forming in the cooler regions of the sodium system. In a reactor where there is a large ΔT in the sodium loop, copper might deposit and inhibit coolant flow, or interfere with value or instrument operation.

Although the results from the 1:1 biaxial tests are still very preliminary, the diametral strain at rupture seems to be more localized and somewhat greater in magnitude than observed on corresponding tests under 1/2:1 biaxial stress conditions. Since the time to rupture was not much different under the two stress conditions, it appears that the 1:1 biaxial stress state accelerates creep in the hoop direction. More studies are needed before these observations can be seriously considered.

Program:	FBR Fuel Cladding and Structural Materials				
AEC Task:	10-D-1, Dynamic Loop Operation				
Project Manager:	J. L. Ballif/J. J. Gill				
Reporting Period:	Fiscal Year 1968				
General Order:	7706	Subaccount:	29541	AEC Category:	04-01-61-01.1

Principal Investigator: R. D. Keen

I. PROJECT OBJECTIVE

The objective of this project is to operate and maintain the 2-in. sodium loop facility in support of activities under S/A 29542 and 29543.

II. TECHNICAL PROGRESS DURING FISCAL YEAR 1968

The 2-in. sodium test loop was operated during the year for testing four series of high flux heaters and clad specimens. The bare heaters were tested as part of the heater development program. The clad specimens were used in stress-rupture testing and mass transfer measurements. In some stress-rupture tests the power to the heater was turned on and off at specified time intervals. After cladding failure due to stress-rupture and removal of the cladding, some heaters were returned to the loop to continue testing in the bare condition. A summary of the heater and clad specimens tests is given in Table 1. These tests are discussed in more detail in the following two sections under Subtask D.

In order to perform the heater cyclic tests, the electrical control system was modified to provide 2- and 12-min on-off cycles. The loop was also modified by installing time delay relays in the control system holding circuits, to allow the loop to restart automatically after power outages.

The loop airblast heat exchanger was rebuilt and restored to good operating condition, with new preheaters installed inside and new insulation outside.

III. EVALUATION OF EFFORT DURING FISCAL YEAR 1968

The integrity, reliability, and operation of the 2-in. dynamic loop for the purpose of testing fuel cladding material under simulated reactor operating conditions has met or exceeded project objectives as to schedule, availability,

and operating costs. The purity of the sodium in the loop has been verified by sodium sampling during periods of loop operation. The plugging temperature of the sodium has been maintained between 250 and 300°F by operation of the cold trap.

TABLE 1

HIGH FLUX HEATER PERFORMANCE

Heater No.	Test Condition and Duration* (hr)		Run Duration With Cladding (hr)	Heater Operation	
	Cyclic	Steady State		Times (hr)	Cycles
11	0	763	0	763	24
12	0	1117	0	1117	26
30	0	330	223	330	35
32	299 †	894	227	1044	1500
36	0	589	589	589	10
38	199 †	0	199	99	1000
40	173 †	498	173	584	865
42	243 §	0	134	122	7308
44	163 §	149	163	230	4902
46	385 †	0	385	193	1925
48	890 †	0	393	445	4457
50	0	182	182	182	0

*Operating in 1200°F Na loop
†Heater cycle: 6 minute on, 6 minute off
§Heater cycle: 1 minute on, 1 minute off

Program: Fuel Cladding and Structural Materials
AEC Task: 10D-2, Dynamic Loop Testing (Mechanical Properties)
Project Manager: J. L. Ballif/J. J. Gill
Reporting Period: Fiscal Year 1968
General Order: 7706 Subaccount: 29542 AEC Category: 04-01-61-01.1

Principal Investigator: J. H. Shively

I. PROJECT OBJECTIVES

Project objectives are to: (1) test, evaluate, and demonstrate the performance capability of candidate fast reactor cladding and structural materials in a dynamic sodium environment, and (2) determine the nature of combined effects of mass transfer, temperature, low-cycle thermal cycling, and biaxial stresses on the stress-supture and creep behavior of these alloys.

II. TECHNICAL PROGRESS DURING FISCAL YEAR 1968

A. SUMMARY

Seven high flux heater assemblies with cladding were fabricated. Ten tests of cladding under both an internal pressure and a 10^6 Btu/ft^2-hr heat flux, and in flowing sodium, were completed. In addition, four internally pressurized control tests were performed, also in flowing sodium. A summary of the conditions and results are presented in Tables 1 and 2.

On the basis of the results of these tests, it was learned that NaK pressurization does not alter the creep behavior, based on the data obtained in static sodium or in helium. The results of tests under steady-state internal heating were in conformance with the behavior anticipated from static sodium tests. It was found that thermal cycling reduced the life, based on predictions derived from static sodium data and secondary creep. The effect of frequency and internal pressure strongly suggests that a nonlinear primary creep mechanism, ratcheting, is primarily responsible for the enhanced creep rate, the lack of grain boundary voids, and the reduced life.

TABLE 1

STRESS-RUPTURE IN DYNAMIC SODIUM WITH INTERNAL HEATING

Specimen No.	Heat Flux (Btu/ft^2-hr)	Heat Flux Condition	Rupture Time (hr)	Mechanical Hoop Stress (psi)
30	1×10^6	Steady	177	21,000
36	1×10^6	Steady	558	16,000
34	1.5×10^6	12 min cycle	5§	21,000
38	1×10^6	12 min cycle	198§	16,000
32	1×10^6	12 min cycle	227	21,000
40	1×10^6	12 min cycle	173	21,000
42	1×10^6	2 min cycle	134	21,000
44	1×10^6	2 min cycle	163	21,000
46	1×10^6	2 min cycle	398	17,700
48	1×10^6	2 min cycle	419	17,700

Specimen No.	Calculated Thermal Stress (psi)	Peak Strain (%)	Peak Strain Rate* (in/in-hr)	Actual Life / Predicted Life†
30	8,300	2.2	1.2×10^{-4}	0.9
36	8,300	2.8	4.5×10^{-5}	1.1
34	12,400	3.6	---	---
38	8,300	1.0	1.1×10^{-4}	---
32	8,300	3.6	3.2×10^{-4}	0.57
40	8,300	3.6	4.2×10^{-4}	0.43
42	8,300	3.6	5.4×10^{-4}	0.33
44	8,300	3.6	4.4×10^{-4}	0.41
46	8,300	3.6	1.8×10^{-4}	0.55
48	8,300	3.6	1.8×10^{-4}	0.56

*Based on the time the heat flux is on

†Prediction is based on isothermal data obtained in static sodium

§Heater failed prior to cladding

TABLE 2

BIAXIAL STRESS RUPTURE WITHOUT INTERNAL HEATING

Specimen No.	Heat Flux (Btu/ft^2-hr)	Heating Condition	Rupture Time (hr)	Mechanical Hoop Strain (psi)
31	0	No Flux	750	26,000
33	0	No Flux	931	19,000
35	0	No Flux	351	26,000
37	0	No Flux	479	26,000

Specimen No.	Maximum Hoop Strain at Failure (%)	Average Temperature (°F)	Actual Life / Predicted Life
31	2	1210	1.0
33	~0	1245	0.88
35	1	1245	0.9
37	1	1235	1.1

B. BACKGROUND

The combined effects of a biaxial stress state created by fission gases and fuel swelling, fast neutron (>1 Mev) exposures to 10^{24} nvt, flowing sodium at 1200°F, clad surface temperatures up to 1400°F, and both static and varying thermal stresses, present a series of complex problems in the selection of alloys for fast reactor fuel pin applications. Naturally, it is desirable to test candidate materials for cladding under those conditions anticipated in the course of application. However, this is not always feasible because of cost and the limited volume of fast reactor test space which cannot sustain extensive experimentation. Therefore it is necessary to attempt to simulate the nonnuclear aspects of these conditions in the laboratory so as to provide reliable selection data. It follows that the factors in the environment and in the metal which influence the life of cladding are germane to the alloy selection procedures, and much interest has been manifested in these factors. In spite of the intense interest, neither selection processes nor design criteria are completely established.

We are currently focussing some effort on the mechanisms and effects of mass transfer.[1] Of particular interest is the influence of mass transfer on the life of stressed cladding. Carburization, decarburization, and depletion of alloying constituents in dynamic sodium are prime examples of this phenomenon. In addition, as a direct consequence of leaching-out of nickel, the γ to α transformation occurs at the surface. It is not clear whether compositional changes and the associated transformation produce a significant change in the stress-rupture and creep behavior. This aspect is under consideration in this phase of the cladding program.

In addition to mass transfer and the formation of ferrite layers on the surface, both static and cyclic thermal stresses may significantly reduce the time to rupture of stressed tubes. For example, a recent theoretical analysis performed in England strongly suggests that low-cycle thermal stresses ought to produce ratcheting and enhanced creep rates.[2,3] There is support in the literature for the concept that dynamic stresses superimposed on static stresses increase the rate of deformation.[4-7] If the strain at failure is a constant, regardless of how this strain is produced, then the increased rate of deformation as a result of both static and cyclic stresses may significantly reduce the life of the material. At present, no experimental studies of the combined effects of static and cyclic stresses have been performed in sodium. Such information would be valuable in the selection procedures, particularly since some materials are known to exhibit different behavior under cyclic thermal stresses.

A technique developed at AI offers a powerful tool with which to determine the influence of mass transfer, static thermal stresses, and low-cycle thermal fatigue on the rupture life and creep rate of potential clad materials.[8] This method consists of inserting a high flux heater ($\sim 10^6$ Btu/ft^2-hr) inside a tube of cladding, sealing the ends, and pressurizing with NaK. In addition, an external shroud assembly which increases the flow rate of sodium past the cladding is attached. The heater assembly is then inserted in the sodium loop for testing. Identical assemblies, except for the absence of a heat flux, were employed as control tests designed to evaluate the effects, if any, of NaK on the stress rupture behavior.

Clearly, the stress-rupture and creep action under biaxial stresses, thermal stresses, and flowing sodium are dependent on microstructural phenomena.

To properly analyze the macroscopic behavior, metallographic studies for identification and distribution of second phases were performed. Carbide precipitation at grain boundaries is particularly significant. In addition, etching techniques, magnetic tests, and x-ray diffraction experiments were employed to detect the presence of ferrite at the surface, arising from mass transfer. It is hoped that with a proper evaluation of the dynamic sodium tests and microstructural studies, a better set of the alloy selection standards will be forthcoming.

C. CONTROL TESTS

In order to establish the validity of the results obtained from specimens which are both heated and pressurized internally, it is necessary to employ control tests. The purpose of the control experiments is to determine the effect, if any, of NaK pressurization on the stress-rupture and creep behavior of cladding. This need arises because NaK may reduce the life of cladding by action at the inside surface of the cladding specimen. For example, the removal of the oxide surface layer may reduce the surface barrier to dislocations, or NaK may penetrate the metal along grain boundaries and reduce the load carrying capacity of the metal. In either case, these experiments will serve to ascertain the influence of NaK on the stress-rupture behavior.

Stress-rupture data on control specimens in dynamic sodium were compared to the stress-rupture data obtained in static sodium.[9] The data for control specimens in flowing sodium superimposes on the stress-rupture data obtained in static sodium within the uncertainty in temperature. This means that NaK pressurization and dynamic sodium did not substantially alter the biaxial stress-rupture life of cladding.

The salient features of the microstructures of control specimens are identical to those observed after testing in static sodium. The presence of voids at grain boundaries, intergranular failures, carbide precipitation phenomena, and the absence of sigma phase are all similar. Thus, the mechanisms leading to failure do not appear to be sensitive to the external environment. Rather, these are related to load, temperature, and geometry. No evidence of intergranular penetration by the NaK or by the sodium was found at either surface.

One important observation from the microstructural observations is that all of the control specimens tested in flowing sodium exhibited a thin surface layer, probably ferrite. The thickness of the layer varied from specimen to specimen depending on the temperature and the duration of exposure to sodium and ranged up to 0.3 mil. Magnetic measurements confirmed the presence of ferrite on three of the specimens.

The presence of a ferrite layer on the control specimens (not internally heated) can be explained. In order for mass transfer effects (corrosion and ferrite layer formation) to occur, two conditions must be fulfilled: (1) the concentration of the transported species must be locally undersaturated in the bulk sodium, and (2) the kinetics of transport must be fast enough to permit transfer to occur in a reasonable amount of time.[1] The kinetic criterion is fulfilled because the sodium velocity was 20 ft/sec and the temperature was above 1200°F. The undersaturation of the bulk sodium with respect to nickel occurred because the temperature of the sodium was raised. This increase in temperature was first created by the presence of a heater upstream from the control specimen. Later, after the heater was removed from the loop, it was necessary to raise the bulk sodium temperature 25°F to simulate the condition used previously. Thus, the control specimens spent the majority of their lives exposed to sodium at a slightly higher temperature.

An important question to this work is what influence does a ferrite layer and associated surface removal have on the mechanical properties of cladding materials at elevated temperatures. While this question is yet unanswered for long term tests, the ferrite layer does not appear to adversely affect the stress-rupture behavior for times less than 1000 hr.

In the case of the control specimens, the cladding interacted with the shroud subassembly which surrounds the cladding. This subassembly is used to promote turbulence and hydraulic centering. A wire helix on the inside surface of the shroud acts in this capacity which is vital to the mass transfer aspects of the behavior of the internally heated specimens. However, the shroud played an active role in the behavior of the control specimens without internal heating. This is evidenced by the presence of a polished zone (corrosion) on the surface of the cladding adjacent to the wire of the helix and in the presence of a ferrite layer on the surface. A polished zone was observed on certain areas of the

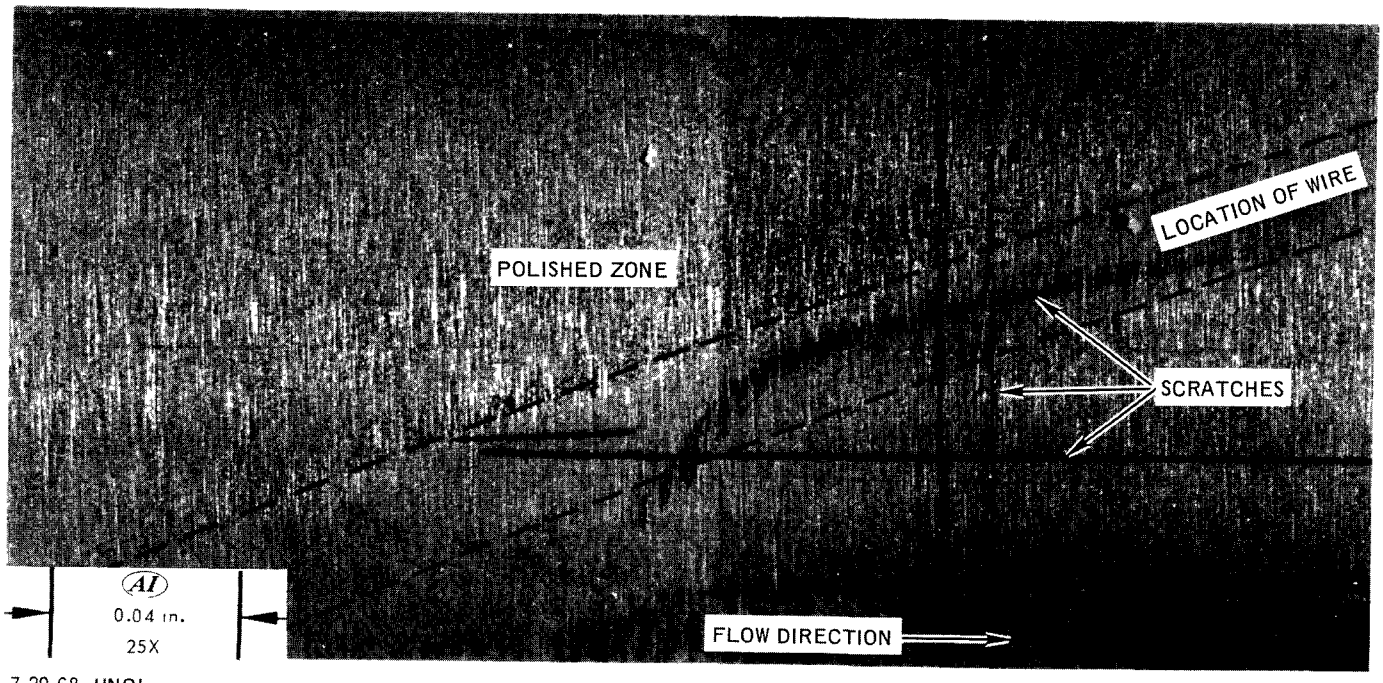

Figure 1. Imprint of Wire Helix and Associated Polishing on the Surface of Control Specimen

surface of the control specimens. This can be seen in Figure 1. While the source of the polishing may be related to corrosion, no effect on the mechanical properties was observed. Cracking was not associated with the polishing or with the ferrite layers.

The wire helix interacted with the cladding in another way which has important implications in the design of fuel assemblies. For the control specimens, the strain was not limited to one region but was more or less uniformly distributed along the length. As a result of the uniform strain, the cladding impinged on the wire helix attached to the inside surface of the shroud. For control test assembly No. 31, which exhibited the largest diametral strain measured, 2%, this resulted in an imprint of the wire in the cladding surface and subsequent failure as seen in Figure 2. While the conditions associated with the shroud assembly-cladding interaction by no means duplicates the conditions normally designed into the fuel pin and spacer assembly of a fuel bundle, it is clear that

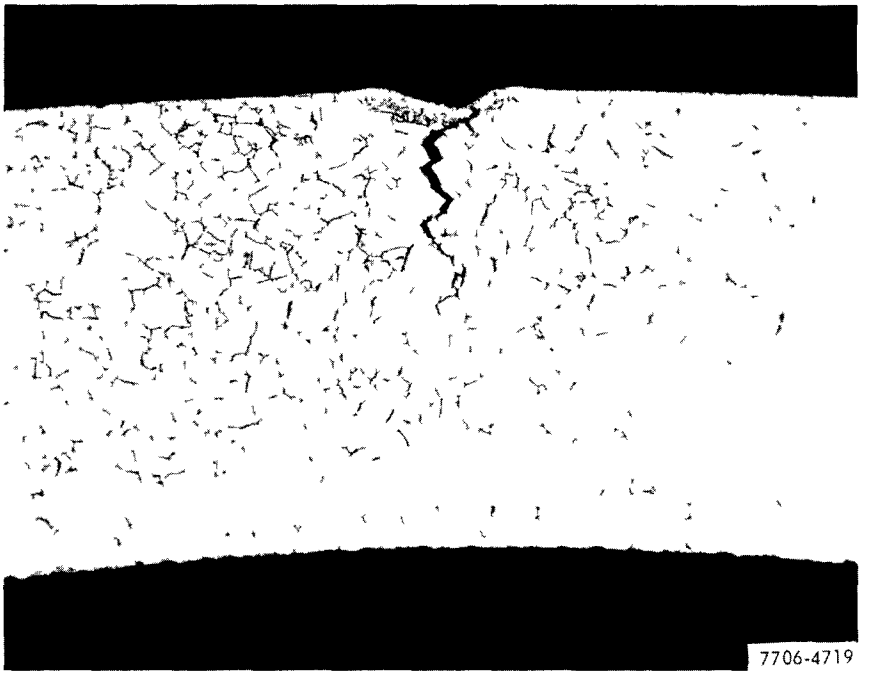

7706-4719
8038-15-1 250X
Rieth's Reagent Assembly No. 31

Figure 2. Fracture Zone Associated With Wire Helix Imprint on Cladding

adverse stress conditions can cause localized deformation zones on the surface of cladding that result in the formation of cracks. It should be noted in Table 2 that the rupture life of this control specimen did not appear to be significantly affected by the imprint.

In addition to the wire imprint interaction described above, another interaction between the wire helix and the cladding was observed. This interaction was a pressure bonding of the cladding to the wire at one point to the test specimen of control test in assembly No. 33. No other welds were found. The weld zone shown in Figure 3 extended 1 mil into the cladding. Flaw detection indicated two possible sites for failure, one at a conventional site and one at the weld region. No cracks were evident in the microstructure. This inability to locate the fracture is not uncommon. A similar difficulty in finding cracks has

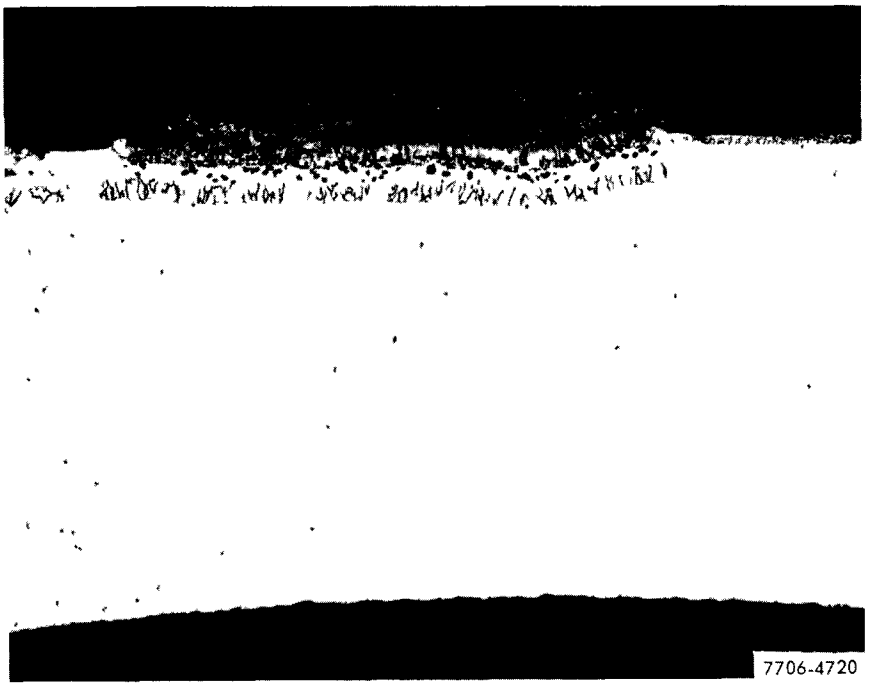

Figure 3.
Weld Zone on Cladding Surface due to Interaction With the Shroud Assembly

8038-12-4 250X
Vilella's Etch Assembly No. 33

sometimes occurred for specimens tested in static sodium.[9] Basically, it is believed that failures in these cases are best described as pinholes rather than tube bursts. In any case, it is entirely possible that incipient cracking took place in the region surrounding the weld zone.

In summary, the effects of NaK pressurization or corrosion on the stress-rupture behavior of internally pressurized tubes in a flowing sodium environment are too small to be detected in the time scale present for these tests. Examples of interactions which are estimated to have no effect on the short term properties remain possible problem areas for long term tests. While these aspects are of interest, the control tests completely verified the use of NaK as a means of internally pressurizing cladding during tests even when cladding is under internal heating.

D. STRESS-RUPTURE UNDER STEADY-STATE HEATING

The purpose of tests of both internally pressurized and heated specimens in dynamic sodium is to simulate conditions anticipated in fast reactors for fuel cladding. As a direct result of internal heating, thermal stresses are generated

and superimposed on the mechanical stresses, interstitials migrate from the outside to the inside material in the wall, and the conditions favoring mass transfer are formed. It is vital to the designer of fuel pins to be able to assess the magnitude of these effects both separately and in concert.

For creep under combined mechanical and thermal stresses, it is to be expected that the thermal stresses will disappear due to stress relaxation. The amount of stress relaxation at the outer fiber due to secondary creep can be estimated from the creep equation. However, this estimate is too low because the initial loading from internal pressure and from the heat flux through the wall will produce a certain amount of primary creep. Since the strain associated with the creation of thermal stresses is small, $\epsilon_t \cong 10^{-5}$, almost all of the thermal stress is removed by deformation on loading. This gives rise to nonuniform straining across the wall of the tube. It is this strain gradient that plays a crucial role in the behavior of the thermally cycled specimens. For the steady-state heating, what is important is that the thermal stress is relaxed completely and creep then occurs under the combined action of the mechanical hoop stress generated by the internal pressurization and of the temperature gradient through the wall.

The influence of the temperature gradient complicates the creep behavior of the tubes. The hotter material on the inside should creep faster than the cooler surrounding materials in the outer fibers, providing these fibers are stressed identically. For the case in point, the fibers are initially stressed differently but this relaxes due to primary creep. The extent of the relaxation may not be as complete as indicated earlier because of the temperature gradient.

If the fibers in the tube wall were stressed the same under a steady-state temperature gradient, the inner fibers would tend to deform faster than the cooler outer fibers. From a standpoint of plasticity, this violates the compatibility relations for plastic flow. What happens, of course, is that the stress gradient induced initially relaxes sufficiently to compensate for the thermal gradient in such a way that the material strains at a uniform rate across the wall. In essence, this means that the stress at the outer fiber decreases by primary creep to give a secondary creep rate which matches the creep rate at the midwall position. As a result of the balance between the inner and outer fibers, due to the difference in temperature, the material in the wall of the tube

creeps uniformly at a stress and temperature corresponding to that at the midwall. In other words, the secondary creep rate of the tubes under the combined action of a mechanical and thermal stress and the temperature gradient is determined by the stress and temperature at the midwall position.

The conclusion that the secondary creep rate at the center of the wall is the overall creep rate for the tubes once the initial compensating aspects have occurred enables the tests in static sodium to be compared directly to the tests of steadily heated specimens in flowing sodium. Before such a direct comparison can be made, some mention of the temperature distribution associated with the tests under steady-state heating should be made. The temperature distributions through and along the wall were calculated by heat transfer analysis.[10] Clearly, creep and the associated failure will occur at the highest temperature and stress point. Therefore, if the tests with internal heating are to be compared directly to the tests in static sodium, then they should be compared at the temperature and stress at the midwall in the peak region.

The comparison between the tests in static sodium and the tests in flowing sodium with internal heating is displayed in Figure 4. The temperature band represents the uncertainty in the expected behavior based on static sodium data

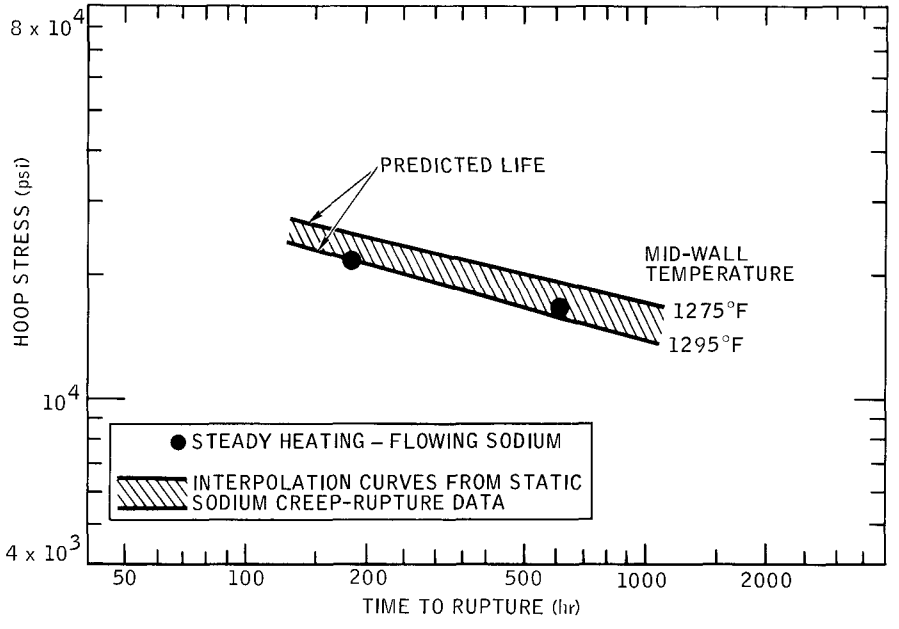

7-016-251-20B

Figure 4. Predicted Life vs Actual Life of Tubes Under Steady-State Heat and Pressure

and was drawn by interpolating the static sodium data for the limits of uncertainty in the peak midwall temperature of the internally heated tubes.[10] On the basis of this interpolation, it appears that the behavior of the tubes under internal heating and pressure can be predicted from isothermal stress-rupture data for the peak temperature conditions. Thus, while the presence of a high heat flux complicates the interpretation of the behavior, in the last analysis creep is, under a steady state thermal gradient, primarily a function of stress and temperature. If these two factors are known with some certainty, the behavior can be predicted directly from isothermal test data.

It is instructive to compare the average strain rate (strain at failure divided by the time to failure) for the hoop direction in both the static and dynamic sodium tests. As before, it is possible to make a comparison by drawing the strain-rate stress curves for the uncertainty in temperatures found at the peak midwall position for the internally heated tubes. By using the stress and temperature range at the midwall point, the results of the present tests are found to fall within the band. This is displayed in Figure 5. The close agreement between the tests in dynamic sodium with internal heating and pressure and the

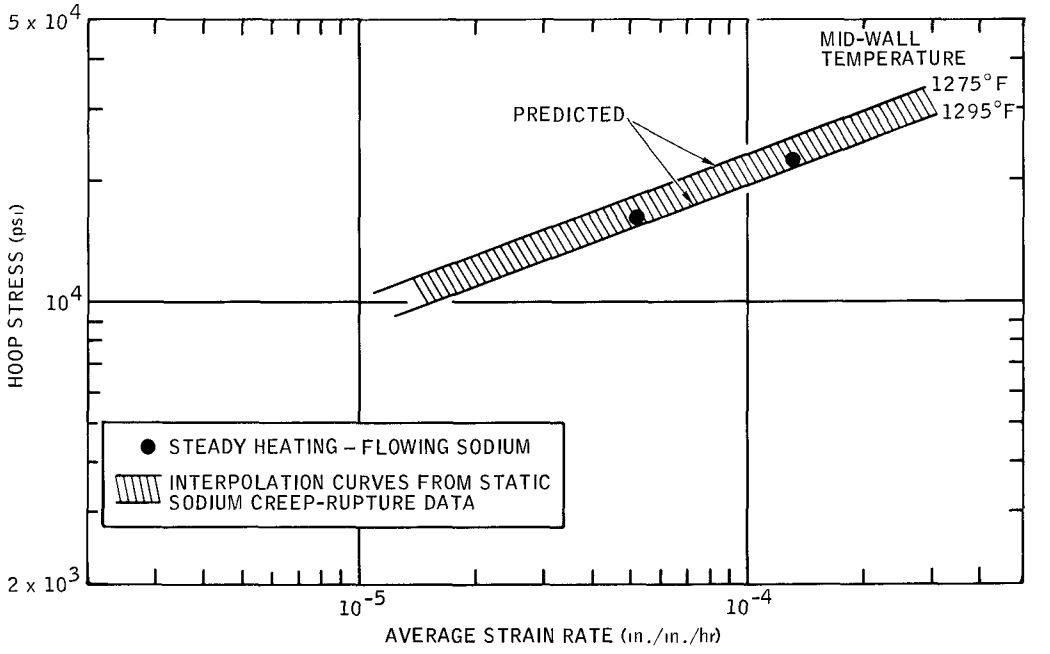

Figure 5. Effect of Stress on the Average Strain Rate

predicted behavior derived from static sodium data strongly supports the concept that the creep behavior, and probably failure, are governed by the stress and temperature at the peak temperature position and at the midwall location.

The microstructures of specimens tested with internal pressure in static sodium and the specimens tested with internal heating and pressure in dynamic sodium are essentially the same. The microstructure of the internally heated specimens are shown in Figure 6. In summary, the microstructures exhibited: (1) intergranular failure, (2) extensive void formation throughout the wall, (3) little or no sigma phase, and (4) carbide precipitate at the grain boundaries. These observations are a further confirmation that internal heating does not radically change the behavior mechanically or metallurgically from that anticipated from isothermal tests.

One important observation concerning the microstructure of the steady heated specimens was the presence of a ferrite layer on the outside surface of the cladding material. This layer can be seen in Figure 6 and is not unexpected, since the conditions associated with an internally heated tube favor corrosion and mass transfer.[1] The maximum thickness of the layer occurred in the peak temperature region and was 0.43 mil thick for the 558-hr test. The growth of the ferrite layer for all specimens appears to be parabolic with time, indicating that the growth is diffusion controlled. On the basis that the ferrite layer does not contribute directly to the load carrying capacity of the tube, it is possible to estimate that the ferrite layer should reduce by 4% the stress-rupture life. This is too small to be seen in the comparison to the static sodium tests.

On the surface of the internally heated tubes, a polished zone was observed in the region of the heating element. This polished zone is undoubtedly associated with the removal of surface by corrosion. However, even for the longest testing time under the steady heat flux, the amount of surface removal was too small to be detected by measurements of the wall thickness. In fact, the extent of surface removal (polishing) was too small to even remove all of the surface scratches introduced in the mill cleaning treatment. Therefore, as was the case for ferrite layer growth, the effect of surface removal was not observable in the stress-rupture behavior of the tubes tested under a steady heat flux. This does not mean that either surface removal of metal or growth of ferrite layers are not problems as far as the prediction of the long term behavior of pressurized tubes with internal heating.

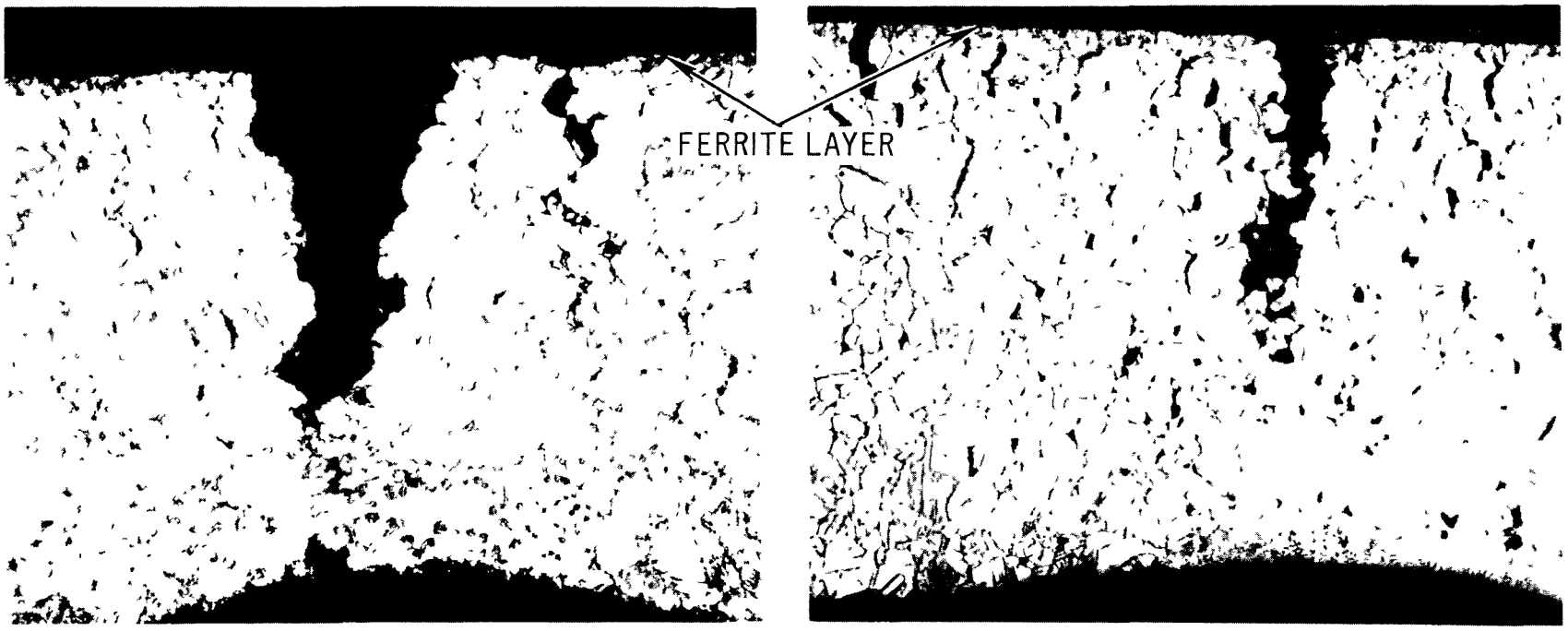

7-016-251-23

Figure 6. Comparison of Microstructures in Rupture Area

In summary, the stress-rupture behavior of tubes of Type 304 stainless steel under a steady internal heat flux of 10^6 Btu/ft^2-hr and with a high internal pressure parallels the same behavior of the same material under an internal pressure in static sodium at the appropriate temperature. In addition, the average strain rate data of the heated tubes was in agreement with that predicted from tests in static sodium for the peak midwall temperature. The similarity in microstructures and cracking morphology coupled with the above indicates that the creep-rupture behavior can be accurately predicted directly from stress-rupture test results, when under internal pressure but without internal heating.

E. STRESS-RUPTURE UNDER CYCLIC HEATING

The main goal of the stress-rupture tests in which tubes of Type 304 stainless steel are pressurized and exposed to a cyclic heating is to simulate the variation in heat flux through the wall of the fuel cladding as a result of load variations in the reactor. In the present tests, the internal heater is turned off and on. This is the only difference between these tests and the steady-state tests. Therefore, it is useful to compare the results of these tests with those of the steady heated tests.

The strain profiles obtained for the tests under a cyclic heat flux exhibited some important differences when compared to those under steady heating. The strain at the peak temperature was 50% greater in the cyclic tests than in the steady heating tests. Also, the strain profile was much sharper for the cyclic heat flux condition, indicating that deformation was more localized under this test condition.

The appearance of the microstructure and the cracking were different for the thermally cycled specimens in contrast to the steady heated specimens. This can be seen by comparing the microstructures in Figure 6. For the cyclic heat flux condition, the amount of void formation is essentially limited to the region surrounding the failure in the tube. On the other hand, voids were present throughout the cross-section of the steady heated tubes. This perhaps means that most of the deformation took place in the region where the cracks were nucleated in the cycled specimens. The absence of extensive void formation, except in the rupture area, indicates that thermal cycling brings into play different deformation mechanisms than steady conditions or isothermal tests in static sodium.

Cracking under thermal cycling and internal pressurization is intergranular. In this sense, the mechanisms of failure are the same for both kinds of test. In three of the tubes tested under a cyclic heat flux, however, multiple fractures were observed. This suggests that cracking may be autocatalytic in nature; viz, once a crack is nucleated, it propagates independent of any other cracks present. Occasionally, multiple cracks have been seen in the isothermal tests in static sodium. No multiple cracks were observed in the two steady heated specimens.

One point of view that can be adopted in evaluation of test results is that the life is determined by competition between creep processes; i.e., thermal recovery and work hardening. If the only effect of cyclic heating is to alter the creep rate through the changes in stress and temperature, then it should be possible to estimate the life by comparing creep rates with and without a heat flux applied. The following creep rates were estimated, by use of data obtained from tests conducted in static sodium.

TABLE 3

CYCLING EFFECT ON CREEP

Thermal Condition	Stress (psi)		Wall Temperature (°F)	Average Creep Rate (in/in-hr)
	Static	Thermal		
Heat-on 1/2 cycle	21,000	8,300	1260	1.3×10^{-4}
Heat-off 1/2 cycle	21,000	0	1220	1.2×10^{-5}

One interpretation of the analysis of the cyclic creep data in this table reveals a very interesting point. On the average, the specimen creeps at a 10 times faster rate during the heat-on portion of the cycle. If creep processes where the stress and temperature are greater determine the life of the specimen, then the difference in creep rates strongly suggests that rupture life is essentially determined by the time the heat flux is passing through the wall. Consequently, an internally heated specimen operated cyclically should last twice as long as a specimen operated under steady heating at the same maximum stress and temperature.

Another interpretation of the analysis of cyclic thermally stressed tubes under biaxial tension is that creep rate is a known function of stress and temperature. We may assume that the average creep rate obeys a law of the form:[11]

$$\dot{\bar{\epsilon}} = A\sigma^n \exp(kn\,T/100) \qquad \ldots(1)$$

where

$\dot{\bar{\epsilon}}$ = average creep rate,

A = material constant,

n = stress parameter = 3*,

kn = temperature parameter = 0.9*, and

T = average temperature in °F.

The specimen spends half its life at $+\Delta T$ and $+\Delta\sigma$ above some average condition and $-\Delta T$ and $-\Delta\sigma$ below; then the net creep rate is given by

$$\dot{\bar{\epsilon}} = \dot{\bar{\epsilon}}_o \left\{ \left[1 + \frac{m(n-1)}{2} \left(\frac{\Delta\sigma}{\sigma} \right)^2 \right] \cosh \frac{kn\,\Delta T}{100} + \left(\frac{n\,\Delta\sigma}{\sigma} \right) \sinh \frac{kn\,\Delta T}{100} \right\}, \qquad \ldots(2)$$

where $\dot{\bar{\epsilon}}_o$ is the creep rate at the average temperature and stress.[11]

The results of the analyses are displayed in Figure 7; as can be seen, neither the prediction for the peak condition nor the prediction based on Equation 2. Therefore, the specimen life was less than anticipated even when the temperature and stress cycling are taken into account. This difference between theory and experiment points out the danger in indiscriminate use of creep equations to predict the behavior of fuel cladding as the result of reactor load cycles.

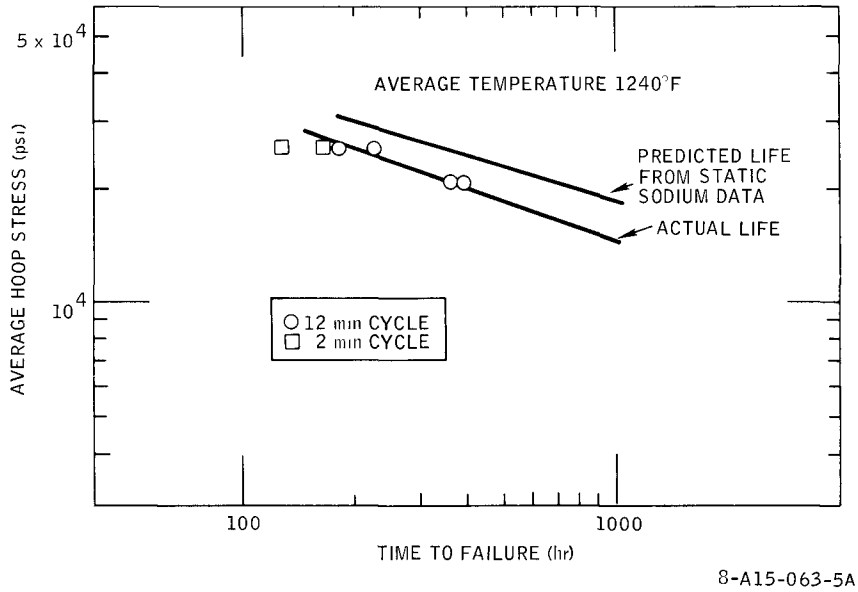

8-A15-063-5A

Figure 7. Predicted Life vs Actual Life of Tubes Under Cyclic Heat and Static Pressure

Two important test parameters were varied for the cyclic tests in dynamic sodium, the frequency and the internal pressure. The frequency dependence is important because it is necessary to extrapolate laboratory test conditions to the lower cycle rates expected in fast reactors. The validity of the results of the cyclic tests depends in part on how the frequency of cycling effects the creep behavior. In the case of the present tests, two frequencies were selected. The 12-min cycle was chosen because it gives 1000 cycles in a 200-hr test. In the course of 1000 days, the reactor fuel cladding will experience at least 1000 daily load variations. The 2-min cycle was selected to determine the frequency effect and this frequency could be conveniently achieved with the present test facilities.

The increased cycle rate did reduce the life of the specimen a small amount, see Figure 7; however, the life was not decreased by as much as the frequency was increased. Thus, if there were no cycling frequency effect, the tubes cycled at a higher rate would have had six times the number of cycles; this is not the case. Thus, the attendant rate of deformation has more to do with the time to failure than the number of cycles per hour. This observation is important because if thermal fatigue were operative, the frequency would be a large factor in the life of the specimen.[12]

F. RATCHETING MECHANISM

The enhancement of creep by a ratchet mechanism is a possible mechanism by which the present observations on the cycled tubes can be explained. During the "on" portion of the heat cycle, the induced thermal stress relaxes by primary creep. This gives rises to a strain gradient in the wall of the tube. During the "off" portion of the heat cycle, only the mechanical stress due to internal pressure and the residual stresses created by the strain gradient are present. The strain induced stresses are opposite to the thermal stresses created by internal heating. Thus, during the "off" half cycle, the nonuniform stresses again relax by primary creep. Because of the lower average temperature during the "off" period, the extent of creep is less than during the "on" period, but may not be complete during the "off" period. As a result, in the next heat cycle less thermal stress can be generated because the strain is present which reduces this stress. After a few cycles, the extent of creep during each half cycle is such that total strain per cycle is constant.

It should be possible to calculate the amount of damage created per cycle by using the creep equation for primary and secondary creep. This equation is

$$\epsilon_T = \epsilon_o + \epsilon_t(1 - e^{-t/\tau}) + \dot{\epsilon}_s t \qquad \ldots(3)$$

where

ϵ_T = the total strain,

ϵ_o = the initial strain on loading,

ϵ = the limiting transient creep strain,

τ = the ratio of transient creep rate to transient creep strain,

t = the time, and

$\dot{\epsilon}_s$ = the secondary or minimum creep rate.[13]

There is some data available from the literature for describing creep in annealed 18-8 stainless steel at 704°C.[13] Since the peak stresses relax during both the on and off half cycles, the application of the data to the present situation is complicated because the parameters in Equation 3 are sensitive to stress. In addition, the temperature of the present work is lower for both half cycles. Nevertheless, the data can be used to estimate the value of the creep strain during each half cycle. In order to estimate the creep strain per cycle, it is necessary to pass through a transient period before a saturation effect in cycling is reached. The transient and saturation behaviors are depicted in Figure 8.

At the beginning of the first half cycle, a thermal stress in the wall is established by the heat flux by differential thermal expansion. The strain gradient and the associated thermal stress decrease during the heat-on part of the cycle due to primary creep. This decrease is evident in the stress and strain profiles at the end of the first half cycle. At the start of the second half cycle, the heat flux is removed and the thermal gradient becomes zero. The strain distribution, however, is nonuniform. Thus, at the start of the second half cycle, the strain gradient gives rise to a residual stress gradient opposite to the thermal stress gradient. Under the combined action of the residual stress and the pressure stress, the material creeps. This creep is nonuniform and partly removes the residual stress. This is because at the lower temperature primary

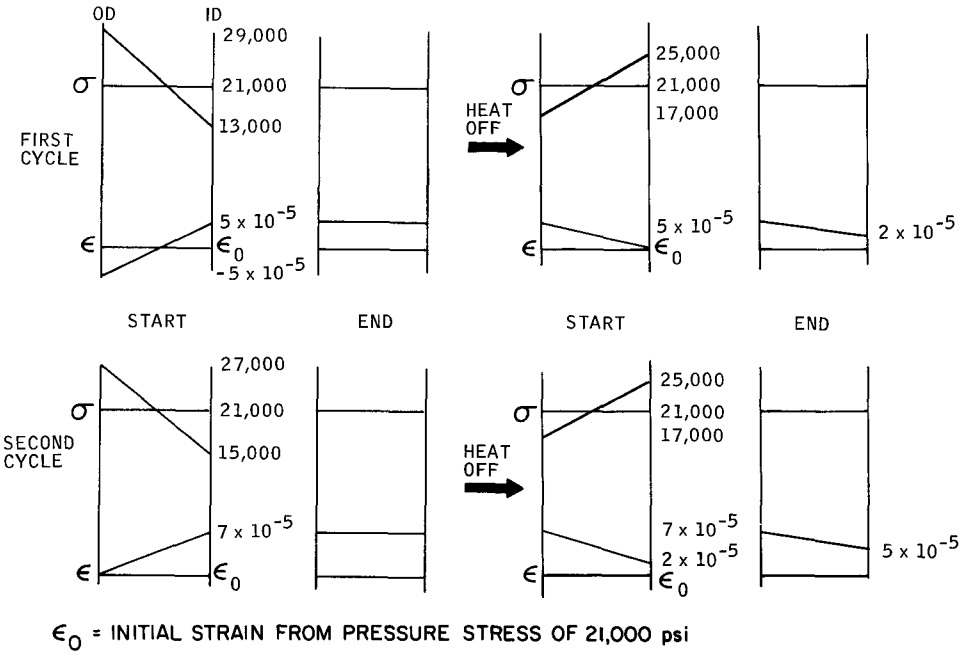

Figure 8. Effect of Thermal Cycling on Stress and Strain Profiles

creep during the heat off half cycle is less than that which took place during the previous half cycle. The situation at the end of the second half cycle shown in Figure 8 reflects the partial stress relaxation.

During subsequent cycles, primary creep is altered. At the start of the third half cycle, the heat flux induces a strain gradient which is partly cancelled by the already existing strain gradient of opposite sign. The net effect produces a smaller strain gradient from internal heating than existed during the first half cycle and consequently a smaller thermal stress. This thermal stress relaxes completely by the end of the third half cycle. As before, when the heat flux is turned off, the nonuniform plastic strain creates reverse residual stress.

As before, this residual stress is partly relaxed by the end of the fourth half cycle. Additional cycles repeat the situation for the second cycle, approaching a minimum amount of creep deformation per cycle. The minimum amount of primary creep is determined by that creep which takes place during the second half of each cycle.

The process of ratcheting will go on until the cladding fails under the internal gas pressure and thermal cycling. Adding the creep strains developed

during the off period of each cycle gives a total creep deformation of 3% for 1000 cycles. While this estimate is lower than the actual deformation of 3.6%, a low estimate can easily be attributed to a neglect of secondary creep and to the initial plastic strain after internal pressurization.

The mechanism described above can be extended to qualitatively explain the effects of frequency of cycling on the stress-rupture life of the internally heated specimens. In review, when the frequency was increased by a factor of 6, the strain per cycle decreased by a factor of 4. This simply reflects the influence of primary creep which is an exponential function of time. At the higher cycle rate, the period of time during which creep takes place is 1/6 that of the earlier tests. Since primary creep is nonlinear in time, proportionally more creep can occur during the one-minute half cycle than during the six-minute half cycle. This means that in one minute the amount of creep strain is more than 1/6 (actually 1/4) that for a 6-min half cycle. In fact, by using the same creep data, it appears that the creep strain per cycle for the higher frequency is indeed one fourth. If all the creep strain were due to secondary creep which is linear in time, then the higher cycle rate should result in one sixth the creep strain per cycle and six times the number of cycles than for the slower cycle rate. This is not observed. In this work, the specimens experienced only 4000 cycles at the higher rate and 1/4 the strain per cycle. Thus, it appears that while secondary creep may occur, most of the deformation is associated with primary creep during each cycle.

The influence of the mean pressure stress can also be explained by using the creep equations described previously. The tests at lower mechanical pressure stress but at the same internal heat flux and cycle rate showed a longer stress-rupture life. This, undoubtedly, is a direct result of a smaller amount of primary creep during the off portion of the cycle. The decreased strain then limits the amount of creep due to increased thermal stress during the next period. The creep rupture life under cyclic behavior paralleled that for the steady heated specimens. The parallel behavior is perhaps a manifestation of the stress dependency of creep. Both secondary creep and primary creep are reported to have the same functional relation to stress.[13]

The British have treated the thermal cyclic effect in detail.[2,3] While many of the ideas presented above are essentially the same as those presented by the British, one important difference must be considered. In the British work, the increased strain resulting from cycling the internal heat flux takes place because of the nonlinear dependence of secondary creep on the stress. This is undoubtedly valid for the case where the specimens are cycled every 100 hr. However, the results for thermal cycling do not conform to use of secondary creep in the analysis. Moreover, it is not possible to rationalize the frequency effect observed in this study by a secondary creep mechanism or incremental creep mechanism. However, secondary creep is likely to play an important role for longer cycle periods such as 24 hr. Nevertheless, for all cycle rates, primary creep should be considered in addition to secondary creep in describing the ratcheting mechanism of deformation.

III. EVALUATION OF EFFORT DURING FISCAL YEAR 1968

The activities of this subaccount during the past fiscal year have defined the goals for determining the combined effects of internal pressure, static and varying heat fluxes, high temperature, and flowing sodium on the creep-rupture behavior of Type 304 stainless steel. While much of the phenomena remain to be studied in greater depth, the impact of a preliminary evaluation of these results for reactor technology has prompted a growing interest in the high flux heater assembly with cladding. Several important milestones were reached which bear a direct relation to the fast reactor industry.

1) NaK pressurization and thermal bonding does not influence the life of cladding under stress for times less than 1000 hours.

2) The effects of a static heat flux superimposed on an internal pressure on the rupture life can be explained completely by the temperature-stress sensitivity of secondary creep.

3) The effects of a cyclic heat flux added to the internal pressure increases the creep rate and decreases the rupture-life of cladding more than expected on the basis of secondary creep.

4) The effects of a cyclic heat flux added to internal pressure can be explained semiquantitatively in terms of a ratcheting mechanism which uses primary creep.

The significance of these results coupled with an increasing interest in the problem of thermal ratcheting implies that additional work is required to factor thermal cycling into the creep and failure criteria in fast reactor design. Hopefully, these preliminary results when added to future studies will identify and define an improved basis of alloy selection and design criteria for fuel cladding for LMFBR.

REFERENCES

1. J. Hopenfeld and D. Darley, "Dynamic Mass Transfer of Stainless Steel in Sodium Under High Heat-Flux Conditions," NAA-SR-12447 (July 15, 1967)
2. J. Bree, "Ratchet and Fatigue Mechanism in Sealed Fuel Pins for Nuclear Reactors," TRG Rep 1214 (D) (March 1966)
3. J. Bree, "Ratchet and Enhanced Creep Strains in Sealed Fuel Pins for Nuclear Reactors," TRG Rep 1311 (D) (August 1966)
4. A. H. Melaka, "Combined Fatigue and Creep," Met. Rev. 7, 43 (1962)
5. G. J. Moyar and G. M. Sinclair, "Cyclic Strain Accumulation Under Complex Multiaxial Loading," Paper 35, International Conference on Creep (1963), Inst. Mech. Eng., London, p 2 (47)
6. A. J. Kennedy, "Interactions Between Creep and Fatigue in Aluminum and in Certain of Its Alloys," Paper 13, International Conference on Creep (1963), Inst. Mech. Eng., London, p 3 (17)
7. S. Tarra and M. Ohnami, "Fracture and Deformation of Metals Subjected to Thermal Cycling Combined With Mechanical Stress," Paper 25, International Conference on Creep (1963), Inst. Mech. Eng., London, p 3-57
8. B. R. Hayward, E. L. Babbe, and D. K. Darley, "High Heat Flux Heater Development Preliminary Performance Tests," NAA-SR-12242 (December 31, 1966)
9. W. T. Lee, "Biaxial Stress Rupture Properties of Austenitic Stainless Steel in Static Sodium," - to be published
10. T. T. Shimazaki and D. K. Darley, "Temperature Distribution of an Internally Heated Tube in Flowing Sodium," NAA-SR-TDR-12565 - to be published
11. I. Finnie and W. R. Heller, "Creep of Engineering Materials," McGraw-Hill, New York (1959), Chapter 10
12. L. F. Coffin, Jr., "The Problem of Thermal Stress Fatigue in Austenitic Steels at Elevated Temperatures," Symposium on Effect of Cyclic Heating and Stressing of Metals, ASTM STP No. 165, Philadelphia (1954)
13. F. Garofalo, Fundamentals of Creep and Creep-Rupture in Metals, Macmillan, New York (1966), p 10-27

PAGE 210 is blank

Program:	FBR Fuel Development, Fuel Cladding and Structural Materials		
AEC Task:	10-D-3, Dynamic Loop Testing		
Project Manager:	J. L. Ballif/J. J. Gill		
Reporting Period:	Fiscal Year 1968		
General Order:	7706	Subaccount: 29543	AEC Category: 04-01-61-01.1

Principal Investigators: R. L. McKisson
J. Hopenfeld

I. PROJECT OBJECTIVES

The project objectives are to: (1) develop a model to describe the mass transfer process in cladding materials in a sodium environment and with a temperature gradient, and (2) develop a high heat flux heater capable of operating for a minimum of 1000 hours at a minimum heat flux of 1×10^6 Btu/hr-ft^2.

II. TECHNICAL PROGRESS DURING FISCAL YEAR 1968

A. HIGH HEAT FLUX HEATER

The development of the high heat flux heater has involved the completion of fourteen tests. Table I summarizes the tests performed and ranks them in order of their total service lives. Of the fourteen tests reported, four were begun during the previous fiscal year as cladding stress-rupture tests (30, 32, 34 and 36), six were stress rupture tests begun in FY 1968 (38, 40, 42, 44, 46 and 48), two were corrosion tests (50 and 52), and two were simple unclad heater performance tests (11 and 12). The basic heater design used in these tests is shown in Figure 1.

The basic heating element (6) is a graphite cylinder 0.125-in. in diameter and 2-in. in length. The graphite is well outgassed in vacuum at 3500°F prior to final machining, and great care is taken to ensure that the ends are normal to the axis and parallel within 0.001 in. maximum. The heater is polished on its cylindrical surface to be a snug slip fit inside the boron nitride insulator sleeve (5) which extends from the downstream end of the graphite heater along the nominal 0.125-in. diameter length of the molybdenum upper electrode (8) and terminates in the lavite insulator (13). The BN sleeve is fabricated with slightly thicker walls than its final size, and it is hand shaped and sized to be a slip-fit inside the neater sheath (10). The heater sheath has two sets of four lobes each, the outer diameter of which are hand shaped to slip freely (but not loosely) to fit the individual piece of cladding being tested. This is detailed in

TABLE I

HEATER PERFORMANCE ANALYSIS

No.	Total Service Life (hr)	Unclad Steady (hr)	Clad Steady (hr)	Unclad Cyclic (hr)	Clad Cyclic (hr)	Heater Heat Flux ($\times 10^{-6}$)	Construction Features	Comment
12	1117	1117	0	0	0	1.9	Double boot $MoSi_2$ coated electrode	Heater still operable at test termination. $MoSi_2$ and BN interacted.
32	1044	898	0	0	146	1.3	Single boot	Heavy oxide buildup on upper electrode. Heater barely operable at test termination.
11	763	763	0	0	0	1.3	Metal bellows	Bellows were quite stiff and heater was difficult to keep operating. $MoSi_2$ and BN interacted. Heater operable at test termination.
36	589	0	589	0	0	1.3	Single boot	Heavy oxide buildup on upper electrode. Heater failed by open circuit. Tungsten-carbon interaction was observed also.
40	585	498	0	0	87	1.3	Metal bellows (thin wall)	Heater still operable at test termination.
48	446	0	0	249	197	1.3	Metal bellows (thin wall)	Heater still operable at test termination.
30	330	107	0	0	223	1.3	Single boot	Heavy oxide buildup on upper electrode. Heater failed by open circuit.
44	231	149	0	0	82*	1.3	Metal bellows (thin wall)	Heater failed at tungsten wafer. Molybdenum electrode bloomed out and punctured BN insulation.
46	193	0	0	0	193	1.3	Metal bellows (thin wall)	Heater operable at test termination, but heater sheath was distorted, and heater was not reinstalled to complete its life. Found severe tungsten-carbon interaction. Heater was in incipient failure condition.
50	182	0	182	0	0	1.3	Metal bellows (thin wall)	Failure at tungsten wafer. Arc developed and punctured heater sheath.
42	122	0	0	55*	67*	1.3	Metal bellows (thin wall)	Failure at tungsten wafer. Molybdenum electrode bloomed out and punctured BN. Some reaction between the tungsten and carbon was found.
38	99	0	0	0	99	1.3	Metal bellows	Failure at tungsten wafer. Bellows was too stiff to permit good operating control of heater.
52	12	0	12	0	0	1.3	Double boot	Failure at tungsten wafer. Arc developed and punctured heater sheath.
34	12	0	12	0	0	1.3	Double boot	Heater did not start up properly. Failure by open circuit.

*One minute "on", one minute "off", other cyclic tests are 6 min "on", 6 min "off".

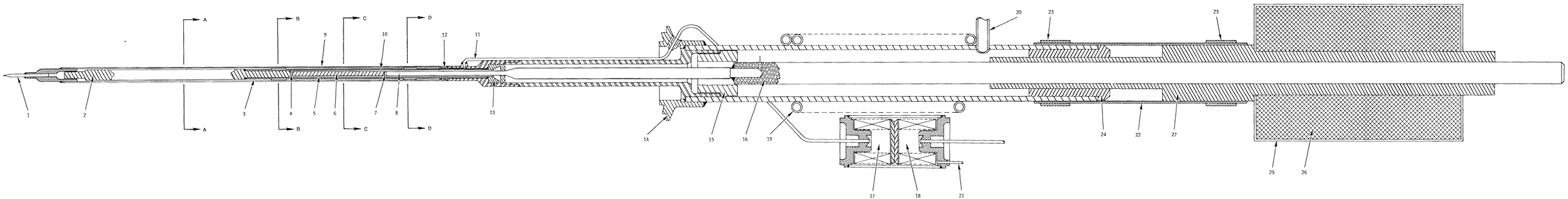

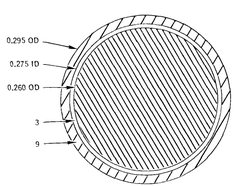

SECTION A-A

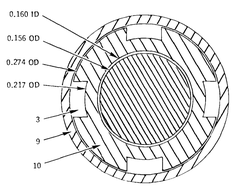

SECTION B-B

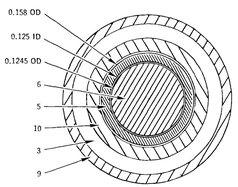

SECTION C-C

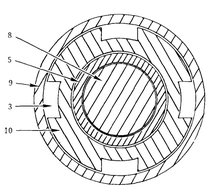

SECTION D-D

5-8-68 UNCL

7706-4732

7706-4732

Figure 1. High Heat Flux Heater Details

Sections B-B and D-D. Section C-C shows a midlength cross section of the heater zone. The section dimensions illustrate the clearances normally obtained.

The upstream end of the Model 3 heater consists of the heater sheath extension (2) which ends in a guide pin. The pin is free to slide in the heater tip. This sliding joint provides thermal expansion relief for the cladding specimen which is welded to the tip. The tip also serves as the means of loading the pressurizing NaK into the tubing (1). After evacuation through the tip (1), the NaK is introduced and flows along the sheath extension (2), fills the regions (3) and then passes through the broached duct (12) in the heater body into the pressurizing tube (11). It then fills the interior of a stainless steel bellows chamber (17). Pressurization of the NaK is accomplished by the application of gas pressure in the bellows chamber (18). The bellows is sized to provide room for thermal expansion of the NaK and to prevent gas from entering the test loop at a cladding failure. The downstream end of the heater extension (2) slips inside the upst ream end of the heater sheath (9) and becomes the lower electrode. Section A-A shows the nature of the fit.

A platinum disc (4), whose O. D. is hand sized so that it fits snugly inside the end of the BN insulator (5) provides a diffusion barrier between the stainless steel electrode and the graphite heating element (6). The upper end of the heater has a tungsten diffusion barrier (7) between the molybdenum electrode (8) and the graphite. The lower end of the molybdenum electrode (Section D-D) has a 0.1245 (+ 0.0000, -0.0010) in. diameter over a 2.56-in. length, at which point it expands smoothly into a nominal 0.25-in. stock diameter rod. A lavite insulator (13) is placed in the lower end of the heater body to support the end of the BN insulator and to generally position the molybdenum. The upper end of the molybdenum electrode is brazed into a 1/2-in. copper rod (16), to whose upper end the power lead is attached. The lower end of the copper rod (16) is guided by a lavite insulator (15) and by a ceramic insulator sleeve (24) at its midpoint to guide the movement of the electrode assembly.

The body of the heater has cooling coils (19) brazed to it as shown in Figure 1, and a tube (20) which is used to evacuate the electrode chamber after assembly. After evacuation, the heater chamber is filled with helium to provide additional heat transfer coupling between the heater (6) and the sheath (10). The lower end of the heater body is fitted with a Conoseal joint fitting (14) at

which point it is supported in the sodium loop. The upper end of the heater body supports the Micarta insulator-guide (24) and provides a smooth surface against which the rubber tubular boot (22) is fastened with a hose clamp (23). (In some of the tests, the boot has been replaced with a metal bellows, which is insulated and sealed with an epoxy seal.) This boot-bellows assembly must provide the needed electrical insulation, the axial flexibility needed to maintain function contact along the electrical train, and the necessary impermeability to air (oxygen) to maintain an inert atmosphere in the electrode chamber. The upper end of the boot (bellows assembly) is clamped to a stainless steel attachment (27) which is brazed to the copper electrode (16). The stainless steel part also provides a support for the weight (26) which is sized to provide an adequate pressure on the electrical joints. Because one line of the low voltage a. c. power for the heater is grounded to the heater body and the sodium loop, a heat shrinkable plastic cover (25) is used to insulate and cover the weight to minimize the chance that the current will be inadvertently shorted out during operation.

Table 1 shows the types of tests performed and minimizes the observed performances. As is shown in the table, all of the clad heaters except 34, 38, 46, 50, and 52 were operated in two modes. (Heaters 11 and 12 were unclad.) In all cases, the first test period was a 'clad' period and may have been carried out either under cyclic heating or under a steady heating mode to test the cladding. After the cladding failed, the heater was removed to test the cladding. After the cladding failed, the heater was removed from the sodium loop, the cladding was removed, and the now bare heater was returned to the loop for test-to-failure.

The earlier tests which were performed with the single layer silicone rubber boot acting as a flexible, electrically insulating sealing member joining the upper electrode to the heater body, generally showed a marked buildup of a strongly adherent molybdenum oxide on the upper electrode. This oxide layer would become quite heavy and was the cause of failure of heaters 36, 30, and 34. Heater 32 also developed a very heavy oxide layer on its upper electrode, but it had not caused complete failure of the heater at the time of the termination of the test (1044 hours service). It was difficult to keep in operation at that time, however, because of the binding and lack of free axial motion which is required to permit the weight to maintain the electrical contact pressures along the heater circuit.

A double-layer silicone rubber boot was used in tests 12 and 52, and it was found that it did quite effectively reduce the inward diffusion of air to the upper electrode chamber. A discoloration of the internal surfaces was noted in both tests, but the amount of oxide was negligible. In addition to the double boot, heater 12 had a $MoSi_2$ coated molybdenum electrode as a second possible method of controlling oxidation of the molybdenum. The double boot proved to be adequate, and the $MoSi_2$ coating is not considered necessary or desirable if the inward oxygen diffusion can be prevented. Further, there was evidence of an interaction between the $MoSi_2$ and the BN insulator in Heaters 12 and 11.

Tests 11 and 38 were prepared to test the effectiveness of a metal bellows in preventing the oxidation of the molybdenum electrode. The bellows was electrically insulated from the heater housing by using a layer of fiberglass tape and epoxy cement as an insulating sealant; however, the bellows used were made of 0.005 to 0.006 in. wall type 304 stainless steel, and were quite stiff. They were quite effective and in both tests there was not the slightest evidence of any oxygen permeation or leakage into the electrode chambers. Their stiffness made their use less than ideal, and it was necessary to maintain and check them more frequently than was desired. A major reason for the lower total service time of Test 11 than that of Test 12 was the fact that on several occasions, the operator would find that Heater 11 had become open-circuited during the night, but could be restarted by merely pushing down on the upper electrode to reestablish the contact. Meanwhile, Test 12, which was running simultaneously, would have logged more hours and ran more continuously.

In order to affirm the validity of the metal bellows solution to the oxygen diffusion problem, Tests 40, 42, 44, 46, and 48 were prepared by using bellows made from 0.003-in. type 304 stainless steel stock. They were much softer than the first bellows used, and performed very well. Heaters 40 and 48 were operable when their tests were terminated. Heaters 42 and 44 failed at the tungsten wafer. The end of the molybdenum electrode had softened, bloomed outward, and punctured the BN insulator sleeve. This is thought to be due to the formation of a high resistance interface in that region and an overheating, softening, and weakening of the materials to permit the observed deformations.

Post test radiographs of Heaters 40, 42, 44, and 48 are shown in Figure 2. The radiograph of Heater 40 shows both the platinum and the tungsten to be

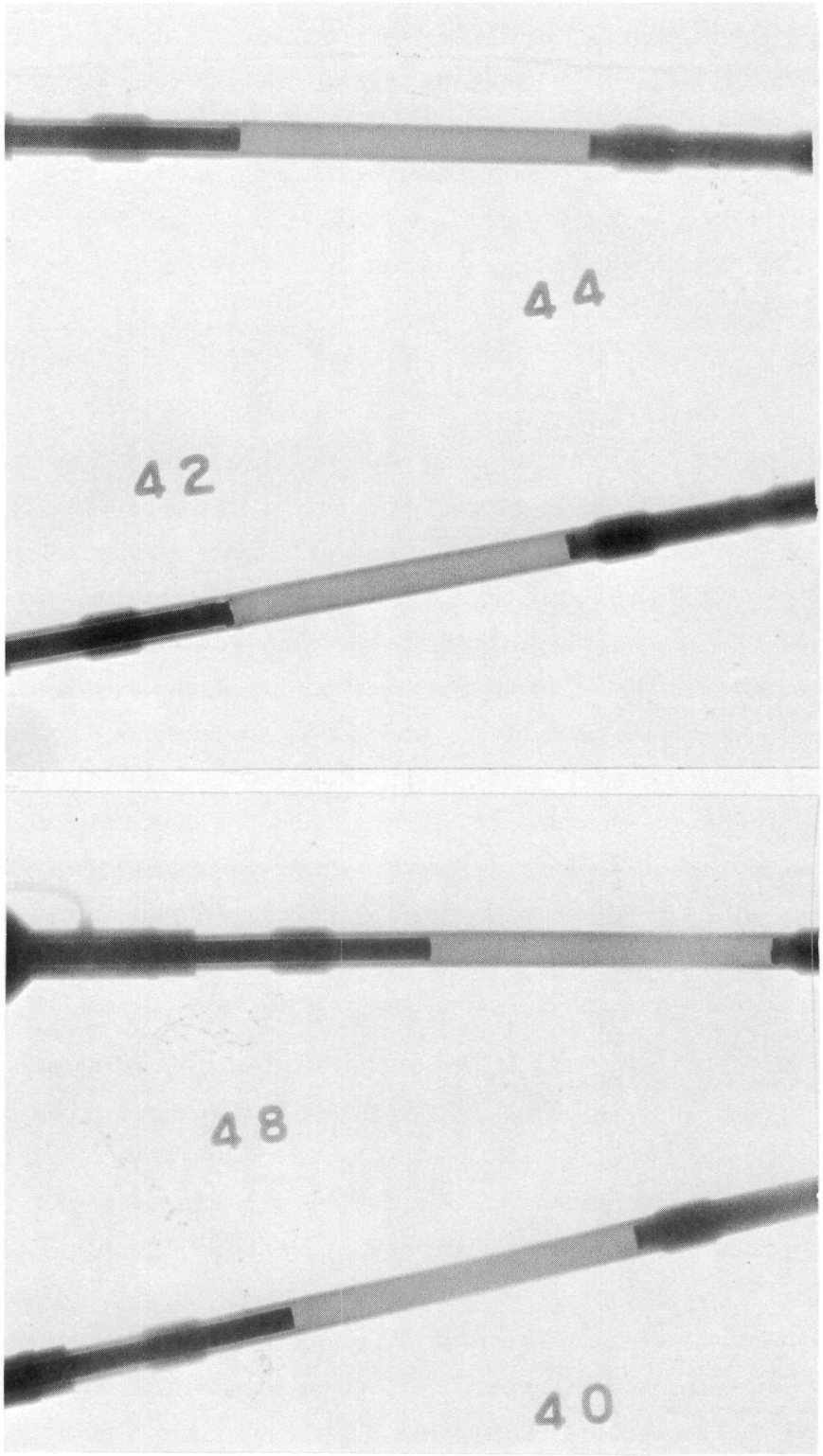

7706-4741

Figure 2. Radiographs of Heater No. 40, 42, 44, and 48

in very good condition with rather square interfaces with the graphite, and only a suggestion of blooming on the molybdenum tip.

The radiograph of Heater 48 shows the unit to be in fair condition, although the molybdenum can be seen to have begun to distort, and the platinum-graphite interface is no longer straight.

The radiograph of Heater 44, which had failed by short circuit, shows the tip of the molybdenum to be deformed and to have breached the BN insulator. The platinum-graphite interface is roughened, but in fair condition.

The radiograph of Heater 42 shows a deformed molybdenum tip and swelling in the sheath. The platinum wafer appears to be in good condition.

In Heater 46, whose cladding surface showed a 0.004-in. expansion and roughening at the level of the tungsten wafer, a large button of tungsten carbide was found to have formed and the parts in the vicinity were expanded. The region had obviously been very hot, and the materials had become subject to plastic deformations, which took the form of radial expansions under the influence of the axial pressure on the joint. Figure 3 shows the region of the tungsten wafer from Test 46.

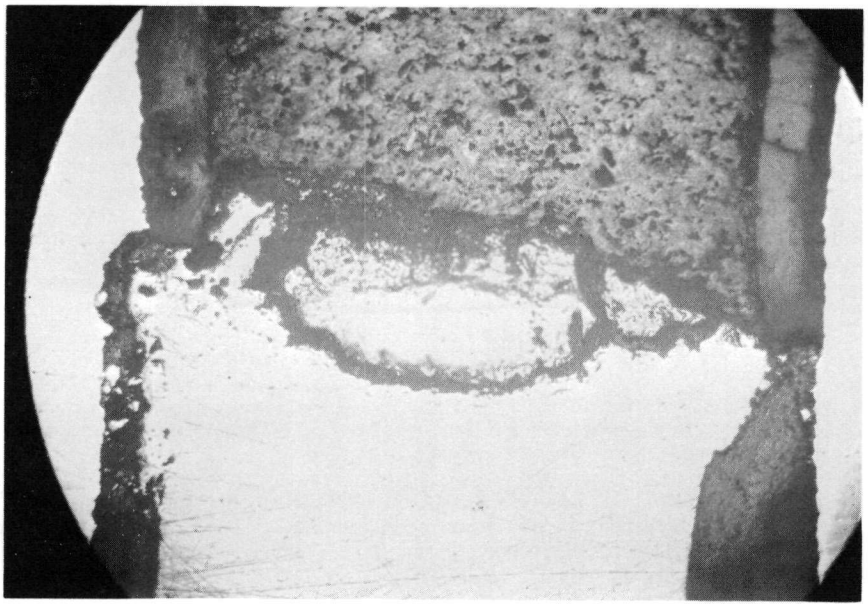

8191-4-3

Figure 3. Tungsten Carbide Formation in Heater No. 46

In Test 34, the heat load was 1.9×10^6 Btu/ft^2 -hr. It appears that this is too severe a service demand for this heater design, because the heater did not operate properly from the beginning and failed after only a 1-hr service.

Tests 50 and 52 were run to obtain corrosion data, and both are considered to have failed prematurely by overheating at the tungsten wafer. Both had very catastrophic failures, and much damage was done to the molybdenum electrode, the insulator, and the heater sheath.

It is of interest to note that in the development of this heater, the failure modes observed in the pre-FY-1968 and the early FY-1968 versons were predominantly traceable to the influx of oxygen into the upper electrode chamber. In the more recent models, the oxygen diffusion has been essentially eliminated, and we are now finding that the failures are occurring in the upper diffusion barrier region, presumably due to overheating. One might wonder why the tungsten wafer joint is now playing such a critical role in heater failure, when there has been no change in the heater operation except to eliminate the oxide formation. There are three possible reasons. First, the bellows which prevent the oxidation also prevent the operator's rotating the electrode. Rotation was a common procedure in restarting heaters with boots whose flexibility would allow a quarter turn of rotation and, probably, a resurfacing action on interfaces which may have become roughened. The simple axially directed tapping permitted by the bellows is not as effective in developing and maintaining a good contact. Second, the heaters listed in Table 1 began their lives as clad heaters (except 11 and 12), and the bulk of the FY-1967 units were bare heaters. The heater sheath heat flux in most cases was the same, 1.3×10^6 Btu/ft^2-hr, but the presence of the layer of NaK and the cladding makes a clad heater run at least 125°F hotter than an unclad one at the tungsten wafer, see AI-AEC-12681. Third, many of the present heaters were tested during a part of their lives at least, under cyclic conditions. This service is very severe and produces large thermal gradients and correspondingly large thermal stresses. These, in conjunction with the high temperatures, may also account for the distortions noted in the heater sheath and in the molybdenum electrodes. As further evidence of the general damaging effect of cycling, one need only examine Table 1. The longest service lives were from units which were subjected to a steady heat flux over most or all of their lives. The cyclic tests show shorter

lives. The one exception is Test 52, which is thought to have developed a poor contact very early in its life.

B. MASS TRANSFER

The goal of the mass transfer phase of this task is to study and attempt to understand the mechanisms of mass transfer in a material in which there is a heat flux. The intent is to develop mass transfer information and to devise a method of predicting mass transfer rates under reactor conditions. The factor of a high heat flux ($> 1 \times 10^6$ Btu/hr-ft^2) is of great concern and the effect of the heat flux on mass transfer is an important aspect of this study. Because of the need for long time tests, this task is dependent upon the development of long lived high heat flux heaters, as described above. Test periods of 1000-hr or longer will be essential.

In addition to the need for a long lived heater, it is also necessary to develop a corrosion-measurement technique by which meaningful data can be obtained with a minimum exposure time. To this end, a study of the use of an irradiated test specimen has been carried out. By irradiating a tubular specimen having a 5-mil wall in a reactor, and then allowing it to cool for several days, one can produce a sample having Fe^{59}, Cr^{51}, and Co^{60} as useful tracer elements in stainless steel. When this specimen is then exposed to a heat flux and sodium coolant sdream, these isotopes will be lost to the sodium in accordance with their individual mass transfer tendencies. Therefore, by measuring the loss of these isotopes from the specimen under known experimental conditions, one can determine their mass transfer coefficients.

The initial activity levels of the useful test isotopes in 2-in. length of a 5-mil-thick tubular sheath are: Cr^{51}, 5.6×10^5 c/sec; Fe^{59}, 2×10^5 c/sec; and Co^{60}, 6.5×10^4 c/sec. At the estimated gross rate of mass transfer, about 3% of the sample will be lost in a 20-day test exposure. An analysis of the expected differences in counting rates between the reference and the test samples indicated that these differences for all three isotopes could be measured to a 1% probable error in a counting time of about 20 min, assuming that the three isotope components are corroded at the average predicated rate.

A simulated test of this concept was carried out by irradiating a 5-mil wall tube in the STIR reactor. Its initial counting rate was determined, and known

amounts of material were removed from the surface to simulate a corrosion action. This removal of material was done by chemical etching. It was then experimentally determined that a mass loss difference corresponding to 0.02 mil can be determined to a 99% accuracy by proper use of the "before" and "after" counting procedures. The corrosion experiment feasibility was therefore established.

Two mass transfer tests (50 and 52) were run. The test durations were shorter than were desired in both cases. Test 50 was terminated by a heater failure after 182 hours, and Test 52 operated only 12-hr before the heater failed. Summaries of the test conditions are shown in Table 1. Both tests involved the use of an irradiated cladding, whose radioactivity was determined before it was assembled onto the heater. A number of DPH hardness indentations were made on the clad surface. Measurements of the change in the radioactivity due to material loss, and of the change in surface size of the DPH hardness indents due to surface recession are the raw data from which the mass transfer rates can be deduced.

The indent technique has an inherent uncertainty in that the formation of an indent cavity forces some metal to move toward the sample surface to form a ridge around the opening. This raised material is more heavily cold worked than the surrounding surface, and may tend to corrode more rapidly. The ridges also protrude slightly into the sodium stream; however, these ridges are smaller in general than the surface roughness, so that the effect of protrusion into the sodium stream must be small.

When Test 50 was removed from the test loop for examination, it was found that the heater failure involved the melting of about 1/4 in. of the end of the molybdenum electrode and a portion of the heater sheath wall. During the heater wall failure, the molten metal became very firmly attached to the inner wall of the cladding, and also distorted the wall. Because of this, it was necessary to cut the clad sample off the heater, and to perform the counting on the recovered piece. The accuracy of the indent size measurements was also affected because of the handling and bending of the sample during the removal operation. The results of both the activation-method and the indent-method analyses are shown in Table 2. The positions of the indents along the length of the tube specimen are shown in Figure 4.

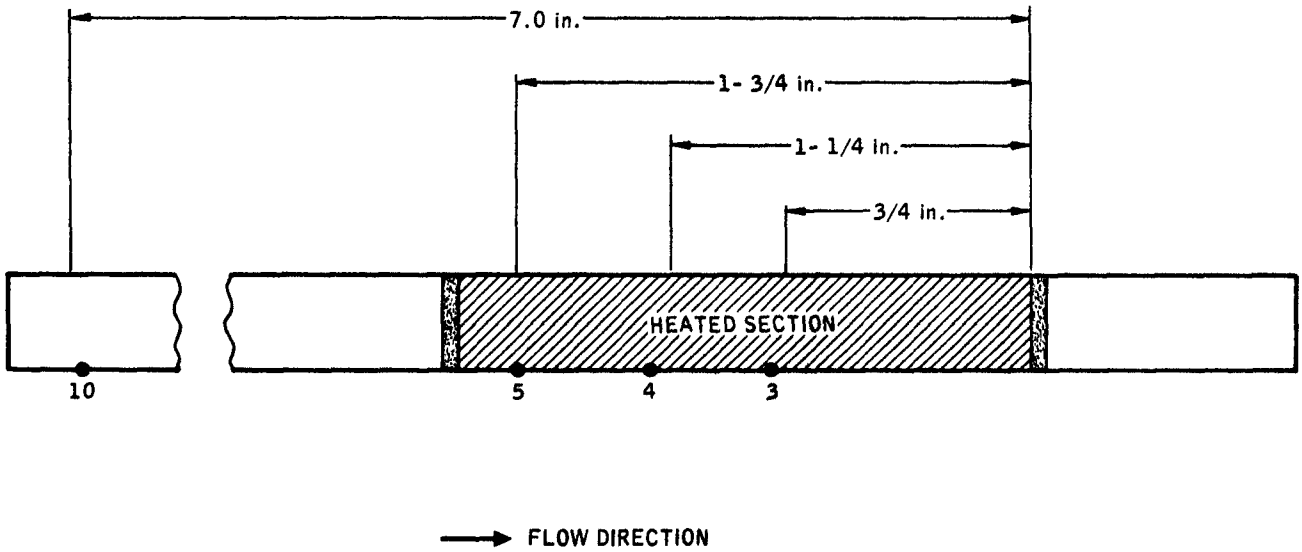

7706-4731

Figure 4. Positions of Indents Along the Length of a Tube Specimen.

The material losses indicated by the indentation method represent average values obtained from one to three indents located 90° apart at each position. The range in the reported corrosion rate represents the uncertainty in the measurements of the size of the indent. The uncertainty in the activation method result represents an estimate of the effects of the loss of material from the cut and the change in the counting geometry from the initial pretest configuration to the post test configuration of the slit tube.

It is of interest to note that both techniques yield data which are in agreement with the results of other researchers, 1 to 2 mils/yr. Further, there is an unmistakable difference in the upstream rate and the rate in the heated zone, as measured by the activation technique. This is in general agreement with the theory of operation of the 2-in. loop because the sodium which approaches the heated section and has been circulating in the loop at 1225°F, should be saturated with metallic corrosion products at 1225°F. Therefore, the corrosion rate of the upstream sample should be nominally zero as found by the activation method. The observance of a small corrosion rate by the indent method may be illustrating, at least in part, the effect of the indent ridge on the corrosion rate. However, based upon these first results, it is concluded that both methods of measurement warrant further study.

A topical report, "High Heat Flux Heater Development Status Report," by R. L. McKisson and E. L. Babbe, AI-AEC-12681, was prepared.

A paper, "A Method for Studying Corrosion Mechanisms in High Temperature Flowing Sodium," by J. Hopenfeld, was presented at the AEC Corrosion Symposium at Battelle Memorial Institute in May, 1968.

III. EVALUATION OF EFFORT DURING FISCAL YEAR 1968

The Model 3 high heat flux heater design shown in Figure 1 appears to have much promise for the desired service of 1000 hr of steady operation at a cladding surface heat flux of 1,000,000 Btu/ft^2-hr. The early troubles (in FY 1967) of reactions of the graphite with the molybdenum and with the stainless steel have been eliminated by the use of diffusion barriers of tungsten and platinum. The difficulty with the diffusion of oxygen (air) through the rubber boot has been resolved in two ways, the double-layer rubber boot, and the bellows with an epoxy seal. There remains, however, the problem of overheating at the tungsten wafer. The solution of this problem will almost certainly give the heaters a major increase in service life. The solution to the problem of minimizing the electrical contact resistance is not yet in hand, but it does seem necessary to reduce the number of unbonded interfaces along the electrical path, and particularly to reduce the number of free interfaces in the region of the upper diffusion barrier.

A radioactive tracer technique for measuring the mass transfer of stainless steel components in flowing sodium has been devised and tested. Although the test period was short, the results are very encouraging and indicate that the technique is sound, and that it is capable of yielding the desired corrosion data in 500 to 1000 hr tests.

An indent method for measuring mass transfer of a metal surface has been devised. A first test of the method indicates the method has merit. Further study is indicated.

Program: FBR Fuel Development, Fuel Cladding and Structural Materials Failure			
AEC Task: 10-E-1 Modes of Failure and Helium Degradation			
Project Manager: J. L. Ballif/J. J. Gill			D. Kramer
Reporting Period: Fiscal Year 1968			
General Order: 7706	Subaccount: 29550	AEC Category: 04-40-02-01.1	

I. PROJECT OBJECTIVES

The objectives of this task are to: (1) obtain a detailed understanding of the motion, agglomeration, and trapping of helium atoms and bubbles in fast reactor cladding and structural materials, including the effects of initial distribution of helium atoms and the ultimate distribution of these trapped product atoms, (2) investigate the basic nature and form of the mechanical property changes induced by fast reactor transmutation damage, and (3) assist in the translation of these into interpretation of environmental behavior of cladding alloys and the selection, heat treatment, and design of fast reactor materials.

II. TECHNICAL PROGRESS DURING FISCAL YEAR 1968

A. CYCLOTRON HELIUM INJECTIONS

Two helium injections were done by employing the University of Washington cyclotron. The alloys used and the measured helium concentrations achieved are presented in Tables 1 and 2.

B. TYPE 316 STAINLESS STEEL

Tensile tests were performed on samples with 2×10^{-5} and 4.0×10^{-5} atom fraction helium at temperatures from 540 to 815°C. Before injection of He, the samples were given one of the two following treatments;

No. 6: 50% cold rolled, and annealed 1 hr at 980°C then 8 hr at 760°C.

No. 13: Annealed 30 min at 1120°C, 25% cold rolled, and annealed 24 hr at 480°C then for 144 hr at 705°C.

Treatment No. 6 resulted in a microstructure of austenite grains with $M_{23}C_6$ carbides on grain boundaries whereas No. 13 produced a fine dispersion of sigma particles (10^{13} cm^{-3}) in deformed austenite grains with $M_{23}C_6$ carbides on grain boundaries.

TABLE 1

THIRD HELIUM INJECTION

Alloy	Number of Samples	Atom Fraction Helium
316 Stainless Steel	27	4×10^{-5}
316 Stainless Steel	60	2×10^{-5}
Incoloy 800	27	4×10^{-5}
Incoloy 800	40	2×10^{-5}
405 Stainless Steel	15	4×10^{-5}
405 Stainless Steel	40	2×10^{-5}
ORNL 304L + Ti	3	4×10^{-5}
ORNL 304L + Ti	4	2×10^{-5}

TABLE 2

FOURTH HELIUM INJECTION

Alloy	Number of Samples	Atom Fraction Helium
304L Stainless Steel	30	3×10^{-5}
304L Stainless Steel	23	2×10^{-6}
316 Stainless Steel	20	2×10^{-5}
316 Stainless Steel	30	2×10^{-6}
Incoloy 800	20	3×10^{-5}
Inconel 625	13	3×10^{-5}
IN-102	13	2×10^{-5}
19-9DL	30	3×10^{-5}
Inconel X-750	12	3×10^{-5}

The total elongation as a function of test temperature is shown in Figure 1. The data for samples with the lower helium content is not shown because of its similarity to the data of the Figure 1. Loss of ductility was always accompanied by partial or complete intergranular failure which originated at grain-boundary carbides. Figure 2 shows voids at these carbides which are joining to form a crack in the grain boundary.

The fine dispersion of sigma particles trapped helium as bubbles in the matrix and delayed the accumulation of helium at grain boundaries. This accounts for the higher temperature at which ductility loss begins in samples with Treatment No. 13. Helium bubbles attached to sigma particles are shown in Figure 3.

A topical report, "Helium Embrittlement of Type 316 Stainless Steel," by D. Kramer, K. R. Garr, C. G. Rhodes, and A. G. Pard, AI-AEC-12670, was issued and presents the above work in detail. An oral presentation of this work was given at the 1968 Annual Meeting of the AIME in New York during February.

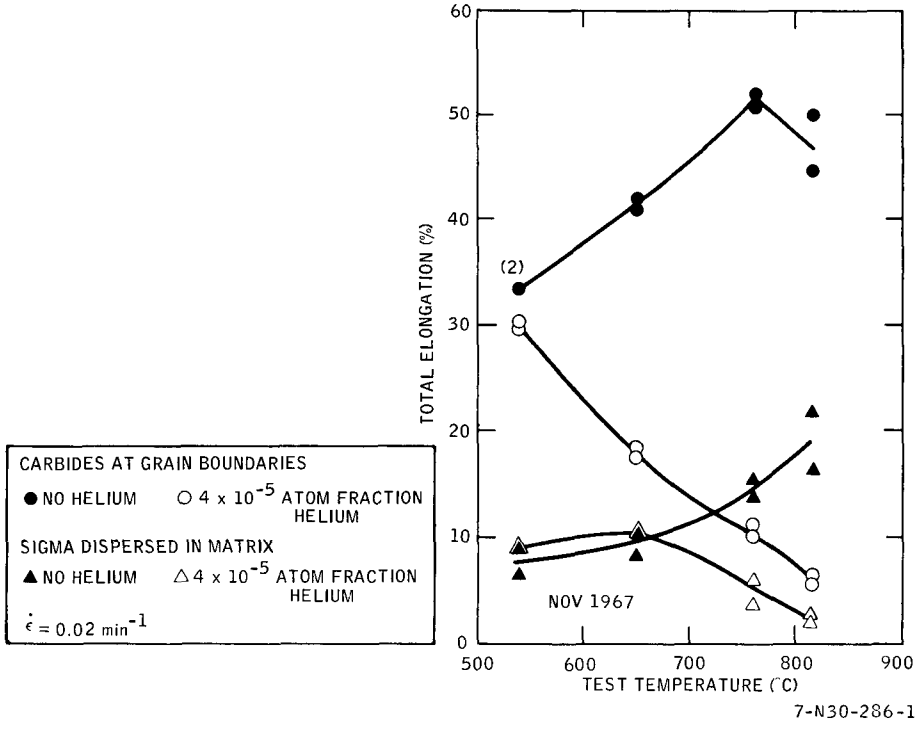

Figure 1. Total Elongation as a Function of Test Temperature for Type 316 Stainless Steel With No Helium and With 4×10^{-5} Atom Fraction Helium

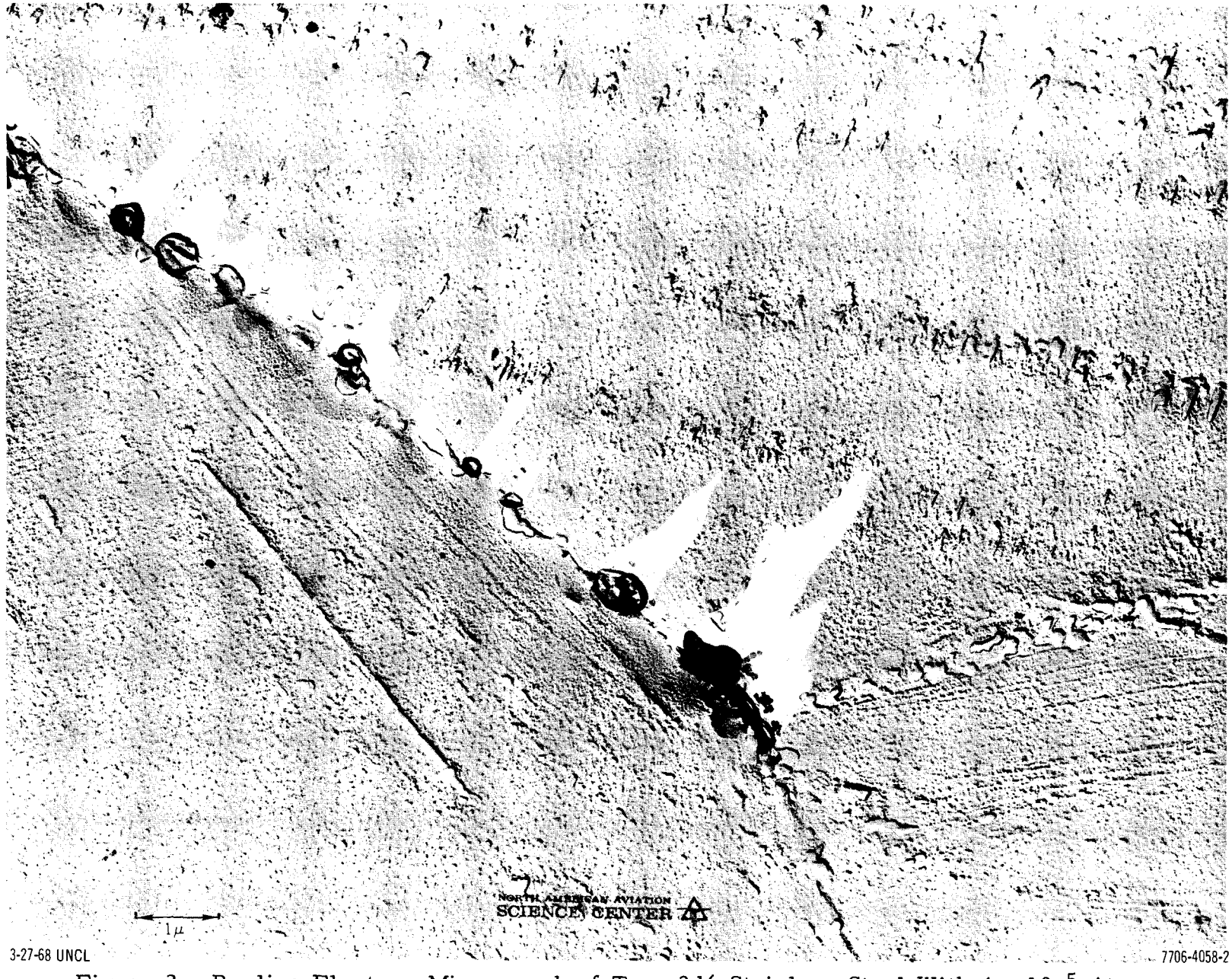

Figure 2. Replica Electron Micrograph of Type 316 Stainless Steel With 4 x 10^{-5} Atom Fraction Helium Tested at 760°C Showing Voids Adjacent to Grain-Boundary Carbines in a Sample Given Treatment 13

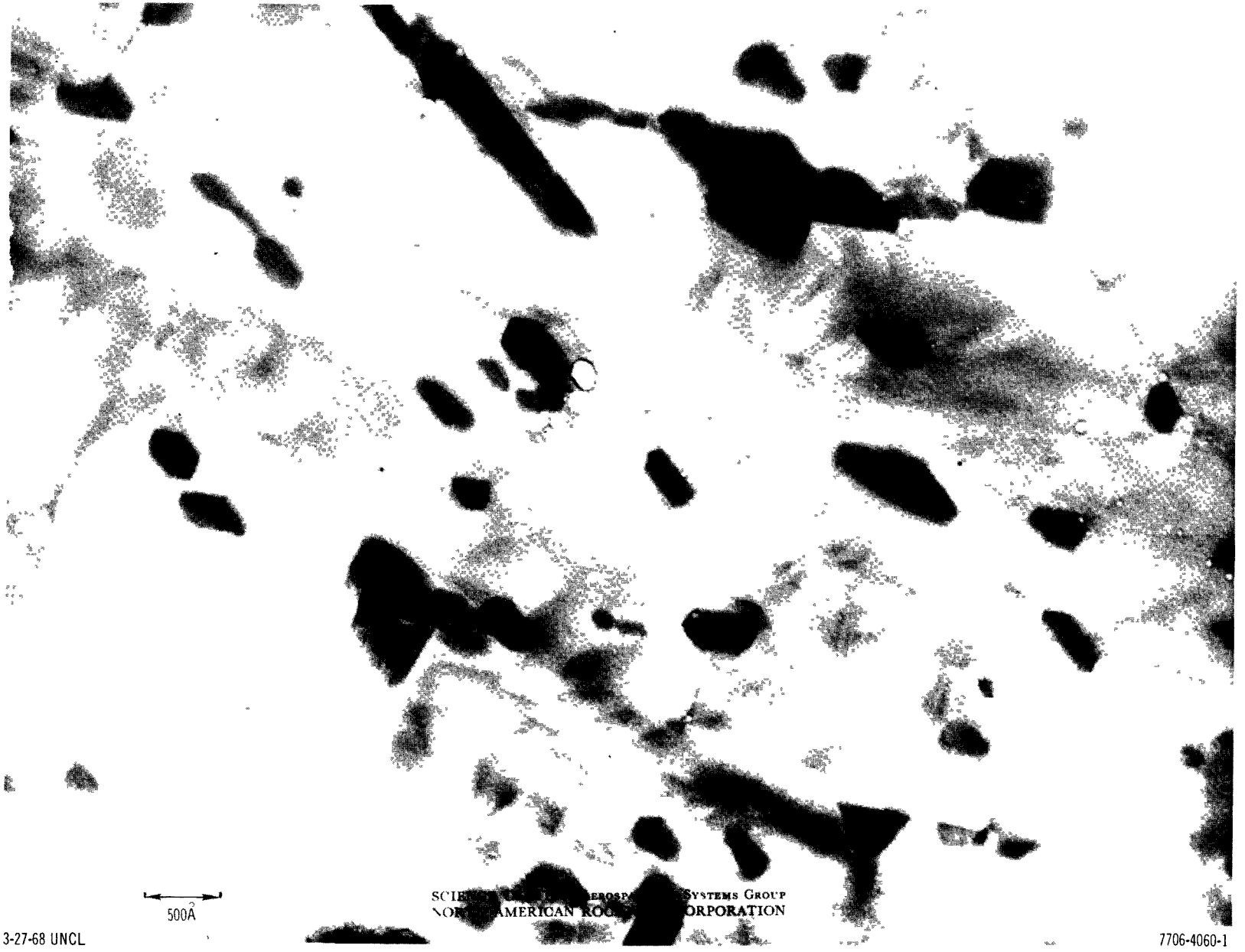

Figure 3. Transmission Electron Micrograph Showing Helium Bubbles Attached To Sigma Particles in Type 316 Stainless Steel Given Treatment 13 With 4×10^{-5} Atom Fraction Helium Tested at 760°C

C. INCOLOY 800

Tensile tests were performed on samples with 4 x 10^{-5} atom fraction helium at temperatures from 500 to 800°C. The total elongation as a function of temperature is shown in Figure 4 for samples with two different treatments. Annealing at 760°C after a solution anneal produced carbides at grain boundaries; whereas, annealing at 760°C after cold rolling produced precipitates within the matrix (10^{12} cm^{-3}) as well as on the grain boundaries.

Detailed light and electron microscopy indicate that the mechanism of embrittlement is the same as that which operates in Types 304 and 316 stainless steels. The matrix precipitates are not dense enough to be effective traps for helium bubbles.

E. TYPE 405 STAINLESS STEEL

The tensile data obtained from Type 405 stainless steel samples are given in Table 3. The values shown are averages from two or more samples. Prior to injection with helium, the samples were given one of the following two treatments:

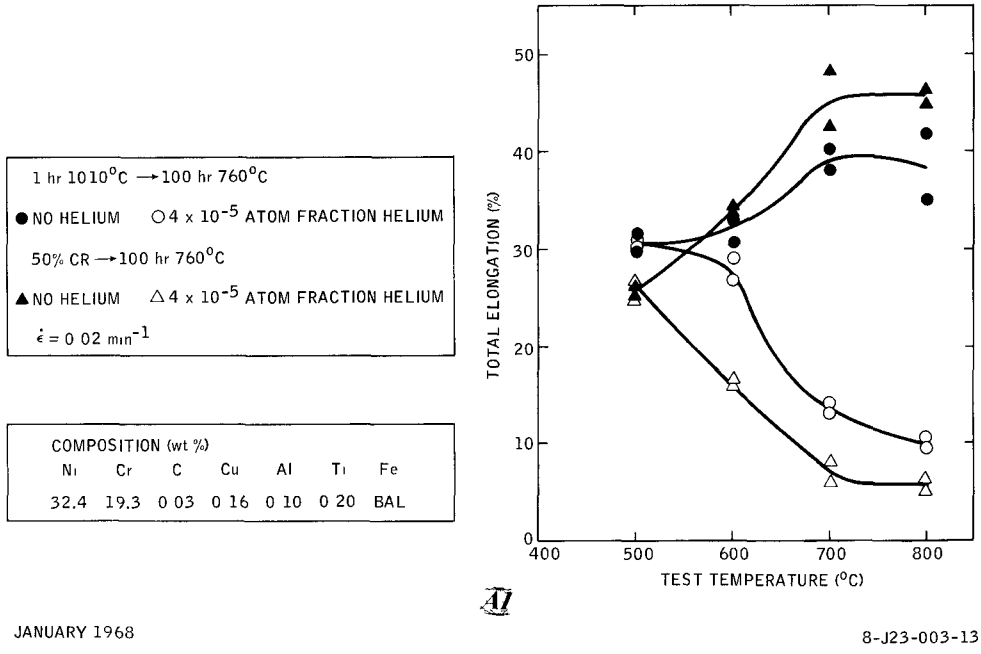

Figure 4. Total Elongation as a Function of Test Temperafor Incoloy 800 With No Helium and With 4 x 10^{-5} Atom Fraction Helium

TABLE 3

TENSILE DATA OF TYPE 405 STAINLESS STEEL

Treatment	Atom Fraction Helium	Test Temp. (°C)	Strengths (kpsi)		Elongations (%)	
			Yield	Tensile	Uniform	Total
5	0	750	5.6	6.6	2.3	44
5	4×10^{-5}	750	6.8	7.5	1.7	28
10	0	750	4.5	4.7	1.7	49
10	4×10^{-5}	750	5.8	6.3	3.5	22
5	0	650	16.9	18.4	3.4	43
5	4×10^{-5}	650	12.5	18.4	3.0	39
10	0	650	9.8	12.1	6.4	54
10	4×10^{-5}	650	10.7	12.7	7.0	43
5	0	550	33.1	55.2	3.1	17
5	4×10^{-5}	550	14.1	52.6	2.7	13
10	0	550	16.8	26.3	12	46
10	4×10^{-5}	550	15.4	26.3	10	44

No. 5: 30% cold rolled, then annealed 1 hr at 980°C,

No. 10: 30 min at 715°C, 30% cold rolled, and annealed 24 hr at 760°C.

F. TYPE 304 STAINLESS STEEL

A topical report, "Helium Embrittlement in Type 304 Stainless Steel" by D. Kramer, H. R. Brager, C. G. Rhodes, and A. G. Pard was issued. The same paper was also published in the Journal of Nuclear Materials, 25, 121, 1968.

Stress-rupture tests were performed on samples with 1×10^{-6} and 3×10^{-5} atom fraction helium and the results are plotted in Figure 5. Data points from samples of either helium concentration fit on one straight line representing a

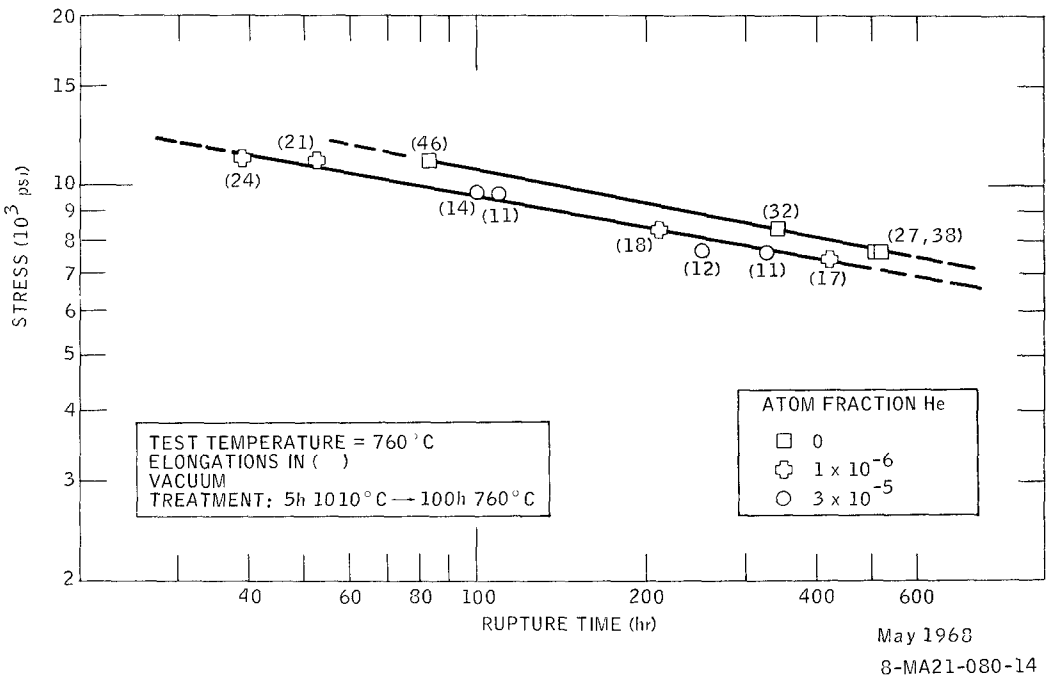

Figure 5. Stress-Rupture of Type 304 Stainless Steel With and Without Helium

rupture life reduced by 40% and showing that rupture time is independent of helium concentration over the present range of variables. The elongations at failure are equivalent to those previously obtained by tensile testing.

G. EBR-II IRRADIATION EXPERIMENT

Three capsules which are part of ORNL-Exp 3 and ORNL-Exp 4 were inserted in Rows 2 and 7 respectively of the EBR-II in February 1968. They are due to be removed from the reactor early in 1969. A total of 250 small tensile samples are being irradiated including Types 304, 316, and 405 stainless steels and Incoloy 800.

In addition to the tensile samples, 30 elements are also being irradiated to determine the effective (n, α) cross-sections in the EBR-II neutron spectrum by subsequent helium analysis on the mass spectrometer.

H. COMPUTER CALCULATIONS OF HELIUM AND VACANCIES IN GAMMA-IRON

Twelve different arrays of vacancies were studied in the present investigation. The energy characteristics are listed in Table 4. The first eight defects

TABLE 4

ENERGY CHARACTERISTICS OF VACANCY CLUSTERS IN fcc γ-IRON

Defect	Description	E_F	E_B	N_B	E_B/N_B
1	Monovacancy	1.481			
2	First nn Divacancy	2.719	0.243	1	0.243
3	Second nn Divacancy	2.974	-0.012	-	-
4	Square Tetravacancy (001)	4.936	0.988	4	0.247
5	Octahedral Hexavacancy	5.913	2.973	12	0.248
6	Square Pentavacancy (001)	6.447	0.958	4	0.239
7	13-Vacancy Square (001)	15.200	4.053	16	0.253
8	16-Vacancy Square (001)	17.278	6.418	24	0.267
9	Equilateral Trivacancy (111)	3.732	0.711	3	0.237
10	13-Vacancy Star (111)	13.341	5.912	24	0.246
11	13-Vacancy Sphere	10.350	8.903	36	0.247
12	43-Vacancy Cluster	24.997	38.686	162	0.239

in Table 4 are illustrated in Figure 6, defects 9 and 10 are shown in Figure 7, and defect 11 is illustrated in Figure 8.

The symbols in Table 4 have the following meanings: (a) E_F is the formation energy in ev with respect to a perfect iron lattice as directly determined by the computer calculation, (b) E_B is the binding energy of the defect and is equal to $E_v N_v - E_F$ where $E_v = 1.481$ ev is the energy of formation of an isolated monovacancy (defect 1) and N_v is the number of vacancies in the cluster, and (c) N_B is the number of first nearest neighbor divacancy interactions or vacancy-vacancy "bonds" in the cluster.

The approximate constancy of the value of the binding energy per vacancy-vacancy bond, $E_B/N_B = 0.250 \pm 0.020$ ev, verifies the bond counting rule reported by Johnson (Phys. Rev. 152, 629, 1966) for a number of different defects than Johnson reported. The application of the rule to large pseudospherical clusters shows that the vacancies that cluster together to form a void fall into two classes: (a) interior vacancies with $N_B = 6N_v$, and (b) surface vacancies where, on the average, $N_B \sim 3N_v$. Inserting these values of N_B into the bond counting rule leads to: (a) $E_B = 1.5$ ev for interior vacancies, and (b) an average value

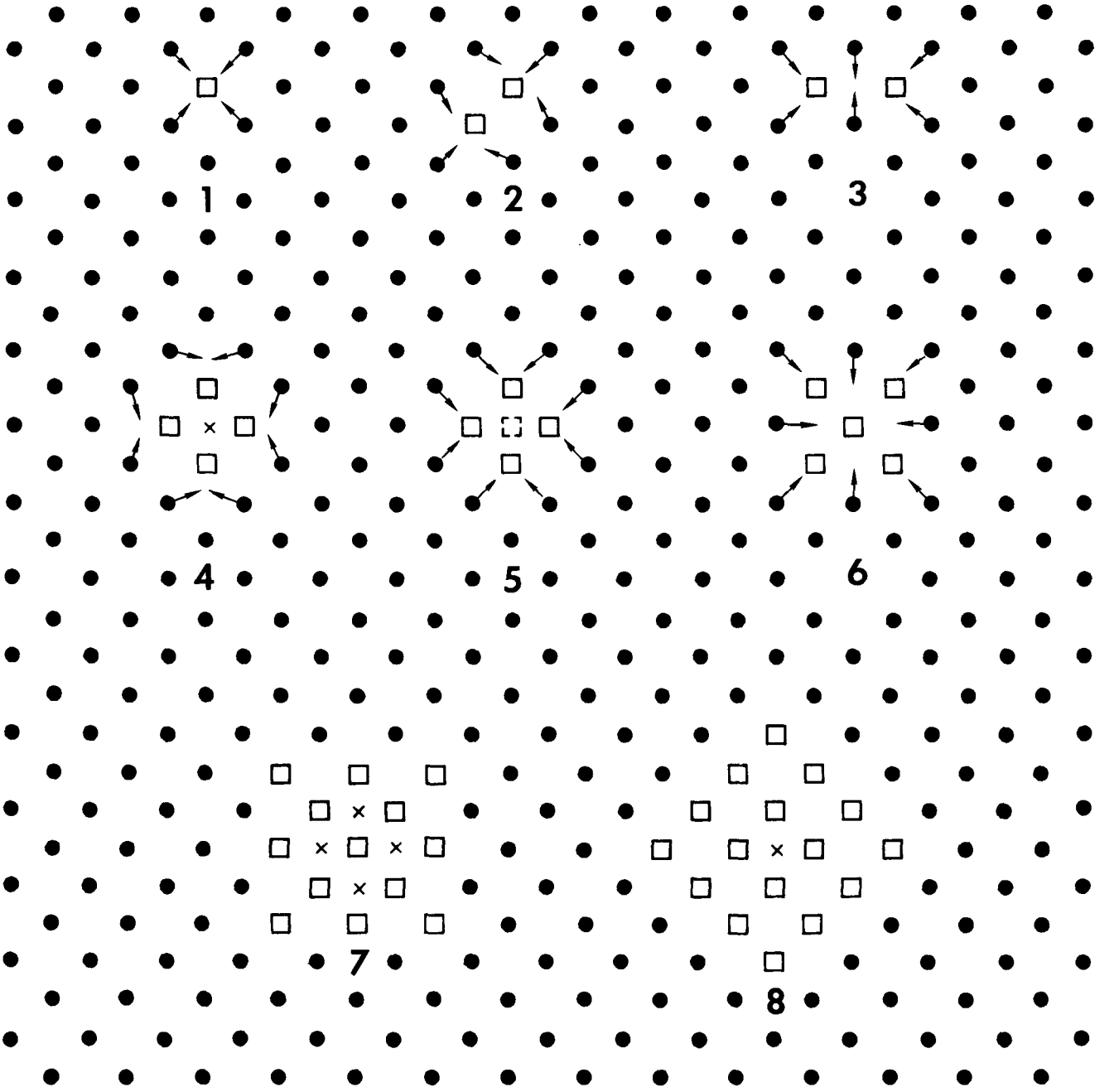

3-5-68 UNCL

7706-4301B

Figure 6. Vacancy Clusters in (001) Plane of fcc γ-Iron

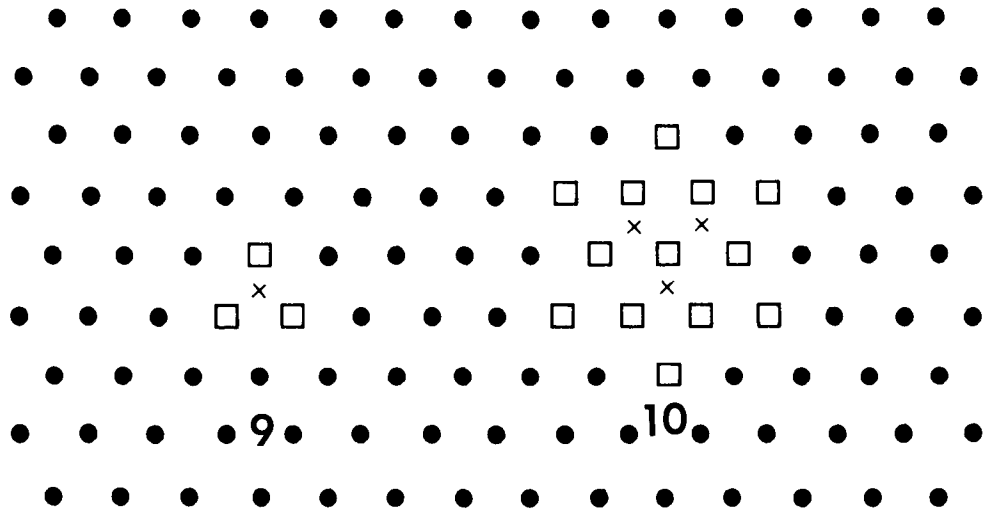

3-22-68 UNCL 7706-1006

Figure 7. Vacancy Clusters in (111) Plane of fcc γ-Iron

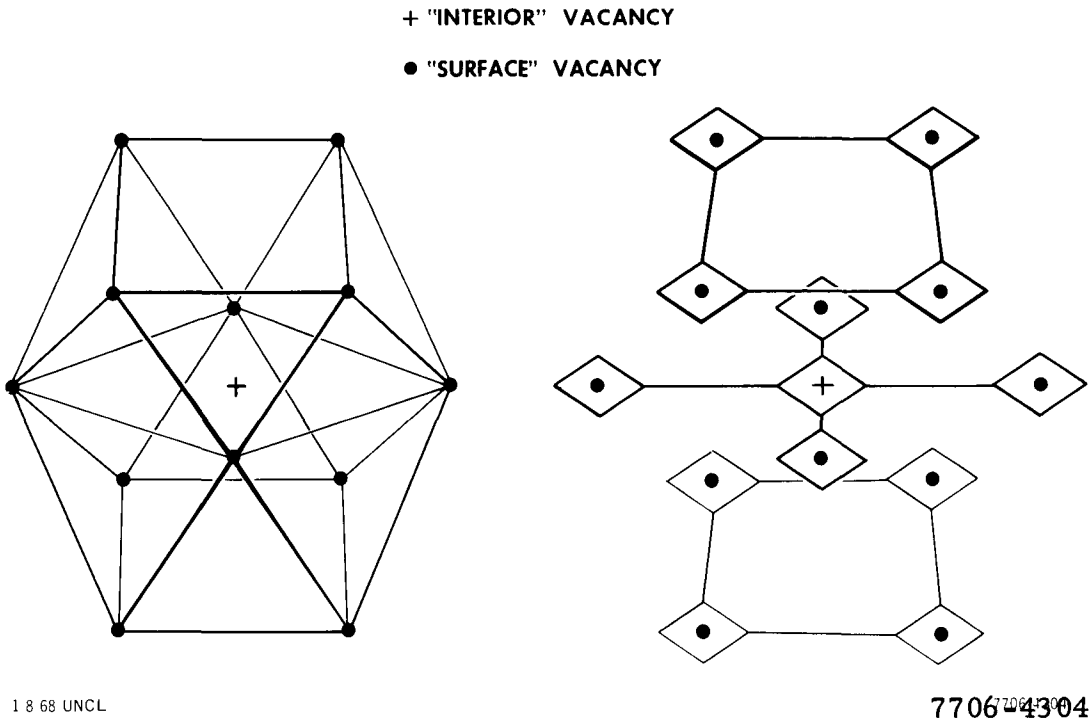

1 8 68 UNCL 7706-4304

Figure 8. Thirteen-Vancancy Sphere in γ-Fe

of $E_B \sim 0.75$ ev for surface vacancies. Thus, the binding energy of interior vacancies exactly equals the cohesive energy which closely approximates the energy of formation of a monovacancy. The energy of formation of a vacancy, therefore, is completely returned to the system if it ends up as an interior vacancy of a void. Similarly, on the average, one-half of the formation energy is returned in the case of surface vacancies.

The arguments of the last paragraph lead to the conclusion that for large voids in which most of the vacancies are of the interior type, a drastic reduction in the internal energy of the system occurs upon the formation of a void. This drastic reduction in the internal energy of the system is the chief reason for the formation of large voids.

An estimate of the magnitude of the reduction in internal energy for the case of a large void can be readily obtained by considering a spherical void with a radius equal to 100 interatomic distances. Such a void would contain approximately 4×10^6 vacancies and, in the case of γ-iron, would have a radius of approximately 500 Å which is in the range of the experimentally observed sizes of voids. We conclude that 97% of the vacancies are of the interior type and 3% are surface vacancies. Thus, 98.5% of the total formation energy of approximately 6×10^6 ev would be returned to the system in this case.

The reduction in energy due to void formation is schematically illustrated in Figure 9. The dashed-in lines merely indicate that the real situation is somewhat more complicated than the idealized calculation of the last paragraph due to the existence of small clusters of 10 vacancies or less in the initial damage state rather than 100% monovacancies.

The small fraction of the formation energy of the monovacancies that is not returned to the system upon void formation is quantitatively equal to the surface energy as is indicated in Figure 9. This leads to an estimate of the surface energy of γ-iron of 1,921 ergs/cm^2. Johnson (Phil. Mag. 16, 553, 1967) has carried out a more accurate calculation of this energy by using computer techniques and arrives at a value within 25%.

The results listed in Table 4 shows that all vacancy clusters in γ-iron exhibit a positive binding energy. Thus there is no minimum size cluster that must be attained before stability with respect to dissociation is achieved. This

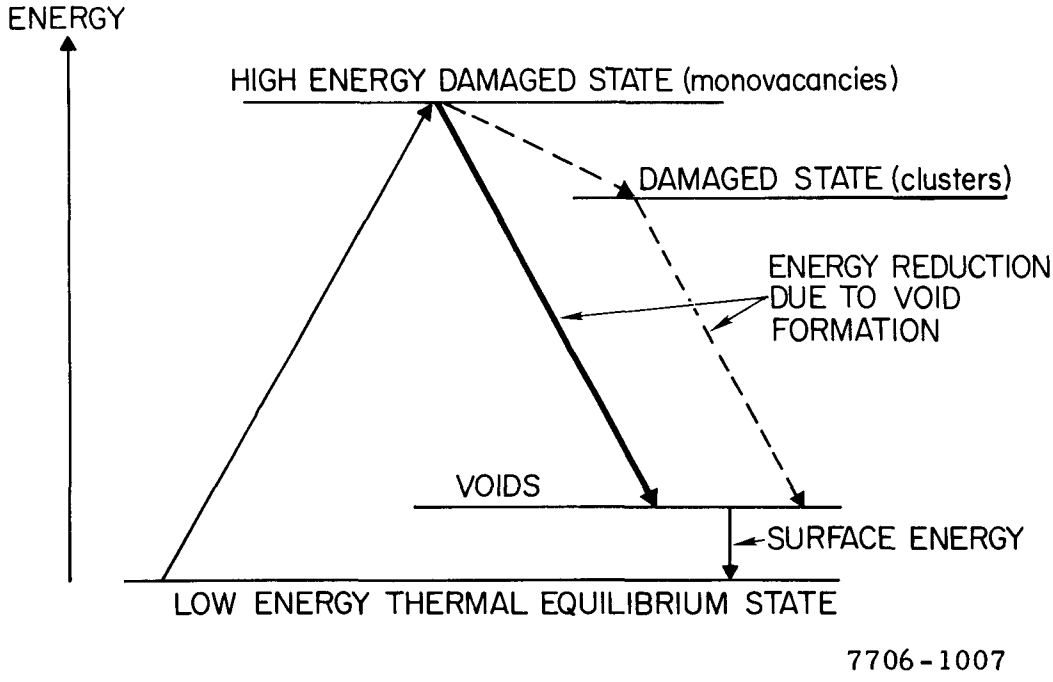

Figure 9. Schematic Representation of Energy Reduction Due to Void Formation

result is contrary to the predictions of classical nucleation theory wherein a minimum size nucleus of a new phase must be attained to overcome the energy barrier imposed by the surface free energy of the interface between the two phases. However, in the present case, we are not condensing a second phase out of a parent phase, but instead are merely redistributing excess vacancies within one and the same phase. Hence, there is no reason to expect to find an energy barrier for the nucleation of vacancy clusters and, indeed, none is found.

The absence of any nucleation barrier means that the mechanism of the nucleation and growth of vacancy clusters is strictly diffusion controlled. That is, the vacancies move about in either the usual random-walk process or parallel to the thermal gradient that commonly exists in nuclear reactor fuel elements. Whenever two vacancies happen to find themselves to be nearest neighbors they will tend to stay together as a stable divacancy. Then, as further vacancies find themselves in juxtaposition with a vacancy cluster, they will add on and cause the cluster to grow.

The key configuration to be considered in the growth of voids is the 13-vacancy sphere, Defect 11, Figure 8. Once this pseudospherical cluster is

formed, growth can continue by the diffusion of other vacancies to the central cluster. The bond counting rule suggests that compact clusters which most closely approach a pseudospherical shape will be the most stable for any given value of N_v since N_B increases with increasing compactness. This conclusion is borne out by a comparison of the 13-vacancy sphere with the (001) and (111) planar 13-vacancy clusters, defects 7 and 10. The values of N_B for Defects 11, 10, and 7 are respectively 36, 24, and 16, and the values of E_B decrease in the same order, as shown in Table 4. This fact does not mean that there is a direct mechanistic path by means of which the planar clusters could transform into a spherical cluster. However, dissociation-recombination processes would on the time average favor such geometrical conversions since the probability of dissociation of a vacancy decreases with an increase in its individual value of N_B.

Two papers have been submitted for publication. They are: "Xenon-Vacancy Defect Clusters in Copper," by A. Anderman and W. A. Gehman; and "Vacancy Clusters and Voids in FCC γ-Iron," by W. A. Gehman.

I. MASS SPECTROMETER ANALYSIS OF HELIUM IN METALS

A series of experiments to measure helium in metals by using a gas mass spectrometer was successfully completed at McMaster University, Hamilton, Canada. The mass spectrometer was constructed so that it could be operated while maintaining a high vacuum with the vacuum pumps valved off. Small quantities of helium (roughly 10^{-5} cc STP) were extracted by melting several samples of helium-injected steel. A similar but modified system was then constructed by using a Veeco GA-4 residual gas analyzer mass spectrometer. Because this instrument does not have as much resolution as the McMaster mass spectrometer, considerably more attention was paid to insure good gettering of hydrogen whose molecule HD can interfere with the measurement of ^3He. A number of better electronic components were also procured along with a high capacity ion pump system. Much of the sample handling system, see Figure 10, was fabricated at Atomics International from either stainless steel or special aluminosilicate glass because helium in the quantities considered for these experiments permeates through most other glasses. A system of calibrated volumes, made of aluminosilicate glass, is attached to the mass spectrometer in order to allow

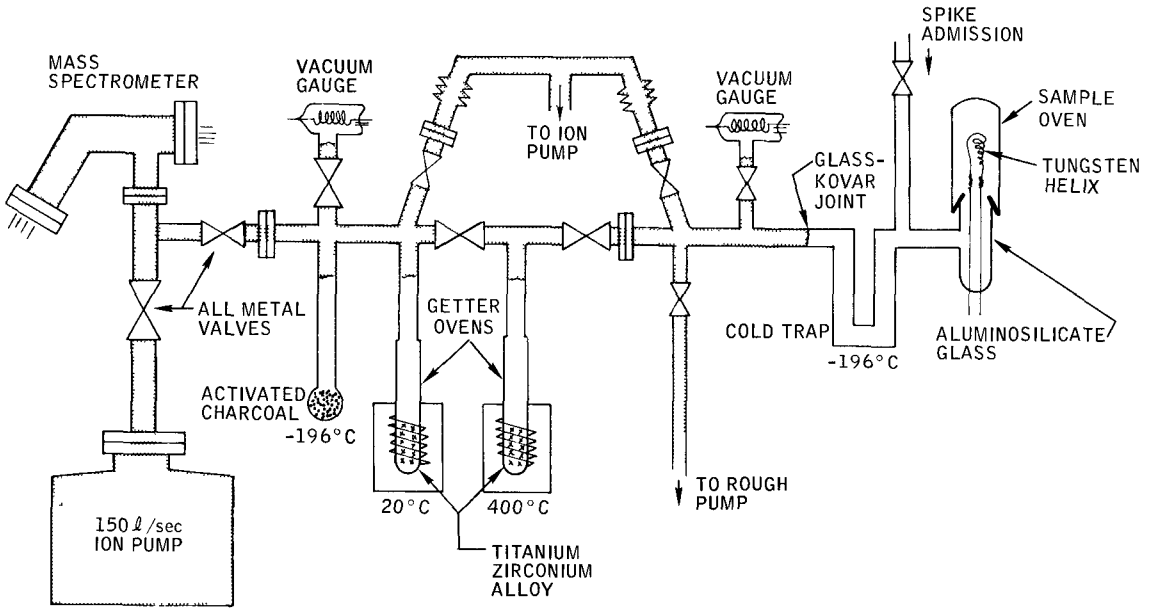

8-J3-079-4

Figure 10. High Sensitivity Gas Mass Spectrometer System for Helium Analysis

small aliquots of helium 3 to be introduced easily. Also included is a volume system to dispense a calibration mixture of equal amounts of ^{3}He and ^{4}He for introduction into the mass spectometer before and after each series of analyses. The mass spectrometer must operate during the analysis without the benefit of vacuum pumps and therefore a bake-out oven was made to surround the entire high vacuum part of the system. A special alloy of zirconium-titanium was made for getters which were placed in individual furnaces. One of the getters is allowed to remain in the mass spectrometer system during an analysis to insure that the nitrogen and oxygen levels remain low.

Determination of helium content is made by cutting a suitable size piece of the material of interest (approximately 1 milligram,) weighing it, and melting it in a tungsten helix furnace under vacuum. Immediately after the material is melted and the ^{4}He is released, a precisely known volume of ^{3}He (approximately 10^{-5} cc STP) is added. Mixing of ^{3}He and ^{4}He occurs in less than 4 sec. Other gases released by the melting material are gettered and part of the $^{3}He/^{4}He$ ratio and a knowledge of the weight of the material that was melted then produced the helium concentration. Two independent checks have been built in

for calibration and measuring isotope discrimination. Two specially prepared steel "helium standards" were analyzed for helium content. The results agree to better than 3% with the calculations based on the production of helium from the thermal neutron irradiation of boron in steel in the reactor STIR. Recent values of helium concentrations obtained at Atomics International are in close agreement with values obtained on the same samples made at McMaster University in June 1967. Repeated measurements on the same sample tensile specimens have given results reproducible to within 1%. Absolute accuracy in concentration is estimated to be better than 3%, for samples whose concentration is above 1×10^{-8} atom fraction.

As a result of the improvements over the McMaster system, the sensitivity of the gas mass spectrometer is much greater than had originally been anticipated. Consequently, early samples of helium although representing no more than 1×10^{-5} atom fraction helium in a few milligrams of stainless steel, were unnecessarily large by a factor of 100. Memory from previous samples usually is in the order of 0.1% the size of the previous sample. To reduce this memory, a number of steps were taken. The interior of the ion pumps were disassembled and cleaned according to manufacturer's specifications. To remove memory from the mass spectrometer itself, the whole system was flushed repeatedly with nitrogen, baked at 300°C several times, and most importantly was operated in a poor vacuum for two days. By operating this way, the ion source produced a very large ion beam (principally nitrogen) which then bombarded the source slits, tube, and electron multiplier, effectively sputtering "memory" helium. The whole source assembly was further chemically and abrasively cleaned when it became necessary to replace the burned-out filament.

It has now been determined that the desorption rate or leak-rate within the mass spectrometer itself is only 4×10^{8} atoms of ^{4}He per minute which is low enough for extremely high sensitivity measurements. A Pyrex part of the sample handling system has a permeation rate of 3×10^{9} atoms of ^{4}He per min which will later be reduced by conversion to aluminosilicate glass. Getter temperatures of 400°C are now used instead of the previous 900°C because the getters operate satisfactorily at the lower temperature and the helium diffusion rate from air through the mullite oven walls is 16 times smaller at the lower temperature.

The following steps have now been taken to reduce the size of future helium aliquots. (1) Small pieces of helium-containing samples are cut. The absolute accuracy of the final concentration is directly proportional to the accuracy of the sample weighing, so that in order to get a standard deviation in weight of 1% in a reasonable period of time, samples are still generally larger than 500 micrograms. (2) The volume of the oven in which the samples are melted and the helium is released has been increased a factor of 10 to 1 liter. (3) A much smaller fraction of the gas in the oven is allowed into the mass spectrometer. Since only the $^{3}He/^{4}He$ ratio is measured it is unimportant what fraction of the gas is analyzed.

Forty samples with concentrations of helium ranging from 10^{-7} to 3×10^{-5} atom fraction have been analyzed. Minor modifications to the system that are now being made are expected to lower the detection limit of the instrument to less than 10^{-9} atom fraction.

The measured helium concentrations of two LAMPRE-irradiated samples have been compared with calculations based on cross sections, assumed neutron spectra, etc. performed by H. Alter (NAA-SR-MEMO-10626). By normalizing the known LAMPRE neutron flux distribution in the high energy region to the "Watt" neutron spectrum assumed by Alter, calculations agree with measurements to within 30% which is considered good in view of the un ertainties of flux, cross sections, and other approximations used.

III. EVALUATION OF EFFORT DURING FISCAL YEAR 1968

Significant advances were made in the understanding of helium embrittlement in austenitic stainless steels. A comparison of Types 304 and 316 stainless steel and Incoloy 800 shows that they all suffer embrittlement to about the same extent except when Type 316 stainless steel is treated to produce a fine dispersion of sigma precipitates. It is therefore likely that any iron-base austenitic alloy will be embrittled by helium unless the helium can be trapped in the matrix and prevented from accumulating in the grain boundaries. The fine dispersion of sigma particles accomplished this in Type 316 stainless. Modification of current austenitic alloys to yield even finer dispersions may significantly reduce their susceptibility to helium embrittlement.

Type 405 stainless steel, a ferritic alloy, experienced significantly less ductility loss due to helium than the austenitic alloys discussed above. Other ferritic alloys have also been reported to be less susceptible to embrittlement after neutron irradiation, than austenitic alloys. Detailed metallography will be employed to explain the behavior of this alloy.

Computer calculations have shown that a vacancy cluster of any size is stable in γ-iron. This means that helium and/or hydrogen need not be present in or on the surface of a void (large vacancy cluster) for stability. The formation of voids from the agglomeration vacancies is controlled by their diffusion.

The construction and operation of a gas-source mass spectrometer has been a signal success. The helium concentrations of samples from the third and fourth injections are now known with high accuracy. The very high sensitivity of the instrument (still being determined but less than 10^{-8} atom fraction helium) will allow very short-time irradiations to be employed for the study of gas production.

Program: FBR Fuel Development, Fuel Cladding and Structural Materials
AEC Task: 10-E-2, Modes of Failure and Helium Degradation (Engineering Properties)
Project Manager: J. L. Ballif/J. J. Gill
Reporting Period: Fiscal Year 1968
General Order: 7706 Subaccount: 29551 AEC Category: 04-01-61-01.1

Principal Investigator: J. H. Shively

I. PROJECT OBJECTIVES

To determine the combined effects of biaxial stresses, helium, and sodium and thermal environment of the LMFBR on the stress-rupture and creep behavior of candidate fuel cladding alloys.

II. TECHNICAL PROGRESS DURING FISCAL YEAR 1968

A. SUMMARY

A target device was designed and built to uniformly inject a pair of thin-walled tubes with helium. Eight tubes were injected for 7-1/2 hours each; two of Type 304 stainless steel and six of Type 316 stainless steel. Two static sodium retorts were built and put on test. One retort was built of Type 304 stainless steel and contains two injected tubes, three control tubes, and seven creep specimens. The other retort was made of Type 316 stainless steel and contains four injected tubes and eight control tubes. Both retorts were put on test at 1200°F, and the tests are expected to be ended by the end of the fiscal year.

B. PROCEDURES

In order to inject thin-walled tubing with helium, a new target device was designed and constructed to be used with the University of Washington Cyclotron. This represents a modification of the previous injection fixture used on small tensile specimens; it is now possible to inject thin-walled tubes as well as flat tensile specimens. The target device with the tubes is shown in Figure 1. The tubes are rotated by means of a gear train connected to a small air motor. In addition, three degrees of translational motion are provided by the injection box. By simultaneous rotation and translation in the beam of α particles, the tubing was injected uniformly to a radial depth of 7 mils in both the circumferential and

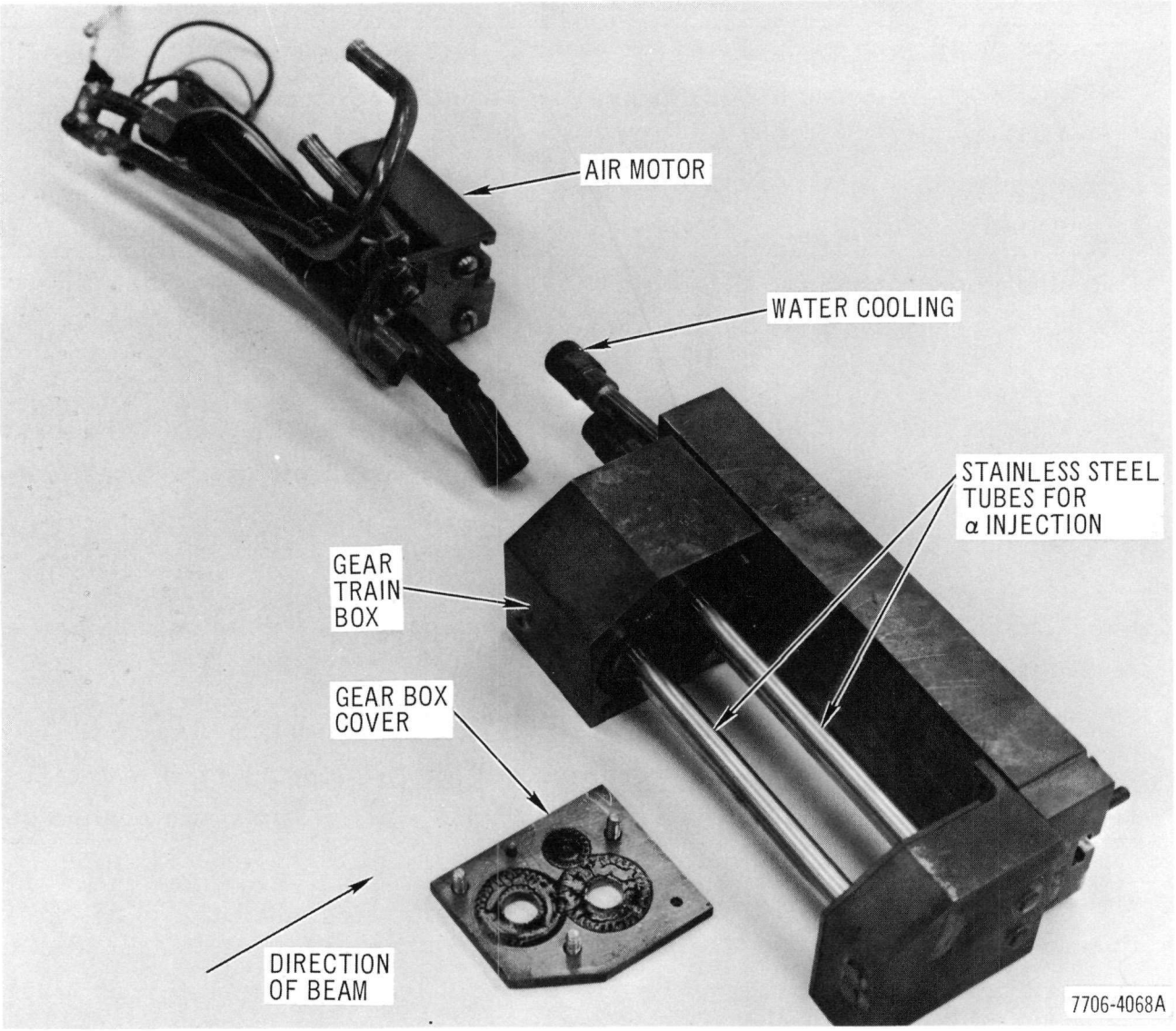

Figure 1. Tubing Injection Target Device

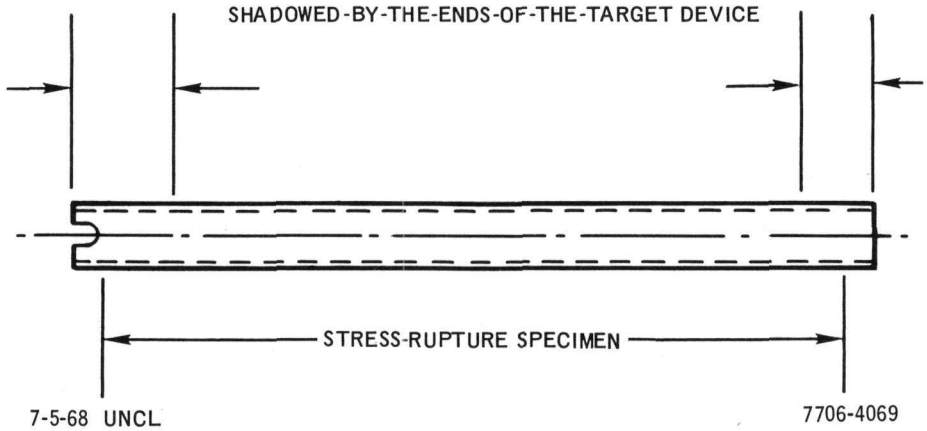

Figure 2. Injected Tube Before Testing

longitudinal directions. Thus, the outer fibers contained most of the helium (estimated to be about 15 ppma).

Eight specimens of austenitic stainless steel were prepared for injection by polishing the ends and the surface near the ends after the groove at one end was cut. This groove fits into a slot in the gear drive of the target device so that the specimen can be rotated without recourse to friction forces. This grooved speciment is shown in Figure 2. Prior to specimen preparation, the tubes were annealed under the following conditions:

1) Type 304 stainless steel, 1/2 hr at 1900°F with a furnace cool, and
2) Type 316 stainless steel, 1/2 hr at 1950°F with a furnace cool.

This treatment left a carbide-free microstructure with a grain size of ASTM-6 to 8.

The eight specimens were shipped to the cyclotron for injection. Table 1 gives the conditions of the injections.

TABLE 1
INJECTION PARAMETER DATA

Stainless Steel Type	Number of Tubes	Metallurgical State	Time Injected (hr)	Beam Current (μ amp)	Approximate He Concentration (ppma)
304	2	Annealed	7-1/2	30	15
316	6	Annealed	7-1/2	30	15

Two retorts for testing biaxially stressed stainless steel tubes which are injected with helium were assembled and loaded with sodium. These retorts are presently under test at 1200°F. Tables 2 and 3 describe the test conditions for both the injected and control specimens in each retort.

C. TECHNICAL APPROACH

A goal of this work is the determination of the effect of injected helium on the stress-rupture behavior of cladding. The effect of strain rate and the material composition on the sensitivity to helium in the lattice will also be determined.

TABLE 2

TEST CONDITIONS FOR RETORT H-1
STAINLESS STEEL

Specimen Number	Hoop Stress (psi)	Type of Test	Approximate Test Duration (hr)	Approximate Helium Level (ppma)
A4H-1-1	26,750	*	200-500	15
A4H-1-2	26,750	*	200-500	15
A4-72	26,750	*	400-500	0
A4-73	26,750	*	400-500	0
A4-74	26,750	*	400-500	0
A4-75	26,750	Creep	0.1	0
A4-76	26,750	Creep	0.5	0
A4-77	26,750	Creep	1.0	0
A4-78	26,750	Creep	16.0	0
A4-79	26,750	Creep	40.0	0
A4-80	26,750	Creep	96.0	0
A4-81	26,750	Creep	240.0	0

*Stress rupture

TABLE 3

TEST CONDITIONS FOR RETORT H-101
TYPE 316 STAINLESS STEEL

Specimen Number	Hoop Stress (psi)	Type of Test	Approximate Test Duration (hr)	Approximate Helium Level (ppma)
A64-1-1	24,000	*	200-500	15
A64-1-2	24,000	*	200-500	15
A6-69	24,000	*	400-500	0
A6-70	24,000	*	400-500	0
A6-71	24,000	*	400-500	0
A6-75	25,375	*	250-350	0
A6-76	25,375	*	250-350	0
A6H-3-1	26,750	*	100-350	15
A6H-3-2	26,750	*	100-350	15
A6-72	26,750	*	150-250	0
A6-73	26,750	*	150-250	0
A6-74	26,750	*	150-250	0

*Stress rupture

Much of the work on injected and irradiated materials has been conducted by using high strain rates and elevated temperatures. From a design viewpoint, it is important to have some insight into the behavior of helium-containing cladding under slow strain rate conditions. This importance arises because helium may influence creep as well as failure mechanisms, and fuel pin failures are more related to biaxial stress-rupture than tensile properties.

In order to predict fuel cladding performance, helium is injected into cladding to simulate the deleterious effects of neutron radiation, a major part of which is suggested to be due to helium produced by the (n,α) reaction. Most of the high strain work done on irradiated and injected cladding cannot be extrapolated to slow strain rate conditions because only the failure mechanisms is studied. Moreover, short-term tensile data on irradiated and injected speciments may only reflect the reduction in area and not the uniform strain. In creep, the time for uniform straining prior to failure occupies most of the time to failure, particularly in the biaxial stress mode.

In creep, considerable speculation exists about the extent of tertiary creep in materials stressed in a biaxial mode. So far, data have not been gathered to show directly that biaxial stresses reduce the amount of tertiary creep. In terms of predicting the stress-rupture life of fuel cladding, this is important to the analysis. For example, if biaxial stresses reduce the amount of tertiary creep, life predictions based on secondary creep equations have merit. If, on the other hand, biaxial stress has no effect on tertiary creep when compared to uniaxial creep, the criteria for life must include both secondary and tertiary creep.

For irradiated or injected tubes, the problem is even more critical. If biaxial stresses remove tertiary creep (creep beyond the stability point), injection should have only a small effect on biaxially stresses specimens compared to the effect on uniaxially stressed specimens. In contrast, if biaxial stresses have no effect on tertiary creep, both biaxially and uniaxially stressed specimens should exhibit the same behavior except for the effect of stress-state. It is apparent from the above discussion that the creep behavior of materials under a biaxial stress state is very important in the correct interpretation of a helium effect in cladding.

This background material points to the need for creep data under a biaxial stress state. Strain gages for use in high temperature sodium, which can be used on uniaxial specimens, are not applicable to biaxial specimens. This is because they could not be located to give a true value of tertiary creep. As an alternative, seven identical noninjected specimens would be stressed equally. These tests will be interrupted at specified times by removing the internal gas pressures. Then, after the last specimen has failed and all of the tubes have been removed from the retort, the creep specimens will be profiled. From these seven data points on creep, it will be possible to estimate the secondary creep rate and the amounts of primary and tertiary creep. More importantly, this creep information will permit the role of helium on creep behavior to be estimated; i.e., whether helium injection affects second or third stage creep or both. From an engineering viewpoint, the distinction is important.

D. RESULTS AND DISCUSSION

At the time of writing, only one pair of helium injected tubes of type 316 stainless steel had failed. These are Specimens A6H-3-1 and A6H-3-2; the respective rupture times are 28 and 68.5 hours. The control specimens A6-72 through A6-74 are still on test and have not ruptured. A comparison of the injected and noninjected stress-rupture behavior is still possible, since the same material was tested earlier as part of Task 10-C. This comparison is illustrated in Figure 3. As can be seen, 15 ppma helium reduced the stress rupture life by a factor of four. A comparison with uniaxial stress-rupture data reported in this quarterly for Type 304 stainless steel specimens shows only a factor of two, change in the rupture life due to helium. If similar results are obtained on uniaxial specimens of Type 316 stainless steel, the biaxial stress state would appear to enhance the effects of helium on the stress rupture life. This difference between biaxial and uniaxial may reflect the difference in helium level. The uniaxial stress rupture behavior was, however, insensitive to helium content between 1 and 30 ppma.

The effect of stress state on the stress-rupture life described above must necessarily be considered preliminary. Nevertheless, it is possible to speculate about (1) the reduced life due to helium for either stress state, and (2) the increased reduction in life due to biaxial stress state. In order to explain the

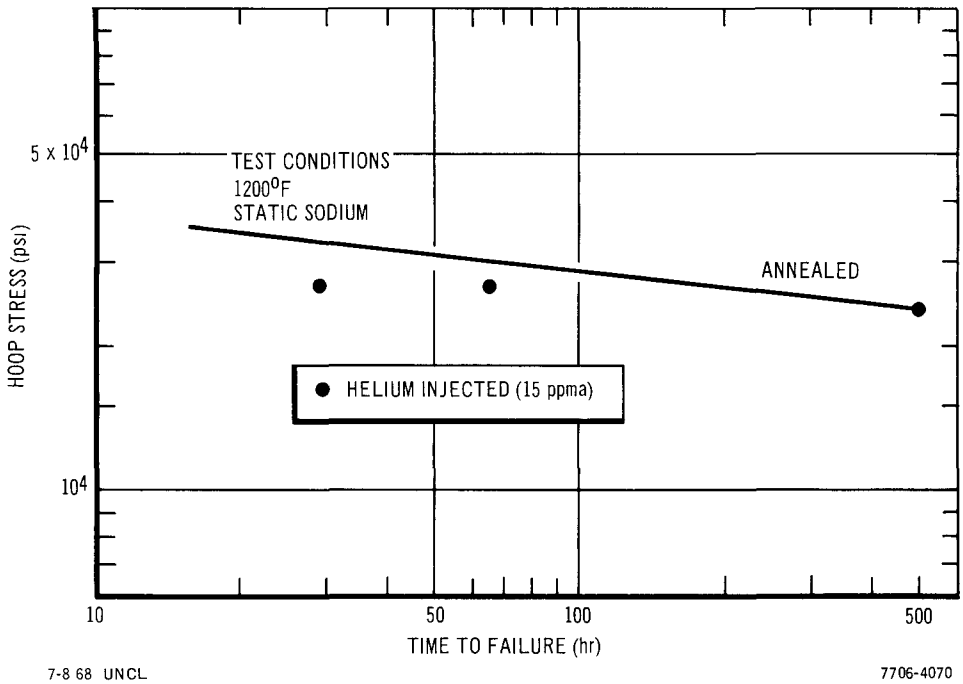

Figure 3. Effect of Helium Injection on the Biaxial Stress-Rupture Life of Annealed Type 316 Stainless Steel

preliminary observations, the Siegfried creep-rupture model can be extended to the test situation.[1] Reduced life can be traced to two possible sources, a reduction in the available ductility, or a reduction in the creep fracture stress (cohesive strength). These two possibilities are not easily separated, since each generally reduce the total strain at failure. What is required, is creep data at constant load under a given stress state.

The reduction in stress rupture life without regard to state of stress is depicted in the top diagram of Figure 4. Rupture of annealed material occurs when the deformation (true) stress equals the cohesive strength (fracture true stress). The deformation stress defined as the load divided by the instantaneous area is governed by creep. Since creep produces a reduction in cross-sectional area (load carrying capacity), the true stress increases at a rate determined by the creep rate. A 2% tensile elongation produces 2% increase in the true stress under constant volume conditions (plastic deformation). The cohesive strength is the instantaneous true stress necessary to cause failure. This idea is currently used to explain the ductile to brittle transition in ferritic steels[2], transgranular

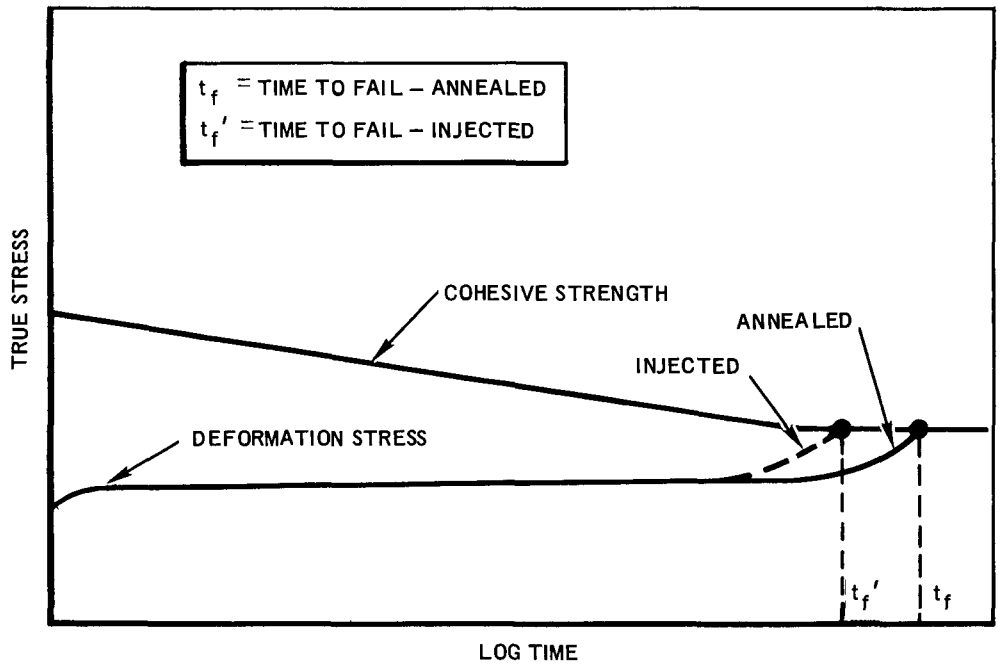

(a) DUCTILITY LIMITED LIFE

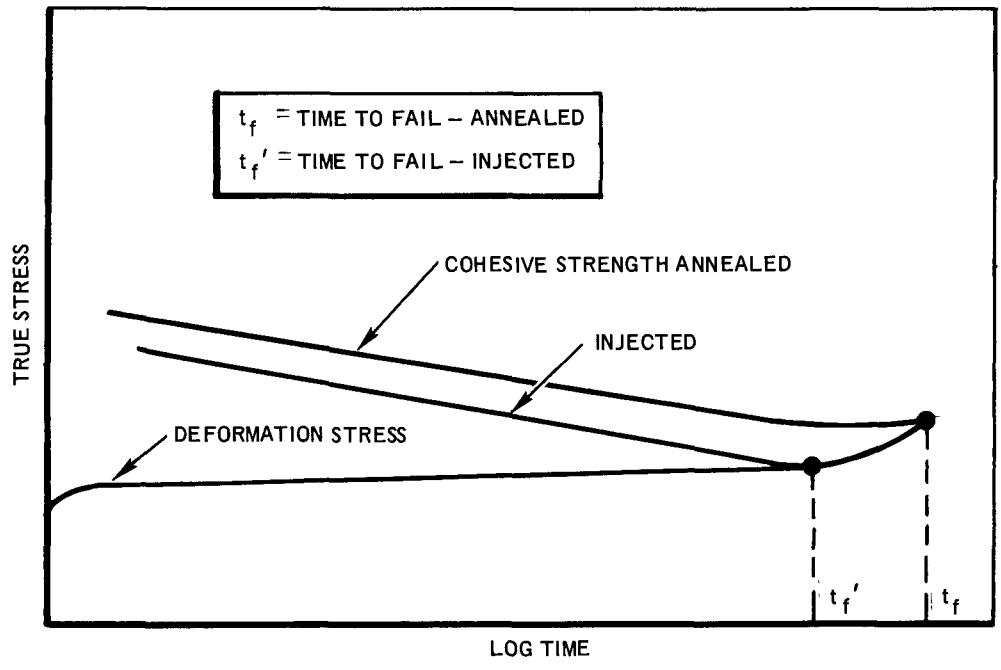

(b) STRENGTH LIMITED LIFE

7-8-68 UNCL

7706-4071

Figure 4. Relationship of Cohesive Strength and Stress Buildup to Rupture Life

to intergranular failures[3], hydrogen embrittlement[4], and crack propagation (fracture toughness)[5]. Moreover, cohesive strength is sensitive to temperature[6], stress state[1], strain rate[6], prior history[1], heat treatment[1], and probably helium content or radiation effects. In the case of creep, the cohesive strength decreases for two reasons, the reduction in the actual cross-section due to void and microcrack formation along grain boundaries, and the decrease in the resistance to crack propagation from precipitation phenomena, work hardening, and microresidual stresses. Therefore, factors in the environment and in the metal which influence creep cohesive strength will also affect the creep strain to rupture.

The behavior of materials in creep rupture can be described as strength limited or ductility limited according to how and when the strength curve intersects the deformation stress curve. This is illustrated in the two diagrams in Figure 4. Consider ductility limited behavior; the life of the specimen is determined by the onset of third stage creep. This stage in creep deformation is characterized by the cross-sectional area reducing faster than the strain hardening[7]; consequently, the stress builds up faster than the material can resist deformation. In third stage creep, the rate of deformation accelerates at faster and faster rates until the true stress equals the cohesive strength. In a sense, it marks the beginning of instability in creep and is therefore analogous to necking in a conventional tensile test. The onset of third stage creep therefore represents the limit of strain before instability sets in. For the case where failure is ductility limited, helium may reduce the life by bringing about an earlier onset of tertiary creep, see Figure 4, top. In addition, if helium present in material enhanced the secondary creep rate, failure would also occur earlier and with less strain prior to instability. This effect on the secondary creep rate by helium is unlikely, because much of deformation in creep involves dislocation motion and grain distortion which would be reduced by helium-dislocation interactions. In fact, the complementary work on helium embrittlement supports the idea that it is action by helium at grain boundaries that limits ductility.

In contrast to the above limitation, helium may reduce the cohesive strength and therefore reduce the stress-rupture life. This action by helium is illustrated in the bottom diagram in Figure 4 for the case where the specimen fails after the beginning of third stage creep. The other possibility is failure before third stage creep, which will be considered later with regard to stress state

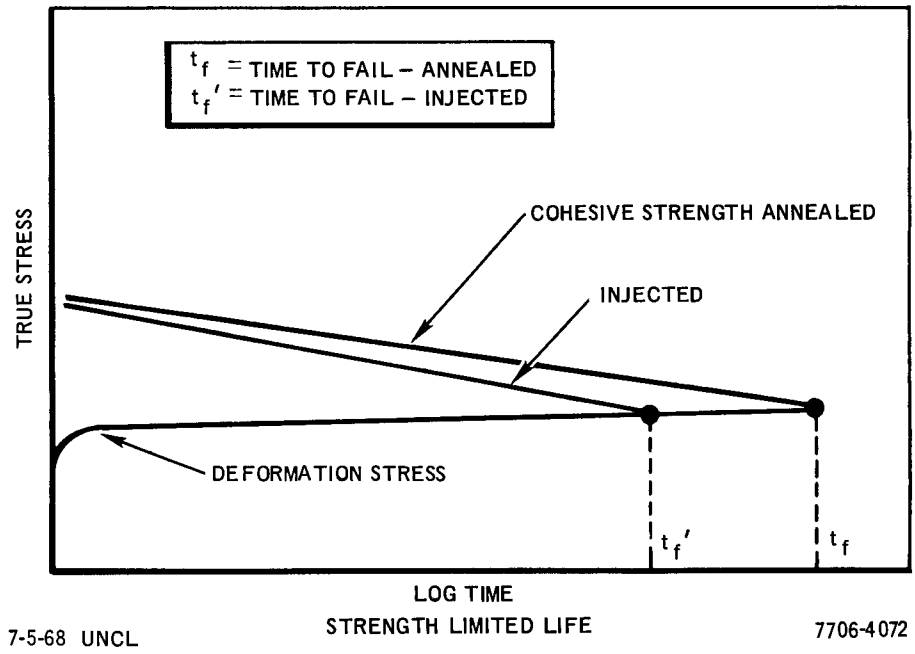

Figure 5. Relationship of Cohesive Strength and Stress Buildup to Rupture Life with No Tertiary Creep

effects. Strength limited stress rupture life with helium is then a reflection of the large shift of cohesive strength due to the presence of helium. The creep behavior of the material is identical, with and without helium, up to the start of third stage creep. Presently, strength limited stress rupture life is a more likely candidate for stress rupture. This is because it has been shown that helium aids void nucleation at grain boundary precipitates. The voids coalesce to form cracks and eventual failure. The cohesive strength will reflect the presence of voids, since it is then easier to cause intergranular rupture. On the other hand, the onset of tertiary creep is related to deformation processes within the grains themselves. Until additional data are available, however, it is not possible to exclude either criteria of failure.

The effect of biaxial stresses on the stress rupture behavior of helium injected tubes requires a knowledge of the creep behavior under the biaxial stress state. For example, if this stress state reduces or eliminates tertiary creep, the effect of helium must be caused by either accelerated secondary creep or reduced cohesive strength is assumed, acceleration of secondary creep does not seem likely, since this would produce an increase in the total strain at failure. The shift in the cohesive strength is perhaps a better candidate to permit rationalization of the reduction in stress-rupture life; this is illustrated in Figure 5.

As can be seen, if injected helium shifts the cohesive strength only slightly, the time to failure can be reduced substantially. This conforms with the large drop in life of biaxially stressed helium injected samples relative to that seen under uniaxial conditions. In the case of uniaxial stress rupture, helium essentially reduces the amount of tertiary creep and perhaps necking. For the uniaxial case where failure is strength limited, the total strain at failure is affected according to tertiary creep response and does not govern failure; therefore, the total strain at failure would vary in unsystematic fashion with little or no effect of helium level on time to failure. For biaxial stresses, the situation is quite different. In the absence of third stage creep, the strain at failure and the life are sensitive to the helium level and would be greatly different for injected and non-injected tubes.

While the above analysis of the effects of helium on the uniaxial and biaxial stress rupture life must be considered incomplete until additional data are obtained, it is clear that these tests have far reaching engineering implications for the design of fuel elements. If helium produced by in-pile n,α reactions plays a role in the deformation and failure mechanisms of fuel cladding, the effects of helium must be factored into performance criteria according to whether life is determined by strain or failure. In order to accomplish the design objectives of maximum fuel element life, the effects of fast reactor radiation and the associated helium buildup on both the creep behavior and the criteria for failure must be known.

III. EVALUATION OF THE EFFORT DURING FISCAL YEAR 1968

Once the last specimen in each retort has failed, the retort will be disassembled, the tubes will be profiled, analysis of helium near the rupture area will be obtained by means of the mass spectrometer, and optical microscopy in the rupture area will be done. This work, when factored into a failure analysis, should enable a preliminary evaluation of the effects of helium on creep-rupture behavior to be made. While this by no means provides a basis of design of fuel cladding for the effects of biaxial stress, helium, temperature, and sodium, it does contribute to an increasing technological base upon which LMFBR and FFTF can be built. Therefore, this subtask will have met the limited technical

goal. In order to provide a maximum value to the nuclear industry and LMFBR, a separate report will be issued next fiscal year describing the test results and evaluation.

REFERENCES

1. W. Seigfried, "Investigations Into the Development of Intercrystalline Fractures in Various Steels Under Triaxial Stress," Creep and Fracture of Metals at High Temperatures, HMSO, London, p 333 (1956)
2. N. N. Davidenkov and F. Wittman, Phys. Tech. Inst. (USSR) 4 300 (1937)
3. Z. Jeffries, Trans. AIME 60, 474 (1919)
4. A. R. Troiano, Trans. ASM 52, 399 (1960)
5. C. T. Hahn, W. S. Owen, B. L. Averbach, and M. Cohen, Welding J. 38 372 (1959)
6. G. E. Dieter, Mechanical Metallurgy, McGraw-Hill, New York, 1961, pp 345-347
7. J. D. Lubahn and R. P. Felgar, Plasticity and Creep of Metals, Wiley, New York, 1961, pp 136-141

Program:	FBR Fuels and Cladding			
AEC Task:	11-A, Mixed Carbide Fuels (Basic Properties)			
Project Manager:	J. L. Ballif			
Reporting Period:	Fiscal Year 1968			
General Order:	7707	Subaccount:	28210	AEC Category: 04-40-02-01

Principal Investigator: G. Ervin, Jr.

I. PROJECT OBJECTIVES

Objectives of this project are to: (1) determine selected microstructural attributes and mechanical and physical properties of mixed carbide fuels both to establish the potential for these materials as nuclear fuels and to provide a basis for interpreting and understanding irradiation behavior in terms of atomistic transport phenomena, and (2) develop, where necessary, preparative techniques for polycrystalline mixed carbide materials of controlled structure and stoichiometry.

II. TECHNICAL PROGRESS DURING FISCAL YEAR 1968

A. THE MIXED CARBIDE LABORATORY FACILITY

A laboratory facility for experimental work with mixed carbides (UC-PuC) has been established. The facility is equipped for powder mixing and pressing and for sintering to make carbide from the oxide, or to sinter pellets of pressed carbide. There is also a furnace for annealing and equilibration experiments at temperatures as high as 2300°C in vacuum, or inert atmospheres of controlled composition may be used.

Auxiliary items available to the mixed carbide work include a chemical analytical laboratory, x-ray fluorescence, and a metallographic laboratory including the preparation of surface replicas for electron microscopy. The carbide glove boxes are a part of a much larger complex for handling mixed oxides. Construction of this facility has just been completed, and experimental work can be started early in the next quarter.

B. STUDY OF CARBON ACTIVITIES IN CARBIDE FUELS

One of the principal tasks planned for this laboratory is a study of carbon activities in mixed carbides with emphasis on the effects of additives designed

to control carbon activity and of fission product carbide formers. In preparation for this laboratory work, an analytical study and literature review has been carried out to assess the level of need for such work and to plan experiments. A general conclusion from this study is that activity data are badly needed for an understanding of the carbon transport problem in carbide fuel elements.

1. The Significance of Carbon Activities

Carbide fuel compositions must have a range of tolerance for changes in carbon/metal ratio without forming either free metal phases or phases which are carburizing towards stainless steel. When bonded with sodium, which is the best way to take full advantage of the superior qualities of carbides as fuels, these second phases will react destructively with stainless steel cladding. Close control of the carbon/metal ratio of the fuel as prepared is not a sufficient measure in that prolonged burnup uses up the fissile elements and produces fission products, only some of which are strong carbide formers, with the result that the effective carbon/metal ratio changes. A simplified study has been made of the change in affective carbon/metal ratio due to burnup, which indicates that the ratio will increase and cause carbon to be released.

Several additives of different types have been proposed as a means for controlling the carburizing power of mixed carbide fuels. These include iron and chromium, titanium, zirconium, and molybdenum. Some preparations have been made and empirical experiments have been performed, with indications of positive effects.

The significant property with regard to both the effects of fission products and of additives is the carbon activity. Measurements have been made of carbon activities on iron and steel (cladding compositions) and on some of the refractory carbide including uranium carbide; but the critical data on mixed carbide and on the effects of the above additives have not been attempted. Efforts to obtain activities based on theoretical or semiempirical models leave uncertainties greater than our need to know, to draw meaningful conclusions. An experimental attack on the specific materials involved seems to be inescapable, if a systematic understanding is to be achieved.

2. Discussion of Existing Data on Carbon Activities and Diffusion

There are substantial amounts of data on free energies of formation of carbides and some data on vapor pressures of metals over carbides from which partial information on carbon activities as a function of carbon/metal ratio at selected temperatures may be deduced. A book by E. K. Storms, The Refractory Carbides, Academic Press, New York (1967), contains up-to-date reviews and discussions of the pertinent data for the refractory metal carbides, including UC and PuC. From the point of view of cladding carburization, it is important to know the carbon activities in various steels as a function of carbon content and temperature, and studies of this problem have been published.

Direct studies of compatibility of cladding with fuel have been made over a period of years. Two notable publications will illustrate the type of information presented, one by P. E. Elkins (NAA-SR-7502, August 1964) and one recently by M. Mouchnino (CEA-R3353, October 1967) which show that even at temperatures as low as 650°C (1200°F), significant carburization of stainless steel by hyperstoichiometric UC or (U, Pu)C occurs in the presence of a sodium bond. In brief, these tests demonstrate that there is an important difficulty but they provide little in the way of quantitative data on the separate processes involved.

Although the emphasis in this discussion is on carbon activity as the driving force in carbon transfer from fuel to cladding, the kinetics need to be examined also. At high enough temperatures such as 900°C and above, kinetics will not be a sufficient limitation to carbon transfer; i.e., carbon diffusion through the carbide fuel and through the steel at these temperatures will be rapid enough to permit damaging carburization of cladding during the life of a fuel element. For example, at 900°C, the diffusion coefficient for carbon in hyperstoichiometric UC was found to be about 10^{-12} cm^2/sec. by extrapolation of G. G. Bentle's data. Although this would correspond to a carbide layer of only about 0.004 in. per year, because of the steep temperature gradient within the fuel slug, the transport of carbon would go much deeper than this; for example, 0.400 in. at 1500°C. At lower temperatures, however, such as 650 to 750°C which are likely to be actual cladding temperatures for fast breeder reactor use, the situation becomes more marginal, and a detailed study of this complex problem seems to be needed. Analysis of kinetics, based on our knowledge of diffusion

coefficients, may explain conflicting reports as to the lesser carburizing effect of hyperstoichiometric (U, Pu)C, where the second phase is discrete particles of $(U,Pu)_2\ C_3$, compared with hyperstoichiometric UC, where the second phase is a platycontinuous network of UC_2. Whether or not enhanced diffusion along the UC_2 network will cause more rapid carburization of cladding will depend not only on the surface temperature of the fuel slug, but very importantly on the radial temperature gradient within the slug. Lack of knowledge of diffusion coefficients of PuC and of mixed carbide will hamper this analysis.

The curves shown in Figure 1 based on data taken from Storms (see reference above), illustrate both the existence of some activity data and its inadequacy to providing important answers. The figure shows two curves of carbon activity vs carbon/metal ratio, one for U-C compositions, and one for Pu-C compositions. The curves are not actually comparable, however, because they are for two different temperatures; more importantly, in reference to cladding-fuel interactions, both temperatures are much higher than those for carbon transport to cladding. Another limitation is that it applies to the individual compounds, and it is not readily apparent what the carbon activity for (U, Pu)C solid solutions will be. The scope and range of composition for the UC phase

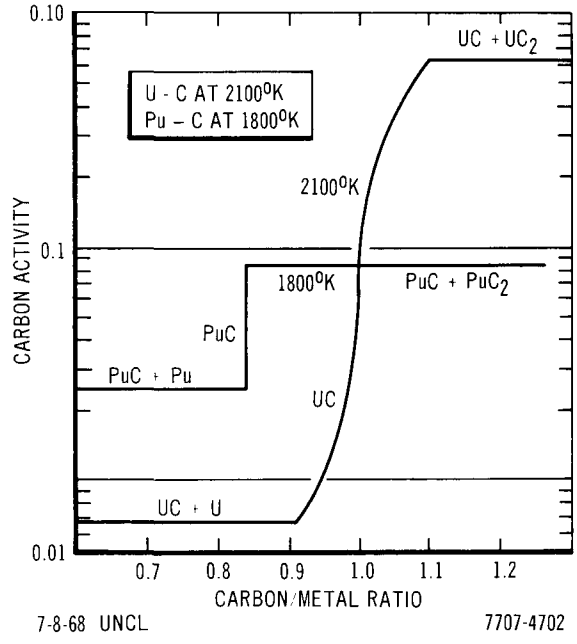

Figure 1. Carbon Activity Data for the U-C and Pu-C Systems

shown is because of the breadth of the UC composition at 2100°K, while the vertical line for PuC at $PuC_{0.85}$ expresses the fact that there is no composition range for PuC at 1800°K. At 700°C (973°K) the reverse is true, there is a broad range for PuC and no range for UC. Also, these data are based on assumptions and thermodynamic data about which there is still some controversy and uncertainty.

It is this type of curve for the actual mixed carbide composition and for the important temperature range 650 to 900°C, together with similar curves for steel compositions that are needed, to describe the potential of carbide fuels for carburizing steels and to show what compositions will be safe. The type of additive that is needed is one that has a curve of flat slope, broad range, and covers a range of carbon activity below that which is capable of carburizing stainless steel. Such compositions will tolerate modest carbon/metal changes without causing cladding interactions.

3. Experimental Approaches Planned

Two experimental approaches are planned. The first is a simple relative stability or compatibility study between the various carbides. Some work of this type has already been done as has been mentioned. The samples are heated in contact with, or in the presence of a carbon transfer medium (H_2 or Na), and the compositions of each are determined by chemical analysis or metallographically. The second method is to equilibrate samples with a gas of known carbon activity provided by passing H_2 over a mixture of a metal and its carbide whose activity is already known as a function of temperature.

A topical report is nearing completion, covering the existing data on carbon activities in the systems of interest, methods of measurement, and the significance of carbon activity for the problem of carbon transport in carbide fuel elements.

III. EVALUATION OF EFFORT DURING FISCAL YEAR 1968

Provision of a laboratory in which experimental work on UC-PuC can be performed is an achievement. The study of the importance and status of carbon activities in pertinent carbides and the completion of a report on this topic will

serve as a strong basis for the initiation of experimental work.

The status of reports and publications on completed studies of basic properties of carbides is as follows:

1) "Oxidation of Uranium Monocarbide at High Temperatures and Low Pressures," by G. Ervin, Jr., a paper, was presented at the High Temperature Technology Symposium at Asilomar in September 1967, and will published in the Proceedings of the Symposium,

2) "Preparation of Fine Refractory Dispersions in UC," by B. D. Pollock and A. C. Hott, a paper accepted for publication in J. Nuclear Materials, and

3) "Diffusion of Uranium and Carbon in Uranium Monocarbide," by G. G. Bentle and G. Ervin, Jr. a manuscript, completed, reviewed, and to be sent to J. Nuclear Materials.

Program: FBR Fuels and Cladding		
AEC Task: 11-B, Mixed Carbide Fuels (Irradiation Studies)		
Project Manager: J. L. Ballif		
Reporting Period: Fiscal Year 1968		
General Order: 7707	Subaccount: 28220	AEC Category: 04-40-02-01

Principal Investigator: G. Ervin, Jr.

I. PROJECT OBJECTIVES

The objective of this project is to apply fundamental technology toward the reduction and control of swelling in mixed carbide fuels and demonstrate the effectiveness of fine dispersion tungsten doping in improving the high temperature irradiation stability of UC.

II. TECHNICAL PROGRESS DURING FISCAL YEAR 1968

A. THE EXP-NRX-9-101 EXPERIMENT

This experiment is a reactor test of the value of a dispersion of fine particles in UC, produced by alloying with tungsten, for trapping fission gas bubbles in order to reduce swelling during high burnup. Construction of the test capsule and preparation of the fuel samples was started last year. During the current year, construction was completed and irradiation to the target burnup in the NRX reactor at Chalk River was completed; disassembly and examination of the fuel slugs will be performed during the next few months.

1. Preparation and Properties of the UC Fuel

The methods of preparation and type of product have been described in previous progress reports, and a topical report on the preparation of the 15% enriched fuel slugs has been issued. Most of the fuel was made by zone melting because this method was found to give the most uniform distribution of tungsten. A zone leveling technique was used to minimize axial concentration gradients. The method of doping with zone leveling is illustrated in Figure 1. The initial molten zone included the excess uranium or carbon, depending on the composition being prepared, and the excess tungsten. These excesses were

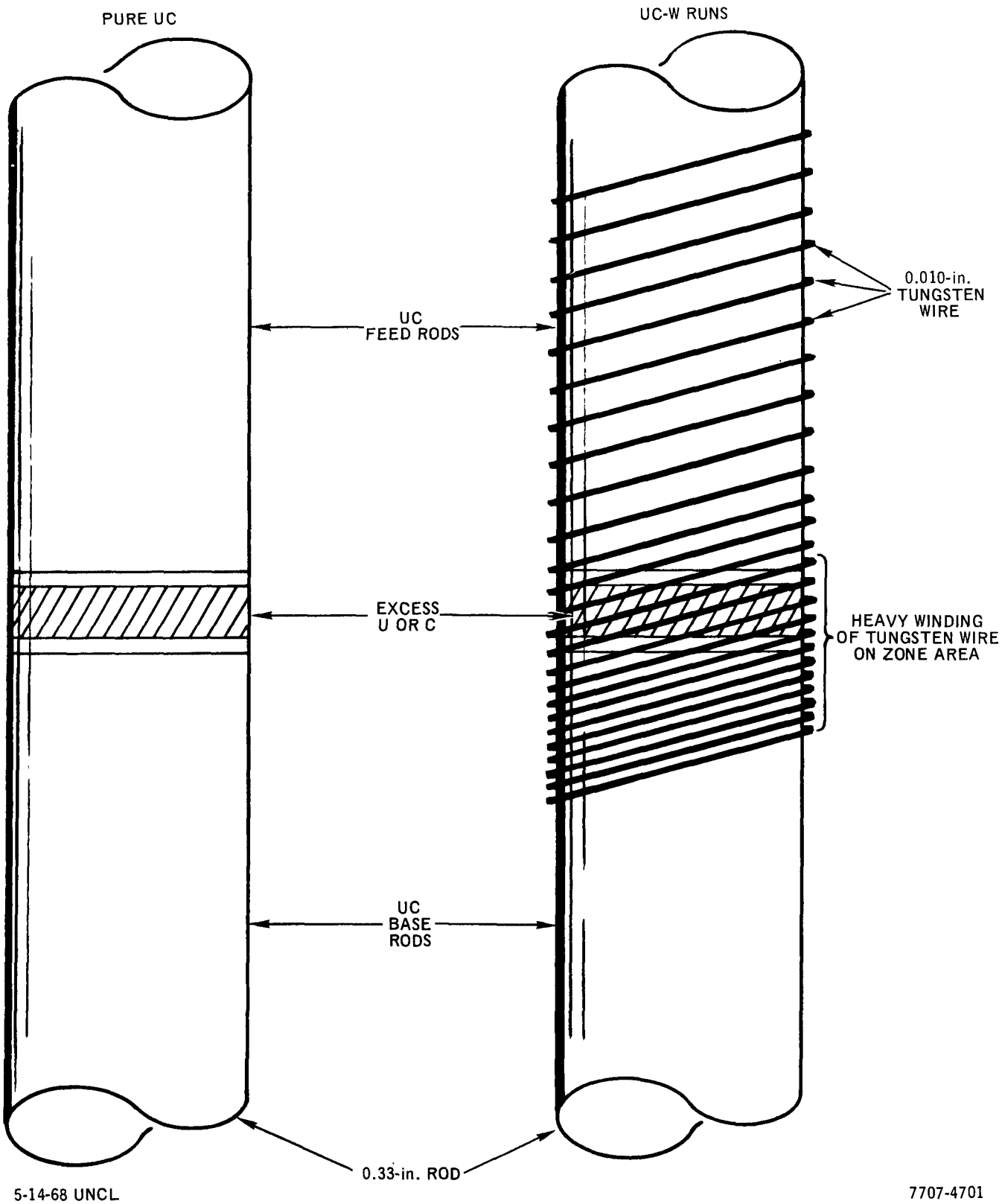

Figure 1. Sketch Showing the Manner of Doping the Zone-Melted Rods

7707-4005

Figure 2. Photograph of the Two Types of Fuel Slugs — Arc Cast and Zone Melted

those calculated to maintain a constant composition as the molten zone was swept along the length of the rod. Figure 2 shows a machined arc cast slug and a finished zone melted slug. These are two of the typical samples used in the reactor test.

There are 114 samples in the capsule including the controls. A small range of carbon/metal stoichiometry and a range of tungsten content as well as two types of structures were included as variables. The chief measure of swelling will be density change; hence, density of each slug prior to irradiation was measured to a precision of ±0.2%. The density ranges found are shown in the table.

Typical microstructures have been illustrated in previous reports. An electron micrograph surface replica showing fine particles in one of the samples actually in the capsule is reproduced in Figure 3.

2. Design and Construction

The design of the experiment was one in which a side-by-side comparison of swelling of unalloyed UC control samples could be made with the UC-W alloy

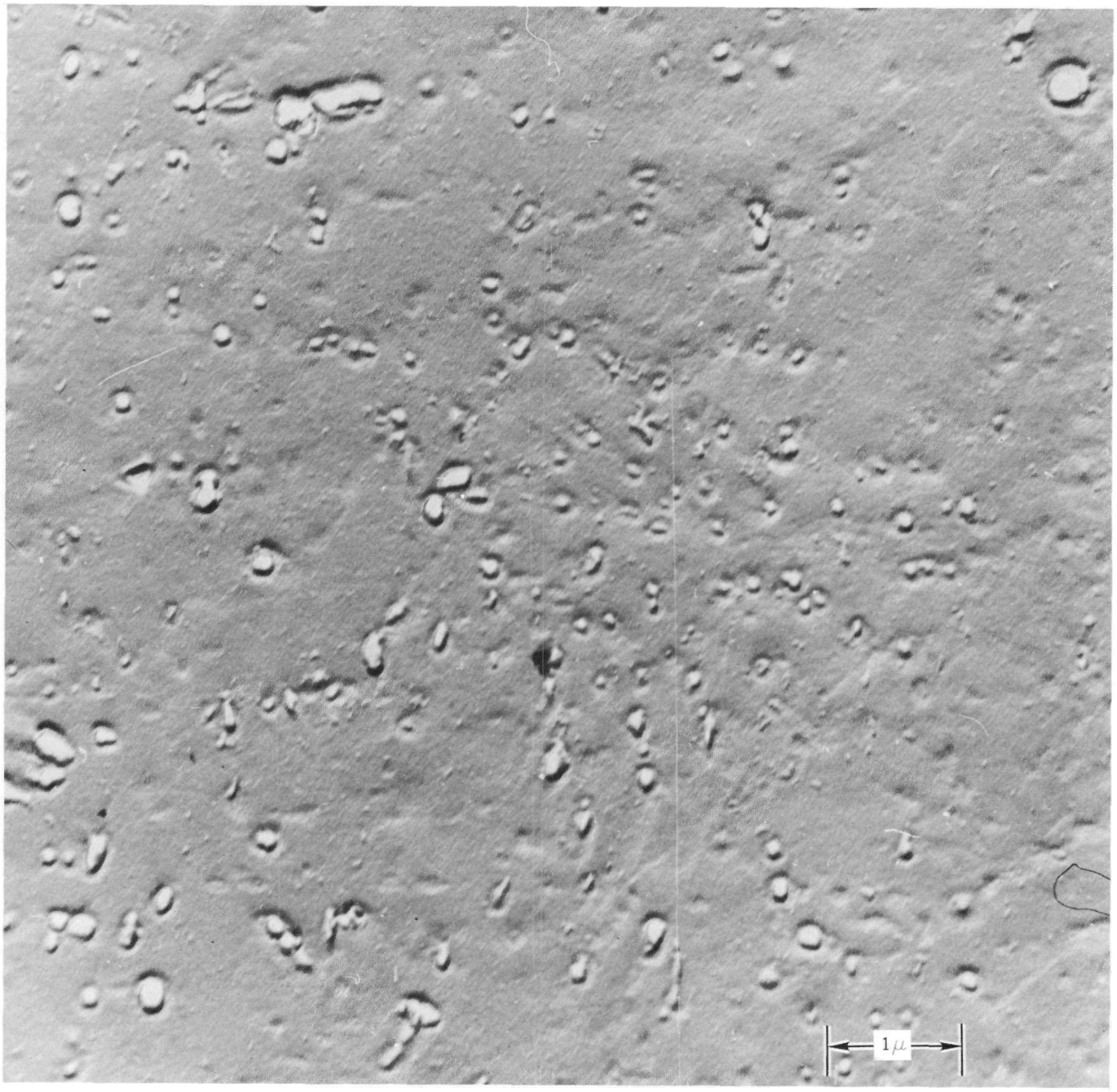

213683

Figure 3. Electron Micrograph Surface Replica Showing Fine Particles in a Zone-Melted Sample, 20,000X

DENSITY RANGES OF FUEL SAMPLES IN THE 101 EXPERIMENT

Carbon Stoichiometry	Tungsten Content (wt %)	Alloy Structure	Density Range (gm/cc)
$MC_{0.97}$	1.6	particle dispersion	13.62 to 13.71
$MC_{0.97}$	1.6	solution	13.64 to 13.72
$MC_{0.97}$	3.0	particle dispersion	13.69 to 13.76
$MC_{0.97}$	3.0	solution	13.71 to 13.77
$MC_{0.99}$	none	-	13.40 to 13.59
$MC_{0.99}$	1.6	particle dispersion	13.61 to 13.69
$MC_{0.99}$	1.6	solution	13.57 to 13.65
$MC_{0.99}$	3.0	particle dispersion	13.60 to 13.72
$MC_{0.99}$	3.0	solution	13.68 to 13.74

samples. The capsule was constructed so as to allow for extensive swelling of the controls without any significant change in the heat transfer characteristics. Furthermore, since the best temperature range for swelling comparison is not known accurately, because of wide scatter in swelling results on UC, it was desired to expose the samples to a range of temperatures. These purposes were accomplished by providing a long string of 1/2-inch long fuel slugs, including numerous control samples, all contained in a NaK heat transfer medium. The cutaway view of Figure 4 gives a good idea of the details of construction. Each slug was contained in a separate can or basket made of niobium metal, each one having identifying marks. This is illustrated further by a longitudinal section shown in Figure 5. The top lid of each can is free to move when the fuel slug swells and there is ample space at the sides also. A portion of the assembled fuel string is shown in Figure 6. Other features seen in Figure 4 are the double containment of the NaK, and the two zirconium cylinders used as thermal barriers to raise the fuel temperature to the desired levels.

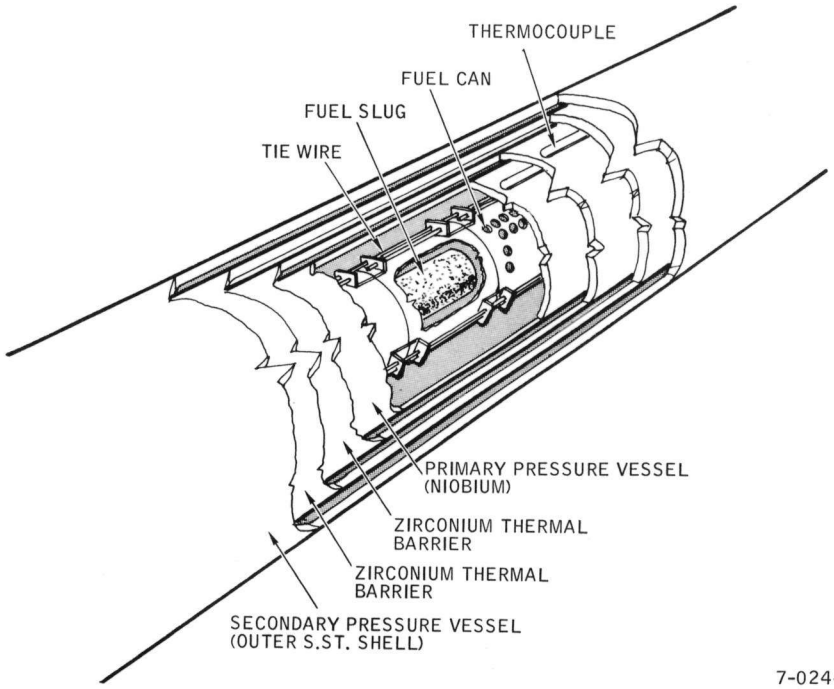

Figure 4. NRX-9-101 Irradiation Capsule Cutaway

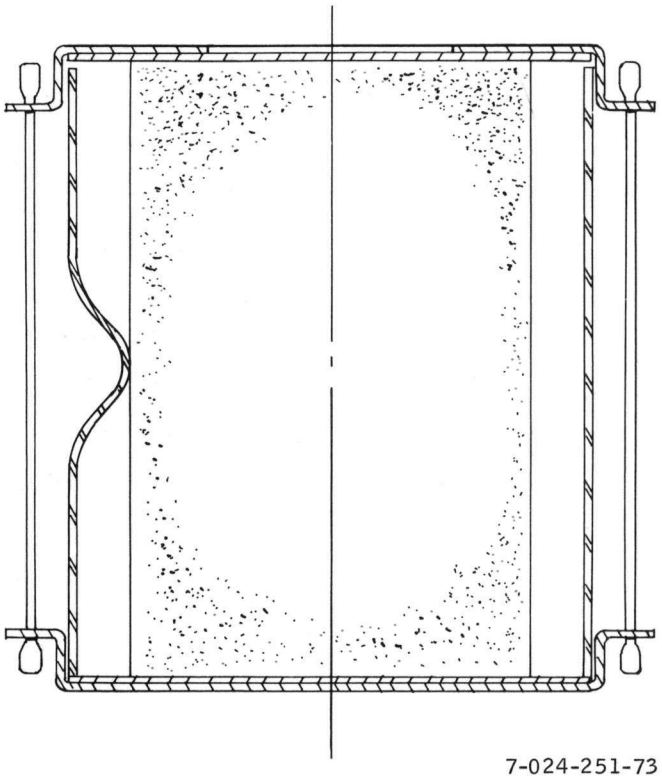

Figure 5. Fuel Can Cross Section

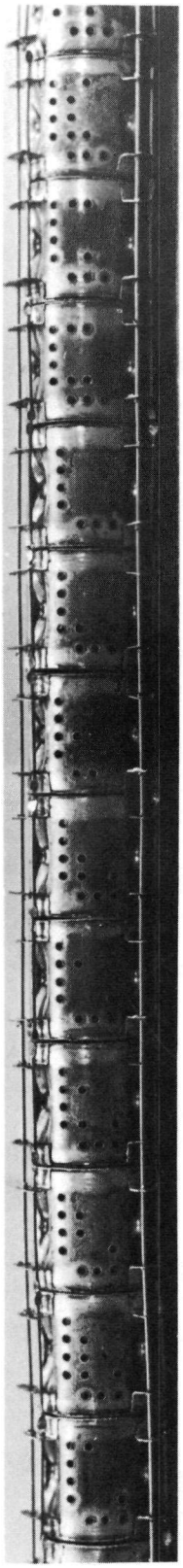

Figure 6.
Fuel String

7707-5147A

Containment of the NaK is illustrated in the schematic longitudinal section of Figure 7. It is seen that the NaK in each chamber is under pressure, which is necessary in order to reach the desired high temperature at the fuel surface without boiling. Boiling would cause loss of thermal bond and a sharp rise in fuel temperature. In the figure, the numbers shown in parentheses are the pressures corresponding to room temperature and the upper numbers are those corresponding to operating temperature. The pressures were chosen within limits which would allow as high a fuel surface temperature as possible without undue stresses on the containment vessels. The outer vessel is pressurized to partially balance the pressure in the inner vessel and thus lower the stresses. The pressures were controlled by the degree of filling with NaK, together with the amount of helium overpressure provided.

The calculated temperature profiles within the capsule are shown in Figure 8, which also indicates the axial locations of the thermocouples used to measure temperatures during operation. The radial locations of these is in slots in the zirconium cylinders as may be seen in Figure 4. In operation, the measured temperatures are used along with the known thermal properties of the materials and the power generation within the fuel to calculate the fuel centerline temperatures.

Construction and assembly of the capsule was completed during November 1967 and the experiment was shipped to Chalk River for insertion in the NRX reactor early in December. However, after its arrival in Chalk River, an error was discovered in the degree of filling of the outer pressure vessel with NaK. It was returned to Canoga Park in order to make a proper repair and adjustment and sent back to Chalk River in time for a reactor startup in late January.

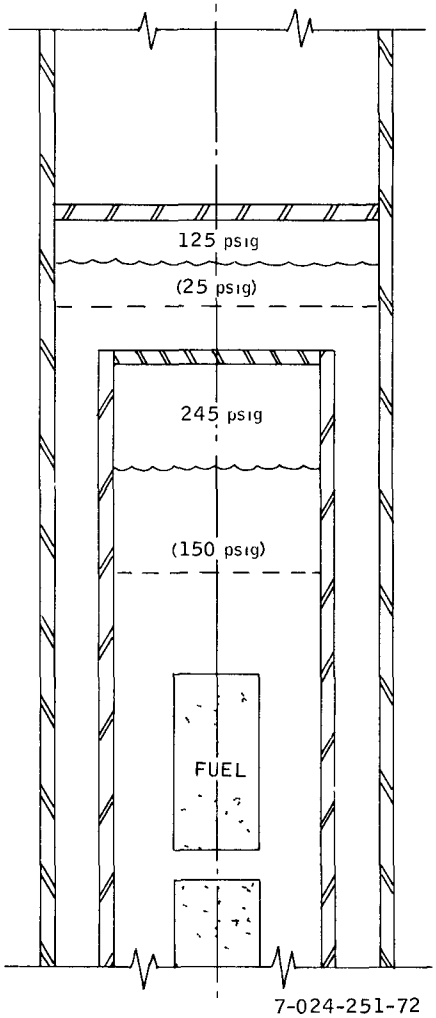

Figure 7. NaK Levels in Capsule

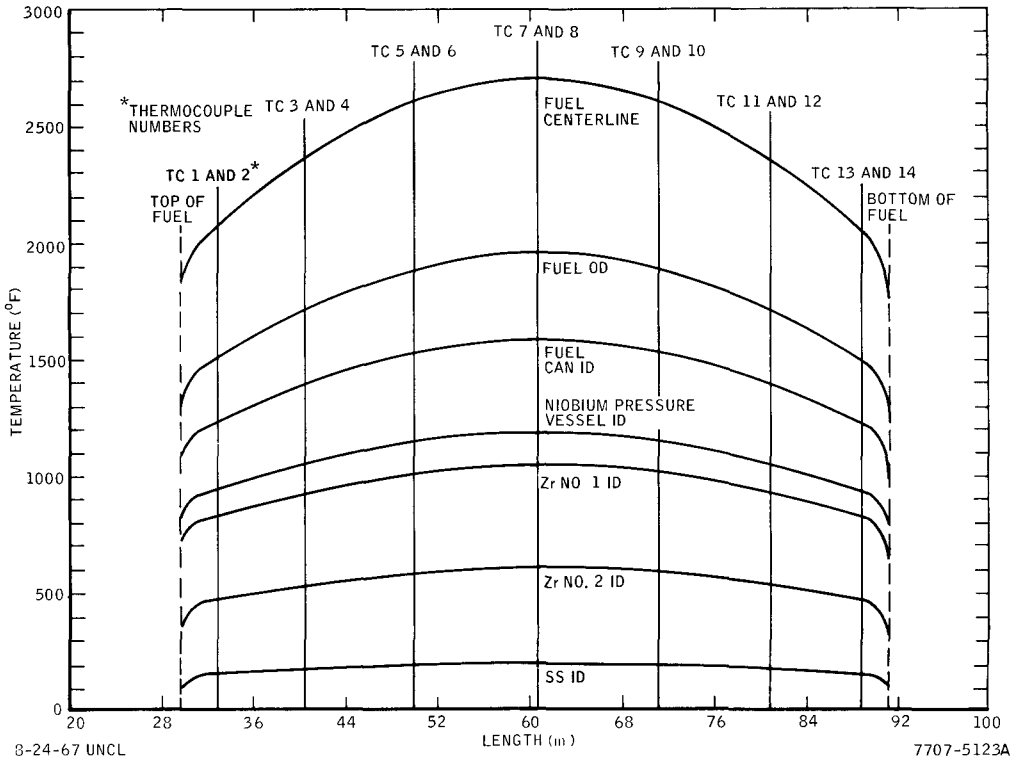

Figure 8. Axial Temperature Profiles

3. Startup and Operation

The experiment was inserted in the reactor during the normal cycle shutdown that began January 22 and was first brought up to power on January 27. The startup produced excellent results, confirming all the major design features of the capsule.

The instrumentation of the capsule permitted three independent indications of the power produced by the fuel string. The first is the set of in-capsule temperature measurements. These are the most important because they are used to extrapolate to the fuel centerline temperatures. The arrangement of these thermocouples is indicated in Figure 9, and the readings obtained during the first operation at power in the reactor are indicated in Figure 10. It may be seen from Figure 10 that the actual temperatures were close to design but with a slight dip near the center which is so far unexplained. These temperatures varied somewhat during a reactor cycle and from cycle to cycle, and the power to the experiment was controlled to some extent by adjustment of neighboring fuel rods in an effort to maintain the temperatures desired.

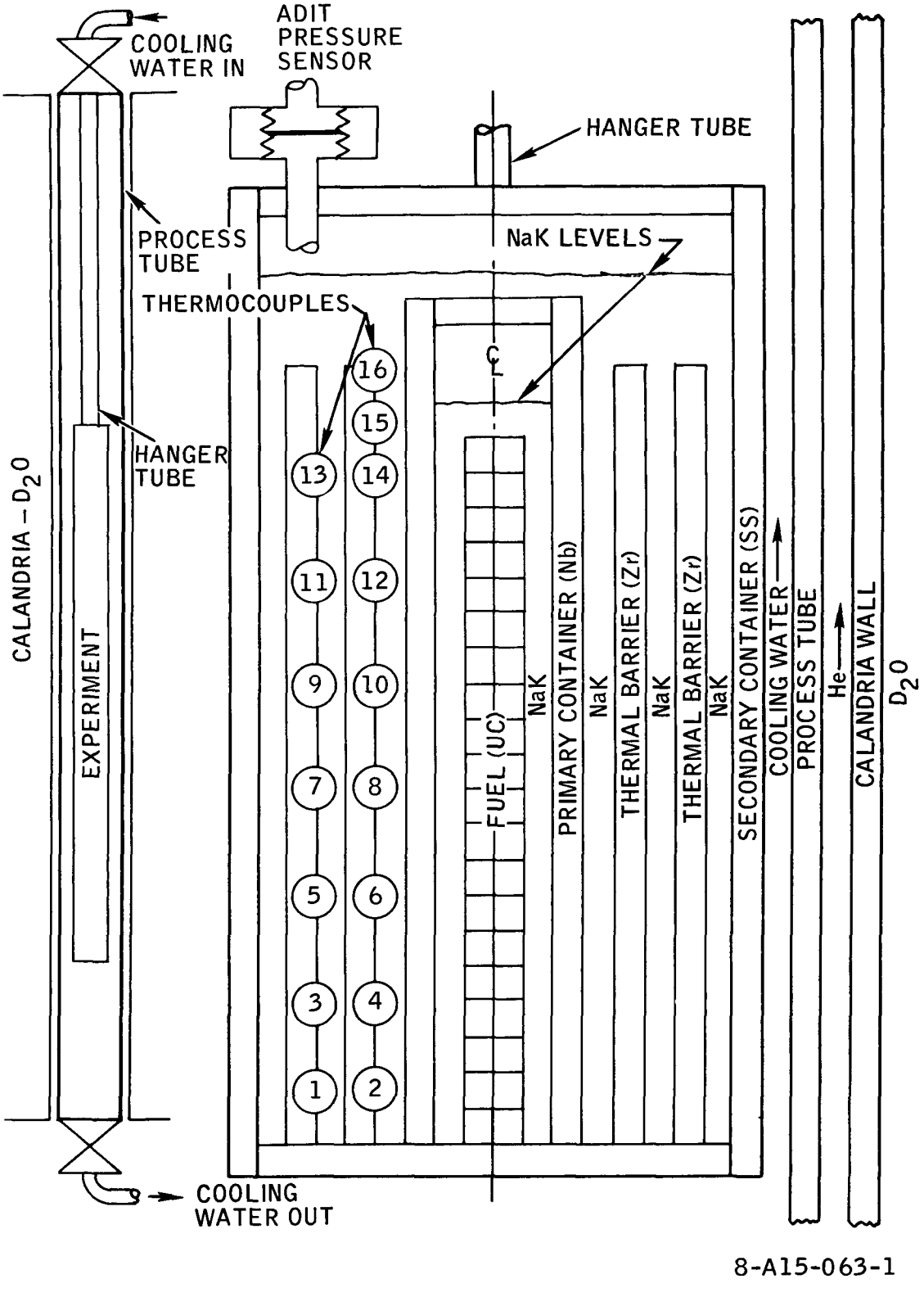

Figure 9. Thermocouple Locations

Figure 10.
Thermocouple Temperature Profile

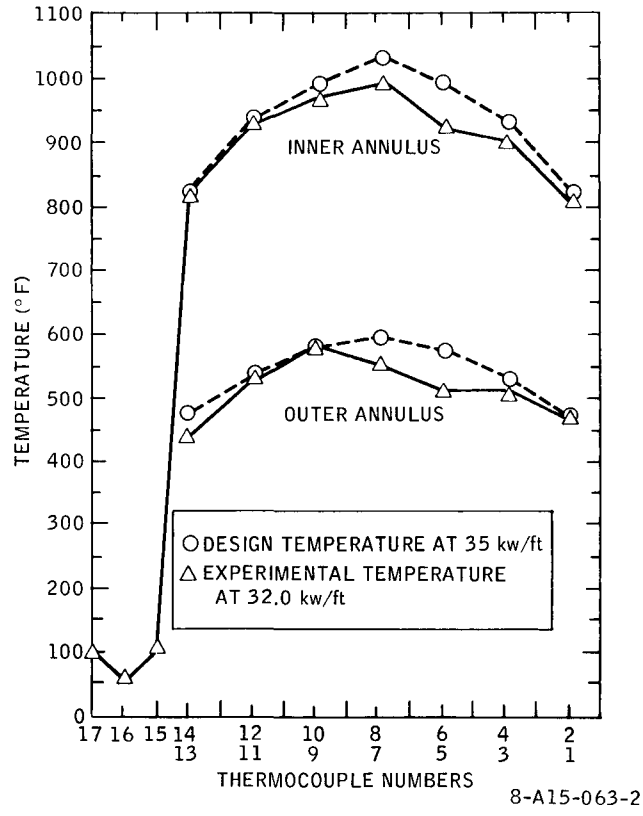

The second indication of power to the experiment is the pressure read on the adit pressure sensor or transducer which measures the pressure in the gas space above the NaK in the secondary containment vessel. The position of this sensor is indicated in Figure 9 and readings taken while coming up to power are shown in Figure 11. The agreement here is an indication that the average temperature and power level were as calculated. The real purpose of the pressure sensor was to serve as an indication of a leak or failure of the primary container which was at a higher pressure; a failure would cause an increase in reading.

Still a third indication of average power output of the 101 fuel string is the rise in water temperature in the channel, shown in Figure 12 as a function of reactor power. Again, there was excellent agreement with design.

Performance of the capsule subsequent to startup continued to be good, except for two over-temperature incidents. A maximum temperature was set to avoid the danger of NaK boiling with loss of thermal bond and extreme overheating of the fuel. The first occurrence was during startup and was due to the

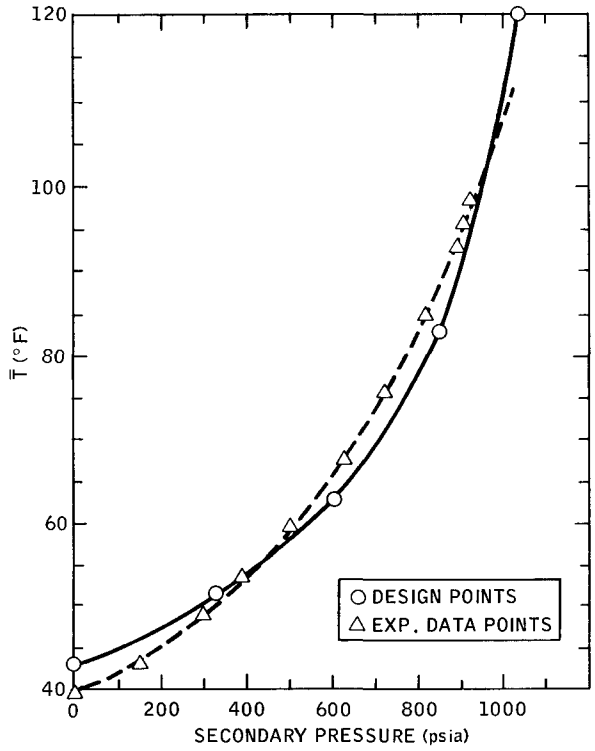

8-A5-063-3

Figure 11.

Pressure in Secondary Containment Vessel vs Average Temperature During Initial Rise to Full Power

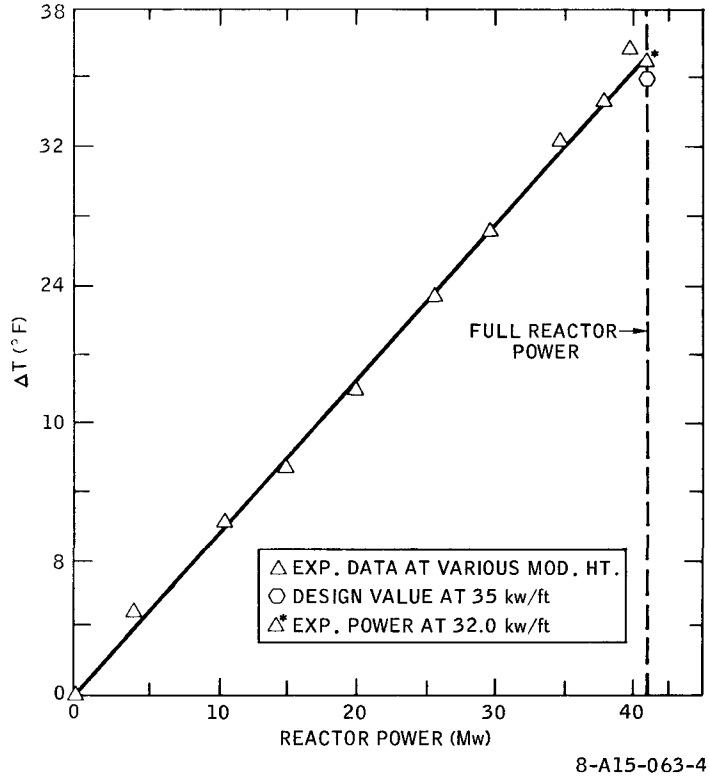

8-A15-063-4

Figure 12.

Temperature Difference in Water Flow Channel During Rise to Power

Figure 13. Summary of Data on the Irradiation of the EXP-NRX-9-101

failure of an alarm on the hottest thermocouple. The second occurrence was also during startup and although the alarm functioned, the temperature was already past the danger point by the time the operator read it and lowered power. Temporary over-heating was then expected during startups due to low moderator level and skewed power distribution, and special precautions were taken during subsequent startups. Indications are that no damage occurred during the two excursions, because temperature distribution as a function of reactor power remained normal.

The power to the experiment has averaged about 33 kw/ft, or somewhat below the design figure. The reason for this is simply the inability to pick a location in the reactor and adjust fuel near the experiment channel with any better precision as to flux. A summary chart is shown as Figure 13, covering maximum linear power and the corresponding maximum fuel centerline temperatures (maximum at the axial center of the fuel string), reactor startups, and accumulated maximum burnup.

The original target burnup was set at 15,000 Mwd/MTU, but this was for fuel centerline temperatures of 2700°F, corresponding to 35 kw/ft. To provide partial compensation for the lower temperatures, it was decided to extend the irradiation beyond the target burnup another half reactor cycle or about three weeks, which will provide about 20,000 Mwd/MTU total burnup. The chart shows an estimated burnup at the end of May of 16,000 Mwd/MTU. As of this writing it is planned to remove the experiment from the reactor on or about June 26 which is expected to be a midcycle shutdown of the reactor.

III. EVALUATION OF EFFORT DURING FISCAL YEAR 1968

The 101 experiment construction and irradiation was completed. In spite of problems and delays, the experiment functioned during irradiation as designed, and it appears now that the objectives of the experiment are likely to have been achieved. The experiment will be regarded as a success if the postirradiation examination provides us with consistent data on the swelling of UC-W alloys compared with UC control samples, whether or not the idea of using fine particles to control swelling proves to be a good one.

PAGE 274 is blank

Program: FBR Fuels and Cladding
AEC Task: 11-C, Mixed Carbide Fuels (Casting Studies)
Project Manager: J. L. Ballif
Reporting Period: Fiscal Year 1968
General Order: 7707 Subaccount: 28230 AEC Category: 04-40-02-01

Principal Investigator: J. W. Carroll

I. PROJECT OBJECTIVES

The objectives of this task are to (1) establish optimum fabrication parameters, by calculation, for the melting and casting of mixed carbides, (2) utilize the calculated parameters in practice by producing laboratory quantities of mixed carbide, and (3) design, procure and pilot-run a furnace for the production of melted and cast mixed carbide fuel.

II. TECHNICAL PROGRESS DURING FISCAL YEAR 1968

A study was completed on the theoretical vapor pressures and loss rates of Pu from UC - 20 wt% PuC fuel during melting and casting. It was shown that the rate of evaporation would be reduced 3000 times by melting in one atmosphere of argon as opposed to melting in a vacuum. Table 1 shows the calculated evaporation rates vs temperature for vacuum melting, and for melting in one atmosphere of argon, krypton, and xenon.

TABLE 1
MAXIMUM RATE OF EVAPORATION OF Pu

Temperature (°K)	Evaporation Rate (μgm/cm^2-sec)			
	Vacuum	Argon	Krypton	Xenon
2000	46.1	0.011	0.008	0.006
2250	509	0.132	0.094	0.071
2500	3,452	0.996	0.712	0.537
2750	16,420	5.23	3.74	2.82
3000	60,260	20.9	14.9	11.3

The results given should be considered as upper limits, since each of the following assumptions involved in the calculations leads to high values for the vapor pressure and diffusion coefficients: (1) ideal behavior of all species in the condensed and gaseous phases, (2) a rigid sphere model for the derivation of the expression for diffusion coefficients, (3) zero concentration of Pu vapor at 1 cm from the surface of the melt, (4) the collision diameter of gaseous Pu atoms is equal to the molar volume of the solid divided by Avogadro's number, and (5) the vapor pressure of Pu over the melt can be obtained by extrapolation from 1900 to 3000°K of the expression obtained from observed pressures over the solid.

A geometric analysis was performed to optimize the size of the molten pool within a skull melting crucible. The results of the analysis are given in Table 2.

TABLE 2

MOLTEN POOL SIZE OPTIMIZATION

Shape	Open Top-Area/Volume	Volume/Cooling-Wall Area
Sphere	-	0.29
Hemisphere	1.91	0.26
Cylinder, D = 2H	1.45	0.23
Cylinder, D = H	0.92	0.22
Cylinder, D = 1/2H	0.58	0.19

These data were incorporated into a computer case, utilizing an existing AI program, to provide data for the design of a melting crucible that controls the heat flow within the melt and maximizes the molten pool volume. The program can accept as variables (1) thermal conductivities of crucible material, (2) wall thickness, (3) crucible shape, and (4) radiation shields above the melt.

Seven process flow diagrams were developed for the fabrication of laboratory specimens of mixed carbide fuel slugs: (1) synthesis of (U-Pu)C from $UO_2 + PuO_2$, (2) preparation of U-Pu alloy, (3) synthesis of (U-Pu)C from U-Pu alloy, (4) preparation of (U-Pu)C slugs from synthesized (U-Pu)C, (5) (U-Pu)C powder preparation, sintered pellet fabrication, and vibratory compaction, (6) helium bonded fuel encapsulation, and (7) sodium bonded fuel encapsulation. Equipment for the

synthesis of mixed carbide from oxide, powder preparation and dry pressing, and sintering of the powder compacts is being provided and installed by North American Rockwell in the Nuclear Materials Development Facility early in next fiscal year. Four glove boxes have been made available for the equipment. Later in the fiscal year, equipment for the arc melting and casting of mixed carbide will be installed.

III. EVALUATION OF EFFORT DURING FISCAL YEAR 1968

Based on theoretical studies, it appears feasible to control the volatilization loss of plutonium from molten mixed carbide by the introduction of an inert atmosphere in the melting furnace. Lower losses should result from the judicious design of the melting crucible to lower the exposed surface area. At the same time, optimization of the heat flow within the crucible will increase the amount of molten charge available for casting into slugs.

PAGE 278 is blank

Program: General Chemistry and Chemical Engineering
AEC Task: 12, Sodium Chemistry
Project Manager: J. L. Ballif
Reporting Period: Fiscal Year 1968
General Order: 7708 Subaccount: 36110 AEC Category: 04-40-04-03.1

Principal Investigators: R. L. McKisson, R. L. Eichelberger,
D. C. Gehri, and J. Guon

I. PROJECT OBJECTIVES

The objectives of this project are to advance the understanding of the chemistry of liquid sodium as a solvent for metals and nonmetals through study of: (1) the solubility of selected metals and nonmetals in liquid sodium, as a function of temperature, by using the highest purity materials available to minimize the perturbations caused by unwanted side reactions, (2) the nature of solute entities and their interactions in liquid sodium, from which thermodynamic properties of the solutions may be deduced, and (3) the analytical chemistry of solutes in liquid sodium at very low concentrations, in order that the data developed under (1) and (2) above may have the greatest possible reliability.

II. TECHNICAL PROGRESS DURING FISCAL YEAR 1968

Progress is reported below in the various areas of activity being pursued on this project. These include the purification of sodium, to provide: the best material possible, as stated in the "Objectives," solubility experiments, and/or evaluations for several metal solutes and for carbon and oxygen; the description of a facility for studying solute interactions in sodium; and research on the analytical chemistry of sodium.

A. SODIUM PURIFICATION

A topical report titled "The Construction and Operation of a Sodium Purification Apparatus," NAA-SR-12444, by R. L. McKisson, R. L. Eichelberger, and J. B. Ott was released. The report describes the purification by distillation of three batches of sodium. The impurity levels were satisfactorily low in all three batches with the exception of the carbon level, which was 14, 27, and 8 ppm respectively. In an attempt to lower the carbon level, a fourth batch was distilled. Stock sodium indicating ~8 ppm carbon was used as a starting material

(instead of the sodium containing 35 ppm C used for the first three batches). Three charges were run through the purification apparatus. The first charge was zirconium gettered at 650°C for 42 hours and then distilled but not collected. The second charge was gettered at 650°C for 18 hours, then distilled but not collected. The third batch was gettered at 660°C for 90 hours, then distilled and collected in the extruder. The two "washing" distillations should have effectively removed the old "high carbon" sodium and washed the surfaces. Triplicate analyses for carbon in the final product showed 7, 9, and 11 ppm, indicating no improvement over the starting material value of 8 ppm. Triplicate oxygen analyses of 1, 2, and 2 ppm were obtained as compared to 8 ppm for the starting material.

It is interesting to note that the 8 to 10 ppm carbon values obtained on sodium prepared in this apparatus by gettering and distillation are not significantly better than values obtained by gettering alone. Two nickel capsules containing zirconium foil were loaded with sodium and heated for 24 hr at 754 and 995°C respectively. Carbon analyses gave 11 and 10 ppm carbon values in the gettered sodium. The "Systems Quality" sodium used as the starting material for the purification is treated by gettering only to remove carbon, and consistently shows 8 to 15 ppm carbon.

A fifth extruder was filled with sodium from the purification system, after three additional still loadings were used to wash the interior surfaces of the system. The analysis for carbon on duplicate samples was reported as 5 and 7 ppm, for an average of 6 ppm. Six samples which varied in weight from 1 to 3 gm were analyzed for oxygen. The average oxygen content was 3.9 ppm, with a range 2.6 to 4.8 ppm. The oxygen blank for the determinations was rather high, 7.8 micrograms, resulting in a larger spread of values than is customary, but the analyses do give assurance that the sodium is of high purity.

It appears that either the distillation process does not effectively remove carbon from sodium at the 10 ppm level, or an "analysis blank" is present in the dry combustion analysis technique used and the carbon levels are actually considerably lower. Discussion of the analysis for carbon is included below in the "Sodium-Carbon Solubility Studies" section.

B. EXPERIMENTAL STUDIES

1. High Vacuum System

Several alterations in the high vacuum system hardware described in NAA-SR-12492 have been required. The bellows-sealed manipulators have been re-welded, since the extreme service to which they were put resulted in leaks. No failures have occurred with the rewelded units. The motor and turbine drive unit for the turbomolecular pump also gave considerable trouble, and has now been replaced with the manufacturer's latest design which uses a varable speed motor (eliminating an unreliable graphite clutch) and a drive system which replaces a belt-and-pulley arrangement with gears. The pump has worked satisfactorily since the rework was completed. A third item that was found to be subject to failure was the extruder ram extension. A design change has been made that will prevent similar failures from occurring.

2. Sodium Chemistry Loop (SCL)

The interaction between oxide on stainless steel and sodium has made the study of the properties of oxygen in sodium difficult in existing facilities. In order to aid in the development of thermodynamic information on solute interactions, a sodium chemistry loop is being designed and fabricated. Nickel-270 was chosen as the loop material in order to minimize interactions of the loop with the sodium phase or the solutes. Nickel does not form a stable carbide, and has not been reported to form a ternary oxide with sodium. In addition, the nickel product chosen is unusually pure for a commercial material, as seen in Table 1. Figure 1 is a schematic representation of the SCL and Figure 2 is the flow diagram. In at least the initial phases of the SCL experimental program, oxygen-metal-sodium interactions will be studied utilizing a United Nuclear Corporation oxygen meter to follow changes of oxygen activity in the sodium. The program as presently planned will be divided into:

Phase 1, Check-out and test of loop and facility, and characterization of the oxygen meter response,

Phase 2, Verification that the oxide-surface interaction with Nickel 270 is suitably low,

Phase 3, Study of the Ni-O-Na ternary system, and

Phase 4, Study of the Fe-O-Na ternary system.

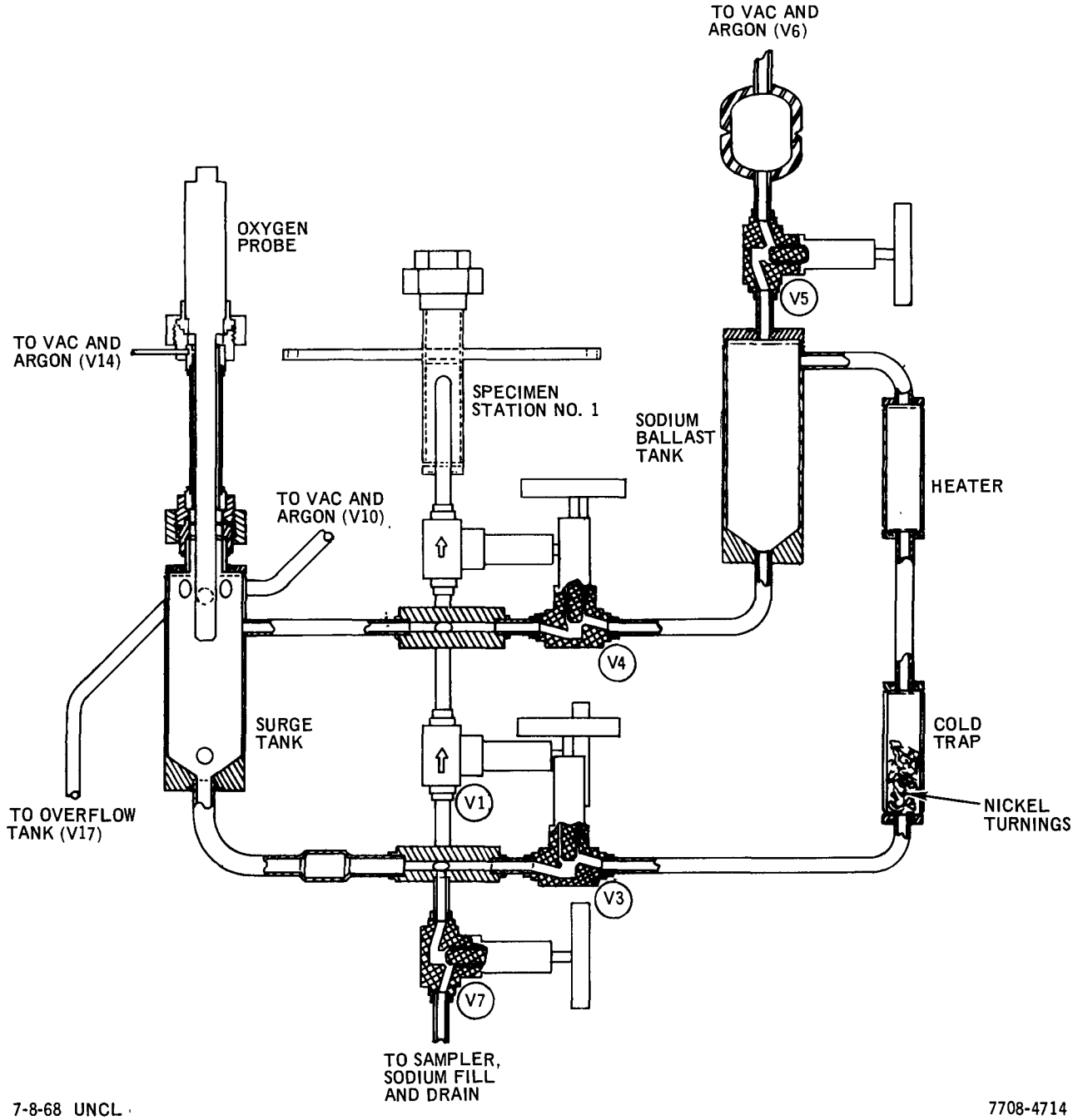

Figure 1. Sodium Chemistry Loop, Schematic

TABLE I

COMPOSITION OF NICKEL 270

Element	Quantity (w/o)	
	Nominal	Limiting
Nickel	99.98	99.97
Carbon	0.01	0.02
Iron	0.001	0.005
Copper, Chromium, Sulfur, Silicon, Magnesium, Manganese, Titanium, Cobalt	Each <0.001	Each 0.001

Additional studies on such ternary systems as Cr-O-Na, Zr-O-Na, and C-O-Na are anticipated. If the surface interactions are sufficiently small, other experiments such as an extension of the oxygen solubility curve may be performed. In performing an experiment in a ternary system, the oxygen concentration in the SCL may be adjusted by using the cold trap; then the cold trap can be isolated from the loop, and a specimen station containing a metal sample valved into the system. By following the change in oxygen activity as measured on the oxygen meter (by using a knowledge of the volume of sodium in the loop, the surface area of the metal sample, and various time dependent parameters to assure equilibrium has been established), calculations may be made relating to the chemical equilibria. The second specimen station can be used to add greater versatility to the SCL.

The status of the loop as of the writing of this report is as follows.

1) All of the nickel required has been procured and analyzed to assure conformity to the purity specification.

2) Machining of all nickel parts, excepting the two manifolds, has been completed. Parts have been helium leak checked.

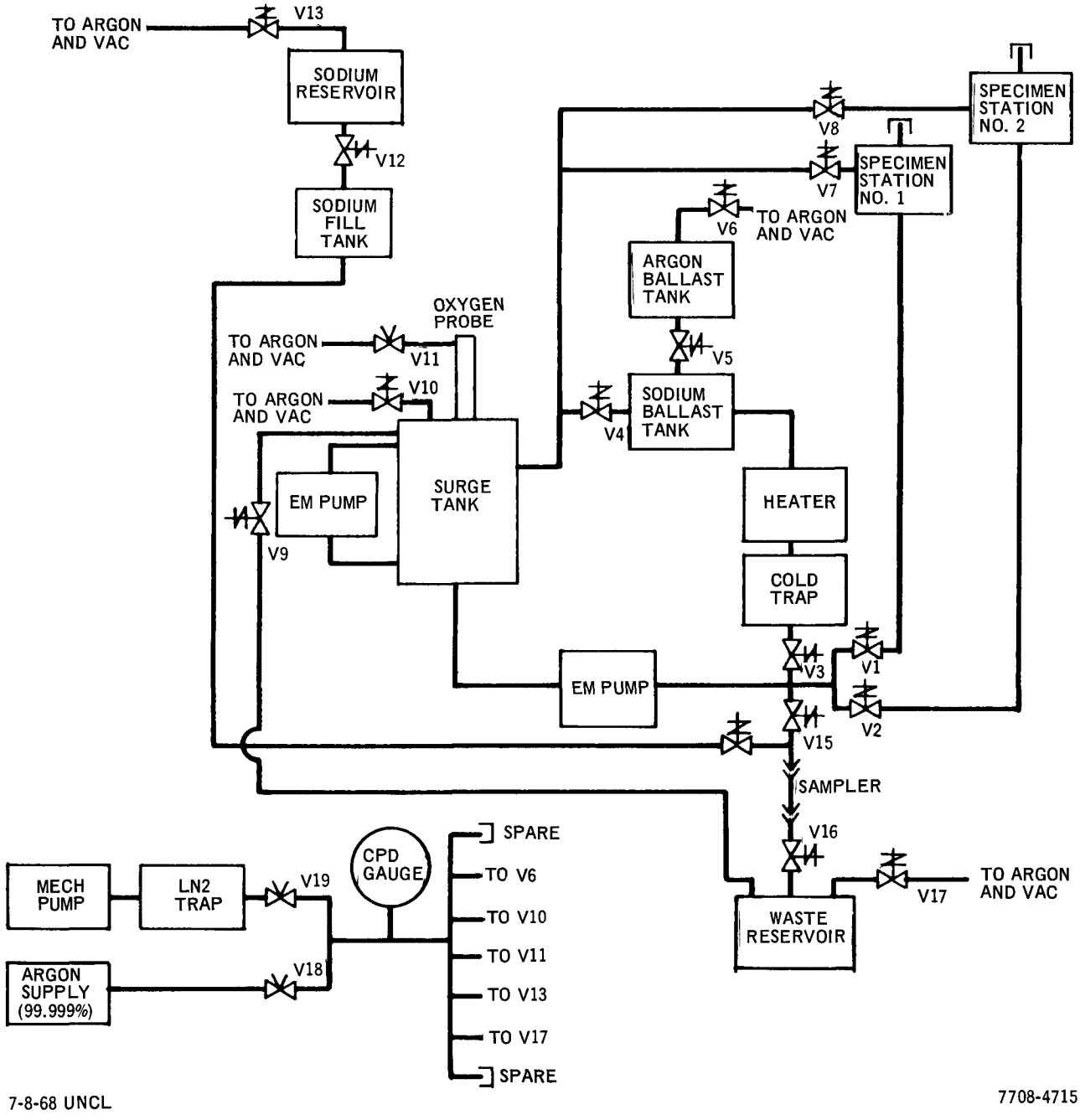

Figure 2. Sodium Chemistry Loop, P & I Diagram

3) The transfer lock has been completed for loading and unloading the specimen stations without contaminating the loop with air.

4) Valves with Nickel 270 bodies and plugs have been procured and helium leak tested (one valve had a leak and is being returned to the vendor for rework; no schedule delay is anticipated).

5) Assembly and test of the inert atmosphere box to be used for loop assembly has started.

6) The pump configuration was tested to determine if problems might exist in the pump because of the ferromagnetic nature of nickel; none was encountered.

7) The control console (to be shared with the Fission Product Behavior Loop, Task 6C) is essentially complete.

8) Preparation of the laboratory to house the SCL has started.

The chemistry of liquid sodium in its interaction with commercially pure nickel of the type used to fabricate the Sodium Chemistry Loop (SCL) is being critically considered from an examination of the literature of the thermodynamic, structural, and transport properties of nickel, nickel oxide, sodium, sodium oxide, and other trace impurities such as carbon and iron, which may be present in sodium or nickel.

A literature search of the pertinent topics has been completed. The literature information is being transposed to "keysort" punched cards and should be a useful and conveniently available source of information relating to the chemistry of the SCL. Thermodynamics of Ni, NiO, and Na_2O in the solvent sodium at high temperatures are being examined in the light of the information gained from this literature search.

C. SOLUBILITY OF METALS IN SODIUM

Work is reported below on solubility experiments with high purity metallic solutes in the high purity sodium described above. The general procedures used were described in the previous annual report NAA-SR-12492, and the specific procedure used for copper is detailed in the report on copper solubility mentioned below.

TABLE 2

RESULTS OF COPPER SOLUBILITY EXPERIMENTS

This Work, Atomics International

Run No.	Temp (°C)	Cu in Na (ppm)	Run No.	Temp (°C)	Cu in Na (ppm)
267	350	3.4	63	500	22.8
264	350	4.2	64	500	29.4
69	350	2.7	74	500	24.8
70	351	4.5	75	502	26.5
270	352	4.3	256	643	244
78	368	5.5	83	648	208
79	371	9.3	82	650	149
81	371	7.5	255	660	330
80	373	7.6	254	672	301
72	395	16.3	253	726	617
71	399	10.8			

Los Alamos Scientific Laboratory[2]

Capsule No.	Temp (°C)	Cu in Na (ppm)
1	500	25
2	500	17-23
3	600	62-75
4	600	70-83
5	600	112-141
6	700	344-443

Brookhaven National Laboratory[1]

Sample No.	Temp (°C)	Cu in Na (ppm)
22D	245	<0.2 (ND)
22E	322	2.2
22F	322	0.79
22G	370	2.1
22H	370	3.0
22I	403	5.0
22J	403	6.5
22K	425	4.2
22L	425	6.5
22M	473	9.4
22N	473	14
22A	547	60

1. Copper

Work on the solubility of copper in sodium was completed. A topical report, "Solubility of Copper in Sodium," AI-AEC-12671, by R. L. Eichelberger and R. L. McKisson, was issued. The data used to establish the copper solubility curve are shown in Table 2, which includes 12 points reported by Brookhaven National Laboratory,[1] 6 points from Los Alamos Scientific Laboratory,[2] and 21 points from the present work. The curve defined by these 39 data points is shown in Figure 3, and is expressed by the equation

$$\log_{10} S \text{ (ppm Cu in Na)} = 5.957 - \frac{3430}{T(°K)} \quad .$$

2. Iron

The iron solute was triple-pass electron-beam zone-refined material which had been machined into a suitable crucible. The results of thirteen experiments using either triple pass zone refined titanium or a commercial Cb-1%Zr alloy as sample collector are shown in Table 3, and plotted in Figure 4. The line through the points has excluded the four points which show iron concentrations in the 25 to 100 ppm range somewhat arbitrarily, on the reasoning that contamination may have occurred during handling and analysis. Results published by other laboratories are also shown in Figure 4. The main point of interest in the work reported is the great difference between the apparent solubility as measured by wet chemical techniques (MSA,[3] KAPL,[4] BNL,[5] AI) and by radiochemical techniques (NRL[6]). The low values for apparent solubility are also corroborated by current radiochemical experiments at BNL.[7] Because of this situation with respect to iron solubility, it was judged not fruitful to pursue experiments which used wet chemical analysis, at this time. Instead, the same crucibles that were used for the experiments listed in Table 3 have been irradiated, and will be used for solubility runs in which the solute concentration is measured by a direct counting technique on the sodium contained in the sample collector.

3. Nickel

The nickel solute was triple-pass electron-beam zone-refined material, fabricated into suitable crucibles. The results of twelve experiments are shown

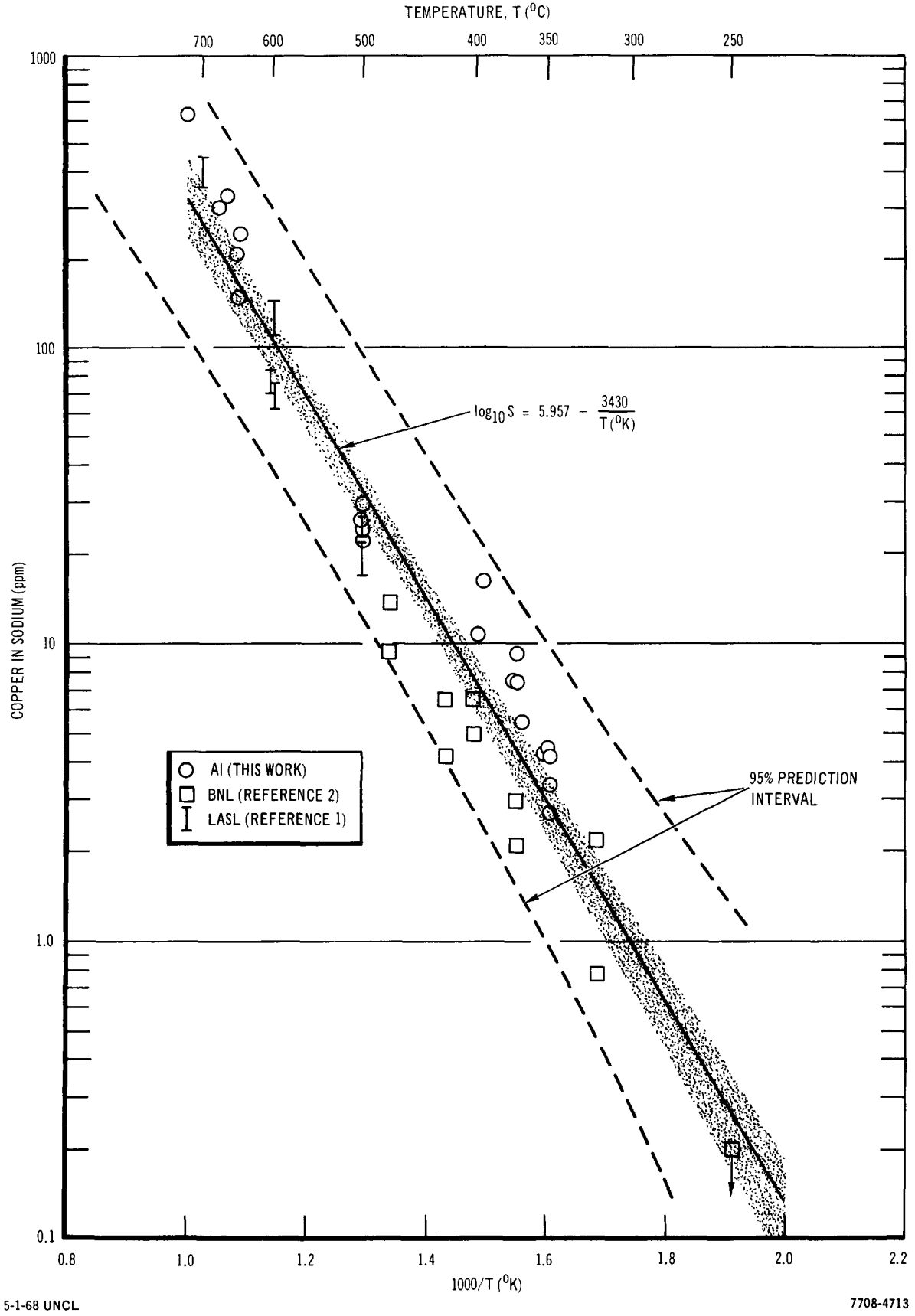

Figure 3. Solubility of Copper in Sodium

TABLE 3

RESULTS OF IRON SOLUBILITY EXPERIMENTS

Run No.	Collector Material	Temp (°C)	Fe in Na (ppm)
84	Cb-1Zr	595	12
251	Cb-1Zr	698	39
252	Cb-1Zr	991	16
277	Ti	709	12.2
278	Ti	800	99.8
279	Ti	900	12.9
280	Ti	600	7.0
281	Ti	800	8.4
294	Ti	1000	*
295	Ti	500	26.8
296	Ti	650	25.0
297	Ti	700	9.9
298	Ti	800	19.6

*Collector ballooned

TABLE 4

RESULTS OF NICKEL SOLUBILITY EXPERIMENTS

Run No.	Collector Material	Temp (°C)	Ni in Na (ppm)
59	Fe	910	<5
60	Fe	914	<5
258	W	800	<2
273	Ti	1000	21
274	Ti	700	65
275	Ti	800	114
276	Ti	900	459
299	Ti	700	3.0
300	Ti	800	4.0
501	Ti	900	4.9
519	Ti	600	*
520	Ti	1000	†

*Awaiting analysis
†Collector ballooned

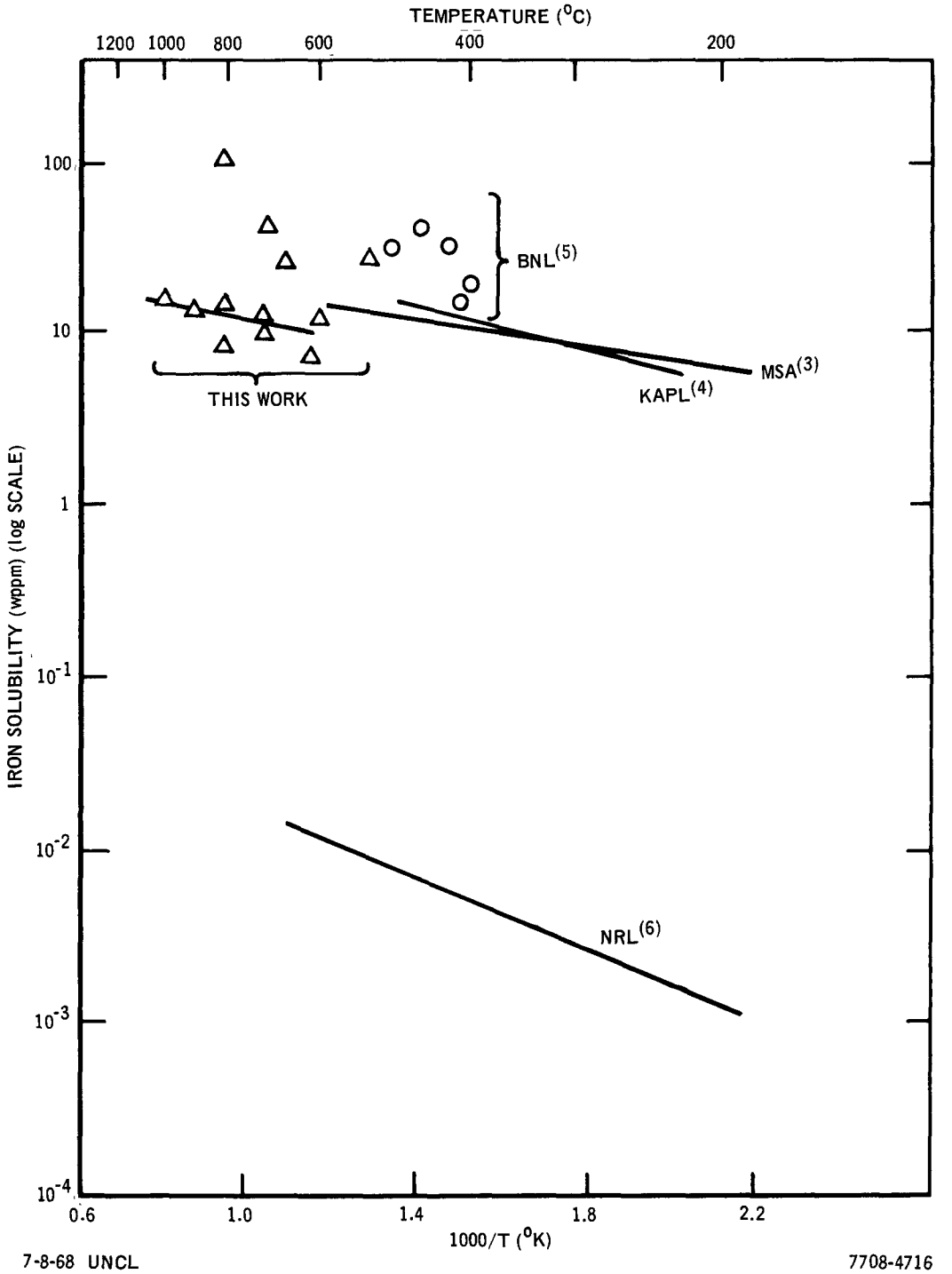

Figure 4. Solubility of Iron in Sodium

TABLE 5

RESULTS OF MOLYBDENUM SOLUBILITY EXPERIMENTS

Run No.	Temp (°C)	Mo in Na (ppm)
282	1000	<1*
283	1000	<1*
284	900	<1*
285	800	<2*
286	700	<2*
505	800	1.4
506	850	0.5
507	900	0.9
508	950	1.2
511	1005	1.3

*Mo was apparently detected in all samples but was not quantitatively determinable. The different apparent sensitivities result from different sample sizes.

in Table 4. The four numbers between 21 and 459 ppm were obtained before adequate measures were employed to remove nickel which may vaporize and redeposit during the crucible-to-collector welding process, and are probably in error. From the other six results shown, the generalization may be drawn that the solubility of nickel in sodium is measurable, but less than 5 ppm in the temperature region studied.

4. Molybdenum

Ten experiments with electron-beam zone-refined molybdenum crucibles and Cb-1%Zr collectors gave solubility results less than 1.5 ppm, in the temperature range 700 to 1005°C, as shown in Table 5. More precise work is dependent on overcoming a limitation in the sensitivity of the analytical method. No more experiments with molybdenum solute are planned.

5. Chromium

Chromium solubility experiments used rod solute samples made from halide purified chromium, following the same procedure described for copper. Four experiments in the temperature range 700 to 1000°C gave results of 2 to 3 ppm, by wet chemical analysis, as shown in Table 6. The same solute rods were then irradiated, and again used in solubility experiments. No results are available yet for these latter solubility runs.

TABLE 6

RESULTS OF CHROMIUM SOLUBILITY EXPERIMENTS

Run No.	Temp (°C)	Cr in Na (ppm)
288	700	3.3
289	800	3.2
290	900	2.1
291	1000	1.6

6. Niobium

Three experiments using electron-beam refined niobium solute crucibles and equally pure titanium collectors were run, but not yet been analyzed. One of the three, heated at 1000°C, ballooned in the collector region, as did those in the iron and nickel experiments at 1000°C with titanium collectors (noted in Tables 3 and 4). It is apparent that the vapor pressure of sodium at 1000°C (about 3 atm) is sufficiently high to deform the pure titanium, which is relatively weak at that temperature.

7. Bismuth

The solubility of bismuth in sodium has recently been determined at Birmingham University, England.[8] To corroborate this work, several points below the melting point of Na_3Bi will be measured. To date, the "bomb" to be used to prepare the Na_3Bi solute has been made.

D. THE SOLUBILITY OF OXYGEN IN SODIUM

Because of the availability of new data on the solubility of oxygen in sodium, all the information on this subject was reviewed for discussion in a topical report. This report, "The Solubility of Oxygen in Liquid Sodium - A Recommended Expression," AI-AEC-12685, by R. L. Eichelberger, is being edited for issue in early fiscal year 1969. The sources of data used are listed in Table 7.

TABLE 7
SOURCES OF DATA FOR OXYGEN SOLUBILITY CURVE

Reference	Total Data Points	Temp Range of Points (°C)	Data Points Used	Reason for Exclusion of Some Points
Bergstresser et al.[11]	22	155-340	22	
Rutkauskas and Meadows[12]	52	125-300	52	
Walters[13]	25	152-549	17	Analytical blank <250°C
Noden and Bagley[14]	46	127-540	7	Glass solubility apparatus
Bogard and Williams[15]	10	110-555	4	Glass solubility apparatus
Dorner[16]	30	130-480	5	Glass samplers
Jahns and Weidmann[17]	27	156-406	None	All glass apparatus
Salmon and Cashman[18]	*	115-495	None	Only average data reported
Thorley[19]	*	114-292	None	Only average data reported

*Unknown

The total number of data points is 212. The number of points not excluded by the considerations below is 107. These 107 points are plotted in Figure 5, with the least squares line which they define. The equation for the line is the recommended solubility expression

$$\log_{10} S\,(\text{wppm O}) = 6.239 - \frac{2447}{T\,(°K)} \quad .$$

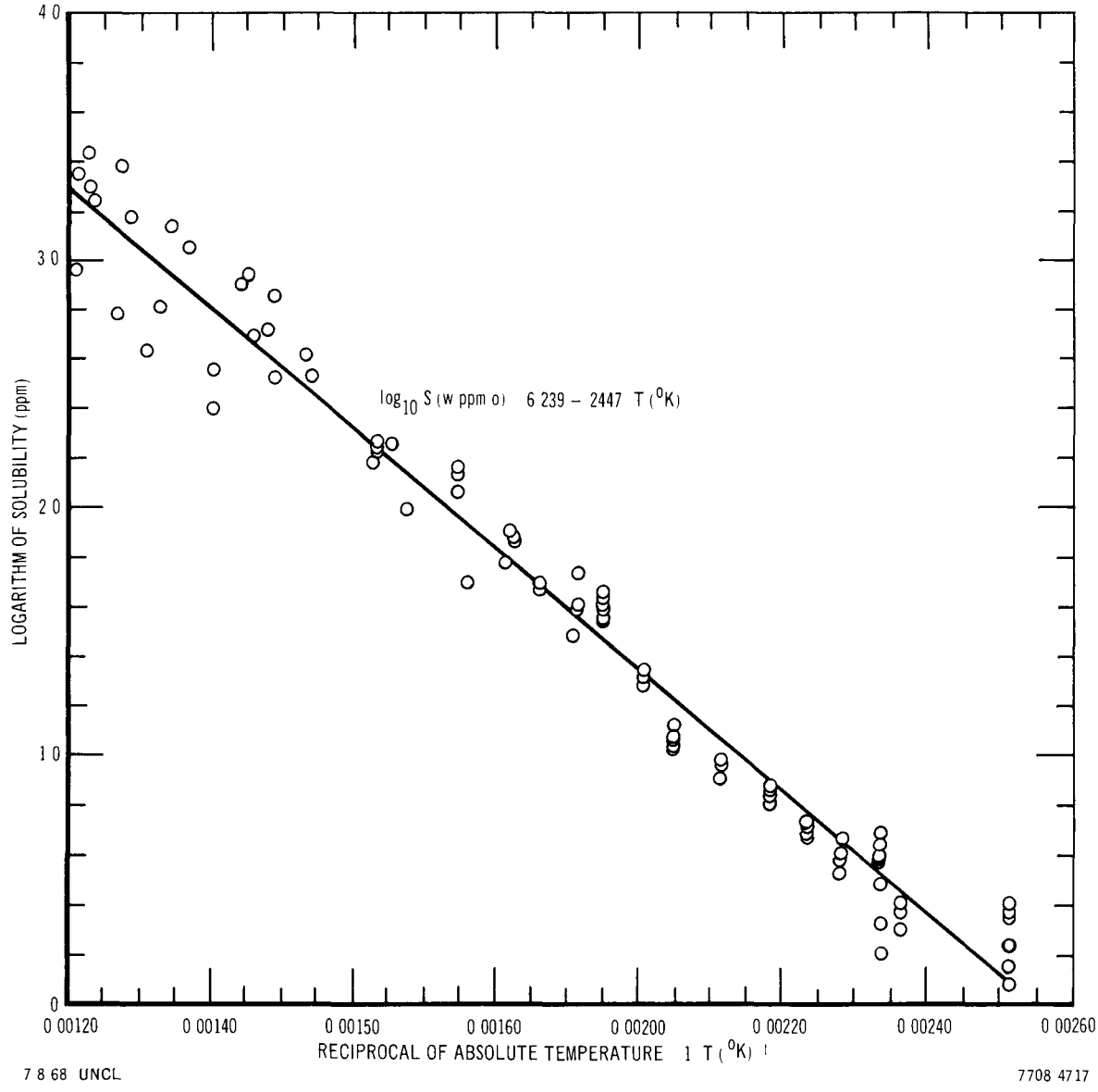

Figure 5. Solubility of Oxygen in Sodium, Recommended Curve

The choice of data points to be included in calculating the recommended curve was made on the basis of the following consideration.

1) No data are included from experiments in which either the equilibration or sampling was carried out in glass. The reaction of sodium with SiO_2 is well known, and although it may not be rapid below, about 250°C, it may still interfere. The lower temperture points would be excluded by the second criterion anyway.

2) No data are included from experiments in which the mercury amalgamation analytical procedure was used for equilibration temperatures below 250°C, at which temperature the solubility is about 35 wppm. The reason for this exclusion is the presence of an analytical blank in the method, a fact which was not generally acknowledged until the recent work of Prach,[9] and Scarborough and DeVries.[10] In routine work, this blank amounts to 5 to 10 micrograms of oxygen equivalent, even when the glassware used is vacuum dried at 150°C before use. Although such a blank may be relatively unimportant at high oxygen levels, it may not be neglected at lower concentrations.

3) No data have been included for which individual data points were not available.

The generalized expressions for oxygen solubility in sodium derived by Claxton[20,21] have beeen reviewed, but the present expression is preferred because of the application of the above criteria to the individual data points. In addition to Claxton's generalized expressions for oxygen solubility, Subbotin et al[22] have published a "generalization of the data of several papers and the results of our experiments," but have not discussed any of the data from which they derived their expression. Kassner and Smith[23] have used the data from Rutkauskas and Meadows[12] and the sampled-in-steel high temperature points from Noden and Bagley[14] to derive a solubility curve similar to the one presented in Figure 5, but with a slightly steeper slope.

E. SODIUM-CARBON SOLUBILITY STUDIES

Additional experiments in the series relating to the solubility of carbon in sodium were conducted during the year. Those which were considered reliable

are summarized in Table 8 and plotted in Figure 6. A least squares fit of these data yields the equation

$$\log_{10} S\,(\text{wppm}) = 1.72 - \frac{610}{T\,°K} \quad .$$

TABLE 8

SUMMARY OF CARBON SOLUBILITY RUNS

Run No.	Solute	Carbon Found (wppm)	Temp of Run (°C)	Duration of Run (hr)	Na From Dist No.
611	Graphite Single Crystal	15	800	24	3
612	Graphite Single Crystal	20.5	995	24	3
613	Graphite Single Crystal	15	897	24	3
614	Graphite Single Crystal	16	1097	24	3
615	Diamond	12	700	24	4
616	Diamond	19.5	999	6	4
617	Diamond	13.5	799	20	4
619	Diamond	16	1100	6	4
9-9	Diamond	22	1000	6	5

from which ΔH (soln) of 2800 cal/mole can be calculated. Both the constants in this equation and the calculated ΔH may be subject to minor changes as the result of experiments that are currently in progress. These experiments are being conducted in the temperature range 700 to 900°C in an attempt to supplement the data in this range, and therefore increase the reliability of the least squares calculation. The equipment and experimental procedures are discussed in NAA-SR-12492, the previous Annual Report; and in AI-AEC-MEMO-12686, "The Solubility of Elemental Carbon in Sodium," by D. C. Gehri and J. B. Ott. The results are subject to the limitations of the high-temperature dry-combustion analysis technique and the capsule sampling procedure, as is discussed in detail in the above-mentioned memo.

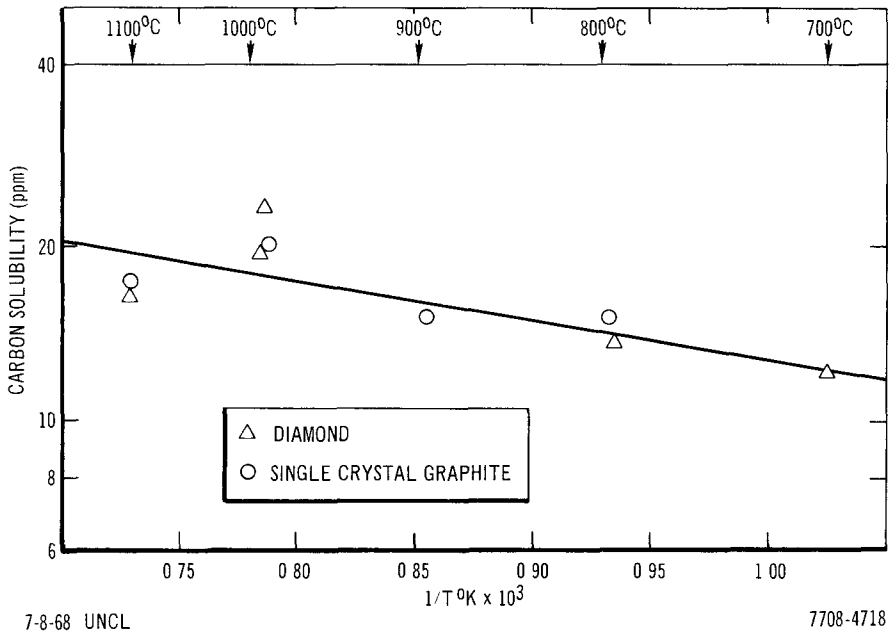

Figure 6. Solubility of Carbon in Sodium

Experience suggests that capsule interactions and "gettering" phenomena may be important in determining initial carbon impurity levels and the nature of the equilibrium in a capsule experiment. Thus, the carbon content of capsules in which a Zr "getter" is added to the sodium, with or without carbon solute, is reproducibly measured as about 10 wppm. Similarly, the carbon content of heated capsules in which nothing is added to the sodium has been measured to be 20 to 30 ppm. The much lower values obtained when the capsules are not heated indicate that carbon transfer from the 270 Ni capsule material may be temperature dependent. As an aid to understanding the nature of these interactions, a ^{14}C analytical capability is being developed and will be employed.

Luner et al[24] have employed ^{14}C techniques in their published results for the solubility of carbon in sodium. The very low solubilities observed are not in agreement with the results plotted in Figure 6, nor are the much higher values reported by Gratton.[25] A second objective in employing ^{14}C techniques in future work will therefore be an attempt to reconcile these differences. On the basis of Luner's work, it now seems reasonable to reject Gratton's data because of oxygen effects. Reasons for the apparent disagreement between the equation suggested above and the ^{14}C work are not, however, immediately obvious. In this connection, it should be noted that the magnitude and direction

of the mentioned disagreement are similar to those found when the results of tracer studies are compared to those of the normal "wet chemical" analyses in the determination of the solubilities of Fe and Ni in sodium.

Any comparison between ^{14}C studies and other carbon analysis technique must necessarily depend on the reliability of the analyses themselves. Work is therefore continuing on the development of the high temperature dry combustion technique as well as ^{14}C counting. A series of experiments has been planned which will serve to augment the previous development work on the combustion procedure. In addition, a modification of the capsule design is being tested in an attempt to standardize sampling procedures and to test the hypothesis that particulate carbon may constitute the predominant form of carbon in sodium. A more complete summary of the scope and direction of the continuing efforts at Atomics International to solve the problems associated with the interaction of carbon and sodium can be found in AI-AEC-MEMO-12686.

F. ANALYTICAL CHEMISTRY RESEARCH

The analytical chemistry effort has centered on the improvement of sensitivity and precision of wet chemical methods (spectrophotometry and atomic absorption spectrometry) for metallic solute species in sodium, and on the adaptation of the spark source mass spectrometer (SSMS) for the analysis of sodium, as discussed in the following sections.

1. Determination of Nickel

A statistical analysis of the data obtained from the preparation of calibration curves for the determination of nickel by the atomic absorption and spectrophotometric (dimethyl glyoxime) methods has been completed. Comparisons were made for standards containing only nickel and those containing the quantity of matrix (Na), collector (Ti), and carrier (La) elements expected in the samples to be analyzed.

The method of Scarborough,[26] et al., was used for atomic absorption. Over the concentration range investigated, the 95% confidence interval for a value estimated from a single observation is equivalent to approximately plus or minus one microgram. Pooled data were used to establish the regression line for the standard curve shown in Figure 7.

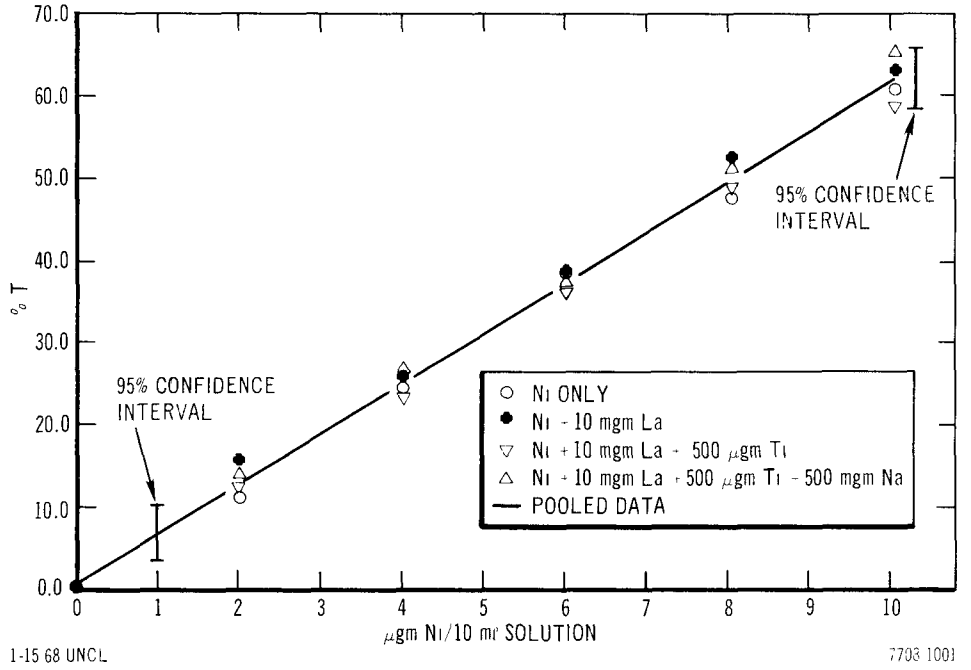

Figure 7. Atomic Absorption Analysis for Nickel

Spectrophotometric determination of nickel was verified by comparing the curves obtained with only nickel in solution and those of solutions containing matrix (Na) and collector (Ti) elements. The dimethyl glyoxime color was developed in the aqueous phase (25 ml total solution volume) and read in 5-cm cells at 520 nm. No statistically significant deviations were apparent; therefore, pooled data were used to generate the regression line shown in Figure 8. Over the concentration range investigated, the 95% confidence interval for a value estimated from a single observation is equivalent to plus-or-minus 1/2 μgm.

2. Determination of Niobium

The reliability of the measurement of traces of niobium in sodium was verified. By use of 4-(2-pyridylazo) resorcinol (PAR) as the chromogenic agent, a spectrophotometric method for determining 0 to 10 μg of Nb in the presence of 0.5 gm of Na and up to 1 mg of Ti has demonstrated a 2σ uncertainty of $\pm 0.65\,\mu$g.

The method involves treating the dissolved sample with tartaric acid, then adjusting to pH 6.0 with NH_4OH/HAc, EDTA is added to complex any foreign ions and boric acid is added to complex fluorides. After readjusting to pH 6.0,

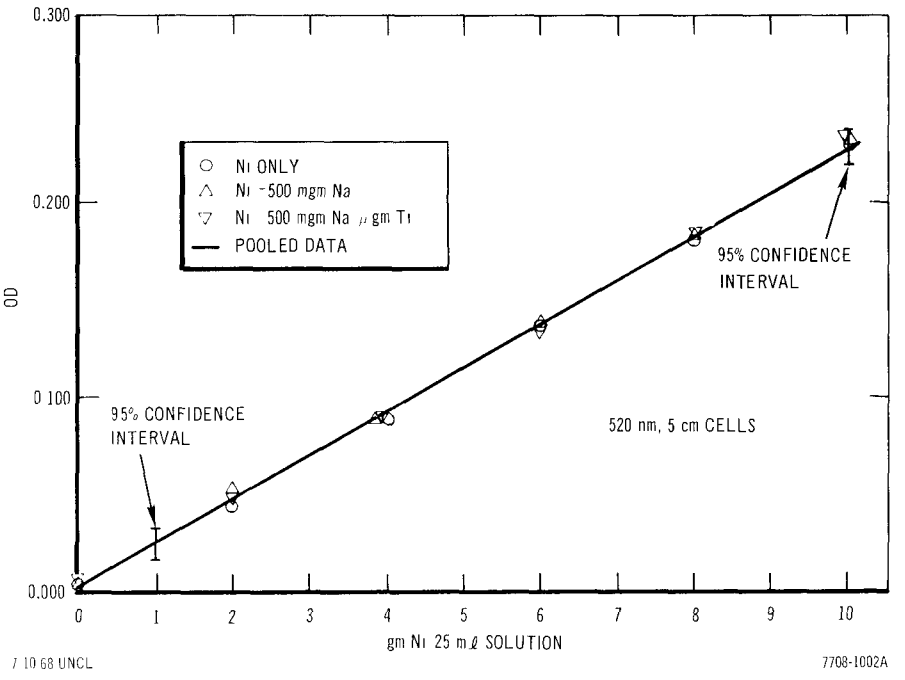

Figure 8. Spectrophotometric Analysis for Nickel

PAR and an NH_4Ac/HAc buffer are added and, after 1 hr, diluted to volume with water. Color is allowed to develop overnight and the solutions are read at 500 mμ in 5-cm cells.

Several series of up to seven calibrated sets were prepared by varying the quantities of potential interfering species. Each set was analyzed statistically; then, the 94 data points were pooled. No attempt was made to exclude data points which appeared to be discrepant. Thus, some unfavorable statistical weighting may have occurred. Of the seven calibration sets analyzed, only one failed to be enclosed by the 2σ envelope. The data from this set were not excluded from the pooled data, however, and the statistical values given above are for all 94 data points.

3. Determination of Bismuth

Ten sets of bismuth standards (10 to 100 ppm) containing 1% sodium, as sodium chloride; with and without impurities (Fe, Ni, Cr, Mn, and Co) were run on the atomic absorption spectrograph to determine their effect on the determination of bismuth. No interference was detected in the presence of 20 ppm of these impurities.

4. Sodium Analyses with Spark Source Mass Spectrometer (SSMS)

To transfer sodium into the mass spectrometer without oxidation, the loading manipulator, shown in Figure 9, was installed on the mass spectrometer source housing. Sodium is loaded under argon or in vacuum into vacuum-tight stainless steel vials. A vial is secured in the manipulator assembly, which is then evaucated along with the mass spectrometer source. The long rod, which is operated through bellows and O-rings, has removable end-tools which are used to open the vial, scoop up a small amount of sodium, and wipe it onto the ends of two suitably placed copper electrodes in the SSMS source. This procedure has proved very satisfactory in preventing contamination of the sodium, and the resulting photoplates show none of the polymers such as Na_2OH, Na_2OH_2, Na_3O, etc., which appear in analyses of sodium loaded in high purity argon.

A major concern in SSMS analysis of alkali metal samples has been the low melting points of these materials, and the consequent high vapor pressure at modest temperatures. The heating caused by the spark can then melt the alkali metal, causing both a change in composition of the sample through fractional distillation, and thermal ionization of the alkali metal. Both of these phenomena

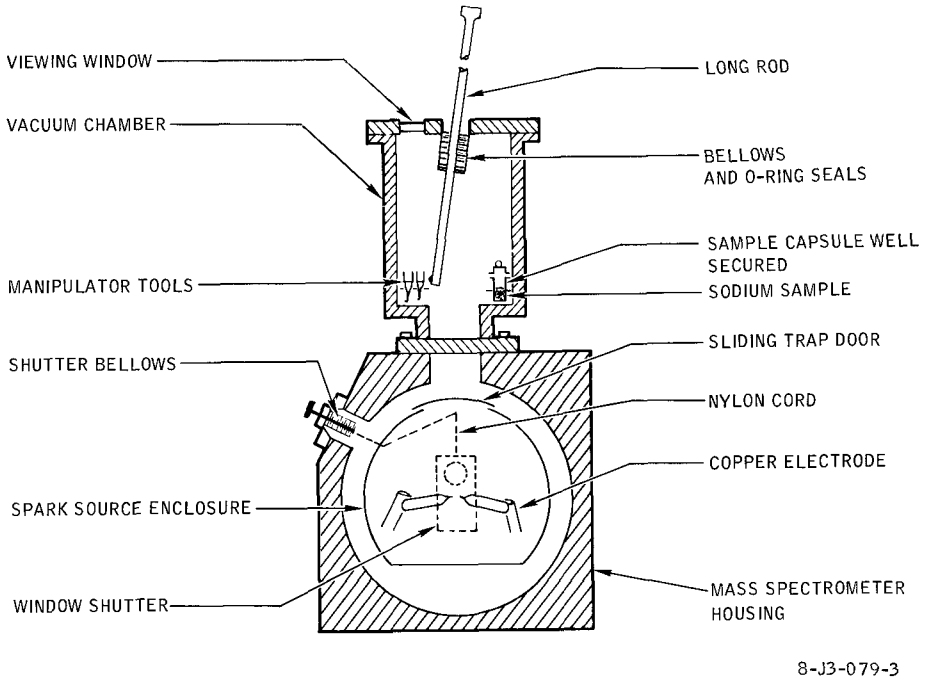

Figure 9. Mass Spectrometer Loading Manipulator

are undesirable and make interpretation of the mass spectra difficult and inconclusive. The fact that fractionation would cause a loss of homogeneity in the sample is obvious. The reason that thermal ionization is undesirable is that the usual method of analyzing the spectra is to compare the intensity of an impurity spectral line with a line from the matrix material, in this case the Na^+ line. If the Na^+ line is enhanced by thermal ionization, this intensity comparison gives a wrong indication of the amount of impurity present.

To reduce, and perhaps eliminate, both fractionation and thermal ionization, the electrodes of the SSMS were redesigned. Two approaches were used: first, to make the electrodes themselves out of a better thermal conductor (copper instead of tantalum); and second, to cool the electrodes with liquid nitrogen. The conversion to an all-copper assembly resulted in markedly improved spectra at room temperature, with sharper and better defined lines than those obtained with the previous assembly. Surprisingly, however, no further difference has been observed when the electrode assembly is cooled with liquid nitrogen. From this it appears probable that the use of copper removes the heat sufficiently well to prevent the sodium from melting, and therefore further cooling makes little difference.

Of particular interest in the analyses of the spectra obtained with the different electrode assemblies is the fact that the Na^+/Na^{++} ratio remained high, between 500 and 1000, and did not change significantly either with electrode cooling, or when the power of the spark was reduced. This ratio rarely exceeds 5 for elements other than the alkali metals. If thermal ionization had contributed appreciably to the Na^+ ion beam in the first place, a sharp reduction in the ratio would be expected. A satisfactory explanation for the fact that the Na^+/Na^{++} ratio did not decrease when the power was reduced and the electrode cooled is that there was no thermal ionization in the first place. There is little enhancement of the Na^+ beam, but instead the Na^{++} beam is greatly suppressed, because of the stable closed shell electron configuration which remains after the first electron is removed. This effect is seen more quantitatively by comparing the ratio of the first two ionization potentials of the alkali metals with those of other metals. These ratios for Na and K are 9.2 and 7.3, respectively, while those for elements in other periodic groups are very nearly 2.0. The conclusion to be drawn is that the Na^+ beam may be used as an internal standard

in much the same way as other singly charged matrix ion beams. Some variation in the Na^+/Na^{++} ration has been observed between analyses, however. A possible explanation is that the large Na^+ beam may be sufficiently dense in some instances that the ions electrically self-repel during the flight from spark to photoplate. This phenomenon has been shown to occur with large ion beams of other elements, and has the effect of broadening the beam. Microdensitometer measurements utilizing the whole area of the spectral line rather than the "maximum density" measurements presently employed are expected to do much to eliminate this source of variation.

The sodium used in the experiments was doped with ten elements. These all appeared in the SSMS analysis, as well as fifteen other impurities. The relative concentrations of the dopants were relatively consistent when compared to the Na^{++} ion beam, displaying an average standard deviation of 21% of the concentration value. This variation, which is quite good for spark source mass spectrometry, gives the important indication that the impurities behave in sodium much as they would in any other metallic matrix. Comparison of impurity values to the Na^+ beam, to obtain quantitative analyses, requires knowledge of what conditions are necessary to ensure reproducible production of the Na^+ ion beam.

To further the effort to understand the factors that affect enhancement of the ion beam of various elements in the RF spark, some irradiated zirconium-uranium alloy containing fission products in the parts per million range was analyzed. Several interesting photoplates have been produced which depict 29 fission product elements, representing every group in the periodic table. Because the relative concentrations of these elements are precisely known, the enhancements of each may be precisely determined in the matrix of zirconium. Thus, the behavior of the alkali metals cesium and rubidium can be compared with known "well behaved" elements such as molybdenum and silver. Data obtained in this prototype "fission product standard" will be used in analyses of other matrices such as sodium in the absence of prepared standards. From the photoplate, it is immediately apparent that the cesium and rubidium are somewhat enhanced with respect to all the other elements. Although this gives no precise information on sodium or potassium, the accurate information on the other elements with respect to rubidium and cesium will be extrapolated to sodium if more specific information is unavailable.

Another modification made to the mass spectrometer is the installation of a shutter over a glass shield covering the viewing window. By keeping the shutter over the glass most of the time, and looking at the spark only ocasionally to make major adjustments, several analyses of sodium may be performed without the need to open the vacuum system to clean the window.

A data digitizing system consisting of a precision microphotometer-comparator with a high-speed digital magnetic tape readout will be delivered in July. This system will improve the accuracy of each analysis with numerous changes in the method of data processing. Corrections for background, line-width, and emulsion calibration will be performed completely and correctly with a code that is now being written. The total time of analysis including sample preparation, sparking, and data reduction is expected to be reduced by a factor of six.

G. OTHER PROJECT ACTIVITIES

Project personnel have been involved in two other areas of work in the preceding year. The revision of the Liquid Metals Handbook, Na-NaK Supplement, is being accomplished by the Liquid Metal Engineering Center, operated by Atomics International. Section 2.4, "Chemical Interactions," of this Handbook has been reorganized and rewritten by senior members of the project staff, and has been submitted to the editor.

Also falling under the scope of this project is the current ASTM round robin on the analysis of sodium for oxygen. All facilities for carrying out the analysis of the round robin samples (prepared by Atomic Power Development Associates) are ready, and the analyses will be performed and results submitted by the July 15, 1968 date as requested.

III. EVALUATION OF EFFORT DURING FISCAL YEAR 1968

The results described above show substantial progress toward the objectives of the project. The sodium purification apparatus has continued to operate well and to provide the very high quality sodium required by the program objectives. Progress in the determination of the solubility of metal solutes in sodium has been significant. The report on the solubility of copper is sufficiently definitive to meet the need in this area. The work on molybdenum is adequate for the

short term, but may be augmented later if LMFBR needs so indicate. The change in method for the study of iron and chromium solubilities (from spectrophotometric or atomic absorption spectrometric analyses to radiochemical techniques) permits the development of very significant information, in view of the years-long disagreement in the results of iron solubility work. It is probable that some rationale will be found to explain the experimental results, and that solubility data will be determined for the constituents of stainless steel, in which data some confidence may be placed.

Planning for the Sodium Chemistry Loop has been thorough and effective. The study, currently underway, of the thermodynamics and kinetics of possible interactions in the SCL materials system will make the interpretation of experimental results, when they are obtained, more rigorous.

The agreement between apparent carbon solubility in sodium using single crystal graphite and diamond solute is significant. The progress in the area of carbon solubility is good, and should point the way to understanding the nature of the carbon-sodium solution. Particularly important is the decision to use tagged ^{14}C as solute. The two-pronged attack on the problem, with the tagged carbon and by a deeper study of the dry combustion analysis, offers a firm foundation for increased understanding.

An exhaustive review of the data on the solubility of oxygen in sodium has been carried out. As a result, a new solubility curve is recommended, based on this critical evaluation of the collected data originating from eight laboratories.

Particularly important to the field of sodium chemistry is the work that has been done in revising the section on Chemical Interactions of the Liquid Metal Handbook Supplement. This work has been thorough, and will provide a sound background for many years of information for those interested in sodium chemistry.

Both wet chemical and atomic absorption methods for determining trace amounts of several metallic elements in sodium have been improved, and a strong beginning has been made on a thorough study of the dry combustion method for carbon. It has been established that the spark source mass spectrometer is effective in identifying even very small concentrations of elements

in sodium. Thermal ionization of sodium has been shown to be absent, giving impetus to the effort to optimize operating conditions in the SSMS to provide quantitative analyses. Although our inability to obtain a representative sample at room temperature for SSMS analysis has prevented its use for solubility determinations, this is a problem in sampling, and does not detract from the potential usefulness of the instrument in circumstances in which adequate sampling is possible. It appears probable that, except for the sampling limitation, SSMS analysis of sodium will achieve the same level of performance as that for other metals.

REFERENCES

1. R. M. Singer and W. Becker in "Quarterly Progress Report of Work Sponsored by the Fuels and Materials Branch, April 1 - June 30, 1967," BNL-50065 (August 1967) p 12 ff

2. J. R. Humphreys, Jr., Interdivisional Document K-3-774, Los Alamos Scientific Laboratory

3. S. J. Rodgers, J. W. Mausteller, and E. F. Batutis, "Iron and Nickel Concentration in Sodium," MSA-TR-27 (June 30, 1954)

4. L. F. Epstein, "Preliminary Studies on the Solubility of Iron in Liquid Sodium," Science 112, 426 (1950)

5. J. R. Weeks (compiler), "Annual Progress Report of Work Sponsored by the Fuels and Materials Branch, January 1 - December 31, 1967," BNL-50092 (March 1968)

6. R. A. Baus, A. D. Bogard, J. A. Grans, L. B. Lockhart R. R. Miller, and D. D. Williams, "The Solubility of Structural Materials in Sodium," Proc., First U. N. Intern. Conf. on Peaceful Uses of At. Energy, Geneva 9, 356 (1955). Also reported in A. D. Bogard, "The Solubility of Iron in Sodium Metal, Sodium-Sodium Oxide, and Sodium-Sodium Oxide-Sodium Hydroxide," NRL-4131 (1953)

7. J. R. Weeks, Brookhaven National Laboratory, Private Communication (May 1968)

8. R. A. Walker, J. N. Pratt, and B. W. Mott, "The Solubility of Metallic Elements in Liquid Sodium," a paper presented at the 1968 AEC Corrosion Symposium, May 6-8 (1968) at Battelle Memorial Institute, Columbus, Ohio

9. T. F. Prach "Determination of Oxygen in Sodium" in "Annual Progress Report of Work Sponsored by the Fuels and Materials Branch, January 1-December 31, 1967," BNL-50092 (1968), p 45

10. J. M. Scarborough and P. F. DeVries, "Characterization of Blank Correction in Determination of Oxygen in Sodium by the Amalgamation Method," Anal. Chem. 39, 826 (1967)

11. K. S. Bergstresser, G. R. Waterbury, and C. F. Metz, "Determination of Trace Amounts of Oxygen Added to Metallic Sodium," LA-3343 (August 24, 1965)

12. V. J. Rutkauskas and G. E. Meadows "Measurement of Impurities and Development of Quality Control Techniques for High Temperature Sodium Coolant Systems" in "Quarterly Status Report on the Advanced Plutonium Fuels Program, April 1-June 30, 1967," LA-3745-MS (1967), p 10. A more detailed discussion of the work described in this reference, including

a few additional data points, is being published by V. J. Rutkauskas, "Determination of the Solubility of Oxygen in Sodium Using the Vacuum Distillation Analytical Technique," LA-3879 (1968), which was not available when this report was written.

13. S. L. Walters, "The Effects of Adding Oxygen to Sodium Flowing in a Stainless Steel System," NP-1955 (1950)

14. J. D. Noden and K. Q. Bagley, "The Solubility of Oxygen in Sodium and Sodium-Potassium Alloy," RDB(C)-TN-80 (1954)

15. A. D. Bogard and D. D. Willams, "Solubility of Sodium Monoxide and of Sodium Hydroxide in Metallic Sodium," NRL-3865 (1951)

16. S. Dorner, "Solubility of Oxygen In Sodium," EURFNR-179P (English translation of Projekt Schneller Bruter (PSB) Report 195/66 (1966)

17. W. Jahns and G. Weidmann, "The Determination of Low Oxygen Concentrations in Sodium," Nukleonik 1, 189 (1959)

18. O. N. Salmon and T. J. Cashman, Jr., "The Solubility of Sodium Monoxide in Liquid Sodium," KAPL-1653 (1956)

19. A. W. Thorley, as quoted in Reference 20

20. K. T. Claxton, "Review of Solubility Data for the Liquid Sodium-Oxygen System," J. Nuclear Energy 19, 849 (1965); also AERE-R4897

21. K. T. Claxton, "Contribution on the Solubility of Oxygen in Liquid Sodium," J. Nucl. Energy 21, 351 (1967)

22. V. I. Subbotin, P. L. Kirillov, and F. A. Kozlov, "Removal of Oxygen from Sodium and Monitoring of Oxygen in Sodium," USSR-701 (in Russian); Translation: Inf. Series 10(r) (1964), p 6; CA62:15799 g

23. T. F. Kassner and D. L. Smith, "Calculations on the Kinetics of Oxygen Solution in Tantalum and Niobium in a Liquid-Sodium Environment," ANL-7335 (1967)

24. C. Luner, A. Cosgarea, Jr., and H. M. Feder, "Solubility of Carbon in Sodium," Alkali Metal Coolants (IAEA, Vienna, 1967), p 171

25. J. G. Gratton, "Solubility of Carbon in Sodium at Elevated Temperature," KAPL-1807 (1957)

26. J. M. Scarborough, C. D. Bingham, and P. F. DeVries, "Determination of Trace Metallic Impurities in High Purity Sodium Using Atomic Absorption Spectrometry," Anal. Chem. 39, 1394 (1967)

Program: HNPF
AEC Task: Task 13, HNPF Retirement
Project Manager: B. F. Ureda
Reporting Period: Fiscal Year 1968
General Order: 7709 Subaccount: All AEC Category: 46-01-00-00.0

Principal Investigator: B. F. Ureda

I. PROJECT OBJECTIVES

The project objective is the accomplishment of the AEC-designated tasks and the CPPD subcontractual tasks in the retirement of the HNPF. During the past year these tasks were as follows.

A. Complete the design of the spent fuel shipping casks, provide quality assurance during the fabrication of the casks, and arrange for the delivery and operational checkout of the casks at HNPF and the Savannah River Plant. The casks had to meet all the requirements specified in Chapter 0529 of the AEC Manual.

B. Continue preparation and obtain approvals of the Activity Specifications outlining the discrete activities comprising the HNPF retirement. The preparation includes conduct of engineering analyses and design in support of the activities.

C. Coordinate the disposal of HNPF excess property and prepare removal and storage requirements for special equipment.

D. Assist CPPD in disposal of irradiated fuel. Assistance to include engineering and design of tools and fixtures, and development techniques for handling and canistering fuel elements.

E. Assist CPPD in: writing of detailed procedures, designing the sodium reaction process system, and accomplishing isolation of secondary sodium systems; and provide technical assistance during operation of the process system.

II. TECHNICAL PROGRESS DURING FISCAL YEAR 1968

A. SPENT FUEL SHIPPING CASKS

The spent fuel shipping casks, after resolution of fabrication difficulties, were delivered to the HNPF on January 28, 1968. A series of tests were conducted at HNPF, by use of dummy fuel. After satisfactory exercise of all the operational features of the casks, a basket of irradiated fuel was loaded into the cask and shipped to the Savannah River Plant. Twenty-two of the twenty-five shipments of fuel have been made without incident. At the present rate of one shipment per week, the fuel will be off site by the end of July 1968. Removal of the fuel is a major accomplishment in the HNPF retirement.

The canistering of irradiated fuel was completed on June 3, 1968. The canistering involved double encapsulation of each fuel element. The canisters, tools, and fixture for remotely handling the fuel in the maintenance cell and the specially designed welding machine were designed, fabricated, or procured by AI for CPPD's use. In addition, an engineer from AI's hot cell laboratory assisted and monitored the operation throughout.

B. ACTIVITY SPECIFICATION DEVELOPMENT

Of the twelve activity specifications, eleven have been prepared and approved by the AEC. Activity Specification No. 10 "Securing of Isolation Structure," has been submitted to CPPD; but since the related question of the final disposition of the reactor building has not been resolved, CPPD is withholding concurrence.

C. SAFETY ANALYSIS REPORT

Supplement 5 to the HNPF Safeguards Analysis was prepared for CPPD. This analysis of the retirement activities was forwarded to DRL and approved by DRL. Additional studies were conducted to support assumptions and conclusions made in Activity Specification No. 7, "Disposition of Contaiminated and Irradiated Material."

D. EXCESS PROPERTY DISPOSAL

Excess property is being shipped off site as soon as it is cut loose from the system. The major sodium components have been shipped. These include the three steam generators, the six intermediate heat exchangers, the three secondary pumps, all large valves, primary and secondary sodium containing fill tanks, E-M pumps, and flowmeters. One scrap sale was conducted and the scrap removed.

A specification delineating the contents and the manner in which the buildings are to be removed, should that be the final building disposition, was prepared and forwarded to AEC Chicago. A building description package was compiled and distributed to contractors with a possible interest in removing the building.

E. CPPD ASSISTANCE

Preparation of detailed procedures as designated by the activity specifications continues. Procedure preparation for removal and sealing of the sodium systems are completed and implemented. CPPD assistance for handling and canistering the spent fuel was completed. The final element of 150 was canistered and placed in a basket for storage, ready for shipment.

A major effort in the past year was the design, fabrication, and operation of a process system for the reaction of the residual sodium in the reactor and in the coolant loops. The operation was very satisfactory and currently a report describing and evaluating the operation is in progress. A special study of the effects of sodium hydroxide on reactor structural materials is being made per an anticipated request of DRL. This study will determine the adequacy of containment of the reactor liner to keep the radioactive materials in when subjected to the action of sodium hydroxide.

III. EVALUATION OF EFFORT DURING FISCAL YEAR 1968

Cask procurement was a serious bottleneck in the beginning of the year. The problems were mainly those of fabrication and necessary, but time consuming, reviews and selections of problem solutions. The cask loading and unloading is a smooth routine operation. The first shipments required minor

adjustments in equipment and procedure. The turn-around time for a fuel shipment, HNPF to SRP and back, is one week. This is one-half that expected and predicted at the outset of the fuel shipments.

Completion of the reaction of the residual sodium in the reactor vessel and in the coolant loops was an important step in the retirement program. Since such an operation had not been previously attempted anywhere, there was considerable concern on the part of the AEC, AI, and CPPD for personnel and equipment safety. The entire operation from conceptual studies, through simulation tests, system fabrication, and system operation was carefully monitored. The results justified the time and care taken.

Removal of excess property particularly of the major items such as the steam generators and intermediate heat exchangers has progressed slowly.

Shipment of excess property has been held up in some instances because of too strict an interpretation of DOT requirements by CPPD.

Completion of the HNPF retirement work on schedule currently hinges on the disposition of the reactor building and the outlying buildings. Many studies by the AEC, AI, and CPPD are being made to determine whether the buildings are to come down, where the buildings would be cut from CPPD structures, and what costs are involved. When these studies are complete, the end date of the HNPF retirement program can be accurately established.

Program:	Advanced Development Program			
AEC Task:	15, High Temperature Chemistry			
Project Manager:	S. J. Yosim			
Reporting Period:	Fiscal Year 1968			
General Order:	7711	Subaccount: 53020	AEC Category:	05-05-01-00.0

I. PROJECT OBJECTIVES

The project is divided into two general areas; namely, the study of fused salts and the study of metal, metal-salt solutions. The objective of the study of fused salts is to achieve an understanding of ionic melts (halides, oxides, oxysalts and glass systems) by (1) establishing the nature of the species existing in ionic melts, (2) determining the physicochemical interactions between species, and (3) formulating systematic relationships between the physicochemical properties of fused salt systems and the molecular parameters of the species.

The objectives of the metal, metal-salt study are to determine phase diagrams for, and the nature of interactions between metals and their salts at high temperatures, to determine the species in those solutions, and finally, to predict the solubilities in metal-salt systems.

II. TECHNICAL PROGRESS DURING FISCAL YEAR 1968

PUBLICATIONS AND TALKS

A. PAPERS PUBLISHED

1. "Thermoelectric Properties of the Molten Bismuth, Bismith-Halide Oxidation-Reduction Thermocells," by J. D. Kellner, J. Phys. Chem. 71, 2434 (1967)

2. "Viscosity of Molten Bismuth-Bismuth Triiodide Solution," by J. D. Kellner, J. Phys. Chem. 71, 3254 (1967)

3. "Electrical Conductivity of Liquid and Saturated Vapor of $BiCl_3$ and H_gCl_2 to Their Critical Temperatures," by L. F. Grantham and S. J. Yosim, J. Phys. Chem. 72, 762 (1968)

4. "Cell Assembly to Measure the Electrical Conductivities of Molten Salts to Their Critical Temperatures," by L. F. Grantham, E. B. Harrelson, P. H. Shaw, and C. M. Larsen, Rev. Sci. Instr. 39, 699 (1968)

5. "Phase Diagrams of the Bismuth Trihalides at High Pressure," by A. J. Darnell and W. A. McCollum, J. Phys. Chem. 72, 1327 (1968)

6. "Viscosity of Molten Bi-Bi Halide Solutions," by Jordan D. Kellner, J. Phys. Chem. 72, 1737 (1968)

The following paper is in press.

7. "Fused Salts," by S. J. Yosim and H. Reiss, Ann. Rev. Phys. Chem.

The following paper was submitted for publication

8. "Interatomic Distance and Polymorphism in the Alkali Halides," by A. J. Darnell and W. A. McCollum

B. TALKS/PAPERS PRESENTED

1. An invited paper, "Electrical Conductivities of Supercritical $BiCl_3$ and $HgCl_2$," was presented at the Fused Salt Gordon Conference, August, 1967, by L. F. Grantham.

2. "Phase Diagrams of the Bismuth Halides at High Pressure," at the 154th National Meeting of the American Chemical Society, Chicago, Ill., September 1967

3. "Thermoelectric Properties of Metal-Metal Salt Thermocells," by J. D. Kellner at the 155th National Meeting of the American Chemical Society, San Francisco, April 1968

4. "Polymorphism and Interatomic Distance in the Alkali Halides," by A. J. Darnell at the High Pressure Gordon Conference, June 1968

5. S. J. Yosim was Chairman of the Transport Session at the Fused Salt Gordon Conference, August 1967

C. SUPERCPITICAL CONDUCTIVITIES OF FUSED SALTS

Sufficient tests were made to verify that the tungsten electrodes were reacting either with the $BiCl_3$ or with an impurity in the melt, presumably to

produce reduced bismuth species which increase the conductivity and which increase the critical temperature. Cells containing gold plated tungsten electrodes were tested. The results indicate that the gold plate is not protective.

One of the impurities may be Bi_2O_3 formed in the final purification step when $BiCl_3$ is distilled under an oxygen atmosphere to oxidize all monovalent bismuth; therefore, in further runs, impurities such as this were removed by filtration and redistillation. In addition, it was found that corrosion of the tungsten electrodes can be controlled by placing a specially treated graphite sleeve over the tungsten.

Control of impurities and corrosion will allow us to obtain valid supercritical conductivity data. It is anticipated that the mechanism of supercritical (low-density) conductivity will be different from that found in high-density constant volume experiments. In the supercritical phase, it is anticipated that the formation of current carrying entities will be the controlling step in conduction while in high-density experiments it is anticipated that in most cases the mobility will limit the conduction.

Two papers have been published on this task.

D. ELECTRICAL CONDUCTIVITY OF Bi HALIDES AT HIGH PRESSURE

Preliminary electrical conductivity measurements of $BiCl_3$, $BiBr_3$, and BiI_3 at "constant volume" were completed. In the constant volume method used in this work, however, while the volume of the entire system is maintained constant, the actual salt sample comprises only a relatively small fraction of the constant volume chamber. Differences in compressibilities and expansivities of the salt sample and the remainder of the chamber could allow a change in volume of the salt during a run even though the volume of the entire chamber is kept constant. Emphasis was shifted, therefore, to conductivity measurements where the experimental parameters pressure and temperature are clearly defined; i.e., conductivity of the molten salt (1) as a function of temperature at constant pressure and (2) as a function of pressure at constant temperatures. Measurements were made on the electrical conductivities of $BiCl_3$, $BiBr_3$, and BiI_3 (1) from their melting points to a temperature of 850°C at a constant pressure of 5 kb, and (2) at pressures from 4 to 18 kb (15 kb in the case of BiI_3) at

a temperature of 625°C. The results from these isobaric tests show that the electrical conductivities of all three salts increase exponentially with increasing temperature at this elevated pressure. This is in contrast to the maximum in the conductivity-vs-temperature curve found by Grantham and Yosim at near atmospheric pressure. In the isothermal experiments, the electrical conductivity increases with increasing pressure. $BiCl_3$ exhibits the largest value for the ratio, $\varkappa$ (18 kb) / $\varkappa$(4 kb) = 1.9. The corresponding conductivity ratios for $BiBr_3$ and BiI_3 are 1.5 and 1.2, respectively. This increase in conductivity with pressure is in contrast to more ionic salts such as the nitrates where the conductivities generally decrease with increasing pressure. Thus, it appears that the effect of pressure is to make bismuth salts more ionic. This completes the experimental phase of this study and the results will be published.

E. COMPRESSIBILITIES AND VOLUMES-OF-FUSION OF MOLTEN $BiCl_3$ AND $AlCl_3$ AT ELEVATED PRESSURES

Measurements of the compressibilities of selected fused salts are being carried out in order to obtain P-V-T data so that electrical conductivity studies can be made on liquids maintained at constant volume. Preliminary compression measurements have been made on molten $BiCl_3$ and $AlCl_3$ up to 1500 bars. As might be expected from the difference in bonding in the liquid state of these two compounds, the initial compressibility of $AlCl_3$ is three to four times higher than that of $BiCl_3$. Preliminary volumes of fusion of these salts were also obtained as a function of pressure. The fractional volume of fusion ($\Delta V_{fusion}/V_{solid}$) decreased from 0.8 at 1 atm to 0.6 at 1,000 bars in the case of $AlCl_3$; whereas, it changed only slightly in the case of $BiCl_3$. The relatively high change of the volume of fusion and compressibility in the case of $AlCl_3$ may be due to an increase in salt-like behavior of $AlCl_3$ at high pressures.

F. PROPERTIES OF ALUMINUM TRIHALIDES AT HIGH PRESSURES

The melting curve of aluminum tribromide was determined at pressures up to 36 kb. The melting point rises from 97°C at atomospheric pressure to 365°C at 36 kb. The pressure dependence of the melting point is less than was found for aluminum trichloride; (197°C at ~ 3 atm to 780°C at 36 kb). At 36 kb, the pressure dependence of the melting temperature of $AlBr_3$ approaches zero. If ΔS_{fusion} is typical for a solid with this melting temperature, this implies

that the volume of fusion is small at this pressure of 36 kb and thus the molar volume of the liquid and solid are approximately the same at this high pressure; whereas, at atmospheric pressure $V_{liquid}/V_{solid} \simeq 1.15$. A significant reduction in the molar volume of molten aluminum bromide is therefore expected with an increase in pressure from atmospheric to 36 kb.

G. POLYMORPHIC TRANSITIONS IN THE ALKALI HALIDES

The experimental work carried out last year on the polymorphic phase changes in the alkali halides has been analyzed. As a result of this work, an empirical rule was developed which relates the transition pressure and the transition volume to the first power of the interatomic distance in the group of alkali halides which have common anions. A paper describing these results has been submitted for publication.

H. ELECTRICAL CONDUCTIVITY OF PURE $AlCl_3$

The electrical conductivity of pure $AlCl_3$ was measured from the melting point (192°C) through the critical point (350°C) to 500°C; (above this temperature, excessive corrosion took place). The specific conductivities were $1\text{-}2 \times 10^{-7}$ $(\text{ohm-cm})^{-1}$. A maximum in specific conductance was observed at about 300°C. This study has been completed and the results will be published.

I. PHASE DIAGRAMS OF $AlCl_3$-ALKALI CHLORIDES

Most alkali-halide, aluminum-halide phase diagrams show a two-liquid phase region on the AlX_3 rich side. Seldom has the consolute temperature been reported. To measure conductivities of such systems at all compositions, it is necessary to know these consolute temperaures; therefore, attempts were made to measure them for $KCl\text{-}AlCl_3$ and $CsCl\text{-}AlCl_3$. However, instead of simple consolute behavior; i.e., a disappearance of the liquid-liquid boundary, the liquid (upper, $AlCl_3$-rich) -vapor boundary disappeared with all the characteristics of critical point behavior. For both mixtures, the temperature at which this occurred was 349 ± 1°C. The critical point of pure $AlCl_3$, by using the same material as was used in the above mixtures, was measured by this same method and found to be 350 ± 2°C which atrees quite well with Cubicciotti's value (private communication) of 347 ± 2°C. Thus, it would appear, for both

mixtures, that the upper liquid phase is essentially pure $AlCl_3$; and under their own vapor pressures, these mixtures cannot exhibit consolute behavior. These measurements also show that the phase diagram for $CsCl-AlCl_3$ which appears in the literature [Morozov, et al, J. Inorg. Chem., USSR (Engl. transl.) 2, No. 8, 311 (1957)] is incorrect, since it shows no two-liquid phase region. This study has been completed.

J. PHASE DIAGRAM OF $NaBr-AlBr_3$

The consolute temperature was measured for 8 mole % $NaBr-AlBr_3$. Normal consolute behavior was observed in this system in contrast with the previously measured $KCl-AlCl_3$ systems where no consolute temperature was observed. A consolute temperature of 255 ± 2°C was observed as compared with a literature value of 232°C. This study has been completed.

K. ELECTRICAL CONDUCTIVITY OF $AlCl_3$-KCl SYSTEM

A study of the electrical conductivities of AlX_3MX systems, where X is a halide and M is an alkali metal, has been initiated. The first system is $AlCl_3$-KCl.

Solutions of KCl containing 15, 25, 33, 40, 50, 67, and 80 mole % $AlCl_3$ were examined. A maximum in the conductivity-vs-temperature curve was observed for 50 mole % $AlCl_3$-KCl near 1000°C. The conductivities exhibit negative deviation from additivity when plotted against composition. A well defined minimum on the conductivity-vs-composition curve was found at a mole ratio of K:Al = 2. The experimental work will soon be completed.

L. ELECTRICAL CONDUCTIVITY OF $AlBr_3$-NaBr SYSTEM

Electrical conductivities of $AlBr_3$-NaBr mixtures have been measured as a function of temperature at 25, 33, 42, 50, 67, 80, and 92 mole % $AlBr_3$. The results are, in general, quite similar to those reported above for $AlCl_3$-KCl. The minimum is actually more pronounced for the bromide than for the chloride system; this indicates that the coordination number of aluminum does not increase (above 4) as thought earlier. Such an increase, unlikely for chloride, would be even less likely for the larger bromide and the conductance minimum would be less pronounced for bromide.

The 80 and 92 mole % $AlBr_3$ mixtures were measured with external pressures on the conductivity cells of 1800 psi at temperatures as great as 900°C. No previous measurements are reported for the solutions highly concentrated in $AlBr_3$, presumably because of the high pressures involved at high temperatures. Both the 80 and 92 mole % $AlBr_3$ mixtures show unusual conductivity changes with temperature. The conductivity-vs-temperature curves at first increase linearly with temperature, as expected; then, at 400 to 500°C, show an increase in slope, gradual in the case of 80 mole % $AlBr_3$, but fairly sharp for the 92 mole % $AlBr_3$. This effect does not appear to be due to a compositional change in the liquid resulting from $AlBr_3$ removal into the vapor phase, since the 92 mole % $AlBr_3$ mixture was repeated with smaller vapor volume and the same effect was obtained.

M. IONIC SALT VAPORS

Calculations for ionic salt vapor equilibria show that the possibility of gaseous ionic species exists. The occurrence of ionic species in the vapor phase should be enhanced in mixtures of salts of widely different cationic charge density. The presence of ions should produce a conducting plasma and can be detected by simple resistance measurements. Preliminary measurements of anhydrous CsCl + LiCl (1.5 mole ratio) in an evacuated sealed Vycor container with tungsten electrodes yielded a specific resistance of about 3.8×10^6 ohms at 800°C. This resistance decreased by a factor slightly greater than two for every 50°C rise in temperature. Although these values corroborate the thesis of ions in the vapor, the possibility of salts absorbing on the electrode surface, dissociating there, and then evaporating as atoms and ions must be considered. In addition, the lowering of the work function of tungsten by the salts, especially CsCl, resulting in emission of electrons is also a possible occurrence. These possibilities will be checked by running cells with no salt and by using other electrodes such as Pt.

N. SOLID STATE GALVANIC CELLS

Studies to measure the free energy of formation (ΔG_f°) of various rare earth compounds; e.g., fluorides, carbides, sulfides, nitrides, phosphides, etc., by means of solid state galvanic cells, are being initiated. These cells will be of

the type (for pure fluorides)

$$R_1RF_3 \; CaF_2 \; M_1MF_x \quad ,$$

where R and M denote rare earth metal and a reference metal whose ΔG_f° is known, and CaF_2 serves as the ionic auxiliary electrolyte. For cells other than fluorides, the compound, e.g., carbide, is merely added to the metal, metal-flouride mixture. For the measurements to be thermodynamically correct, no electronic conductivity must occur through the CaF_2. With highly electropositive metal systems such as those of the rare earths, however, electronic conduction might be induced in the CaF_2. To ascertain this occurrence and correct for it, both the total and electronic conductivities of CaF_2 in contact with $R + RF_3$ must be measured. In a preliminary experiment, the conductivity of a cell assembly consisting of a disk of single crystal CaF_2 sandwiched between two pressed pellets of intimately mixed powdered $Al + AlF_3$ was run between 550 and 650°C. At all temperatures, the specific resistance was higher than the literature value by a factor of about two. Since the measured resistances were decreasing slowly from day to day, it seems that the difference in conductivities is due to poor contact between the CaF_3 and the pressed pellet electrodes. Further, the powdered Al used was obtained commercially and undoubtedly had an oxide film which would also enhance the resistance. In future experiments, the metal will be powdered by filing in an inert atmosphere; the pellets and cells also will be fabricated in an inert atmosphere.

O. FUSED SALT REVIEW

A critical review of fused salt work from 1965 to the present was made by Yosim and Reiss. This review will be published in the 1968 Annual Reviews of Physical Chemistry.

P. THERMOELECTRIC PROPERTIES OF METAL, METAL-SALT SYSTEMS

Earlier, it was reported that the Soret effects (a partial demixing when a mixture is placed in a thermal gradient) were extremely large in bismuth, bismuth-halide solutions. For example, a solution of $BiBr_3$ containing

3 mole % Bi exhibited a steady state thermoelectric potential of about 16,000 μv/deg at 500°C. However, in an attempt to exploit this phenomenon to develop an efficient thermoelectric device, it was shown in a different program that these high potentials were not due to the Soret effect. The cells were therefore redesigned and the true Soret potentials of the Bi-$BiBr_3$ system were redetermined. The potentials were found to be between -50 and +50 μv/deg. This completes the study of the Soret effect in metal, metal-salt solutions. A paper describing the above results will be prepared.

Q. ELECTRICAL CONDUCTIVITY OF $CuCl$-$CuCl_2$ SOLUTIONS

This study has been resumed. The electrical conductivities of pure $CuCl_2$ and CuCl solutions containing 5, 10, 14, 20, 30, 40, 50, 60, and 80 mole % $CuCl_2$ have been measured from the liquidus temperature to above 700°C. Conductivity-vs-composition plots show maxima at all temperatures. Both the magnitude of conduction and the "activation energy" for conduction are much larger in the intermediate concentration range than for either pure salt. This suggests that semiconduction is occurring at intermediate concentrations. As expected, the system is differnt from the Bi-BiX system in that the conductivity of the pure subhalide (CuCl) is much less than the conductivity of molten mixtures of the subhalide and pure salt. This is probably due to stability of the Cu_2Cl_2 dimer.

R. THE ELECTRICAL CONDUCTIVITY OF Hg-HgX_2 SYSTEMS

The electrical conductivity of HgI_2 containing 5 and 25 mole % Hg was measured. In the case of the 5% solution, the specific conductivity decreased monatomically from 0.135 $(\Omega_{cm})^{-1}$ at 250°C (the lowest temperature at which a single phase exists at this composition) to 0.015 $(\Omega_{cm})^{-1}$ at 600°C. In the case of the 25% solution, the electrical conductivity of 25 mole % HgI_2 was measured to 500°C. The expected conductivity maximum occurred at 430°C. The data obtained are in line with previous results and therefore substantiate those conclusions.

The electrical conductivity of molten $HgCl_2$ containing 20 mole % Hg was measured. The specific conductivity decreased from 0.13 $(\Omega_{cm})^{-1}$ at 252°C (the lowest temperature at which a single phase exists at this compositon) to 0.015 at 600°C. This concludes the Hg-HgX_2 conductivity work and the results will be published.

III. EVALUATION OF EFFORT DURING FISCAL YEAR 1968

Many studies have been completed this fiscal year. These include:

1) Electrical Conductivity of Bismuth Halides at High Pressure,

2) Polymorphic Transitions in the Alkali Halides,

3) Electrical Conductivity of Pure Aluminum Trichloride,

4) Phase Diagrams of Aluminum Trichloride-Alkali Chlorides,

5) Phase Diagram of Aluminum Tribromide-Sodium Bromide,

6) Fused Salt Review,

7) The Electrical Conductivities of Mercury-Mercuric Halide Systems, and

8) Thermoelectric Properties of Metal, Metal-Salt Systems.

The emphasis on fused salts continues in high pressure and transport studies. Emphasis is being placed on the study of salts near and above the critical temperature. Such studies will prove informative in the transition from ionic gases to liquids. In the case of metal, metal-salt solutions, emphasis is still being placed on experiments carried out above the temperature of complete miscibility as well as above the critical temperature of the salt. Such studies will shed considerable light on the gradual transition from salt-to-metallic behavior.

Program: Advanced Development, Physical Research		
AEC Task: 16, Radiation Chemistry		
Project Manager: R. A. Holroyd		
Reporting Period: Fiscal Year 1968		
General Order: 7712	Subaccount: 53050	AEC Category: 05-05-02-00.0

I. PROJECT OBJECTIVES

The objectives of this project are to delineate the fundamental physico-chemical processes occurring in the radiolysis of organic systems and to study these processes in separate experiments designed to increase our understanding of their nature and their role in radiolysis.

II. TECHNICAL PROGRESS DURING FISCAL YEAR 1968

A. PAPERS AND PRESENTATIONS

The following papers have been published.

1. R. A. Holroyd, J. Y. Yang, and F. M. Servedio, "Vacuum Ultraviolet Photolysis of Liquid Organic Mixtures-Energy Transfer from Neutral Excited Cyclohexane," J. Chem. Phys., 46, 4540 (1967)

2. G. T. Tiedeman and R. B. Ingalls, "An ESR Investigation of the Reactions of Hydrogen and Deuterium Atoms with Alkylstyrene Polymers," J. Phys. Chem., 71, 3092 (1967)

3. L. M. Theard, F. C. Peterson, R. L. Wilson, J. F. Ward, L. S. Myers, Jr., and R. B. Ingalls, "A High-Resolution Pulse Radiolysis Apparatus – Some Initial Studies with Systems of Biological Interest," Rad. Research, 31, 581 (1967)

4. R. A. Holroyd, "The Reaction of Nitrous Oxide with Excited Molecules in the Radiolysis and Photolysis of Liquid Alkanes," J. Phys. Chem., 72, 759 (1968)

5. J. Y. Yang, F. M. Servedio and R. A. Holroyd, "Photolysis of Liquid Cyclohexane and Cyclohexane Solutions in the Vacuum Ultraviolet," J. Chem. Phys., 48, 1331 (1968)

The following papers have been accepted for publication.

6. R. A. Holroyd, "Radical Yields in the Radiolysis of Hydrocarbons," a review to be published in Aspects of Hydrocarbon Radiolysis by Academic Press

7. R. A. Holroyd, "Radiolysis of Organic Liquids," a review to be published in Fundamental Processes in Radiation Chemistry by Wiley

8. R. A. Holroyd, "The Reaction of Nitrous Oxide with Excited Molecules in the Radiolysis and Photolysis of Liquid Alkanes," to be published in the Advances in Chemistry series

The following paper was presented.

9. R. A. Holroyd, "The Reaction of Nitrous Oxide with Excited Molecules in the Radiolysis and Photolysis of Liquid Alkanes," Am. Chem. Soc. Meeting, San Francisco, April 1968

B. REACTION OF NITROUS OXIDE WITH MOLECULES

In the 1470 Å photolysis of cyclohexane, nitrous-oxide solutions, it was found that nitrous oxide reacts with excited cyclohexane molecules to form nitrogen and oxygen atoms. The reaction of N_2O with photo-excited 2,2,4-trimethylpentane molecules is much less efficient that with cyclohexane. In the radiolysis of these solutions, $G(N)_2$ is the same for different alkanes at low ($\leq$5mM) N_2O concentrations. At higher concentrations, $G(N)_2$ from the radiolysis of cyclohexane is greater than $G(N)_2$ from the radiolysis of 2,2,4-trimethylpentane solutions. The N_2 yields from 2,2,4-trimethylpentane are in excellent agreement with the theoretical yields of electrons expected to be scavenged by N_2O. The yield of N_2 in the radiolysis of cyclohexane which is in excess of that due to electrons is attributed to energy transfer from excited cyclohexane molecules to nitrous oxide:

$$C_6H_{12}^* + N_2O \rightarrow C_6H_{12} + N_2 + O \quad .$$

A preliminary report of this has been published and a complete report has been accepted for publication.

C. PHOTOLYSIS OF HYDROCARBONS AT 1470 Å, EFFECT OF QUENCHERS

The effect of solutes such as carbon tetrachloride and carbon dioxide on the photolysis of hydrocarbons is being investigated. These solutes are used in radiation chemical studies and are considered to be electron scavengers. The purpose of this study is to determine if they behave like nitrous oxide and also quench excited cyclohexane molecules. Carbon dioxide does not affect the yield

of H_2 in the photolysis of cyclopentane but does reduce $\phi(H_2)$ from cyclohexane by quenching excited molecules. Carbon tetrachloride also quenches excited molecules and is even more effective in this respect than either nitrous oxide or carbon dioxide.

D. PHOTOLYSIS OF LIQUID n-PENTANE, 2,2-DIMETHYLBUTANE AND 2,2,4-TRIMETHYLPENTANE AT 1470 Å

Several alkanes were photolyzed in the liquid phase at 1470 Å in order to determine the modes of decomposition of excited molecules. The most important primary processes in the photolysis of 2,2,4-trimethylpentane are alkane elimination reactions. Radicals also arise from homolytic cleavage of carbon-carbon bonds; butyl, methyl, and heptyl radicals are the most important. In the photolysis of 2,2-dimethylbutane, alkane eliminations of methane and ethane occur, and alkyl radicals are also formed. In n-pentane, the principal primary process is H_2-elimination and the most important radical formation process is a split into H and C_5H_{11}.

The role of excited molecules in the radiolysis of alkanes is evaluated in light of these photolysis results. The fragmentation of the parent alkane molecule into smaller radicals is shown to be similar in photolysis and radiolysis. The major products of the photolysis, which are molecular, are also found as major products in the radiolysis of these alkanes. Decomposition of excited molecules provides an explanation for the formation of isomerized radicals, such as isopropyl in the radiolysis of n-pentane. A major difference is that radical formation is much more important in radiolysis than in the 1470Å photolysis of alkanes. This work is complete and a report is being prepared.

E. RADIOLYSIS AND PHOTOLYSIS OF TETRAHYDROFURAN

The radiolysis of substituted tetrahydrofuran compounds is of biochemical interest since the backbone of DNA consists of substituted tetrahydrofuran rings and phosphate groups. It has been shown that radiation ruptures the tetrahydrofuran ring and smaller molecules are formed; $G(C_3H_6) = 1.0$ and $G(C_2H_4) = 0.5$. The role of excited molecules in this radiolysis is being evaluated by studying the 1470 Å photolysis of the liquid. The following primary processes have been identified:

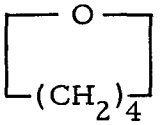

$$+ h\upsilon \rightarrow C_3H_6 + CH_2O, \quad \phi = 0.2$$
$$\rightarrow C_2H_4 + CH_3CHO, \quad \phi = 0.1$$

The same ring cleavage reactions occur in the photolysis and the ratio $(C_3H_6)/(C_2H_4)$ is two in both cases. Thus, ring cleavage in radiolysis can be attributed to excitation processes. Additional studies of substituted compounds are underway.

F. PULSE RADIOLYSIS

The pulse radiolysis of some aromatic compounds is being investigated. Transients produced by the pulses are detected on the nanosecond time scale. For the compounds under study, absorption and emission spectra are already known for anticipated transients such as excited states and aromatic ions. The main purpose of this study is to investigate the mechanism of triplet excitation in liquids.

1. Naphthalene

In molten naphthalene, the excited singlet was detected by its fluorescence. Also, a transient absorbing between 450 and 600 mμ was identified as the singlet since its lifetime correlated with the lifetime of the fluorescence. The lifetime of the singlet is 32 ns at 100°C and 21 ns at 175°C; these values are much less than the lifetime of the naphthalene singlet in solution (70 ns). These facts and the observed fluorescence spectrum demonstrate that the excited singlet is largely in the excited dimer, or excimer, form.

The excited triplet state was detected by absorption spectroscopy. It absorbs in the blue with peaks at 390 and 415 mμ. G(triplets) is 2.6 independent of temperature based on $\epsilon_{415} = 1.4 \times 10^4$. This yield of triplets is present at the end on a 10-ns pulse, and there is no further grow-in of triplets that can be associated with intersystem crossing. Delayed fluorescence was also observed, indicating that triplet-triplet annihilation, $T^* + T^* \rightarrow S^* + S^\circ$, also occurs.

2. Biphenyl

In the pulse radiolysis of molten biphenyl, the excited singlet state, as detected by its fluorescence, is present as an excited monomer at 200°C; its

lifetime is 31 ns. At 100°C, some excimer is present which decays with a 12-ns halflife.

The transient absorption spectrum shows peaks at 390 and 410 mμ. The former is associated with the triplet state and the latter with ions. Both species are present at the end of a 10-ns pulse and there is no grow-in of the triplet absorption during the fluorescence decay. There is also an absorption at 575 mμ. If this is assumed to be due to ions, there is no fast decay of ions between 10 and 100 ns that can be associated with spur recombination.

3. Benzophenone

The pulse radiolysis of benzophenone was studied at 30°C, since this compound is readily supercooled (m.p. = 48°C). No fluorescence was observed, but the transient triplet state was identified by its absorption spectrum. G(triplets) is 2.6, assuming $\epsilon_{540} = 1.1 \times 10^4$. The excited triplets are present at this yield immediately after a 2-ns pulse and there is no fast decay that can be attributed to spur effects. With anthracene present as a solute, triplet-triplet transfer from benzophenone to anthracene is observed.

Further work on the pulse radiolysis of these and related systems is planned.

G. REACTION OF HYDROGEN ATOMS WITH ORGANIC ACIDS

A new and much faster technique of sample preparation has been devised for studying H-atom reactions. Samples are in the form of porous powder plugs which are prepared by packing a mixture of the powder and quartz wool in a quartz tube. The resolution in the ESR spectra obtained with these powder plugs is superior to that obtained with fluff samples.

A study of the reactions of hydrogen atoms with amino acids and other organic acids has been initiated. Electron spin resonance is used to identify the radicals formed; the relative rates of reaction at various sites will be determined. The results show that hydrogen atoms abstract tertiary and secondary hydrogen atoms from the side chains in leucine, isoleucine, valine, arginnine, and lysine and add to benzine rings in phenylalanine and tyrosine. The alpha hydrogen position in amino acids is unreactive; specifically, the rate constant for abstraction of the alpha hydrogen is $<6 \times 10^6$ M^{-1}-sec^{-1}.

An unusual result was obtained with leucine in that the ESR spectra of the radical formed depended on the method of preparation of the leucine sample. This was shown to be a crystal structure effect. It was found that leucine exists in two crystalline modifications; and although the same radical if formed in both by H-atoms, the ESR spectra are different because of a different molecular orientation in the two crystals. This work is continuing.

III. EVALUATION OF EFFORT DURING FISCAL 1968

In the pulse radiolysis studies of aromatic liquids, excited states have been detected without the necessity of scavenger solutes. It is shown that triplets states are formed in high yield by direct excitation or ionic processes rather than by intersystem crossing from the singlet state. This study is providing a good deal of insight into mechanisms of excitation and energy transfer in radiolysis.

The vacuum ultraviolet studies have shown that nitrous oxide, carbon dioxide, and carbon tetrachloride quench excited cyclohexane molecules. Also, the decomposition of excited molecules can account for many of the molecular and radical products formed in the radiolysis of alkanes, and for ring cleavage in the radiolysis of tetrahydrofuran. Kinetic rate data have been obtained on the reactions of hydrogen atoms and it has been shown that hydrogen atoms react preferentially at specific sties on amino acids.

Program: Physical Research Program			
AEC Task: 17, Electronic Structure of Metals and Alloys			
Project Manager: R. G. Breckenridge			
Reporting Period: Fiscal Year 1968			
General Order: 7713	Subaccount: 54010	AEC Category: 05-06-02-00.0	

Principal Scientists: R. G. Breckenridge, L. J. Barnes, H. J. Fink, and W. J. Tomasch

I. PROJECT OBJECTIVES

This effort is devoted to the acquisition of knowledge regarding the electronic structure of metals and alloys (configuration of electronic energy states in momentum space) and the role of this structure in determining electrical, thermal, magnetic, vibrational, and alloying characteristics. Detailed information on the shape of the Fermi surface is provided by de Haas-van Alphen studies in magnetic fields up to 200 kilogauss, and the density of electronic states at the Fermi level is deduced from low-temperature specific heat measurements. The latter also yield information on lattice vibrational modes and on the interactions involved in superconductivity and magnetic interactions is accomplished by means of conventional magnetic susceptibility techniques. Considerable effort is devoted to the exploration of high-field superconductivity with emphasis on thermodynamic and transport characteristics, and on the electron energy spectrum as deduced from thin-film electron-tunneling measurements. These experimental investigations are correlated with current theory, and attempts are made to characterize quantitatively the relationship between superconductivity and the normal-state electronic structure.

II. TECHNICAL PROGRESS DURING FISCAL YEAR 1968

A. PUBLICATIONS

1. A. S. Joseph, W. J. Tomasch, and H. J. Fink, "Intrinsic Size Effects in Type II Superconducting Films," Phys. Rev. 157, 315 (1967)

2. H. J. Fink, "Low Frequency Permeabilities of a Superconductor Due to Surface Currents," Phys. Rev. 161, 417 (1967)

3. H. J. Fink, "Low Frequency Losses of a Type II Superconductor Due to Persistent Surface Currents," Proc. of the XII International Conference of Refrigeration (1967), Paper 1.25

4. H. J. Fink and R. D. Kessinger, "The Exact κ and Field Dependence of the Magnetic Field Penetration of the Meissner State," Phys. Letters 25A, 241 (1967)

5. H. J. Fink, "New Metastable Solutions of the Ginzberg-Landau Equations," Phys. Letters 25A, 357 (1967)

6. H. J. Fink and A. G. Presson, "Superheating of the Meissner State and the Giant Vortex State of a Cylinder of Finite Extent," Phys. Rev. 168, 399 (1968)

7. A. G. Presson and H. J. Fink, "Analog Relaxation Solution of the Non-Linear Ginzburg-Landau Equations," submitted to Symposium International sur le Calcul Analogique et Hybride Applique a l'energie Nucleaire

8. W. J. Tomasch, "Tunneling from In Films with Superconductive and Ferromagnetic Overlays," Phys. Letters 26A, 379 (1968)

9. W. J. Tomasch, "Calculation of Conductance Structure for Tunneling Between Superconductors," Bull. Am. Phys. Soc., 13, 475 (1968)

10. W. J. Tomasch, "Geometrical Resonances in the Tunneling Characteristics of Thick Superconducting Films," Proceedings of the Advanced Study Institute on Tunneling Phenomena in Solids (Riso, Denmark, 1967)

B. TECHNICAL PROGRESS DURING FISCAL YEAR 1968

1. Superheating of the Meissner State and the Giant Vortex State of A Cylinder of Finite Extent, H. J. Fink and A. G. Presson

By magnetic superheating of a superconductor, one usually means that as the magnetic field is increased, the total energy of the specimen is increased beyond that of the normal state while the specimen is still superconducting, so that the nucleation of the normal state is delayed. Early experiments and theories on Type-I superconductors met with little success in demonstrating this effect reliably, and the first serious theoretical treatment of superheating was given by Ginzburg, who has solved the Ginzburg-Landau(GL) equations for

a semi-infite half-space. Others have followed the same approach or similar ones. Essentially, it was found that flux can be delayed from entering the Meissner state beyond H_c for a Type-I superconductor; beyond H_{c1}, for a Type-II superconductor; that the maximum superheating field $H_{sh} = H_c$ for $\kappa \to \infty$; and that for $\kappa \to 0$, the value of $H_{sh} \to \infty$. For example, for $\kappa = 1$, the value of $H_{sh}/H_c = 1.27$; and for $\kappa = 0.3$, it is 1.81, which means that large superheating effects should have a good chance of being observable. A recent calculation of the superheating field of a cylinder with $\kappa = 0.5$ and $R/\lambda = 14.4$ (R = radius of cylinder, λ = low field penetration depth) is in agreement with that of the semi-infinite half-space. However, Galaiko has calculated that the superheated Meissner state of a bulk specimen is stable up to approximately 0.8 H_c when $\kappa \gg 1$, and Takacs finds that flux can be delayed from entering the Meissner state of a semi-infinite half-space with $\kappa \gg 1$ up to approximately 0.5 H_c. It was shown experimentally that flux can easily be delayed from entering Type-II specimens for applied magnetic fields $H_o > H_{c1}$; and that for materials with κ values of about 3.6, the maximum experimentally observed field for flux delay beyond H_{c1} is in the close neighborhood of H_c. Other experimenters, who have worked with small Type-I spheres, with bulk Type-II superconductors with κ values of about unity, and with thin Type-I cylinders seem to get fair agreement with the above theory.

We have already calculated the maximum superheating fields for a slab of finite thickness 2L as a function of κ and L/λ. This calculation is based on a method employed in computing the giant vortex state and is different from that of Marcus, who has also computed the superheating field of a slab of finite thickness, though over a very limited range of parameters κ and L/λ.

Here we have calculated, for a very long cylinder of radius R, the size-dependent critical field H_s of the Meissner state, the maximum superheating field H_{sh} of the Meissner state, and the superheating field of the giant vortex state for κ values between 0.3 and 2.4, and size parameters R/λ between 2.5 and 20.

2. New Metastable Solutions of the Ginzburg-Landau Equations, H. J. Fink

We have found new one-dimensional surface solutions of the Ginzburg-Landau Equations which could possibly exist as metastable solutions in a Type I

superconductor or as stable solutions surrounding the mixed state of a Type II superconductor. They are solutions essentially similar to the surface sheath but of a periodic nature with critical fields to smaller than H_{c3}. Thus, they would be favored in small magnetic fields, namely below H_{c2}.

3. The Stability Limit of the Superheated Meissner State, H. J. Fink

We have previously calculated the maximum critical field when the Meissner state is superheated magnetically. In these calculations, the critical fluctuations which always occur in nature were disregarded. They, however, should give rise to a lowering of the superheating field; the latter is strongly dependent on the material parameter κ. We have investigated theoretical two-dimensional fluctuations in the order parameter and the vector potential, but machine calculations of these important critical field value has not been completed.

4. Analog Relaxation Solution of the Nonlinear Ginzburg-Landau Equations, A. G. Presson and H. J. Fink

Boundary value solutions of the nonlinear Ginzburg-Landau equations have been obtained on the analog computer for both cylindrical and slab geometry. A relaxation technique was used to solve the sensitive two-point boundary problem. Parametric studies were made for the transition between the superconducting and normal state in a continuous manner for a fixed number of fluxoids when the applied magnetic field was used as an independently acting variable. The relaxation technique was automated on the computer to obtain a continuous input-output operation which was controlled by the applied magnetic field. Current, energy, order parameter, and other variables of interest were computed as a function of the applied magnetic field while the latter was varied continuously.

5. Superconducting Point Contacts, L. J. Barnes

The primary objective of this task has been to investigate the electrical conductance of superconducting point contacts and in particular to study tunneling phenomena. It is hoped, and there is now considerable supporting evidence, that point contact tunneling will become as useful a tool in the study of alloy superconductivity as thin film diodes have proved to be in the study of elemental superconductors.

The first efforts were focused on point contacts where there was actual metal-metal contact. Their behavior was interesting; however, in general, it was extremely complicated. At first, measurements were made only of the critical current of such contacts, but it quickly became apparent that the current-voltage (I-V) characteristics might prove more interesting and informative. The behavior of these point contacts can in general be characterized by that of the so called "weak links." Such weak links are formed by connecting two bulk superconductors together by an extremely thin oxide layer ($\sim$20Å) or by very small metallic links. When such an oxide layer is thin enough, one can obtain tunneling of superconducting electron pairs (so called Josephson tunneling), the oxide layer acting in this case as a superconducting metallic link. The ability of a weak link to carry a lossless current (with zero voltage) is quenched rather easily by a suitably large transport current. Once a voltage (V) is established across such a device (where $eV < \Delta_1 + \Delta_2$, Δ_1 and Δ_2 being half energy gaps of the two superconductors involved), a superconducting AC current is generated with a frequency $\upsilon = \frac{2eV}{h}$. The weak link is highly nonlinear and can radiate at the harmonics and subharmonics as well as the fundamental. We observed what was apparently self-detection of its own radiation by some of the point contacts. Owing, no doubt, to the strong nonlinear behavior of the relatively strong coupling of the metal-metal contacts, the I-V characteristics were unusually complicated. It seemed possible to use the weak link behavior to study the materials of the contacts rather than the weak link phenomena themselves; consequently, a more simple situation was desired.

As a more suitable device evolved for "making" and "breaking" the point contacts in the liquid helium bath, it became apparent that tunneling behavior could be obtained with very gentle contact. This tunneling behavior represented a simple and better understood phenomenon than was dealt with at first. It also became apparent that the behavior of the point contact could be to some extent varied between pure tunneling, exactly as in superconducting thin film diodes, to the behavior characteristic of metallic shorts.

One immediately thinks of using the point contact tunneling to determine the energy gaps of various superconducting alloys just as one uses tunnel diodes to investigate elemental superconductors. Many superconducting alloys are very difficult to fabricate into thin film diodes and quite often are not even superconducting

when it is achieved. It appears that in many cases, point contacts will offer the best method of determining the energy gaps of many alloys.

Some work is yet to be done before the point contact tunneling method can be used with reasonable assurance. Quite often after different "break" and "make's," slightly different gaps are measured. The conjecture is that this represents the well known anisotropy of the gap due to crystalline anisotropy; this anisotropy should not be present in many alloys.

Another interesting aspect of the point contact tunneling concerns the probable observation of multiple particle and photon assisted tunneling. The photon assisted tunneling in our case is also a weak-link phenomenon. The contact can radiate photons (due to the AC supercurrent) which in turn can be absorbed into the junction aiding the tunneling of electrons. This has been predicted to give structure at subharmonics of the energy gap frequency $\nu = \frac{2\Delta}{h}$. We have observed such subharmonic structure in the dynamic conductance of various contacts, although it is not in full agreement with various theories. The multiparticle tunneling involves two or more electrons tunneling simultaneously. This also leads to structure in the I-V characteristics below the energy gap, some of which has rather unambiguously been identified. These are interesting phenomena in themselves, and they also can serve to determine the energy gaps involved.

Recently we have studied some alloy thin film diodes which exhibit quite similar behavior to the point contacts although the observed structure is somewhat better defined in the thin film case. This may prove to be a useful way of characterizing the point contact tunneling.

The task before us involves clearing up (if possible) the ambiguities involved in determining the energy gaps of alloys from point contact tunneling data. We have, in the process of developing the experimental techniques, measured the energy gaps of Nb, Nb + 50% Ta, Ta, Nb + 5% Ti, Pb, and Pb-Ti alloys, and our values are in good agreement where they can be compared with thin film data.

6. Electronic Tunneling from Superconductors, W. J. Tomasch

Film diode structure utilized in the tunneling program have invariably employed a 20 to 40 Å layer of natural aluminum oxide as the tunnel barrier.

This limits one to diodes of the form Al-AlO_x - S, where S is the superconductor under study. For reasons of sensitivity, the Al must also be superconducting during the course of an experiment. This limits one to the temperature range 1.05 to 1.35 °K, the higher figure being the transition temperature of Al, the lower being the limit of our current cryogenic capability. Investigations of intrinsic temperature effects are impossible under these circumstances. This is one reason for the attractiveness of diodes having the form Pb-PbO_x - S; (another reason involves the ability to obtain Josephson junctions of high quality). Unfortunately, natural Pb-oxide layers tend to have isolated defects which subsequently cause short circuits. In order to obtain an acceptable yield ratio, the active junction area must be made quite small, on the order of 5×10^{-4} cm^2 as compared with 10^{-2} cm^2 for Al based diodes. In view of these considerations, photoetched evaporation masks have been prepared and used in successful attempts to produce acceptable diodes. Junctions having approximate dimensions 10 mils x 10 mils have displayed tunneling resistances in the range 0.1 to 1.0 ohm. These units display Josephson tunneling characteristics at low current levels.

As reported previously, a computer program has been compiled for the purpose of synthesizing diode characteristics corresponding to tunneling between two superconductors, one of which has had a model perturbation added to its density of states. Preliminary calculations employing this program have already materially aided our understanding of the transformation of density of states structure into differential conductance structure. In particular, it has been found that the percentage effect in the differential conductance can exceed that in the density of states by as much as a factor of six at very low temperatures. Such a magnification effect came as something of a surprise since it has no counterpart in the more familiar case of tunneling between a normal metal and superconductor, the latter having a structured density of states. Subsequent analytical investigations have demonstrated that a degree of magnification is indeed to be anticipated, although quantitative results can not be obtained analytically owing to the general intractability of the problem, forcing one to rely on computer calculations. Tentatively, it appears that the degree of magnification decreases significantly as thermal smearing is introduced; i.e., as the temperature is raised. Hence, it appears that relatively detailed calculations are

required for intercomparison with experimental results. Although the original program has been adequate for illuminating certain general features of the transformation from density of states structure to differential conductance structure, it is not adequate for the task of making sufficiently detailed calculations. Furthermore, it tends to be relatively inefficient, increasing execution times and costs. For these reasons, a new program free of such criticism is being compiled. Trial runs with unperturbed density of states functions have yielded most encouraging results. The major accomplishment of the computer calculation effort to date is a general downward revision of the density of states perturbation amplitudes necessary to account for the magnitude of experimentally observed structure.

As indicated above, two programs have been written for the simulation of geometrical resonance structure. The first of these computes I(V) by evaluation of an integral, and then generates the conductance dI/dV from this result via the finite difference approximation. Due to poles in the integrand at the limits of integration, this method is incapable of dealing with the interesting bias region corresponding to the gap-edge. Also, noise limitations inherent in the finite difference method preclude calculation of higher derivatives. To avoid these limitations, the second program is based on a mathematically transformed version of the original problem, a version in which poles no longer occur in the integrand. Furthermore, the differentiation is accomplished by entirely analytical methods. Although highly satisfactory results have been obtained with this program, the analytical differentiation feature requires a special subroutine for each model perturbation. Furthermore, such subroutines become prohibitively involved for all but the simplest model perturbations. This is a serious limitation in view of the complex perturbations suggested by recent theoretical studies (T. Wolfram, NAR Science Center, to appear in the Physical Review). A third approach which combines the strong points of the two previous programs is currently under study. Again, it would be based on the transformed problem; but instead of a completely analytical approach to differentiation, it would apply the finite difference approximation only to integrands appearing in analytical expressions for derivatives. In principle, the "smoothing" due to subsequent integration would offset the "noise" introduced by the finite difference approximation. If indeed feasible, such a program could comfortably

handle relatively arbitrary perturbations (even tabular, numerical forms) without undue programming complexity.

In a related effort (T. Wolgram) considerable headway has been made on the theory of quasiparticle interference in thick superconducting films, (T. Wolfram, "Tomasch Oscillations in the Density of States of Superconducting Films," to appear in the Phys. Rev. 1968). The mechanisms which give rise to the oscillatory structure in the quasiparticle density of states of superconducting films with spatially varying electron-electron interactions has been sucessfully investigated. It has been shown that observed effects result from processes in which a quasiparticle is condensed into the seal of Copper pairs, leaving behind a different (but energetically degenerate) quasiparticle. The tunneling density of states has been obtained for a composite, two region superconductor. The nature of the density of states structure is found to depend strongly upon the ratio of the energy gaps of the two regions. In the low energy range, bound eigen states characterized by the quantization of the difference of the momenta of the degenerate quasiparticles have been developed for the case of infinite mean free path. Beyond this, explicit results have been presented for the composite film systems (thick film plus thin overlayer film); In-Al and In-Pb, for several values of the electronic mean free path.

Due to the mathematical complexity of Wolfram's analytical results, it is not fruitful to pursue the analytical decompositions required to employ the second program in order to examine the agreement between experiment and theory. It is primarily for this reason that the third program was written, see previous paragraph. Preliminary computer results have been encouraging, although critical comparisons between experimental and theoretical results are not yet available.

Subassembly development and construction activities have continued on the He-3 refrigerator project. Recent efforts have been directed towards demonstrating the effectiveness of a prototype impurity trap (cooled with liquid He-4) which has been fabricated. Design of the electrical system to be used in conjunction with two Ge semiconductor thermometers has also been completed.

III. EVALUATION OF EFFORT DURING FISCAL YEAR 1968

This program has been in a period of shifting emphasis and reorientation but still has maintained a high productivity. The theoretical interest has shifted somewhat from the sheath phase studies and has concentrated more on the details of the stability of the mixed state near the supernormal transition. The Ginzburg-Landau theory is capable of treating these situations but an increasing use is being made of computers to obtain quantitative results.

The task studying the properties of superconducting point contacts has made excellent progress even though the situation is one of considerable complexity. The experimental techniques are being brought under control and there is a growing confidence in the reliability of the results. There is every indication, in fact, that this method will become a major tool for the study of superconductors since it is not restricted to materials that can be made into thin film diodes. During this report period, the film tunneling work has concentrated on the analysis of the Tomasch effect and in detailed interpretation of the experimental results in terms of the density of electronic states. This has required some extensive computer programming but these problems have now been solved and rapid progress is anticipated.

Program:	Physical Research				
AEC Task:	18, Radiation Damage in Crystalline Solids				
Project Manager:	R. G. Breckenridge				
Reporting Period:	Fiscal Year 1968				
General Order:	7714	Subaccount:	54040	AEC Category:	05-06-02-03.0

PRINCIPAL SCIENTISTS: W. Bauer, D. W. Keefer, H. H. Neely, A. Sosin, K. H. Thommen, K. R. Garr, and D. D. Vawter

I. PROJECT OBJECTIVES

The materials requirements of modern technology demand an increased understanding of the effects of lattice defects on the physical properties of crystalline solids, and on their behavior when subjected to various kinds of radiation. Studies of radiation damage in solids not only directly yield information on the effects of radiation, but also provide a means of investigating defects in solids. It is the objective of this project to study the production of defects in crystalline solids by radiation, and to attain an understanding of their structure, their interactions with each other and with impurities and dislocations, their effect on the physical properties of solids, and their recovery kinetics. Comprehension of these points should assist in the understanding of lattice defects produced in solids by other means, and help make possible the development of materials of superior properties as the ability to better control their defect structure is developed. The materials chosen for study are metals, metal alloys, and semiconductors.

II. TECHNICAL PROGRESS DURING FISCAL YEAR 1968

A. PUBLICATIONS WERE AS FOLLOWS

1. A. Sosin and W. Bauer, "Defect Production in Metals by Irradiation at Low Temperatures," Proceedings of the International Conference on Solid State Physics Research with Accelerators, Brookhaven National Laboratory Report BNL 50083, p. 204 (1968)

2. Walter Bauer, "Damage Rate Measurements in Platinum and Other Metals by Electron Irradiation," in Lattice Defects and Their Interactions, edited by R.R. Hasiguti, (Gordon Breach New York), p. 567 (1967)

3. A. Sosin and W. Bauer, "Atomic Displacement Mechanisms in Metals and Semiconductors," to be published in "Studies in Radiation Effects in Solids", 3, edited by G. J. Dienes (Gordon Breach, New York), manuscript approved by editor

4. W. Bauer, A. Sosin and K. R. Garr, "Stage III Recovery of Electron Irradiated Aluminum," Bull. Am. Phys. Soc., 13, 381 (1968)

5. Walter Bauer and A. Sosin, "Recent Threshold Energy and Displacement Cross Section Measurements in Metals," in Radiation Effects (New York, Gordon Breach. 1967, Metallurgical Society Conferences, 37) edited by W. F. Sheely

6. H. H. Neely and D. W. Keefer, "Resistivity Studies of Electron Irradiated Iron," Phys. Stat. Sol. 24, 217 (1967)

7. H. H. Neely, "Recovery of Electron Irradiated Zirconium at Low Temperatures," Can. J. Phys. 46, 321 (1968)

8. H. H. Neely, D. W. Keefer and A. Sosin, "Electron Irradiation and Recovery of Tungsten," accepted for publication in Phys. Stat. Sol.

9. A. Sosin and K. R. Garr, "Clustering in Al-G.P. Zone Alloys After Low Temperature Irradiation," Acta. Met. 15, 1250 (1967)

10. A. Sosin and K. R. Garr, "Recovery of Electron Irradiated Aluminum and Aluminum Alloys I. Stage I," Phys. Rev. 161, 664 (1967)

11. K. R. Garr and A. Sosin, "Recovery of Electron Irradiated Aluminum and Aluminum Alloys II. Stage II," Phys. Rev. 162, 669 (1967)

12. K. R. Garr and A. Sosin, "Recovery of Electron Irradiated Aluminum and Aluminum Alloys III. Stage III," Phys. Rev. 162, 681 (1967)

13. K. Thommen, "Effects of Low Temperature Electron Irradiation on the Electrical Properties of Undoped GaSb," Phys. Rev. 161, 769 (1967)

14. K. Thommen, "Effect of Low Temperature Electron Irradiation on the Electrical Properties of Undoped GaSb," IEEE Transactions on Nuclear Science, NS-14, 40 (1967)

15. K. Thommen, "Energy and Orientation Dependence of Electron Irradiation Induced Damage in Undoped GaSb," Bull. Am. Phys. Soc. 13, 380 (1968)

16. K. Thommen, "Energy and Orientation Dependence of Electron Irradiation Induced Damage in Undoped GaSb," submitted to the Physical Review

17. D. W. Keefer and R. Vitt, "Low Frequency Internal Friction in Electron Irradiated Copper," Acta Met. 15, 1501 (1967)

18. O. Buck, D. W. Keefer, J. Robinson, A. Sosin and H. Wiedersich, "Low Temperature Deformation of Electron Irradiated Aluminum," Acta Met 16, 195 (1968)

19. A. Sosin and D. W. Keefer, "Effects of Irradiation on the Internal Friction, Elastic Moduli and Magnetic After Effects of Metals," Microplasticity (Advances in Materials Research, II), Wiley, New York (1968)

20. D. W. Keefer, J. C. Robinson and A. Sosin, "Modulus Effects in Metals after Low Temperature Electron Irradiation - III. Aluminum," accepted for publication in Acta Metallurgica

21. D. W. Keefer, "Temperature Dependence of Dislocation Pinning in Electron Irradiated Copper," a paper to be presented at the Symposium on the Interactions Between Dislocations and Point Defects, Harwell, July 8-11, 1968 A paper by the same title is being prepared for publication.

B. TECHNICAL PROGRESS DURING FISCAL YEAR 1968

1. Study of the Production and Recovery of Point Defects by Use of Resistivity Measurements

a. Aluminum and Aluminum Alloys, K. R. Garr and A. Sosin

A series of three papers dealing with low temperature recovery have been published in the Physical Review.

STAGE I

The recovery in Stage I of the increase in electrical resistivity due to electron bombardment of aluminum has been examined by using a "ratio-plot" technique. The differences in annealing between two samples with either different preirradiation histories or varying irradiation conditions are emphasized by this technique. By use of samples irradiated to different doses (i.e., different initial defect concentration), the temperature region of non-first-order processes is clearly delineated; this region encompasses free interstitial migration. By use of samples with 0.1 at. % copper or zinc and comparing with pure aluminum, the suppression of recovery by impurity doping is shown to be consistent with previous doping studies.

STAGE II

The recovery of the residual electrical resistivities of pure Al and the Al (nominally 0.1 atom %) alloys Al-Mg, Al-Ga, and Al-Ag has been investigated following 1-MeV electron irradiation near 4°K. The addition of solute atoms caused a suppression of recovery normally observed in Stage I (< 70°K) for pure Al. This suppression amounted to 20-27% of the recovery of the pure sample. The Stage II (70-170°K) recovery of pure Al occurs throughout the whole temperature range. However, well-defined recovery regions were observed between 70 and 90°K and between 120 and 140°K. In the alloy system, the recovery characteristics varied with the particular solute addition. Specifically, Al-Mg showed two distinct substages of recovery in Stage II, centered at 81 and 127°K. Al-Ga showed a doublet (two partially overlapping substages) centered at about 111°K. Al-Ag showed no distinct substages of recovery which could be attributed to the addition of the solute. None of the substage kinetics follow integral reaction orders when analyzed with chemical rate theory, indicating complex annealing processes.

STAGE III

The recovery of the residual electrical resistivities of pure Al and the Al alloys (nominally 0.1 atom % Al-Mg, Al-Ga, and Al-Ag have been investigated following 1-MeV electron irradiation near 4°K. Analysis of the data for nominally pure Al in Stage III (170-300°K) discloses substructure. (A very

small substage occurs at lower temperatures and appears to be influenced by the residual impurities.) The main portion of the stage shows a variation in the observed activation energy with purity: The higher the purity of the "as-received" material, the lower the observed activation energy. A range of 0.46 to 0.59 eV was found for the materials investigated. The effective frequency factor for these materials showed a concurrent systematic variation. These effects are believed to be due to the interaction of migrating defects with residual impurities in the material. The recovery of the alloys in the Stage III region is more complex than in the pure material. There is more substructure in the recovery spectrum of the alloys, and the observed activation energies in Stage III are higher. Al-Ag showed a resistivity decrease followed by an increase which is attributed to the clustering of Ag atoms. The observations are interpreted in terms of interstitial migration, restricted by impurities, in the earlier portion of Stage III; vacancy migration becomes important in the latter portion of Stage III. Stated differently, interstitials migrate in Stage III and vacancies migrate in Stage IV; but in Al, these stages overlap appreciably.

b. Resistivity Recovery in 6-9's Aluminum Near Room Temperature (Stage III-IV), W. Bauer, A. Sosin and K. Garr

Some of the experimental results which bear most directly on the interpretation of the Stage III recovery of 6-9's pure Al have been reported at the Berkeley meeting of the APS. Additional experiments and further analysis has provided information which points toward complex recovery mechanisms in the Stage III-IV region in aluminum. A contributed paper by the first author dealing with these results has been accepted for presentation at the International Conference on Vacancies and Interstitials in Metals at Julich. The abstract is included here.

We have studied the resistivity recovery from 200 to 340°K of 99.9999% pure aluminum foils irradiated near 10°K. In some of the experiments, one of a pair of specimens was prequenched. The prequenched specimen exhibited two distinct recovery peaks, at 245 and 321°K (Stage IV), whereas the unquenched speciment exhibited only one peak at 255°K (Stage III). These results provide direct evidence for interstitial migration in Stage III and

vacancy migration in Stage IV, and are also in good agreement with work by Budin and Lucasson* who irradiated near 80°K. The similarity of the results is significant insofar that the irradiations were carried out below and above the temperature (35-45°K) where long range interstitial migration takes place. The role of interstitial clusters is substantially inhibited in the Budin and Lucasson experiments.

The activation energy, E, of a major portion of the Stage III recovery has been analyzed by the Meechan-Brinkman method to be, E = 0.60 ± 0.08 eV; and, on the basis of second order kinetics, to be E = 0.48 ± 0.05 eV. The former value of E is in good agreement with Budin and Lucasson and the latter with Sosin and Rachal†. It is shown that under certain conditions the assumptions inherent in the second order analysis are not met in these experiments. Thus, the higher value of the activation energy is to be preferred. The reaction kinetics of the Stage III recovery (isochronal and isothermal annealing) were found to be second order when using conventional analysis. However, application of the more sensitive method of Nihoul and Stals§ yielded non-unique reaction kinetics, ranging from above three at the beginning to below two near the end of the state.

c. Continuous Annealing in Stage I, W. Bauer, H. H. Neely and A. Sosin

We have now essentially completed the process of assembling equipment for a novel approach to continuous annealing. This approach involves reading the difference in resistance, ΔV, between an irradiated specimen and a dummy specimen as a function of annealing temperature. If the specimen resistances have been suitably matched prior to the irradiation, readings of ΔV represent essentially the radiation damage recovery and deviations from Mathiessen's Rule. The deviation from Mathiessen's is a slowly varying function of temperature in comparison to the recovery substages in Stage I. Therefore, one can identify the number and relative height of the substages, but not the absolute height and therefore absolute amount of recovery. The number of recovery substages in Stage I region, especially of copper, is of immediate interest due to the bearing on the recovery models.

*C. Budin and P. Lucasson, Interaction of Radiation with Solids (Plenum Press, 1967)
†A. Sosin and L. H. Rachal, Phys. Rev. 130, 2238 (1963)
§J. Nihoul and L. Stals, Phys. Stat. Sol. 17, 295 (1966)

The experimental approach to the measurement of ΔV as a function of time (temperature at constant heat up rate) involves an entirely electronic display, digital voltmeter coupled to a punched tape. The system which is now assembled allows several readings per second. This speed, in combination with an optimized heat up rate results in a resistance reading every 0.05°K temperature annealing interval. This is approximately five times better than can be achieved by conventional isochronal methods.

The cryostat to be used for the continuous annealing experiments is the same one that is being used currently for the aluminum experiments. The latter experiments are nearly completed. We expect to start the continuous annealing experiments shortly.

d. Point Defect Studies of Nickel, W. Bauer and W. F. Goeppinger

We have completed the experimental portion of the damage production and recovery in nickel. These results are analyzed currently. A few observations may be made: (1) the long range or uncorrelated migration of an interstitial defect occurs near 62 -65°K and (2) the effect of residual impurities near and above 60°K is pronounced. It is felt that this is due primarily to higher residual impurity concentrations.

e. Resistivity Recovery of Polycrystalline Iron, H. Neely and D.Keefer

A paper entitled "Resistivity Studies of Electron Irradiated Iron" has been completed on the work previously reported, and published in Physica Status Solid; the abstract follows.

"Ischronal annealing studies of 1.3 MeV electron irradiated iron have been performed. Results indicate long range interstitial migration occurs in resistivity annealing Substate I_E (120 - 150°K).

The conclusions reached in this study are listed below:

a. The recovery spectrum of polycrystalline iron is qualitatively the same as many fcc metals after electron irradiation.

b. Stage I consists of six principal substages, lies between 33 and and 150°K. The substages are centered at 39, 51, 66, 87, 100 and (typically) 128°K.

c. Stage II consists of two substages which are centered at 165 and 223°K and account for about 9% of the total recovery.

d. Stage III is centered at 340°K and accounts for only 2% of the total recovery.

e. Studies of recovery after irradiation doping and concentration dependence irradiations strongly suggest long range migration of interstitials in substage I_E (128°K).

Recent results after irradiation of iron wires that had been doped with increasing amounts of carbon show a suppression of Stage I recovery. This suppression of Stage I has been seen by other investigators after doping fcc materials. However, the suppression in iron seems to be only in Substage I_E. The difference may be that carbon is an interstitial impurity whereas the other dopants were substitutional. This effect has been checked by precipitating the sample for long times at low temperatures, taking the carbon from solution then reirradiating. The recovery was enhanced by about 5% although all of the carbon was not precipitated in the sample."

f. Recovery of Electron Irradiated Zirconium, H. H. Neely

The preliminary study of electron irradiated zirconium is completed and the manuscript is written. The manuscript has been published in the Canadian Journal of Physics; following is the abstract.

"The low-temperature recovery of the electrical resistivity of polycrystalline zirconium was measured after electron irradiation below 8°K. The material used in this irradiation was the same low oxygen material (0.015 atom %) used by Swanson to study recovery after deformation at 4.2°K. Substage I_B was found to be only of the order of 4% of the irradiation-induced resistivity change, compared to ~ 6% observed by Swanson after deformation. Stage I (4.2 to 160°K) in Zr contains six substages while Stage II (160 to 310°) contains only one substage after electron irradiation. While no study of kinetics was made, it seems likely that close pair annihilation processes are responsible for the recovery spectrum below 118°K and that longer range defect migration occurs in the neighborhood of 140°K."

g. Recovery of Irradiated Tungsten, H. H. Neely, D. W. Keefer and A. Sosin

The preliminary investigation of electron-irradiated tungsten is completed and the manuscript has been written. The manuscript has been accepted for publication in Physica Status Solid; following is the abstract.

"Electron Irradiation and Recovery of Tungsten - Damage rates and recovery of 99.99% pure tungsten have been investigated after electron irradiation near 4°K by means of electrical resistivity. The damage rate data though not corrected tend to a value of T_o = 38 to 42 eV. The recovery of the residual electrical resistivity shows three major stages; Stage I from 4.2 to 100°K; Stage II from 100 to 500°K, Stage III from 500 to 1000°K. Stage I is dominated by only one major peak at 70°K; this peak was analyzed assuming first and second order kinetics. The first order process did not fit a straight line in the activation energy analysis. The second order plot fit a straight line for over two decades of data, yielding an energy of 0.17 eV. This data is convincing evidence that the 70° peak is due to a process in which considerable interstitial migration is involved. Since only ~ 26% recovery is seen in Stage I we propose that the suppression is due to interstitial trapping with impurities. Other models were investigated. Stage II seems to be due to release from impurity traps as seen in other materials. Stage III accounts for about 40% of the induced resistivity recovery and has a center temperature of 760°K. The stage was analyzed assuming second order kinetics, this analysis gave an energy of 1.1 eV."

h. Defect Production in Metals by Irradiations at Low Temperatures, A. Sosin and W. Bauer

An invited review paper for the International Conference on Solid State Physics Research with Accelerators, at Brookhaven, September 24, was prepared. Following is the introduction of that paper.

"Radiation damage studies are frequently divided into two areas: The production of defects during irradiation and the characteristics and disposition of these defects subsequent to their creation. The latter area has received the lion's share of attention in the past, fueled by a disagreement

among investigators concerning the nature of the observed annealing stages. Production aspects, the topic of this paper, are acquiring more prominence in recent times, however. It is the purpose of this paper to review the trends in this area, providing some evaluation of these trends and predictions as to the directions future effort may be expected to take.

A complete description of defect production requires consideration of bombardment by a variety of particles — neutrons, positive ions, electrons, gammas — over a wide range of temperatures. Space does not allow such completeness here. Furthermore, the most notable progress in recent times has been made in the simplest case: electron bombardment at low temperatures. Accordingly, we shall emphasize these results. Fortunately, the progress made in this simpler case will certainly reflect itself in the description of defect production under more complex conditions, a description which we anticipate will be forthcoming in the future.

An early experimental survey of defect production, using electron irradiation at low temperatures, was made by Lucasson and Walker. Subsequent work with greater experimental accuracy and purer materials has pointed toward increased complexity in interpretation over the original description; we shall indicate the nature of these complexities. In addition, whereas most of the earlier work has been carried out on polycrystalline materials, results obtained using single crystals have appeared lately in the literature. The use of single crystals represents a refinement in technique -- a refinement which, in retrospect, may appear to have been tardy in arriving. But we shall see that the difficulties in applying this refinement are imposing.

In the discussion of such results we shall be mainly concerned with low energy (< 3 MeV), low dose (< 10^{-4} fractional defect concentration) electron irradiation experiments and their interpretations. We shall, later in this paper, turn to the results of higher energy bombardment (generally using other forms of irradiation than electron irradiation) and to additional phenomena which give further insight into both the nature of defect production and defect characteristics. Among these phenomena are saturation defects (i.e., high dose effects) and the influence of residual defects on damage production.

It is clear, then, that the results with which we will be concerned are intimately associated with accelerators and their usage. The importance

of accelerators in the exploration of defect characteristics in metals is underlined, for example, by the recent proliferation of electron irradiation centers, particularly in the United States and Europe."

Stimulated by the above review article an extensive review article on "Atomic Displacement Mechanisms in Metals and Semiconductors" has been prepared for the series, "Studies in Radiation Effects in Solids," edited by G. J. Dienes.

i. Displacement Processes in Iron Whiskers, W. Bauer and W. F. Goeppinger

Damage rate measurements as a function of energy and orientation are continuing. Although a considerable body of data has been obtained it is difficult to draw any detailed conclusions from the data without further experiments. The reason for this is inherent in the small voltage increases observed upon irradiation at near threshold energies. Many factors contribute to this limitation some of which have been only recently recognized:

1) The value of the measuring current is limited by self-induced changes in the domain structure, as reflected by irreproducible magnetoresistance.

2) We have also observed resistance changes due to differing orientation of the whiskers with respect to the earth's magnetic field.

3) The geometrical factor of the thinnest whiskers is unfavorable since the irradiated length is usually only a few mm.

Despite these severe limitations, progress is being made in this very interesting and important problem. We also plan to irradiate recently obtained copper whiskers in order to eliminate the first two of the above mentioned limitations.

j. Directional Effects in Electron-Irradiated Gold, W. Bauer, A. Sosin and W. F. Goeppinger

A note describing this work has been submitted for publication. Some of the results are discussed below:

1) It is felt that $T_d(110) \approx T_o \simeq 36$ eV, where T_o is the minimum threshold displacement energy measured in the polycrystalline sample.

2) The onset of damage in the ⟨111⟩ sample was also observed near 36 eV but may heavily reflect glancing collisions.

3) These results are in good agreement with the predictions of Andersen and Sigmund, who using a Born-Mayer potential based on experimental T_o values predicted T_d (110) = 41 eV and T_d (100) - 36 eV.

2. Mechanical Property Studies

a. Modulus Changes at Low Temperatures, Dislocation Pinning in Metals - D. W. Keefer and J. C. Robinson

An examination of the effect of temperature on dislocation pinning in copper during electron irradiation is virtually complete. In this study, two types of experiment have been carried out: (1) "direct procedure," in which irradiation at 90, 125, 150, or 175°K is followed by measurement of the resonant frequency and damping at 77 and/or 4.2°K, and (2) "alternate procedure" in which irradiation is performed at 77°K followed by annealing at 90, 125, or 150°K, and measurements at 77 and/or 4.2°K. (3) Following both the direct and alternate procedures, at-temperture measurements of the frequency and decrement between 4.2 and 150°K were made. In all cases, the electron flux has been kept at the low value of 2.5×10^{12} electrons/cm^2-sec, and the number of pinners per initial dislocation loop length has always been below 1.0 at the end of a complete experiment. The principal results observed are as follows. (1) If the alternate procedure is carried out at 90, 125, or 150°K; the amount of dislocation pinning for a given electron dose, as detected at 77°K, is slightly less than that obtained during only irradiation at 77°K. This reduction is due to some thermally activated rearrangement of interstitial pinners on dislocation during the anneals. Similar results have been observed previously in our isochronal annealing work. (2) During an alternate procedure, if measurements are made at 4.2°K, we find that an anneal at 125 or 150°K leads to an increase in the number of dislocation pinners. This is the reverse to the effect seen at 77°K, and is taken as evidence that different portions of the dislocation population are being used as point defect monitors at 77 and 4.2°K. If, after the introduction of a small number of pinners via the alternate procedure, we switch immediately to the direct procedure, using 90, 125, or 150°K as the

irradiation temperature, the change in number of pinning points falls on an extrapolation of the data obtained during the alternate procedure for the particular temperature. At this point, therefore, the two procedures are equivalent. If however, the alternate procedure is now readopted, using either 125 or 150°K, but not 90°K as the annealing temperature, two effects are observed when measurements are made at 77°K: (a) the number of pinning points added during the first irradiation at 77°K is considerably higher than that obtained, at the same defect concentration, in a sample which has only been irradiated at 77°K and never annealed, and (b) the number of pinners added per unit electron dose during the remainder of this alternate procedure is higher than that obtained during the previous alternate procedure. At-temperature measurements show that this enhanced pinning can only be observed at measuring temperatures between 40 and 150°K. It is precisely over this temperature range that a Bordoni peak occurs in the samples, and the enhanced pinning effects have been found to be related to the dislocations responsible for this peak. The model for the effects is based on the presence of two dislocation components. As has been discussed previously, these components are characterized primarily by the ease with which the contributing dislocations are pinned during irradiation and are referred to as the "soft" and "hard" components because of this. In the present work, we find that the soft dislocations which contribute to the Bordoni peak allow some mobility of point defects along them, while the hard dislocations apparently do not. Annealing in the course of an alternate procedure thus results in an unexpected enhancement of the frequency defect of the soft component and leads to the enhanced pinning rate upon a subsequent irradiation. The fact that a similar effect does not occur on the soft dislocations which cosntribute to the frequency defect below 40°K is believed to be evidence that these dislocations contain large numbers of geometrical kinks. These kinks, although mobile under stress at very low temperatures, may severely restrict the migration of point defects down dislocation lines.

b. Dislocation Pinning in Silver

A study of dislocation pinning in electron irradiated silver has recently been initiated. A sample has been irradiated at 4.2°K with 1.5 MeV electrons to a dose of 1.125×10^{16} e/cm^2. A detailed isochronal annealing study between 4.2 and 680°K has revealed the presence of several pinning stages.

The first of these begins at 30°K and is complete by 50°K. This is followed by a temperature interval of some 150°K over which three contiguous stages occur. Between 290 and 340°K, a slight amount of unpinning occurs. This is followed by the final pinning stage between 340 and 410°K. The wide temperature interval between this stage and its predecessors is an unusual result and will allow us to study the stage in some detail. The final release of pinning points from dislocations occurs between 420 and 680°K. Continuing research will include a study of samples from other sources in an effort to delineate the possible effect of impurities on the several low temperature stages.

3. Semiconductor Irradiations

a. Semiconductor Irradiations, GaSb, K. Thommen and D. D. Vawter

A study of the energy and orientation dependence of the production rates for the four types of defects corresponding to the four major recovery stages in undoped GaSb has been completed. The main purpose of this investigation was to assess which portions of the electron irradiation induced damage in GaSb is related to the displacement of Ga and Sb atoms respectively, and to determine the minimum amount of energy which has to be imparted on either of these two atoms to effect its permanent displacement. A paper reporting the results of this investigation has been submitted to Physical Review for publication. The abstract is given below.

"Undoped GaSb single crystals were irradiated at 77°K with electrons having energies between 0.23 and 1.00 MeV. The incident electron beam was aligned with either the [111]- or the $[\bar{1}\bar{1}\bar{1}]$-direction of the sample. The isochronal recovery of the Hall coefficient and the electrical resistivity was measured after each irradiation. The positions and widths of the four major recovery stages were independent of the irradiation energy. The production rates of the defects corresponding to the four stages differed in their energy dependence. Their threshold electron energies were evaluated as o.34 MeV for Stage I, 0.17 MeV for Stage II, 0.33 MeV for Stage III, and 0.34 MeV for [111]-direction than in the $[\bar{1}\bar{1}\bar{1}]$-direction. The reverse was the case for Stage II-, III- and IV-defect production. Stage I is attributed to the recovery of defects created by the displacement of single Sb atoms. The threshold displacements energy for Sb atoms is larger than 7.5 eV but smaller than 13.1 eV. Stage II is interpreted as recovery of defects produced by the displacement of a single

Ga atoms. The threshold displacement energy for Ga atoms is about 6.2 eV. It is suggested that Stage III and IV represent the recovery of defects created by multiple displacement processes starting with the displacement of a Ga atom."

b. Semiconductor Irradiations, GaAs, K. Thommen and D. D. Vawter

A study of the effects of low temperature electron irradiation on the electrical resistivity and the Hall coefficient of GaAs has been initiated. Emphasis has been on the exploration of the main features of the recovery after electron irradiation with energies near 1 MeV. Sample mounting proved to be considerably more difficult with GaAs than with InSb or GaSb, and a more sophisticated mounting technique had to be developed. Irradiations of undoped GaAs single crystals (n-type) were performed at liquid helium temperature and liquid nitrogen temperatures. Postirradiation treatments included isochronal pulse annealing, exposure to short bursts of electron irradiation, and illumination with light from a tungsten filament lamp. The short electron irradiations and the illumination with light were used to produce temporarily an excess of free electrons and holes in the sample. Measurement of the temperature dependence of the Hall coefficient indicated that impurity conduction dominated near 4°K before and after irradiation. Therefore, for recovery measurements between 4 and 77°K, the damage was monitored by resistivity measurements only.

Irradiation at liquid helium temperature produces an initial decrease of the resistivity followed by a monotonic increase with increasing dose. After cessation of the irradiation the resistivity continues to increase while the sample is held at 4.2°K. A saturation value of the resistivity is reached about 20 hours after the end of the irradiation. Upon subsequent pulse annealing, a further resistivity increase occurs between 25 and 75°K. Both the increase at 4.2°K after irradiation and the increase between 25 and 75°K can be reversed either by exposing the sample to short bursts of electron irradiation or by illuminating it with white light. By "reversed" we mean that the resistivity returned to the value which it had immediately after the original electron irradiation. These results indicate that the resistivity changes which occur after the irradiation and during pulse annealing up to 75°K are associated with purely electronic processes, probably release of trapped charged carriers by thermal

activation. There is no indication that irreversible relocation or annihilation of electron irradiation produced defects involving atomic migration occurred during the annealing up to 75°K.

Resistivity and Hall measurements at 77°K showed that electron irradiation reduces both the carrier concentration and the mobility. Large scale recovery of carrier concentration and mobility was observed between 190 and 300°K, and above 450°K. (The highest possible annealing temperature in our experiements was 520°K.) The recovery in these temperature ranges cannot be reversed by exposure to ionizing radiation. We attribute it to annihilation or relocation of radiation produced defects involving atomic migration. The recovery between 190 and 300°K consists of two large, fairly well separated stages centered near 237 and 280°K, and one much smaller stage centered near 200°K. The latter is only poorly resolved. We believe that the recovery which we observed above 450°K is identical with the recovery stage found by Aukerman after room temperature electron irradiation.

It is interesting to note that the main features of the recovery above liquid nitrogen temperature in undoped GaAs are similar to those found previously in undoped GaSb. In both cases, the recovery spectrum consists of a triplet of stages at low temperatures and a single stage well above room temperature. Investigation of the recovery in GaAs after electron irradiation at various energies and in various directions should clarify if there is indeed a close analogy in the recovery behavior of GaAs and GaSb. Work along these lines is in progress.

III. EVALUATION OF EFFORT DURING FISCAL YEAR 1968

This reporting period has been a highly productive one on this project. A large number of papers have been produced including a major review article and several interesting and novel tasks were described. The reinvestigation of aluminum radiation damage occasioned by the development of the two interstitial model last year has been completed and it is felt that a satisfactory picture of the situation in this metal is now available. Although work is in progress on nickel, the emphasis of the program has shifted to the bcc metals and rapid progress is being made even though the results are rather complicated and difficult to interpret. The preliminary studies on polycrystalline iron,

zirconium, and tungsten that have been completed all show many of the general features observed in the fcc metals but there are usually a number of substages that will require extended investigations to give a detailed analysis. The studies on pure metal whiskers and oriented single crystals initiated last year are proving to be unusually challenging and instructive. The experiments are difficult to carry out because of the sample sizes but the importance of the results in the nearly perfect crystals provides a strong incentive to pursue the work vigorously.

The mechanical property studies have been extended to include copper and silver. The results are complex (as they were in aluminum) but the copper behavior has been analyzed in some detail and a reasonable interpretation of the results has been obtained.

The studies on irradiated III-V compounds have progressed to a level of considerable sophistication. It is now possible to identify recovery processes with the individual atoms involved and to give displacement energies for Ga and Sb in GaSb. The additional disgnostic tools available in semiconductor studies as compared to the metal case allow a more complete investigation of the radiation effects. This improved understanding of the lattice processes is a significant advance and a real contribution to the subject.

PAGE 356 is blank

Program: Advanced Development
AEC Task: 22, Radiation Chemistry of Chromosomes*
Project Manager: R. A. Holroyd
Reporting Period: Fiscal Year 1968
General Order: 7724 Subaccount: 17001 AEC Category: 06-04-00-00.0

I. PROJECT OBJECTIVES

The long range objective of this study is to obtain information which will correlate molecular alterations and biological damage to mammalian chromosomes, caused by radiation. The immediate objective is a better understanding of the radiation chemistry of chromosomes and their main constituents: nucleic acids and proteins.

II. TECHNICAL PROGRESS DURING FISCAL YEAR 1968

A. PUBLICATIONS AND PRESENTATIONS

The following papers have been published.

1. D. E. Holmes, R. B. Ingalls, and L. S. Myers, Jr., "An ESR Study of Free Radicals Formed by Reaction of Nucleotides and their Constituents with Hydrogen Atoms," International J. Rad. Biol. 12, 415 (1967)
2. R. B. Ingalls, L. S. Myers, Jr., D. E. Holmes, and J. W. Glass, "An ESR Study of Reactions of 1,3-dideuterouracil and 1,3-dideutero-5-bromouracil with Hydrogen Atoms," Radiation Research 31, 545 (1967), Abstract
3. D. E. Holmes, R. B. Ingalls, and L. S. Myers, Jr., "ESR Spectra of Free Radicals Induced in Pyrimidines, Purines and Related Analogs by Exposure to Hydrogen Atoms," International J. Rad. Biol. 13, 225 (1968)

The following papers have been submitted for publication.

4. R. A. Holroyd and J. W. Glass, "Radicals formed by Electron Transfer to Pyrimidine Derivatives," International J. Rad. Biol.
5. R. A. Holroyd and J. W. Glass, "Reactions of Hydrogen Atoms with DNA and Nucleoproteins," Radiation Research (in press), Abstract

*A more comprehensive annual report will be issued in July

The following presentation was made.

6. R. A. Holroyd and J. W. Glass, "Reaction of Hydrogen Atoms with DNA and Nucleoproteins," at the 16th annual meeting of the Radiation Research Society, Houston, April (1968)

B. PROGRESS DURING REPORT PERIOD

1. Reaction of Hydrogen Atoms with DNA

The reaction of hydrogen atoms with various samples of DNA was investigated at 25 and -90°C. In the case of salmon sperm and calf marrow DNA at 25°C, the resulting ESR spectrum consists of eleven resolved hyperfine lines spread over 130 gauss. By means of a computer spectrum simulation technique it was determined that the radicals formed in DNA by hydrogen atom bombardment were 22% on thymine, 33% on cytosine, 8% on purine bases and 37% on sugar groups.

The ESR spectrum obtained with DNA was dependent on the temperature of the reaction. At -90°C, the spectrum obtained was very similar to that obtained with deoxycytidine-5'-phosphate (dCMP). Therefore, hydrogen atom addition to thymine is much less important at -90°C than at 25°C. Since thymyl radicals are formed in the radiolysis of DNA at -74°C (Ehrenberg, et al., Science 157, 1317, 1967), our results support a low yield of hydrogen atoms in the radiolysis of DNA as suggested by the work of Muller and Dertinger, Zietschrift für Naturforschung 23, 83 (1968). A paper describing our results for the reaction of hydrogen atoms with DNA is in preparation.

2. Reaction of Hydrogen Atoms with Nucleotides

The reactions of hydrogen atoms with DNA nucleotides were examined to facilitate interpretation of the results obtained on DNA, see Section B-1. The ESR spectra obtained by H-atom attack were analyzed by utilizing the computer program GLAD to determine the percentage of base and sugar radicals. Reaction with deoxyribose produces a spectrum consisting of five resolved hyperfine lines spread over 42 gauss (contrary to earlier findings by Holmes, et al., Internatl. J. Rad. Biol., 12, 415 (1967). This spectrum is very characteristic, a fact which facilitates evaluation of sugar attack in nucleotides. For deoxyguanosine-5'-phosphate, 60% of the radicals result from abstraction from the sugar and 40% from addition to guanine. For thymidine-5'-phosphate, 40%

of the radicals are on the sugar group and 60% on thymine. The latter result was surprising since in a one-to-one mixture of thymine and deoxyribose only thymine is attacked by H-atoms. The reactivity of the sugar group is enhanced in the nucleotide. For dCMP our analysis indicates hydrogen atom addition to cytosine accounts for 65% of the radicals formed.

3. Reactions of Hydrogen Atoms with Chromosomes

Samples of lyophilized meta-phase and interphase (whole nuclei) chromosomes (~2 mg each) prepared from mouse tumors, were bombarded with hydrogen atoms at 25 and -80°C. The low temperature was used to increase the sensitivity for detection of radicals and to stabilize the radicals formed in the samples. For both types of chromosomes, the resulting ESR spectra were similar at -80°C, in that three broad hyperfine lines were observed. The central line is the strongest and the triplet splitting is 43 ± 5 gauss. These spectra are unlike that obtained upon reaction of hydrogen atoms with DNA, Section B-1, but similar to that obtained with nucleohistone samples at -90°C. They are also quite similar to the spectra obtained when H-atoms react with phenylalanine and tyrosine (see Section B-4). These results suggest that at -90°C, hydrogen atoms do not attack the genes in these chromosomes but add to phenyl rings in the protein component. This study is continuing in order to further characterize the sites of reaction in meta-phase chromosomes.

4. Gamma Radiolysis of Chromosomes and Constituents

Dry lyophilized samples of nuclear material have been gamma irradiated at room temperature. Stable radicals are formed and, in the case of interphase chromosome samples, the yield is 0.7 radicals/100 ev. When dry DNA was irradiated, the ESR spectrum showed unmistakedly the hyperfine structure of the thymyl radical. These thymyl radicals represent a small percentage of the total yield (G = 1.3) of radicals. Irradiation of a dry nucleohistone sample (about 42% DNA) resulted in the formation of a high yield of stable radicals (G = 3.5) of which again a small percentage were thymyl radicals.

5. Reaction of Hydrogen Atoms with Proteins

Since a large percentage of the chromosome consists of proteins known as histones, the reaction of hydrogen atoms with some lyophilized histone samples was investigated. The ESR spectrum obtained upon bombardment of histone

samples was investigated. The ESR spectrum obtained upon bombardment of a histone sample at 25°C, is an asymmetric doublet; that is, two wide lines separated by ~18 gauss. This spectrum is similar to that obtained in the radiolysis of proteins and also similar to that obtained by H-atom bombardment of glycylglycine and leucylleucine. The formation of this doublet spectrum in the leucine dipeptide demonstrates that it is formed by hydrogen atom reaction with the peptide bond since reaction of H-atoms with leucine leads to a much different 16-line spectrum (Snipes and Schmidt, Radiation Research, 29, 194 (1966). It is postulated on the basis of these results that the prominent radical formed in most proteins at 25°C by either gamma radiation or H-atoms has the free spin located on nitrogen: that is, -CONCHR-.

The ESR spectra obtained on reaction of hydrogen atoms with histones at -90°C are triplets of 45 ± 4 gauss splitting. These spectra are very similar to those obtained for phenylalanine, tyrosine, and alanyl-phenylalanine at 25°C. For these, the spectra are triplets of 45 ± 3 gauss splitting. This is the splitting expected for the cyclohexadienyl-like radicals (Fessenden and Schuler, J. Chem. Phys. 38, 773 (1963). Hydrogen atoms apparently add to the phenyl groups in the these amino acids. They also add to phenyl groups in histones and this effect is most apparent at -90°C.

6. Reaction of Electrons

The reactions of electrons with some pyrimidine derivatives were investigated. The electrons, produced photolytically in alkaline glasses, were reacted with solutes to form anions. It was found that anions of thymidine and thymidine-5'-phosphate easily undergo proton transfer from surrounding water molecules to the C_6 position of the thymine ring. Anions of uracil and deoxycytidine do not undergo corresponding proton transfer reactions in the aqueous matrix at low temperatures. This work demonstrates that electron reactions can account for the formation of the eight-lined ESR spectrum observed to be formed in the radiolysis of DNA. A paper covering this work has been submitted to the Internat. J. of Radiation Biol. for publication.

III. EVALUATION OF EFFORT TO DATE

The reactions of hydrogen atoms and electrons with chromosomes and their principal components have been investigated during this period. Both of these intermediate species may be produced either by direct or indirect action during radiolysis of chromosomes in cells. It has been shown that hydrogen atoms react with DNA by addition to template molecules and by abstraction from deoxyribose. The reaction with DNA is temperature sensitive. Hydrogen atoms attack the protein component of chromosomes and do not react with the genes to any great extent.

Reactions of electrons with DNA nucleotides leads to anions. In the case of TMP, the anion is found to readily protonate in aqueous media. This work has led to a postulated mechanism of base damage in DNA.

PAGE 362 is blank

Program: LMFBR Component Development		
AEC Task: 25, Noise Analysis Instrumentation		
Project Manager: C. W. Wheelock		
Reporting Period: Fiscal Year 1968		
General Order: 7757	Subaccount: 53100	AEC Category: 04-01-61-03.4

Principal Investigator R. L. Randall

I. PROGRAM OBJECTIVES

The objective of the program is demonstration of the feasibility of liquid metal flow rate measurement by use of noise analysis techniques and development of an operating instrument for use in calibration of, and as an alternative to, conventional flow measurement methods. The technique involves detecting small temperature variations (caused by thermal eddies) at two points in the flowing stream. The two signals are cross-correlated with a variable delay time. The delay time which gives maximum correlation is the transit time of the fluid between the sensors.

Two methods for detecting the thermal eddies are being investigated. The first senses thermal variations by use of thermocouples with matched response times. The second senses thermally induced resistivity variations by use of electrical conductivity probes the latter technique has the advantages of simplicity and fast, localized response.

The first phase of the development program will be the experimental demonstration of the conductivity cell cross-correlation method in a 50 gpm water loop. The objective of this phase is to establish the accuracy of the method in cylindrical flow sections and to determine variations of uncertainty with flow rate, fluid density, viscosity, and channel size.

The second phase of the program will be the extension of the knowledge gained in the first phase to the measurement of water flow rates in cylindrical sections, by use of thermocouples. The objective of this phase is to provide the knowledge required to extend the technique for use with liquid metal.

The third and fourth phases, which are extensions of Phases 1 and 2, are concerned with the application of the techniques developed in Phase 1 and 2 to a liquid metal system.

II. TECHNICAL PROGRESS DURING FISCAL YEAR 1968

The authorization to initiate work on this project was received in January 1968. Initial studies and test planning were started immediately, and work has progressed to the initiation of loop testing with both conductivity sensors and thermocouples.

The basic technique involves detection of thermal eddies or some other physical property of the fluid, with two or more in-line sensors and measurement of the average delay time relating the sensor signals. The correlation method for measuring fluid transit time is illustrated in Figure 1. Future efforts will involve development of methods for on-line transit time measurements; however, during the demonstration and sensor development tests, correlation measurements will be performed off-line from tape recorded sensor signals.

Since the objective of the program is to develop an instrument system and measurement techniques that can be used for calibration of flow measuring

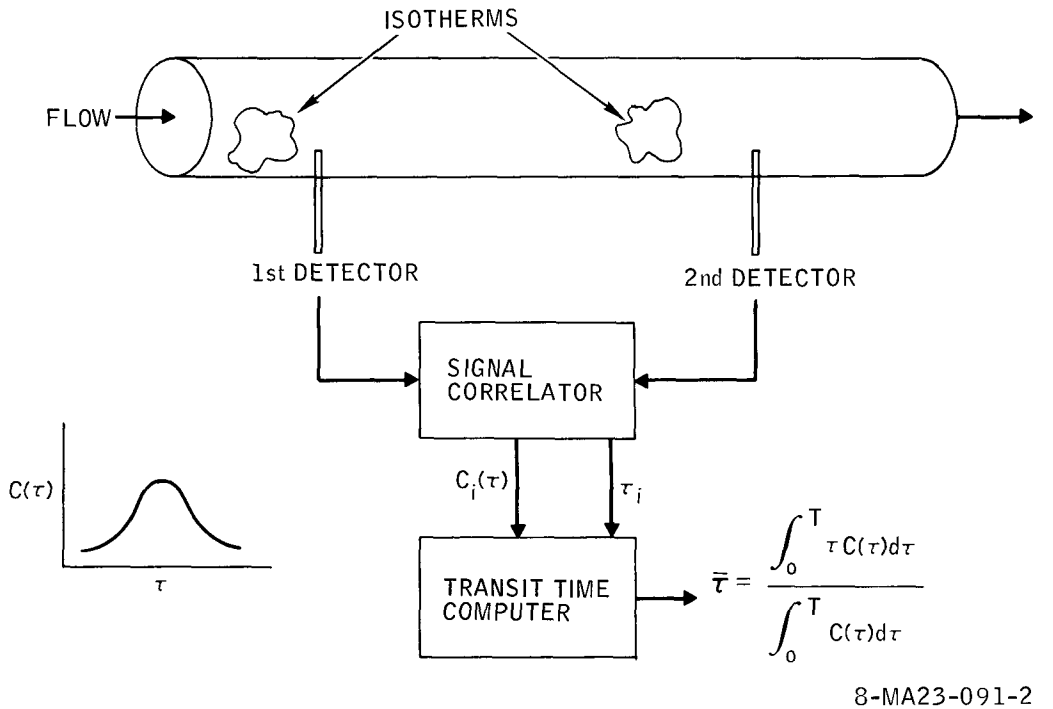

Figure 1. Measurements Using Correlation Method

instruments, major emphasis is being placed on measurement accuracy and means for reducing measurement uncertainties. Work efforts are grouped into the following categories: (1) sensor time response; (2) sensor design and installation, (3) hydraulic test loop, (4) data acquisition, signal conditioning, and recording, (5) signal correlation and interpretation, and (6) preliminary loop tests. The significance, requirements, and activities in each of these are discussed below.

A. SENSOR TIME RESPONSE

The principal criteria to be met by "satisfactory" sensors include high sensitivity, a short time response, and a mechanical design which will withstand the rigors of temperature and high velocity flow without restraining flow significantly. Typical fluid transit times between sensor pairs will range from about 1000 down to about 100 milliseconds; therefore, sensor time response should be in the range of 100 to 10 milliseconds. Variations among sensors around 1 millisecond or less is desirable. This could be achieved by using extremely small thermocouples. However, problems with fabrication and requirements for durability in liquid metal environments limit the practical size to about 20 mil diameter. Grounded junction, sheathed thermocouples of this size have a time response in the range 20 to 50 milliseconds, which appear to be satisfactory for most applications.

Techniques for measuring and comparing thermocouple time responses were investigated. An apparatus for comparing thermocouple response was designed and breadboarded. It utilized a hot air source which was modulated by a rotating disk with slots. The time response of two thermocouples exposed to the modulated air current was compared with a phase meter to establish the feasibility of the technique.

An apparatus for measuring and comparing thermocouple time response was assembled and checked out. Preliminary testing indicated that the system was capable of resolving thermocouple time response differences of about 1 millisecond. The time response of two 20 mil sheathed thermocouples was matched by comparing the relative response time of two TC's; filing a few mils of sheath material from the junction end of the slow TC, and repeating the response comparison. The second filing attempt brought the response difference

to less than 1 millisecond. After demonstrating the feasibility of this approach, the apparatus was modified to simplify operation and improve measurement stability. A lamp and solar cell were added to provide a standard reference signal for checking operation of the apparatus, a suitable signal for the tachometer, and a phase reference signal with negligible delay (response time on the order of 10 microseconds) for comparison with thermocouple signals.

The system, called the Thermocouple Response Comparator is shown in Figures 2 and 3; a block diagram is shown in Figure 4. This system has been used in the thermocouple lab for comparing and matching the time response of forty 20-mil, sheathed, chromel-alumel thermocouples to be used in the test program. Phase comparisons, by use of the light source and solar cell were made at modulation frequencies ranging from 10 to 20 Hz. By filing material from the junction end-cap, the time response of thirty-seven out of forty thermocouples was matched to within ±1 millisecond. Nominal phase lag between the solar cell and each thermocouple was adjusted to 104 degrees ±3 degrees at 15 Hz.

This system appears to provide a practical means of significantly reducing potential errors in transit time measurements resulting from differences in thermocouple time response.

B. SENSOR DESIGN AND INSTALLATION

The size, material, insulation, and electrode configuration to be used in the conductivity sensor test sections were studied. The sensitivity, reaching distance, and field linearity of various electrode configurations were compared by use of Teledeltos paper. Results indicated that flush-mounted electrodes, while suitable for very small channels, are not suitable for large channels unless the ratio of electrode diameter, insulator diameter, and channel diameter remains constant. To achieve a moderately linear field gradient with electrodes in a 3-in. diameter pipe would require electrode diameters in excess of 1 in. and insulator diameters in excess of 2 in. Comparison of various in-stream electrode configurations led to selection of two basic types for use in the first test section. The first electrode is simply a thin metal rod extending across the pipe diameter. It is installed by use of glass seal headers for insulators. This type of electrode has excellent field linearity and is applicable to

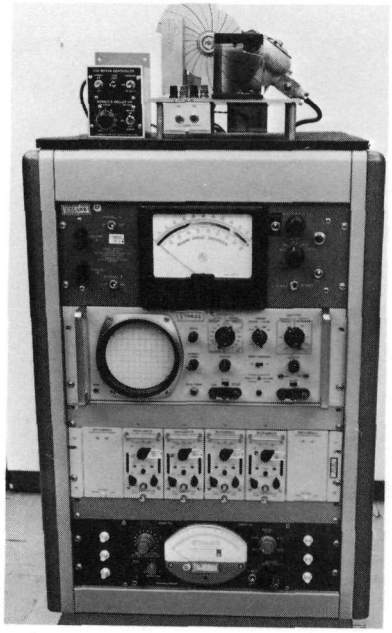

7757-1801

Figure 2. Thermocouple Response Comparitor System

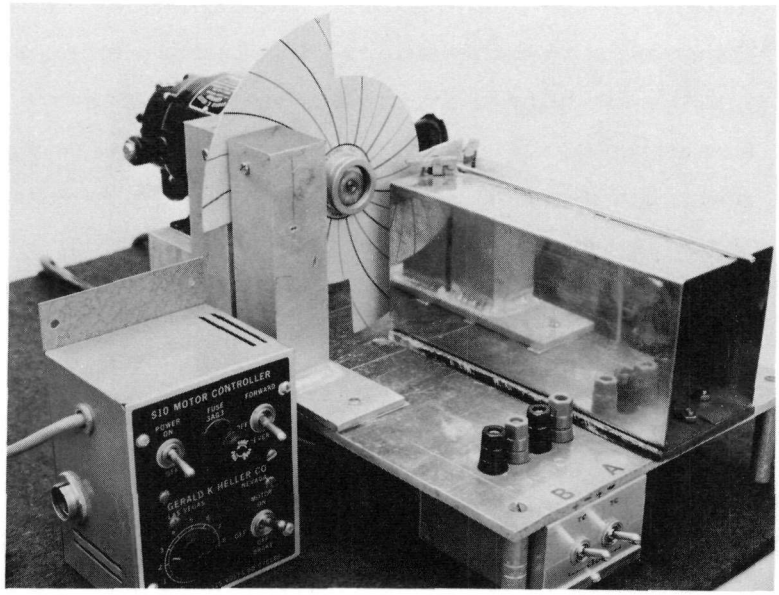

7757-1802

Figure 3. Blower & Modulator Assembly of the Thermocouple Response Comparitor System

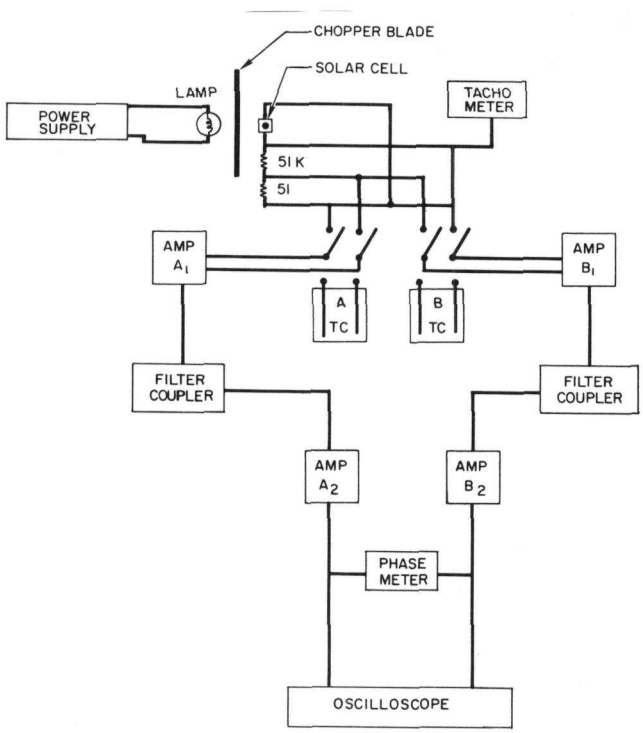

7757-4701

Figure 4. Signal Circuits in the Thermocouple Response Comparitor System

essentially any pipe size. The second electrode design uses two rods, one directly behind the other. The latter configuration has a shorter feeling distance and should have a sharper response to passing eddies. Glass seal headers suitable for use as electrode insulators were obtained. These headers are used to support 40 mil electrodes. The electrodes were made from 40 mil stainless steel welding rods.

The problems of installing instream thermocouples at a large number of axial and radial positions, with high position stability, were studied. Such installations will be required to study the size, propagation, and diffusion of thermal eddies. Test sections were designed in three basic sizes, each with multiple sensor configurations. Test sections built with TC's for use initially in water also are suitable for later use in sodium or NaK. To meet these requirements, a fin structure was designed for instream mounting of up to thirteen 20-mil, sheathed, thermocouples. The mounting fins for use in the first thermocouple test section (2-in diameter) were machined from stainless steel 2-1/2 inches by 1/2-in. by 60 mils. The side of each fin was hollowed out and 13 holes were drilled in the leading edge to permit the TC's to protrude about 1/16-in. The TC wires extend through one end of the fin and then through a seal cap. The side of the fin and the seal cap are filled by use of a furance brazing technique. The assembly is then inserted into a slotted test section with mating seals. Leak-tight seals suitable for service in either water or sodium are used to permit the fins to be replaced or moved to ther locations in a given test section. In a test section, the fins will be mounted one behind the other to measure velocity profiles and to study eddy propagation. This fin design provides accurate positioning and is mechanically stable. It introduces little flow perturbation and is easily installed, or replaced. The design concept is applicable to essentially any pipe size.

Thirteen thermocouples were installed in the first thermocouple mounting fin. Brazing of the thermocouples into the hollowed fin was accomplished in a special furnace. In preparing the first fin, a problem with the temperature indicator on the furnace necessitated two heating cycles to 1800°F (rather than the one normally required). It was expected that the extreme temperature cycles would destroy some of the 20-mil grounded junction thermocouples; however, after the unit was returned to the TC lab and new leads were attached,

all TC's were found to be operational. The fin was mounted on the apparatus for measuring and comparing TC time response; normal signals were observed on all TC's. Although fabrication of the first thermocouple mounting fin was successful, it was decided that anticipated service requirements would allow use of a braze material with a lower melting point which would be less likely to damage the thermocouple sheaths. Therefore, additional fins are being fabricated with 1600°F braze alloy.

The first test section for use with conductivity sensors was machined from a 2-in. diameter pipe. Provisions were made to install single or double conductivity electrodes at 5 axial locations in one plane and 2 axial locations in the perpendicular plane. A second 2-in. test section was prepared for use with thermocouples. Provisions were made to install thermocouple mounting fins at the same relative positions as the conductivity electrodes. These test sections are illustrated in Figures 5 and 6.

C. HYDRAULIC TEST LOOP

An existing 50-gpm test loop was modified to provide higher flow output, greater flow stability, and a mass flow measurement capability. The loop components were disassembled, cleaned, and the loop piping rearranged to provide the desired configuration of controls, flow straighteners, orifice flow meter, 5-ft test section, and a larger storage tank. A second pump, from a former test loop, with twice the capacity of the existing pump, was also installed in the loop. High speed solenoid valves were installed to permit flow from the test section to be diverted to a calibrated dump tank system during the flow tests in order to achieve accurate flow determinations. The test loop is illustrated in Figure 7. In addition to the previously described features, the loop is provided with a hot water injection line, injection line heaters, storage tank heaters, flowmeter manometers, and a pneumatic control valve. The hot water injection line is used to induce thermal eddies into the test section.

A control panel called the Flow Test Programmer was designed, assembled, and checked out. This unit operates the storage and dump tank solenoids and the tape recorder during flow tests. Its operating sequence is as follows:

Prior to starting a flow test, flow and temperature conditions are set at the desired level and signals from all conductivity cells or thermocouples

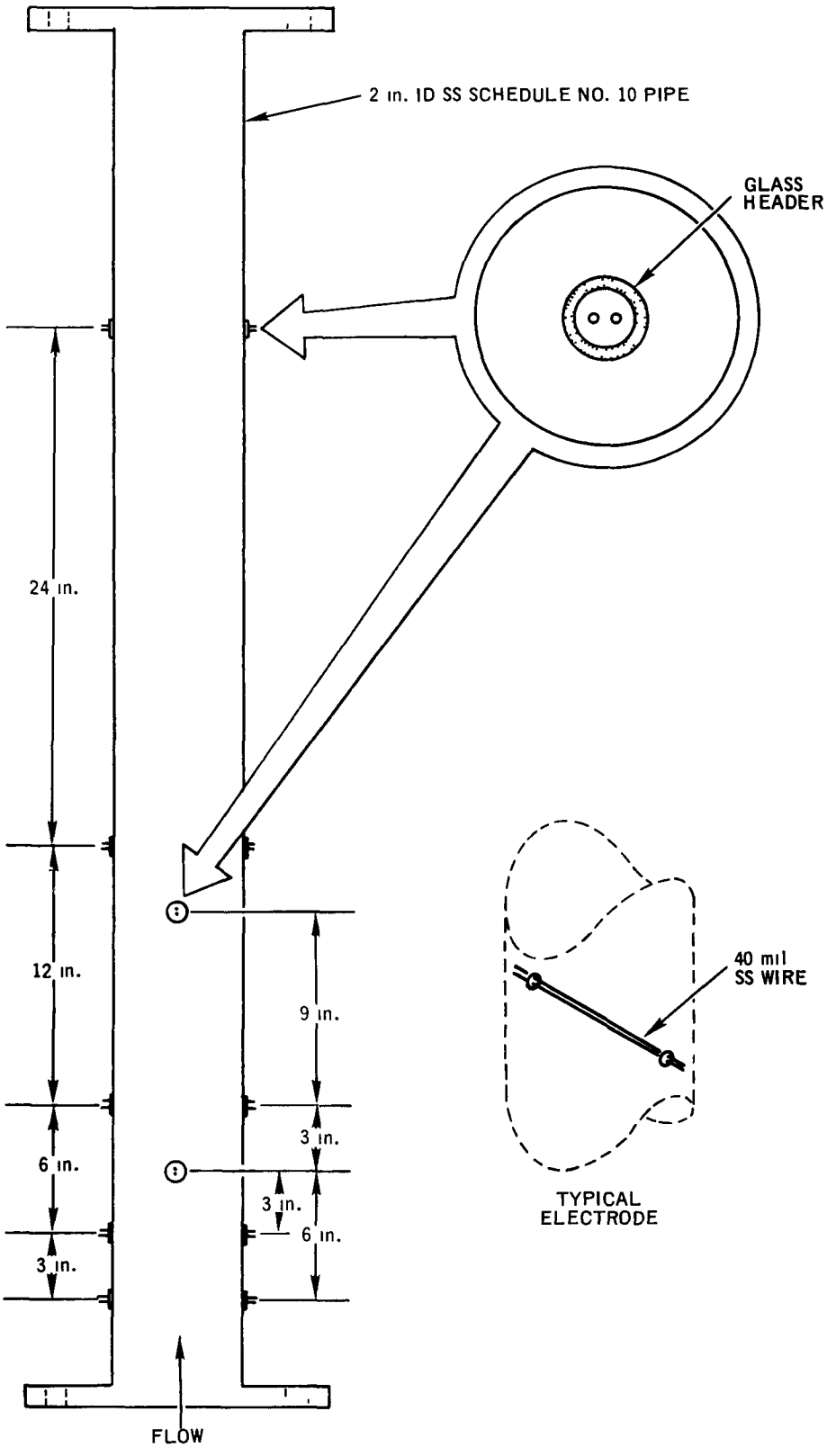

Figure 5. Test Section Instrumented with Conductivity Electrodes

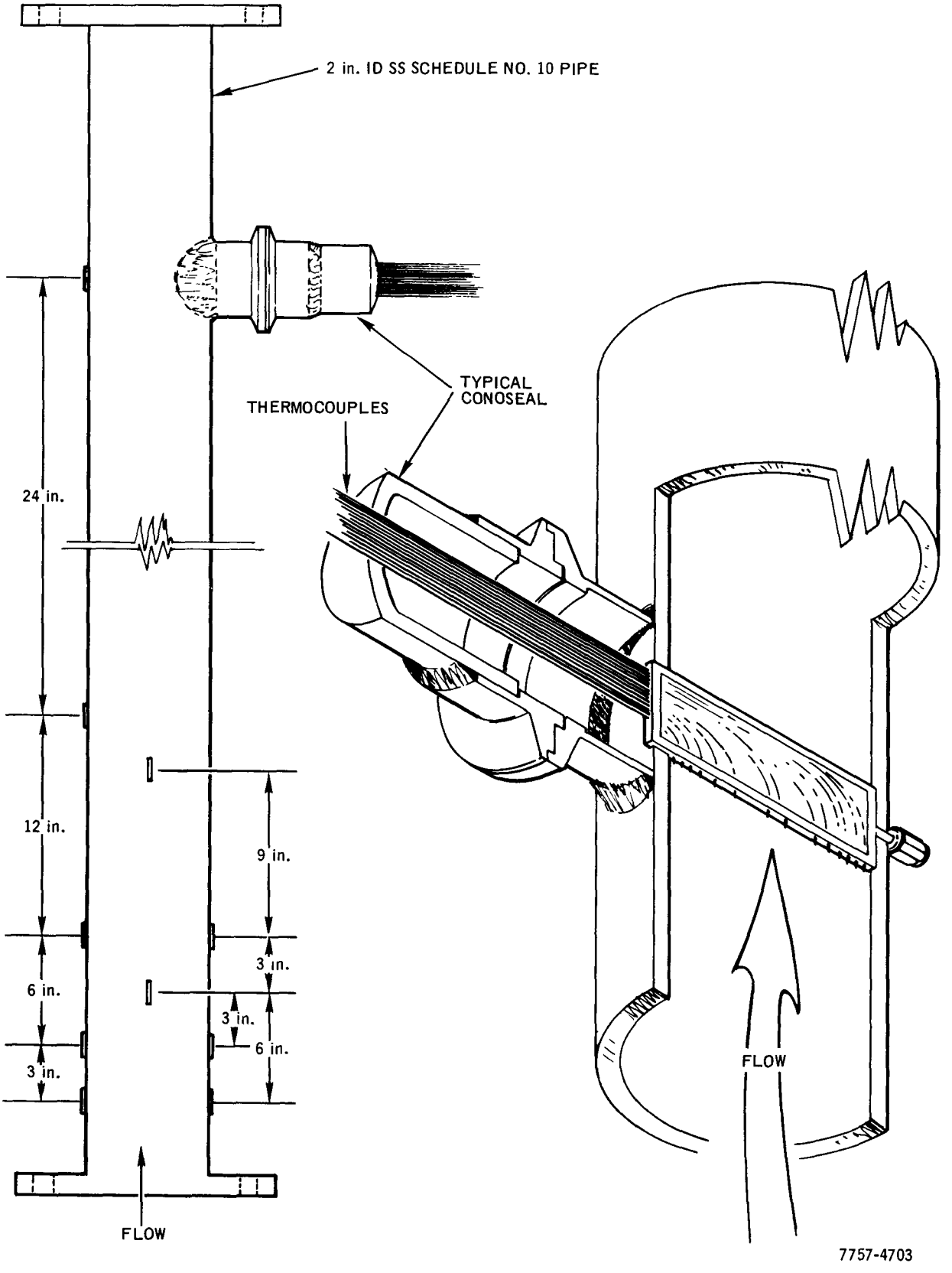

Figure 6. Test Section Instrumented with Thermocouples

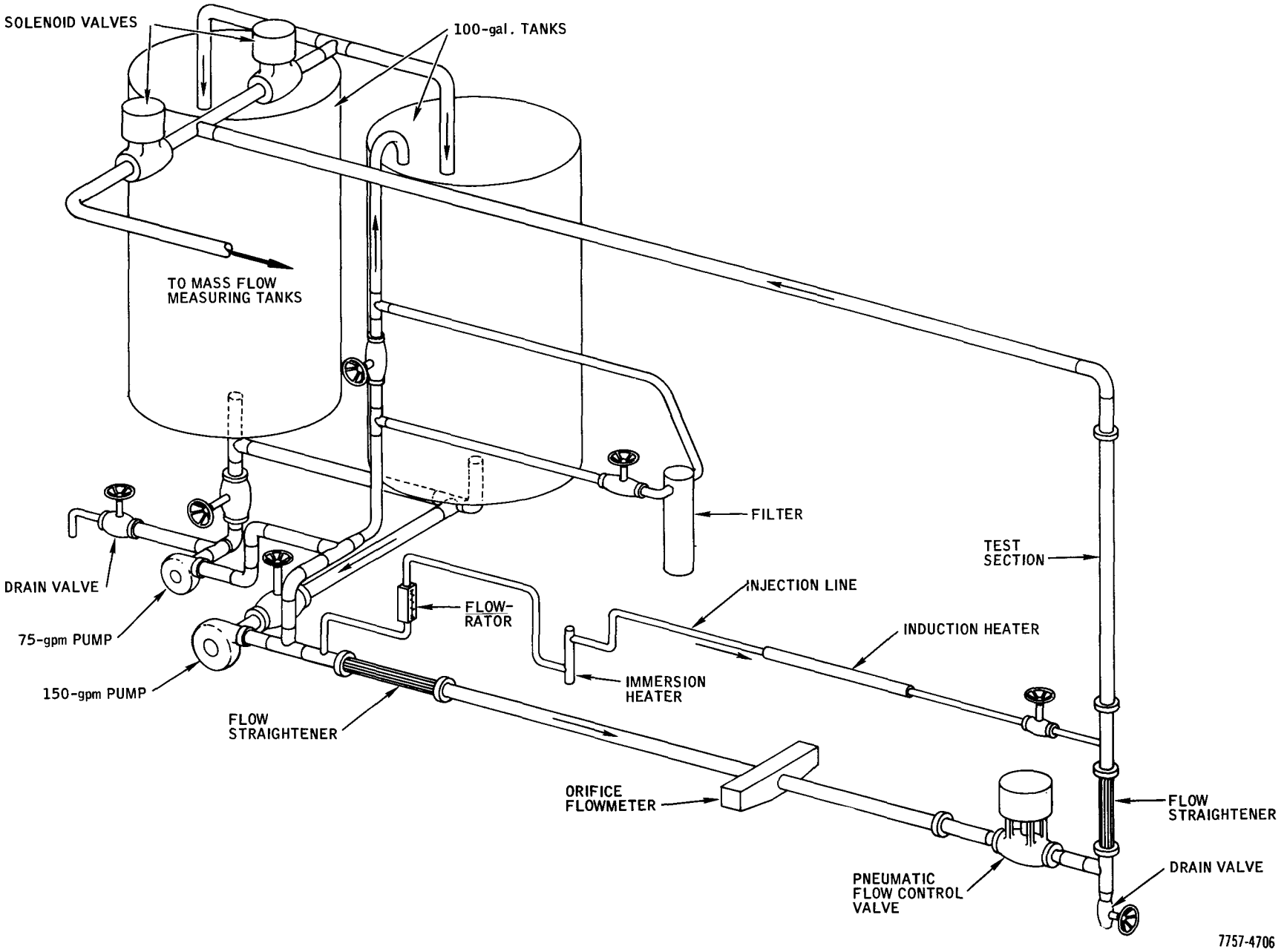

Figure 7. Modified Test Loop

are checked out. Next the tape recorder is placed in the record mode. During this period, a control voltage of -1.5 volts from the Flow Test Programmer is recorded on one channel of the tape recorder. After about 10 to 20 seconds, the loop operator pushes the dump control which transfers control of the loop and recorder operation to the Flow Test Programmer.

During the dump mode, all water passing through the test section is diverted by means of solenoid valves to a dump tank with a precise volume readout, a control signal of 0 volts is recorded on one channel of the tape recorder, a preset timer is actuated, and a manual stop-dump switch is armed in case it is necessary to stop the test before the timer runs out.

When the dump mode is ended, either automatically or manually, the flow is again diverted to the main loop storage tanks. At this point, a control signal of +1.5 volts is recorded on the data tape for a preset interval. Next, a signal of -1.5 volts is recorded for a preset interval. Then power to the recorder is interrupted for about 1 sec. This causes the recorder to drop out of the record mode and the drive controls to return to neutral.

The recorded control signals will be used during the data reduction phase to operate the signal correlator unit. This provides automatic syncronization of correlation measurements to the period of time that flow is diverted to the dump tanks. This automatic control of loop operation should lead to flow measurement accuracy in the range of 0.1 to 0.2%. Basic measurements with this level of accuracy are desired to perform error analyses of the various test and measurement parameters.

D. DATA ACQUISITION, SIGNAL CONDITIONING, RECORDING

Sensor output signals are amplified and filtered before recording, to optimize the signal-to-noise ratios. Filters are passive RC circuits that are specially phase matched to assure uniform response on all channels. Band pass response extends from about 2 to 30 Hz. Figure 8 is a photograph showing the amplifiers, filters, and tape recording system. The flow test programmer for controlling the dump system, and the detector modulator for activating the conductivity electrodes are not shown. The digital clock that provides precise 1 and 10 Hz timing signals to the tape recorder system also is not shown.

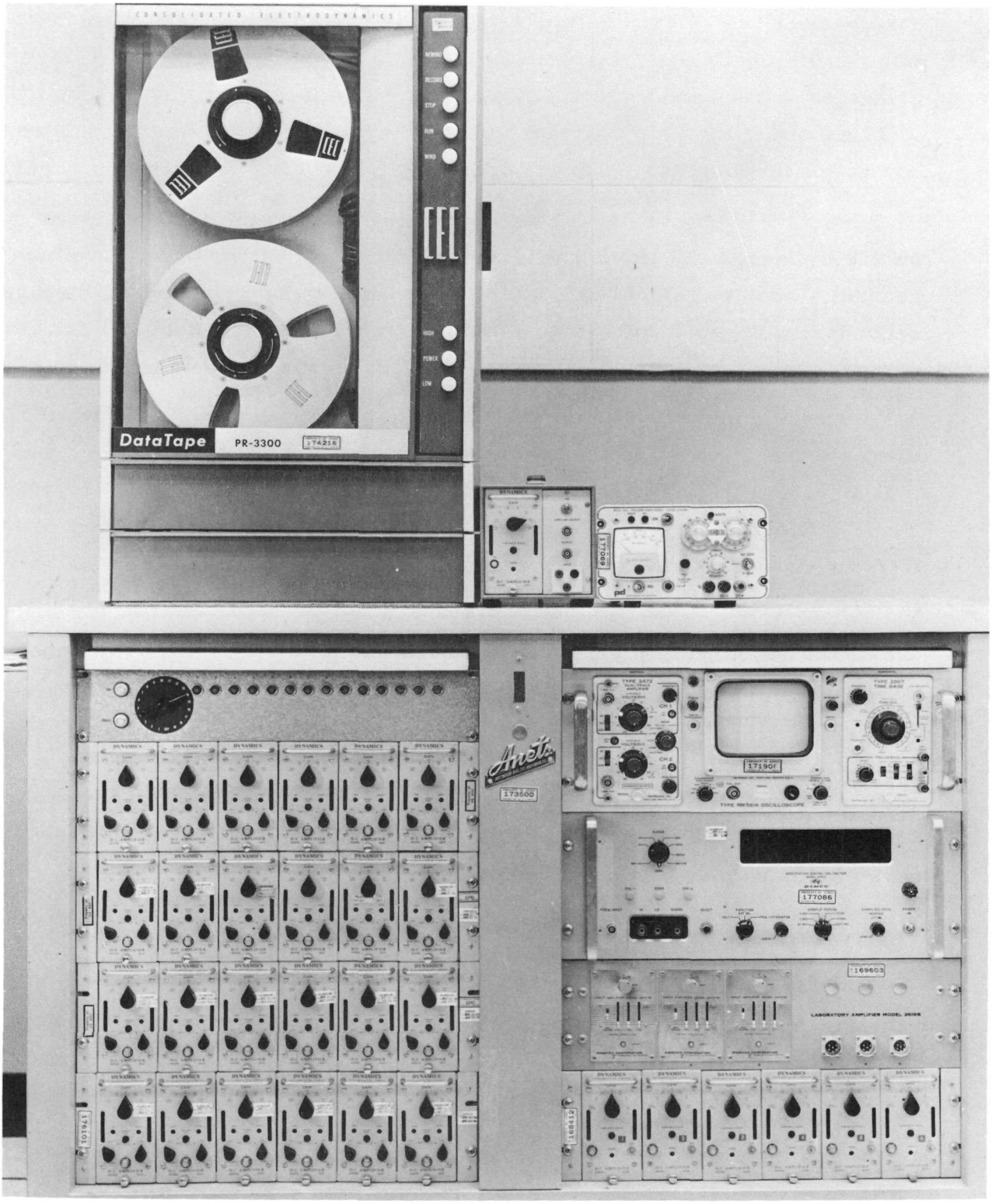

7757-1804

Figure 8. Data Recording System

E. SIGNAL CORRELATION AND INTERPRETATION

Experience prior to the initiation of this program has shown that the accuracy of the correlation flow measurement technique was affected by phase distortion in the correlator delay line. Modifications were made in the existing delay line to improve phase linearity versus frequency and to simplify cross correlation measurements. The unit was checked out in preparation for reducing data from preliminary loop tests. A block diagram of the modified correlation system is shown in Figure 9. Although the modified system worked satisfactorily, a commercial unit with higher accuracy and faster operation became available which made use of this existing system unnecessary. However, the gating circuitry and input limiters in the existing system were used to control the operation and provide high level signals to the commercial correlator.

The commercial signal correlator, capable of simultaneous on-line computation of 100 points in the cross correlation function relating two signals, continuously, using 100% of the data, was purchased from Princeton Applied Research. A minor modification to this unit was made to permit readout and

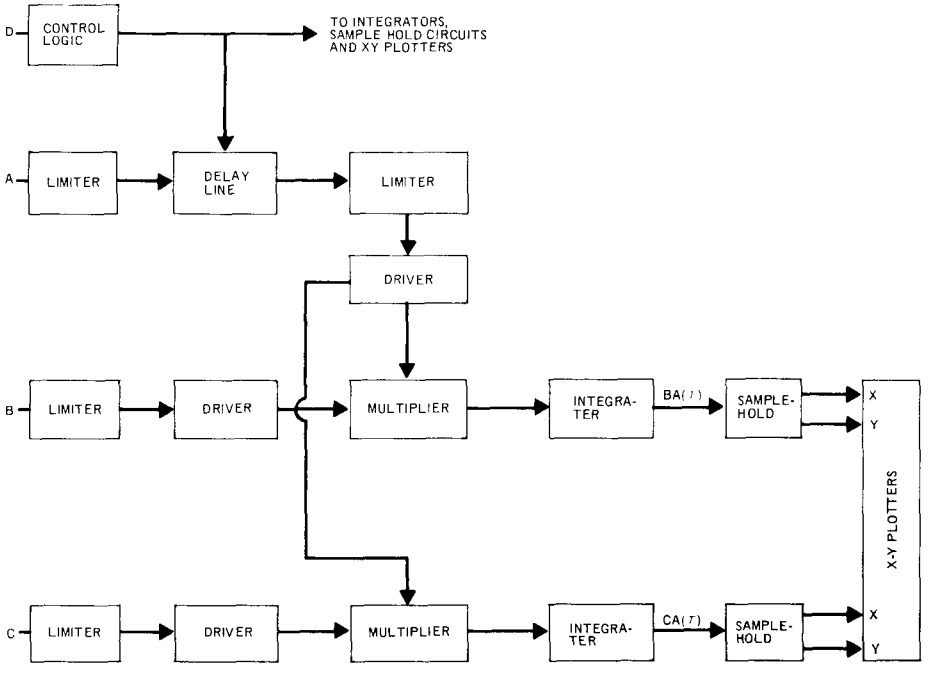

7757-4704

Figure 9. Modified Cross Correlation Computer System

external calibration of the shift register clock frequency. This improved the time delay accuracy from a nominal 2% of full scale to 0.2%. Higher accuracy could be readily achieved if necessary by use of an external frequency standard. This system eventually will be adapted to provide direct on-line readout of fluid transit time or flow velocity. The unit was delivered in time for use in reducing data from the first preliminary loop test.

F. PRELIMINARY LOOP TESTS

Several preliminary demonstration tests were conducted with conductivity electrodes and thermocouples. These tests were designed to (1) check out operation of the hydraulic test loop, (2) verify that thermal eddies can be detected with conductivity electrodes, (3) demonstrate the correlation flow measurement techniques, (4) compare flow velocity measurements obtained simultaneously by using conductivity sensors and thermocouples, (5) provide preliminary estimates of flow measurement precision versus data sample time, and (6) checkout mechanical operation of the water dump system for mass flow measurement.

A series of three tests was conducted at nominal flow rates, around 50 gpm, in the hydraulic test loop, using a 2-in. diameter cylindrical test section. The test section was instrumented with seven sets of conductivity electrodes in one test. In the other two tests, four sets of removable electrodes were replaced with two pair of in-stream thermocouples. The 20-mil, sheathed thermocouples were inserted into 40-mil sleeves and then inserted through the glass headers to a depth of 300 mils. A circle drawn in a cross sectional view of the 2-in. diameter pipe at a depth of 300 mils would enclose approximately half the cross sectional area. Other penetration depths, pipe sizes, and flow conditions will be investigated in subsequent tests.

The objective of the first test was to study loop stability and relate measurement precision to data sample length. Cross correlation measurements were recorded continuously on a strip chart recorder as the recording of electrode signals was played back at various tape speeds. For this study, two electodes with a 12-in. spacing were selected. By reproducing the tape at various speeds it was possible to effectively vary the averaging time constants of the signal correlator. With a minimum 4-sec time constant, the correlator scans

the 100 correlation coefficients each 12 sec. Thus, for a 9 min run, it was possible to obtain 44 correlation measurements with a 4 sec time constant, 22 with an 8 sec time constant, 11 with a 16 sec-time constant, etc. Transit time estimates were obtained from each correlation measurement by using a graphical technique. Figure 10 shows a plot of the measured transit times versus time, for three different averaging time constants. These results indicate that there was negligible drift in loop flowrate and for these particular test conditions, there is negligible scatter in transit time estimates made with averaging times of 16 sec or greater. Other factors affecting statistical scatter in transit time estimates will be considered in later tests.

The objective of the second test was to compare flow velocities measured with conductivity electrodes and thermocouples. The four electrodes shown perpendicular to the page in Figure 5 were removed. The top hole in each glass header was sealed with solder. Thermocouples were inserted as described earlier, in the bottom hole in each of the four headers, one on each side of the pipe at two vertical positions 12 in. apart. The thermocouples had been selected for uniform time response by use of the Thermocouple Response Comparitor.

Correlation measurements between the various thermocouples revealed that the eddies detected by thermocouples on opposite sides of the pipe were not related. However, as expected, there was strong correlation between signals from in-line thermocouples.

The velocities measured with the instream thermocouples and two electrode pairs are listed in Table 1. The close relation between the measurements in Runs 2 and 3, which were made on different days, gives an indication of the stability and precision of the test loop instrumentation. The close relation between the velocities obtained with thermocouples and those obtained with electrodes was probably coincidence related to the particular penetration depth chosen for these tests. These effects will be studied in more detail in later tests.

These preliminary tests were conducted with water at room temperature, since the storage tank heaters had not been installed. Thermal eddies were induced by injecting a stream of heated water into the main flow line ahead of the test section. The flow rate in the injection line was about 2% of the total

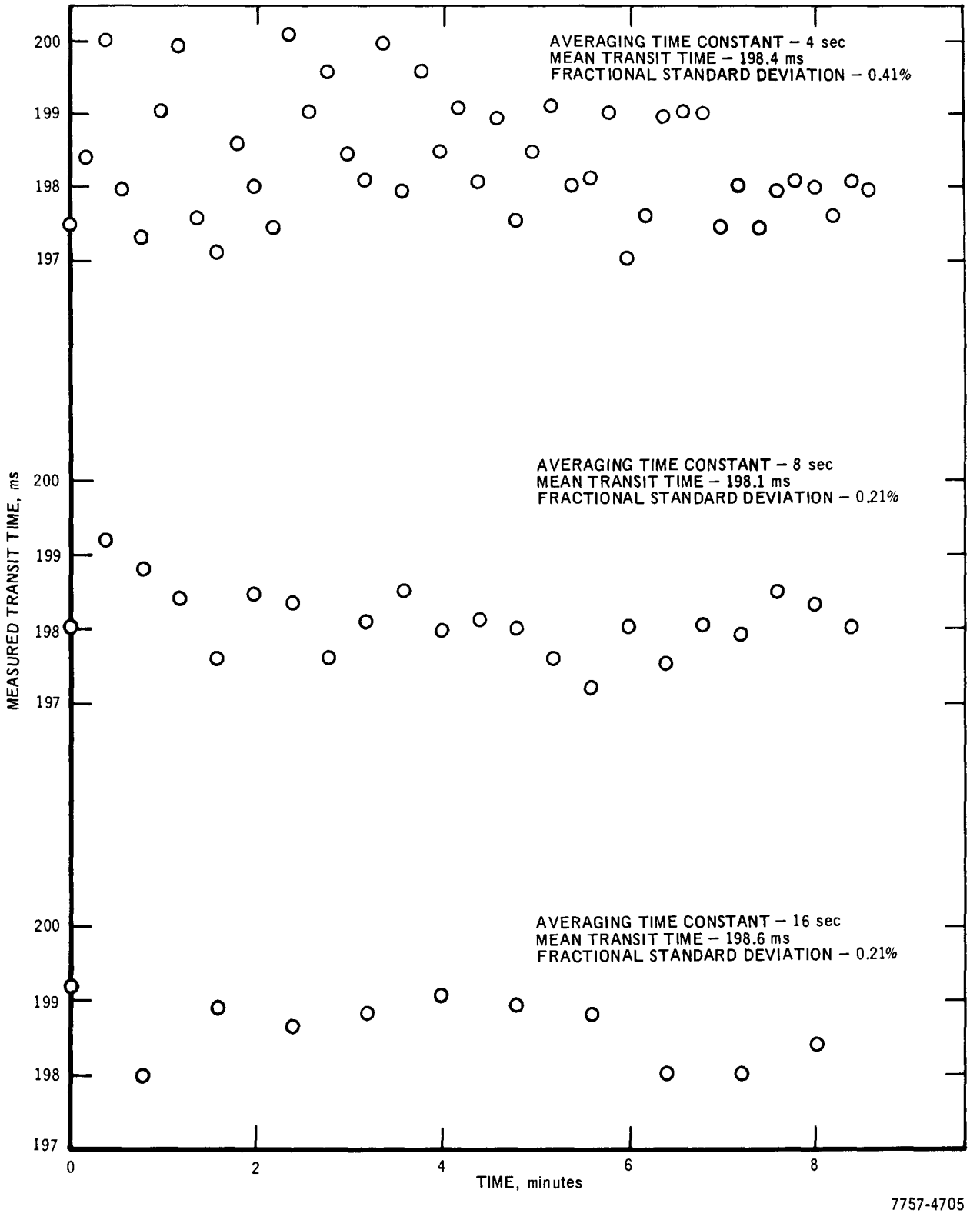

Figure 10. Transit Time Estimates versus Time and Averaging Time Constant for Two Conductivity Sensors 12-Inches Apart

TABLE 1

COMPARISON OF FLOW VELOCITIES MEASURED BETWEEN PAIRS OF CONDUCTIVITY ELECTRODES AND BETWEEN PAIRS OF THERMOCOUPLES

Sensor	Distance (in.)	Measured Velocity (ft/sec)	
		Run 2	Run 3
Electrode Pair A - B	6	4.93	4.91
Electrode Pair B - C	12	4.96	4.94
Thermocouple Pair A - B	12	4.77	4.79
Thermocouple Pair C - D	12	4.94	4.91

flow, and temperature in the line was about 8° above room temperature. In the third test, the mass flow measurement system was used. The system worked satisfactorily; however, the dump tanks have not yet been calibrated.

During previous experimental programs, flow measurements in water with conductivity sensors, involved injecting salt solution into the flow stream ahead of the sensors. After a few minutes of testing, the loop system became contaminated with salt and had to be flushed. This technique was feasible for use in hydraulic test loops but offered no direct application to reactor systems.

Prior to preliminary loop operation, measurements of the electrical resistivity of the water to be used in the test loop were performed. These measurements revaled a temperature coefficient of about 0.5% per °F. Feasibility tests were conducted to determine if thermal eddies could be detected by conductivity sensors. Positive results would imply that conductivity sensors could possibly be used to measure flow velocity in water reactors. If thermal eddies could be detected by using conductivity sensors, it would not be necessary to inject salt solution in the test loop and tests could be run continuously for long periods without loop contamination.

To check on this possibility, a simple test was conducted in the test loop by using the first conductivity test section. Signals from five in-line electrodes were recorded on the Brush chart recorder as a small stream of hot water was injected into the flow stream at the inlet to the test section. Results indicate

that thermal eddies can readily be detected by use of conductivity electrodes. Eddy patterns observed in the chart recording were found to propagate for distances up to at least 5 ft and for periods up to at least 4 sec, depending on flow velocity.

Plans for preliminary loop testing were changed to eliminate the use of salt injection and, instead, demonstrate the correlation flow measurement technique by using hot water injection only.

III. EVALUATION OF EFFORT TO DATE

The planning, sensor studies, instrumentation development, loop fabrication and initial loop testing have progressed well. Specific accomplishments since the start of the program in late January 1968 include: preparation of first conductivity test section; analysis of thermocouple mounting and time response problems; development of a fin structure for mounting and supporting in-stream thermocouples; development of a thermocouple response comparitor for assembly line matching of thermocouple time response; fabrication of sixty, 20-mil, grounded-junction, sheathed thermocouples; design of the first thermocouple test section; completion of the first two-thermocouple fin assemblies; fabrication of matched signal conditioning filters for the recording system; modification of the delay line to improve phase linearity versus frequency and simplify cross correlation measurements; modification of the hydraulic test loop to include a water dump system for accurate flow measurement; fabrication of a flow test programmer for automatically controlling the recorder and dump system during tests; feasibility tests involving detection of thermal eddies by conductivity electrodes; fabrication of the first TC test section; demonstration of the correlation flow measurement technique; checkout operation of the hydraulic test loop; verification that thermal eddies can be detected with conductivity cells; simultaneously obtaining flow velocity measurements with conductivity electrodes and thermocouples; and provision of preliminary estimates relating flow measurement precision to data sample length and averaging time.

The initial studies performed with thermocouples have shown that the required time response matching can be readily achieved. Conductivity cell studies have resulted in several possible designs for use in large pipes. The

indications that conductivity cells can be used to detect thermal eddies, mean that no longer is it necessary to inject salt solution in the hydraulic loops to make flow measurements. Hydraulic flow tests, therefore, could be conducted continuously without contaminating the test loop. These results also imply that conductivity sensors could possibly be used to measure flow velocity in water reactors.

During the next quarter, detailed parameter tests will be conducted with thermocouples and conductivity sensors in various: sizes of test sections, installation configurations, and flow conditions.